# Motion-Corrected Magnetic Resonance Imaging of the Fetal Heart

Van Amerom, Joshua Frederik Pieter

*Awarding institution:*
King's College London

# Motion-Corrected Magnetic Resonance Imaging of the Fetal Heart

Joshua FP VAN AMEROM

Thesis submitted in partial fulfilment of the requirement for the degree of
**Doctor of Philosophy** of **King's College London**

2018

School of Biomedical Engineering & Imaging Sciences
King's College London

KING'S College LONDON

# Abstract

Magnetic resonance imaging (MRI) is a versatile imaging modality that is widely used to assess the morphology, function and tissue characteristics of the human heart. However, evaluation of the fetal heart relies principally on ultrasound, as fetal cardiac MRI is limited by the challenges associated with imaging a small, rapidly beating heart that is subject to various regular and spontaneous movements. If these challenges can be overcome, MRI has the potential to provide multi-planar and volumetric images that may serve as an adjunct to ultrasound for screening of structural cardiac anomalies.

This thesis explores the strengths and limitations of MRI with the aim of developing an acquisition and reconstruction strategy to visualise the fetal cardiovascular system in the presence of fetal and maternal motion. Methods are presented that use rapid dynamic MRI to resolve the beating fetal heart in utero and retrospective image-based techniques to achieve cardiac synchronisation, motion correction, outlier rejection and cine reconstruction. When combined, these techniques form a motion-tolerant framework for fetal cardiac MRI.

The framework is first established for two-dimensional cine reconstruction from single-slice dynamic balanced steady state free precession MRI. The framework is then extended to three-dimensions using volumetric reconstruction techniques for scattered multi-planar images. Finally, the potential for simultaneous reconstruction of a three-dimensional cine and fully-encoded velocity mapping is explored in a preliminary study using the velocity information encoded in the phase of MRI data.

The proposed frameworks were tested on human fetal subjects, including many with congenital heart disease, imaged at 1.5T, and validated using in vivo and simulation data. The results show this is a promising framework for comprehensive fetal cardiac MRI, overcoming the key challenge of motion to enable further detail in studies of the fetal heart and great vessels.

# Acknowledgements

I am forever grateful to have participated in some small way in the advancement of biomedical science and to those that have supported these endeavours.

First, I must acknowledge my supervisor, Jo Hajnal, and his wisdom and insight, and my gratitude to him for his endless willingness to share some of it with me. His continued support and understanding throughout this work has been immeasurable, and his ability nurture the strengths of those around him and find ways for them to succeed has been of particular benefit to me.

It has been a pleasure working with all of the amazing people at King's College London and Evelina Children's Hospital. I've gained a lot interacting with so many talented physicists, engineers, cardiologists, radiographers and coordinators. The many achievements made by this group is a testament to the people behind them. I'd like to thank everyone that facilitated the work in this thesis, particularly David Lloyd, Maria Deprez, Shaihan Malik, Anthony Price and Kuberan Pushparajah.

On a more personal note, I'd like to acknowledge the role of Chris Macgowan and Mike Seed whose early mentorship succeeded in developing my interest in this field and helped build the confidence to make the leap to take on this research.

There are also those outside the medical science community who's support has been critical. Thank you to my sister, mother and family for always being there despite the distance. And to my friends here in London, who might not understand my work but who've understood me and that means more to me than they probably know.

None of this would have been possible without the support of my partner, Caitlin. I am thankful for her courage in taking on this adventure and for being there with me through the highs and lows. Despite some sacrifices, we've learned a lot. I look forward to casting our eyes upwards together and finding new stars to sail by.

# Contents

# List of Figures

# List of Tables

# List of Acronyms and Abbreviations

**Acronyms**

| | |
|---|---|
| 2D | two dimensional |
| 3D | three dimensional |
| bSSFP | Balanced Steady State Free Precession |
| CHD | congenital heart disease |
| DAQ | data acquisition |
| ECG | electrocardiogram |
| FOV | field of view |
| FWHM | full width at half maximum |
| GRAPPA | generalised autocalibrating partially parallel acquisition |
| GRE | gradient echo |
| MC | motion correction |
| MOG | metric optimised gating |
| MR | magnetic resonance |
| MRI | magnetic resonance imaging |
| NMR | nuclear magnetic resonance |
| NRMSE | normalised root mean square error |
| PE | pericardial effusion |
| PNS | peripheral nerve stimulation |

| | |
|---|---|
| PSF | point spread function |
| RF | radio frequency |
| RMSE | root mean square error |
| ROI | region of interest |
| SAR | specific absorption rate |
| SENSE | sensitivity encoding |
| SNR | signal-to-noise ratio |
| SPL | sound pressure level |
| ssTSE | single-shot turbo spin echo |
| STIC | spatio-temporal image correlation |
| TE | echo time |
| TR | repetition time |
| TRE | target registration error |
| US | ultrasound |

**Anatomical Abbreviations**

| | |
|---|---|
| AAo | ascending aorta |
| Ao | aorta |
| DA | ductal arch |
| DAo | descending aorta |
| IVC | inferior vena cava |
| LA | left atrium |
| LV | left ventricle |
| PA | pulmonary artery |
| RA | right atrium |
| RV | right ventricle |
| RVOT | right ventricular outflow tract |
| SVC | superior vena cava |

# Chapter 1

# Introduction

The ability to visualise the heart in utero has transformed fetal cardiac medicine. Fetal echocardiography, the primary imaging modality used in fetal cardiac medicine, has advanced our understanding of prenatal cardiovascular development and contributed significantly to improved outcomes of high-risk cardiac pathologies. In postnatal subjects, magnetic resonance imaging (MRI) is the standard for the assessment of cardiac morphology and function, however MRI of the fetal heart has been limited by the challenges associated with imaging a small, rapidly beating heart that is subject to various regular and spontaneous movements within the context of the maternal torso.

While motion remains a significant challenge in fetal cardiac MRI, the success of emerging techniques for high-resolution depiction of the fetal brain using retrospective motion correction and volumetric image reconstruction of two-dimensional MRI suggest a unique potential for three-dimensional mapping of the fetal heart and great vessels.

## 1.1 Aims

This thesis explores the use of dynamic imaging to resolve the beating fetal heart in conjunction with retrospective reconstruction to combine the data as a single cardiac cycle in a cine image series. The aim of this work is to develop an MRI acquisition and reconstruction strategy to visualise the fetal cardiovascular system in the presence of maternal and fetal motion, first in two spatial dimensions (2D) and

then in three (3D).

## 1.2 Thesis Outline

This thesis is divided in to six main chapters. The chapters that follow this introduction are described below.

**Chapter 2 - Background** provides an overview of the background central to an understanding of the challenges and potential utility of in utero MRI of the fetal heart. The structure and function of the fetal heart and fetal movements are first described in detail, followed by a review of the screening and management of fetal congenital heart disease and structural cardiac anomalies using ultrasound and MRI.

**Chapter 3 - Methodology** reviews the MRI methodology that form the basis of the work in the following chapters. The first sections cover the fundamentals of MRI and the balanced steady state precession imaging sequence, commonly used in cardiac MRI. The remaining sections review various aspects of MRI that inform the approach to fetal cardiac MRI in this thesis, including k-space sampling strategies, time-resolved acquisition, minimisation of image artefacts and techniques for rapid imaging.

**Chapter 4 - 2D Cine Reconstruction from Single-Slice Dynamic MRI** describes the development of a dynamic MRI acquisition and image-domain 2D cine reconstruction strategy to depict the fetal heart in the presence of maternal and fetal motion using retrospective motion correction and outlier rejection.

**Chapter 5 - 3D Whole-Heart Cine Reconstruction from Multi-Planar Dynamic MRI** describes work, building on the previous chapter, to generate a 3D cine representation of fetal cardiovascular anatomy in utero from multi-planar 2D dynamic MR images, without the need for maternal breath-hold or significant manual processing.

**Chapter 6 - Conclusions** closes the thesis with a summary of results and the impact of this research, along with a discussion of potential future directions and a survey of concurrent developments in fetal cardiac cine MRI.

**Publications and Software** lists the journal articles, conference presentations and code repositories published in relation to the work in this thesis.

# Chapter 2

# Background

This chapter is an overview of the background central to an understanding of the challenges and potential utility of in utero MRI of the fetal heart. Topics discussed include the structure and function of the fetal heart (§2.1), fetal movements (§2.2), screening and management of fetal congenital heart disease and other structural cardiac anomalies (§2.3) and prenatal ultrasound (§2.4) and MRI (§2.5). Additional details related to the methodological basis of the novel contributions of this thesis are provided in Chapter 3.

## 2.1 The Fetal Heart

The fetal heart begins development with the formation of a primary heart tube during the third week of gestation and begins to pump blood [1]. Over the next five weeks this structure combines with cells contributed by additional heart fields and undergoes a process of looping and septation to form the four chambers and paired arterial trunks seen in the neonatal heart. At twelve weeks gestational age the heart is normally positioned within the chest and the atrioventricular and arterial valves have developed to the point that the fetal heart resemble a miniaturised adult heart [2].

### 2.1.1 Anatomy

#### Cardiovascular Structures

The fetal cardiovascular system is made up of four chambers and the vessels that connect the heart to the pulmonary and systemic vascular systems, much as it is in the postnatal heart, as shown in Figure 2.1. Two upper chambers, called atria, receive blood in to the heart from the pulmonary and systemic systems while two lower chambers, called ventricles, discharge blood from the heart. Septa divide the chambers. The base and apex describe the upper portion of the atria and the tip of the left ventricle, respectively. The right atrium receives blood from the venae cavae while the left atrium receives blood from the pulmonary veins. The right ventricle receives blood from the right atrium via the tricuspid valve and discharges blood to the pulmonary artery via the semilunar pulmonary valve. The right ventricle is characterised by coarse thick muscular tissue bands called trabeculations at the apex. The prominent trabeculation crossing the lower part of the ventricles is called the moderator band. The left ventricle receives blood from the left atrium via the mitral valve and discharges blood to the aorta via the semilunar aortic valve. Fine, rather than coarse, trabeculations appear in the left ventricle as well as two prominent papillary muscles. The entire heart is surrounded by the pericardium, a sac filled with fluid that protects the heart located in the middle of the thorax.

The fetal heart differs from the postnatal heart in the open shunts that allow for streaming of blood between structures that are normally isolated in the neonatal heart (§2.1.2). These shunts include an opening in the atrial septum, called the foramen ovale, and a vessel connecting the pulmonary artery to the proximal descending aorta, called the ductus arteriosus. These shunts normally close within minutes to hours after birth.

#### Position

The heart is normally positioned in the chest with the morphological left side of the heart on the left side of the fetus. The true long axis of the heart traces a line from the apex to the middle of the left atrioventricular valve. The long axis of the fetal heart is oriented 45 degrees to the left of the anterior-posterior plane and is nearly in the transverse plane as the large fetal liver lifts the diaphragm and apex of heart so that it sits slightly inferior to the base [3]. This differs from the postnatal heart where there is a clear superior-inferior tilt in the long axis. The long axis defines the standard

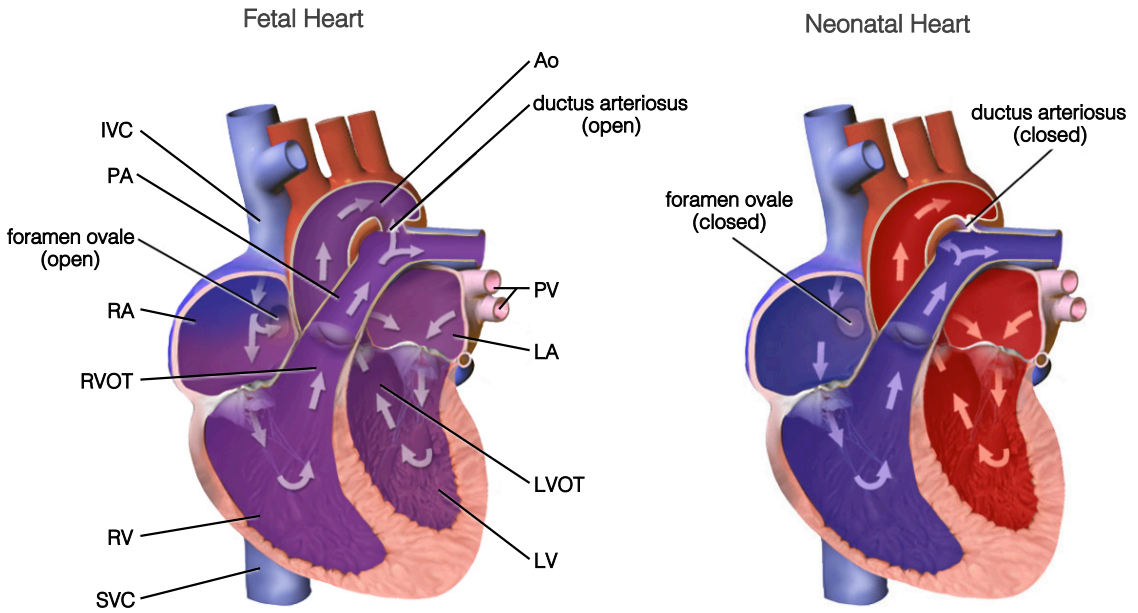


**Figure 2.1:** Structures of the fetal and neonatal heart. Shunts connecting the atria (foramen ovale) and great arteries (ductus arteriosus) are open in the fetal heart and normally close within minutes to hours after birth. Cardiac anatomy is labelled as inferior (IVC) and superior (SVC) vena cava, pulmonary veins (PV) and artery (PA), left (LA) and right (RA) atria, left (LV) and right (RV) ventricles, left (LVOT) and right (ROVT) outflow tracts, and aorta (Ao). Colour represents oxygenated (red) and deoxygenated (blue) blood. Figure adapted from perinatal circulation diagram by Blausen Medical under CC BY-SA 4.0.

planes of the heart, namely the short axis plane and the horizontal and vertical long axis planes. The short axis of the heart is a plane perpendicular to the long axis at the middle of the left ventricle. The horizontal long axis plane is perpendicular to the short axis plane and approximately transverse relative to the fetal torso. The vertical long axis plane is oriented in the superior-inferior direction and perpendicular to the short axis. These axes are used as standard cardiac imaging planes with additional planes often referred to as 'double oblique'.

### Size

Viewed in a transverse cross-section of the fetal torso, the heart occupies approximately one third of the thorax and has a circumference of about one half of the thorax [4]. The dimensions of the heart increase with advanced gestational age as the fetus grows [5]. At twelve weeks gestational age, the total length of the heart is no more than 8 mm and increases with rapid fetal development to double in size by the 17th week and triple in size by the 21st week [2]. Figure 2.2 shows fetal cardiac dimensions measured in 130 singleton pregnancies using ultrasound [6]. According to these data, the inner diameter of the right ventricle at end-second

trimester (26 weeks) and mid-third trimester (33 weeks) is 10 and 14 mm, respectively, while the inner diameter of the left ventricle is 9 and 13 mm, the ascending aorta is 4 and 6 mm, the pulmonary artery is 5 and 7mm, the ductal arch is 3 and 4 mm, and the inferior vena cava is 3 and 4 mm.

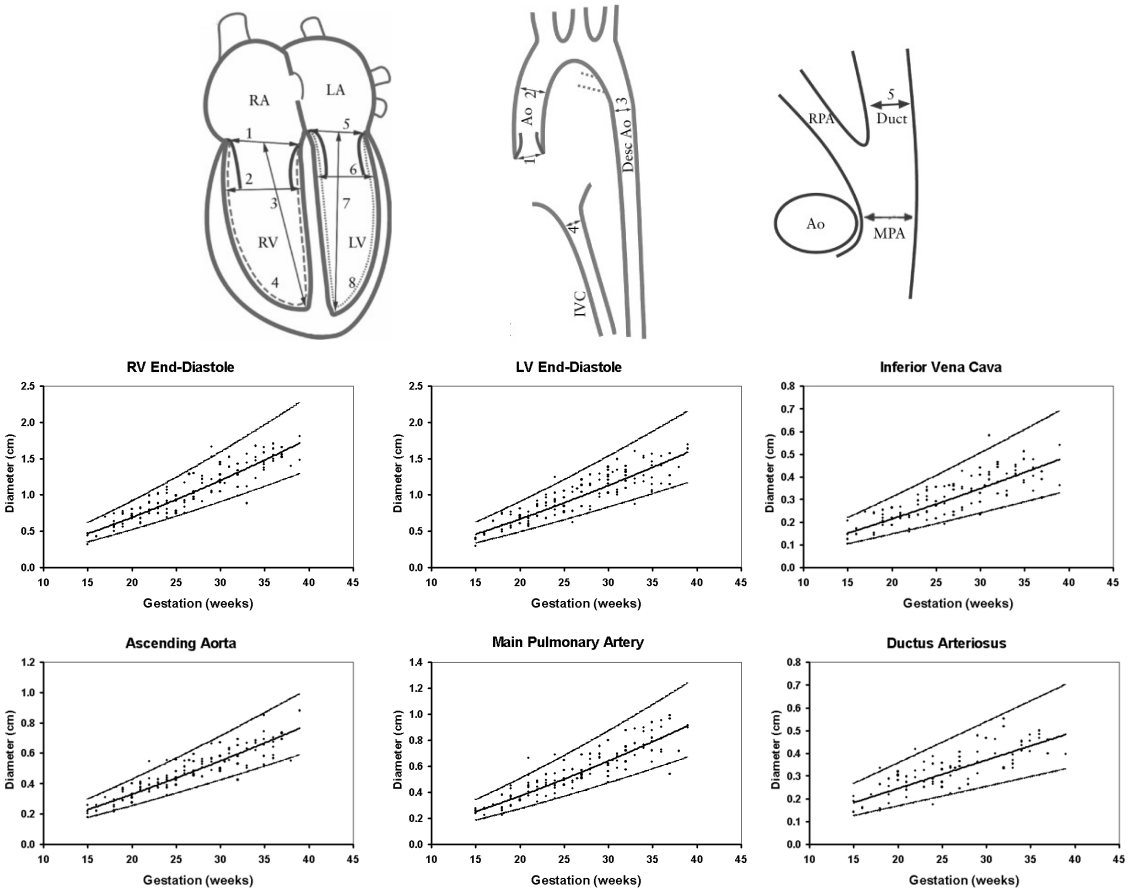


**Figure 2.2:** Fetal cardiac dimensions measured in 130 singleton fetuses using ultrasound. Scatter plots show the relationship between the size of the respective cardiac dimension gestational age with solid lines representing the regression fit and 95% confidence interval. Adapted from 'Development of Z-scores for fetal cardiac dimensions from echocardiography' by Schneider *et al.* [6] Figure 1 and Supporting Figure 1 under license from John Wiley & Sons, Ltd.

## 2.1.2 Physiology

### Cardiac Cycle

The heart beats in a periodic manner as the heart muscles contract to eject blood (systole) and then relax so that the chambers fill with blood (diastole). Ventricular systole starts with the Q deflection immediately preceding the R wave in the electrocardiogram waveform. The duration of the cardiac cycle is called the RR-interval, and is often stated as heart rate in beats per minute (bpm). The range

of normal fetal heart rates is 120–160 bpm ($5^{th}$–$95^{th}$ percentiles) [7]. As shown in Figure 2.3, the range is broader when considering a larger percentile spread, e.g., 105–180 bpm ($0.5^{th}$–$99.5^{th}$ percentiles). Beat-to-beat variation is generally low in the fetus; the median standard deviation of the RR-interval over 5 minutes of ECG recordings performed in a study of 56 mid- to late-gestational age fetal subjects was 15.3 ms, ranging from 11.2 to 18.7 ms [8]. The fetal heart rate is stable during MRI [9], though an increase in heart rate will occur during fetal motion.

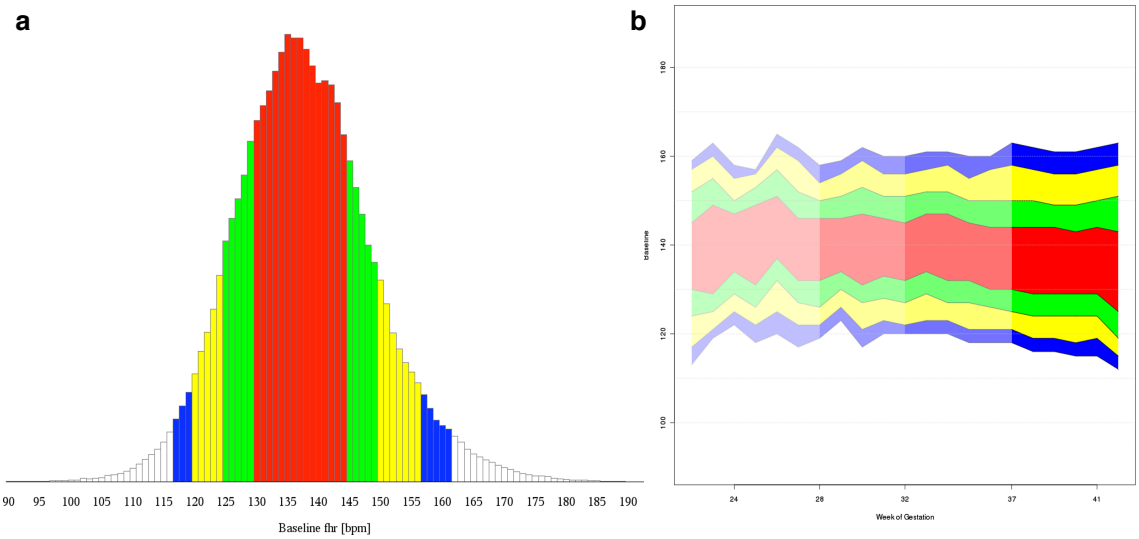


**Figure 2.3:** Distribution of baseline fetal heart rate (fhr), in beats per minutes (bpm), measured in over 78,000 cardiotography tracings [7]. (**a**) Histogram of all measured baseline fetal heart rate values and (**b**) quantile bands plotted against fetal gestational age. Red bars comprise $25^{th}$ to $75^{th}$ percentile, red and green ones $12.5^{th}$ to $87.5^{th}$ percentile, red, green and yellow bars $5^{th}$ to $95^{th}$ percentile and all bars except white ones comprise $2.5^{th}$ to $97.5^{th}$ percentile. Adapted from Figures 1c and 2 in 'What is the normal fetal heart rate' by Pildner von Steinburg *et al.* under CC BY 3.0.

### Circulation

In the postnatal heart, blood follows a serial path, once the ductus arterious and foramen ovale close, as streaming is no longer possible (Fig. 2.1). Deoxygenated blood returning from the systemic system enters the right atrium through the vena cava and then passes to the right ventricle. The right ventricle then pumps blood through the pulmonary arteries to the lungs to be oxygenated. Oxygenated blood returning from the lungs enters the left atrium through the pulmonary veins. This blood then fills the left ventricle which delivers the blood to the systemic system.

Fetal circulation differs from postnatal circulation due to the presence of shunts that modify the circulatory system to include placenta, as described in Figure 2.4. In the

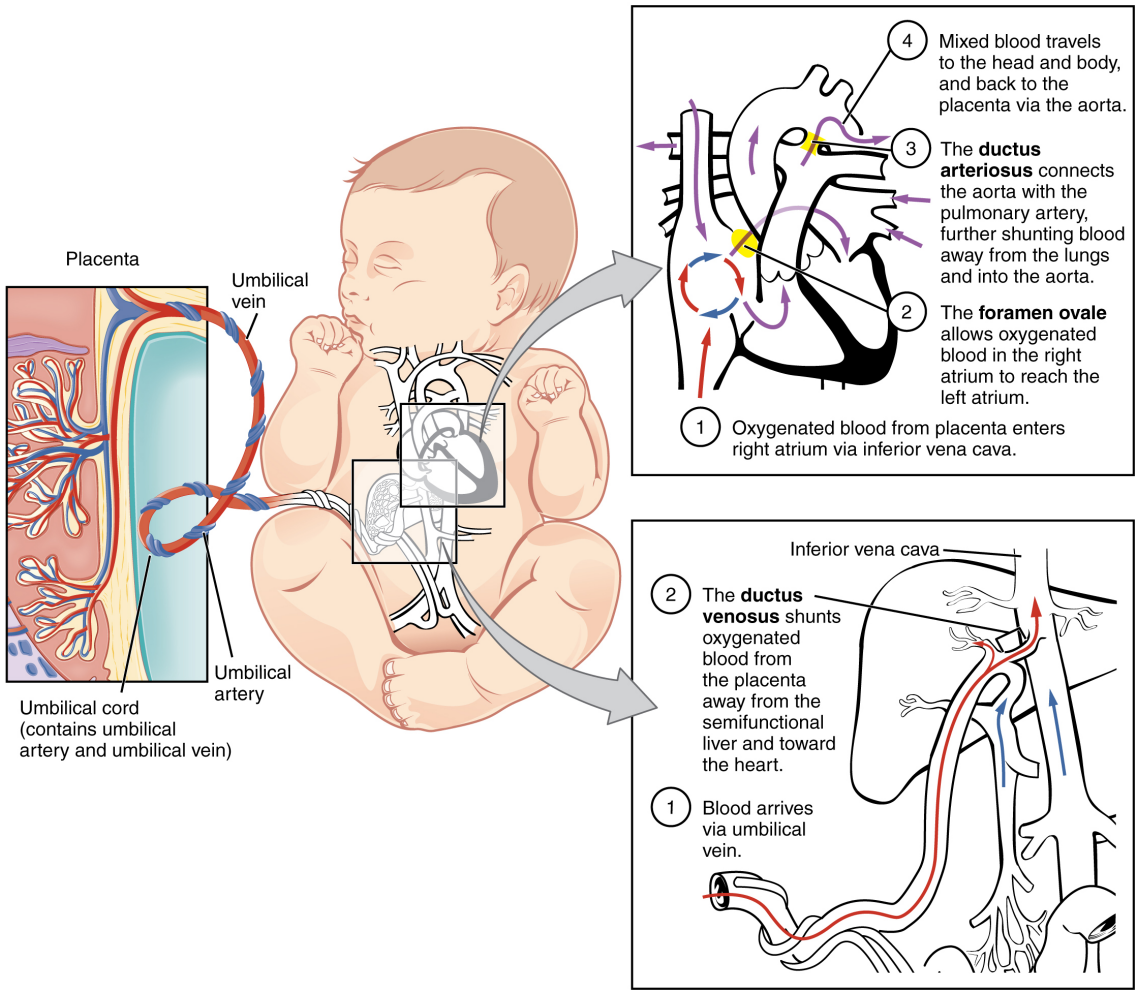


**Figure 2.4:** The fetal circulatory system includes three shunts to divert blood from undeveloped and partially functioning organs, as well as blood supply to and from the placenta. Fetal circulation diagram by OpenStax used under CC BY 3.0.

fetus, gas exchange occurs in placenta, rather than in the lungs. Nutrient delivery, waste elimination and thermoregulation also occur at the placenta via the maternal circulation. Oxygenated blood is carried from the placenta to the fetus by the umbilical vein. The ductus venosus shunts this oxygenated blood away from the liver and toward the fetal heart via the inverior vena cava. Some of this oxygenated blood is then shunted through the foramen ovale from the right to the left atrium so that it can be supplied to the head and upper body by the left ventricle. As no blood flow is required to the lungs for gas exchange, some of the blood leaving the right ventricle is shunted through the ductus arteriosus to the descending aorta, redirecting blood to the placenta instead of the lungs. This circulation allows for adaptation and survival in utero in the presence of a disrupted cardiovascular anatomy, that may not be possible after transition to postnatal circulation.

## 2.2 Fetal Movements

The fetus exhibits a range of movements in utero, including full-body general movements, localised movements involving isolated segments of the fetal body, and breathing movements comprising deep diaphragmatic and abdominal wall muscular activity. Fetal movements in the last fifteen weeks of gestation have been described comprehensively in a recent book by Piontelli [10] on which the majority of the description in this section is based. Many of the findings shared by Piontelli are derived from ultrasound observation sessions lasting 30 minutes or longer. Examples of typical in utero observation sessions are shown in Figure 2.5 for fetuses of 15, 27 and 38 weeks gestational age, including coding of episodes of fetal movement.

### 2.2.1 General Movements

General fetal movements are bursts of full-body motion lasting from a few seconds to minutes, excluding short disturbances such as hiccups and startles. General movements change with gestational age. From about twelve weeks gestational age gyrations of the whole body are very frequent and may include positional changes, which become less common from 25 weeks. There is an overall decrease in the frequency of general movements from 27 weeks, however the duration of the episodes increases. From 29 weeks, the fetal head becomes increasingly prominent in general movements and in the last few weeks of pregnancy head rotations often lead the body though mobility is reduced with increased occupancy of the uterus. However, the frequency of fetal trunk movements during MRI is relatively constant across gestational age, occurring a median of 12% of the time according to a MRI study of motion of 37 healthy fetuses [11].

### 2.2.2 Localised Movements

Piontelli describes isolated motion of the head, arms and legs as localised movements. These movements increase in frequency and duration from mid-gestation to term, but are usually shorter in duration than general movements. Hand and arm motions include reaching and touching or grasping, such as hand-face contact, which is common from 30 weeks gestational age. The legs are used for movement in early gestation while stepping motions are more common in later gestation. Leg movements increase from 25 weeks gestational age, with flexion occurring more

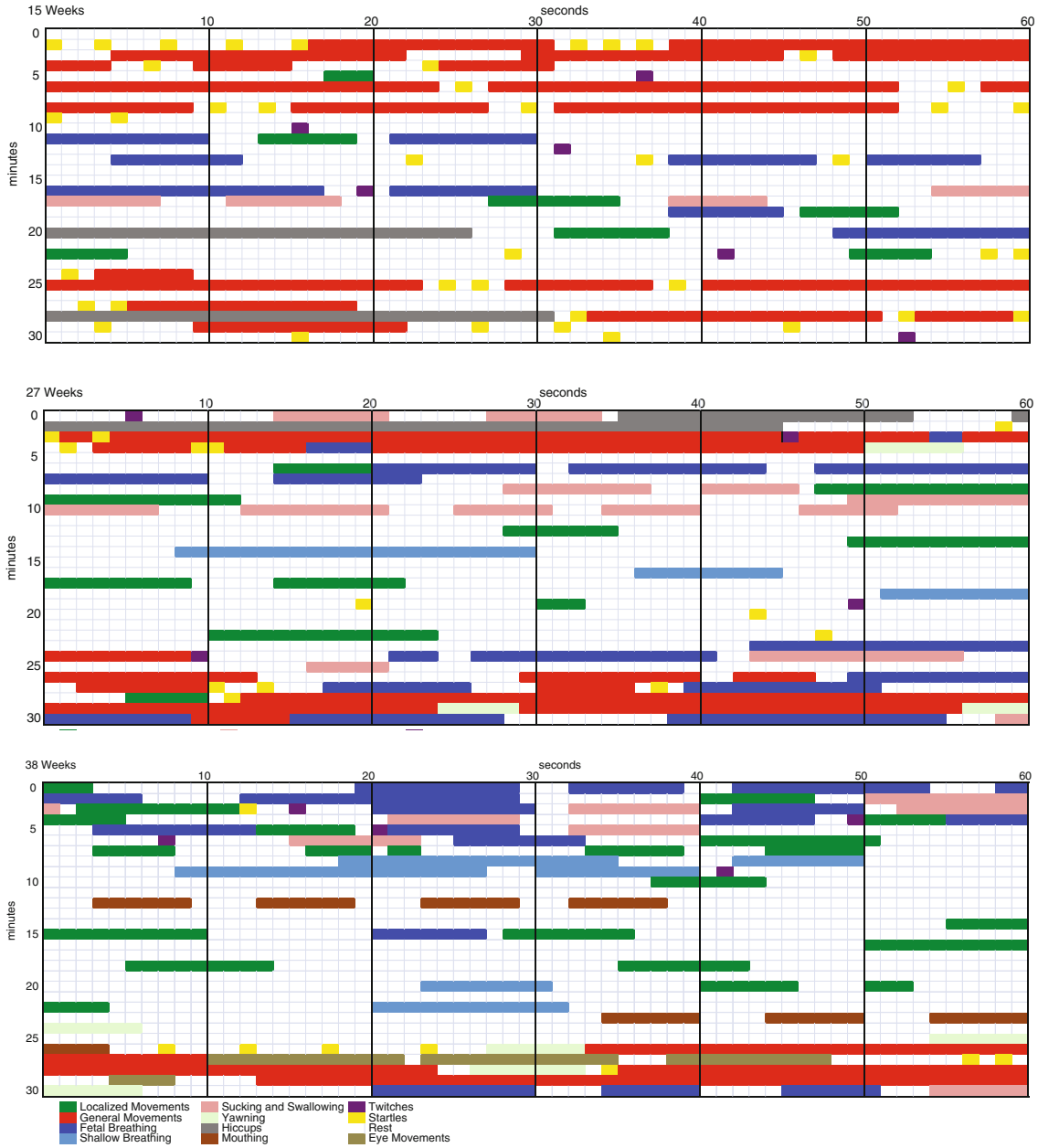


**Figure 2.5:** Fetal movements observed during ultrasound observation sessions at 15, 27 and 38 weeks gestational age. Each small rectangle represents one second of observation, with the observation time proceeding left to right (seconds) and top to bottom (minutes). Each fetal movement is represented by a coloured bar corresponding to a specific movement. General movements (red) are fragmented at 15 weeks but merge in to longer episodes at later gestational ages. At the same time, both localised movements (green) and deep (dark blue) and shallow (light blue) breathing movements become more prevalent with increased gestational age. Adapted from 'Development of Normal Fetal Movements' (2015) by Piontelli [10] Tables 2.1 and 9.1 under license from Springer Nature.

frequently than extension.

### 2.2.3 Breathing Movements

Prenatal breathing movements occurs in all animals that rely on aerial respiration after birth in order to prepare for the requirements of the postnatal environment. In the human fetus these movements are episodic, increasing in duration and frequency as pregnancy advances, though long episodes ($>$30 s) are rare, and the mean breath-to-breath period is 0.8 seconds. Prior to 26 weeks, breathing movements do not occur at the same time as other movements, but from 27 weeks there is occasional coincidence of breathing and general movements. Breathing movements involve either deep or shallow diaphragmatic and abdominal wall muscular activity. Deep breathing consists of vigorous downward movement of the diaphragm accompanied by slight inward motion of the anterior thorax (2-5 mm) and greater outward movement of the anterior abdomen (3-8 mm) at the level of the umbilicus. These movements can cause displacement of the heart. Shallow breathing consists of low outward movement of the the thorax and abdomen and do not cause significant displacement of the heart. Shallow breathing movements emerge at 20 weeks as short episodes during period of rest.

## 2.3 Structural Anomalies of the Fetal Heart

### 2.3.1 Congenital Heart Disease

Congenital heart disease (CHD) is a general term for a range of structural or functional abnormalities of the heart and intra-thoracic great vessels present at birth that arises from abnormal formation during fetal development [12]. Though reported incidence varies, it is widely accepted that CHD is present in 8 of 1000 live births [13]. CHD is the leading cause of infant morbidity in the Western world [14] making up 28% of all major congenital anomalies [13]. It is estimated that half of all children born with CHD will require medical or surgical intervention [15] and around 15% of all neonates born with CHD have a cardiovascular malformation that could cause circulatory collapse and death if undetected [16]. CHD can be present prenatally, where it is more prevalent than in the postnatal population due to fetal demise associated with the disease [15]. Furthermore, CHD present in the fetus results in widespread brain abnormalities and is associated with global impairment in devel-

opment, similar to premature newborns [17].

Major chromosomal abnormalities are the cause CHD in 5-8% of cases while environmental factors are the sole cause in a very small percentage of cases [18]. In most cases of CHD it is the interplay genetic abnormalities and environmental factors in most cases that leads to the malformation of the heart. Most lesions are well-tolerated in utero due to ability of fetal circulation to adapt, but become problematic when the heart transitions to postnatal circulation shortly after birth.

There are many types of CHD, ranging from minor structural alterations that resolve without intervention to complex defects, including combinations of small lesions to gross malformations, leading to morbidity and mortality. These lesions occur in the septa, valves or great vessels and impact the normal circulation and function of the fetal heart. The subtypes of CHD can be broadly categorised as malposition, discordance, septal defects, obstructions, hypoplasia, anomalous vessels and complex defects. Gross defects include malposition, such as abnormal situs, and discordance, including transposition of the great arteries where the aorta is connected to the right ventricle and the pulmonary artery is connected to the left ventricle. Septal defects may occur in the atrial, ventricular or atrioventricular septa. Obstructions include narrowing of the valve or vessel (stenosis), occlusion of the valves (atresia) or coarctation of the aorta (constriction). Hypoplasia describes the underdevelopment of either left or right side of heart leading to univentricular physiology, such as in hypoplastic left heart syndrome where the left ventricle and ascending aorta are very small. Anomalies of the vessels may occur as right aortic arch where the aorta passes to the right of the trachea, double aortic arch leading to a vascular ring, or missing connections between the pulmonary veins and the left atrium leading to either partial or total anomalous pulmonary venous connections. Complex defects are a combination of lesions, such as in tetralogy of Fallot that includes a large ventricular septal defect, pulmonary stenosis, hypertrophic right ventricle and an overriding aorta. Diagrammatic representations of fetal hearts with discordance (transposition of the great arteries), septal defect (ventricular septal defect), obstruction (coarctation of the aorta), hypoplasia (hypoplastic left heart syndrome) and complex defect (tetralogy of Fallot) are shown in Figure 2.6.

The worldwide birth prevalence of CHD subtypes was reported in a meta-analysis by van der Linde *et al.* [13], and is summarised in Figure 2.7. The most prevalent types of CHD are ventricular septal defects (34% of all neonates with CHD), atrial septal defects (13%), patent ductus arteriosus (10%), pulmonary stenosis (8%), tetralogy of Fallot (5%), coarctation of the aorta (5%), transposition of the great arteries (5%) and aortic stenosis (4%).

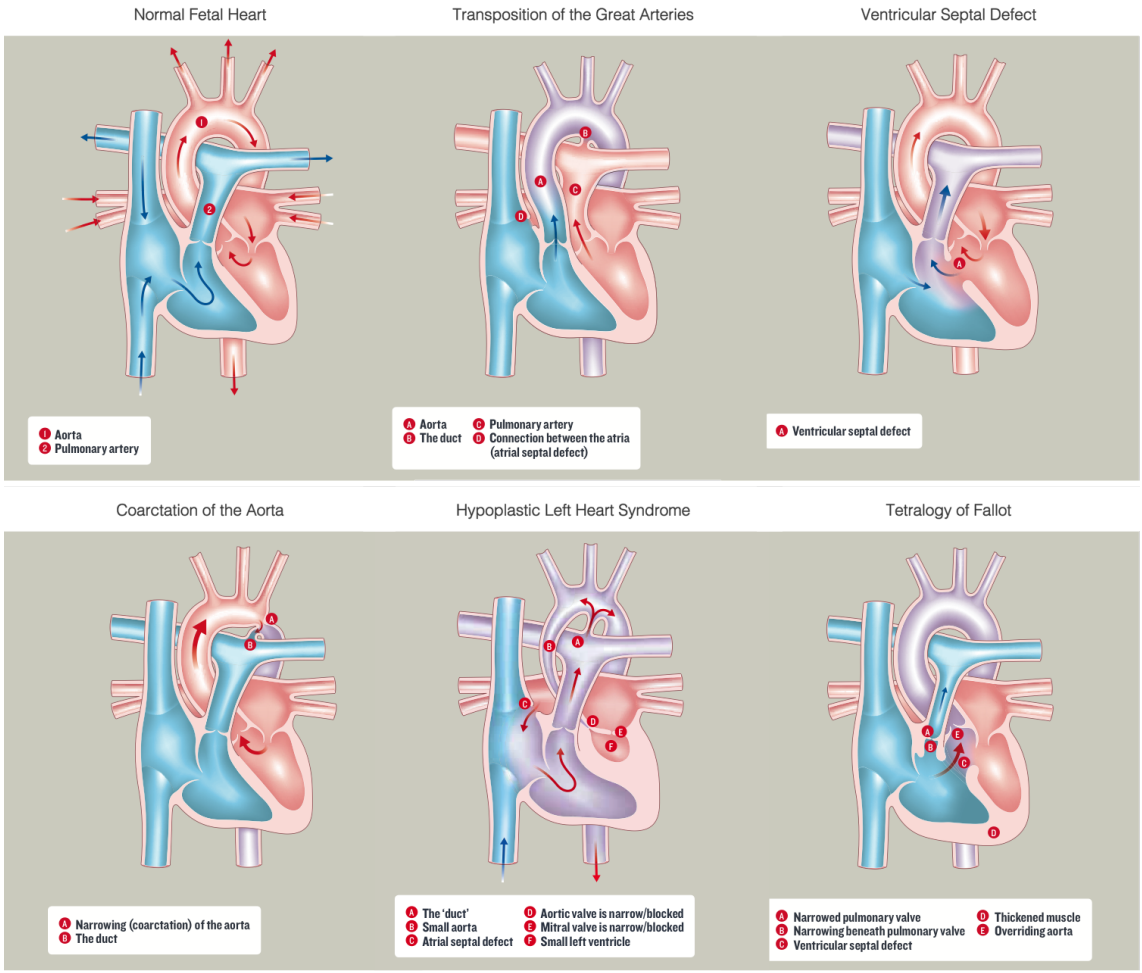


**Figure 2.6:** Diagrammatic depiction of a normal fetal heart and five different forms of congenital heart disease, including transposition of the great arteries, ventricular septal defect, coarctation of the aorta, hypoplastic left heart syndrome and tetralogy of Fallot. Adapted from British Heart Foundation congenital heart disease educational publication series.

A severity level of severe, moderate or mild describes the degree of neonatal care required [19]. Fetuses with severe CHD present as highly ill neonates and require intensive expert care. All cyanotic CHD, where the systemic blood is low in oxygen, are described as severe, including complete or dextro-transposition of the great arteries, both hypoplastic left and right heart syndromes, common arterial trunk, total anomalous pulmonary venous connections and any critical obstructions. Some acyanotic lesions are also considered severe, such as atrioventricular septal defects, large ventricular septal defects and severe obstructions. Fetuses with moderate CHD require monitoring as neonates but less intensive expert care than those with severe CHD. Moderate forms of CHD include aortic and pulmonary stenoses, coarctation of the aorta, large atrial septal defects and complex ventricular septal defects. Fetuses with mild CHD are often asymptomatic as neonates and lesions may resolve spontaneously, such as with small septal defects and mild obstructions.

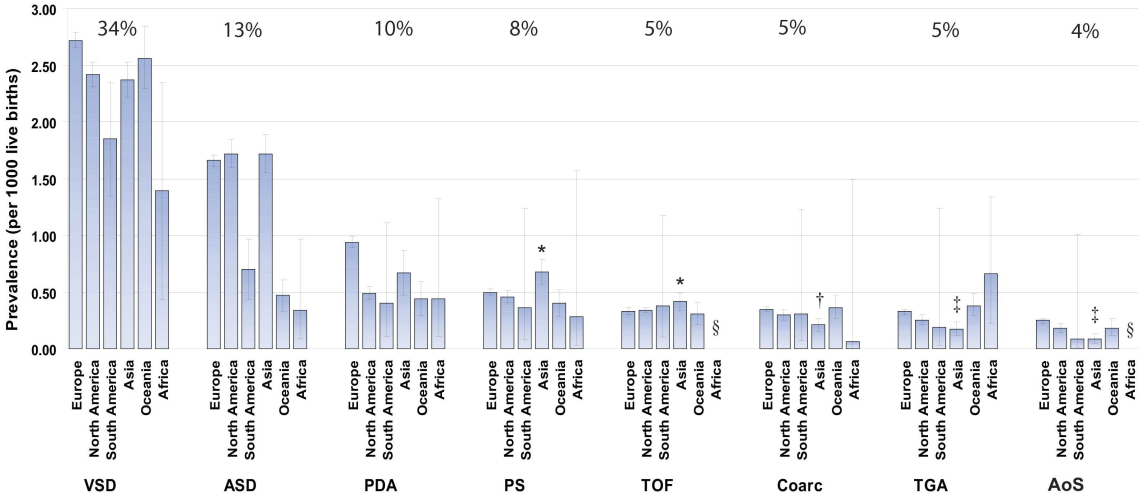


**Figure 2.7:** Birth prevalence of the eight most common congenital heart disease (CHD) subtypes by continent. Distribution of subtypes across all CHD cases is given as percentages above bars. The most common CHD subtypes at birth are ventricular septal defects (VSD), atrial septal defects (ASD), patent ductus arteriosus (PDA), pulmonary stenosis (PS), tetralogy of Fallot (TOF), coarctation (Coarc), transposition of the great arteries (TGA) and aortic stenosis (AoS). §No data on TOF and AoS birth prevalence in Africa were available. *Reported PS and TOF birth prevalence in Asia was significantly higher than in Europe and North America. †Reported Coarc birth prevalence in Asia was significantly lower than in Europe. ‡Reported TGA and AoS birth prevalence in Asia was significantly lower than in Europe , North America and Oceania. Chart from 'Birth Prevalence of Congenital Heart Disease Worldwide: A Systematic Review and Meta-Analysis' (2011) by van der Linde *et al.* [13] used under license from Elsevier.

### 2.3.2 Other Anomalies

#### Cardiac Tumours

Though most cardiac tumours are benign all cardiac tumours can disturb the development and function of the fetal and postnatal heart depending on the size and location of the tumour [20]. The most common benign cardiac tumours are rhabdomyoma, teratoma and fibroma [21], though the overall incidence of cardiac tumours in the paediatric population is rare [22].

#### Congenital Cardiac Diverticula

Congenital cardiac diverticula are a very rare malformation appearing as a pouch or sac branching out from the ventricles of the heart [23]. Aneurysms, commonly at the apex or base of the left ventricle, are fibrous and usually isolated. However, a muscular diverticulum, usually emerging from the apex of the left ventricle, is frequently associated with other congenital anomalies. Diverticula can alter the function of the

heart and are usually surgically resectioned due to the risk of rupture, heart failure and arrhythmia.

### 2.3.3 Screening

Obstetric screening is usually performed using ultrasound between 18 and 20 weeks gestational age to confirm gestational age, measure growth, check for multiple pregnancies and assess congenital malformation, including CHD. In cases with risk of cardiac anomalies, a dedicated follow-up fetal cardiac evaluation using ultrasound, described in detail in Section 2.4.1, is typically used to diagnose prenatal CHD. Indications for fetal cardiac evaluation include abnormal findings on routine obstetric screening as well as various risk factors including maternal metabolic disease and family history of CHD.

### 2.3.4 Management

Prenatal diagnosis of CHD plays a crucial role in the management of life-threatening malformations resulting in improved postnatal preoperative status and reduced postoperative morbidity and mortality [24]. Management may include further assessment using advanced techniques, counselling, intervention and planning for specialised delivery and perinatal care.

Advanced techniques may be used for further assessment in complex cases or when echocardiography is limited. Fetal heart rhythm can be measured by electrocardiography or magnetocardiography. Myocardial motion and mechanics using tissue Doppler and 2D speckle tracking ultrasound, while morphology and volumetry can be assessed by 3D and 4D ultrasound (§2.4.2). Techniques for fetal cardiovascular MRI (§2.5) are emerging for morphological assessment and flow quantification that may be used as complement to fetal echocardiography. MRI can also be used to check for associated extracardiac anomalies, particularly in the brain and lungs. Extracardiac anomalies can also be investigated using genetic testing or a detailed anatomical survey using ultrasound.

Insights regarding perinatal health derived from screening assessments inform parental counselling and manage parental stress [25]. Such information aids decisions around treatment, termination and palliative care.

As diagnostic capacities and accuracy have improved, management and treatment

of the fetus as a patient have become possible. Current fetal therapies range from administration of medication to minimally-invasive catheter procedures, with procedures for open fetal heart surgery being explored. Medication is mostly used for arrhythmia management and is administered to the mother and is delivered to the fetus via the placenta. Catheter procedures are used for some cardiac lesions that can progress from mild to severe during gestation resulting in irreversible damage and may be lifesaving or disease modifying for fetuses with certain types types of hypoplastic left heart syndrome, aortic stenosis or pulmonary atresia [26].

Prenatal screening also informs planning for specialised delivery and neonatal care. Such planning may include scheduling of an elective delivery at optimal gestational age and selection of a location with appropriate facilities for cases with postnatal compromise. For example, the transitional circulation can be managed by administering prostaglandin shortly after birth to prevent the duct from closing thus avoiding postnatal hemodynamic instability during the transition from fetal to neonatal circulation in cases with duct-dependent lesions. Other specialised postnatal interventions include ventilation for certain types of tetralogy of Fallot, atrial septosomy to enlarge the foramen ovale in newborns with transposition of the great arteries and atrial septoplasty in newborns with hypoplastic left heart syndrome.

## 2.4 Fetal Echocardiography

Ultrasound of the heart, referred to as echocardiography, is the standard for detailed diagnosis and evaluation of the fetal heart. In this modality, sonograms are produced by sending pulsed sound waves into tissue using a probe and creating an image from the sound echoes depicting the acoustic impedance of the tissue imaged. Two-dimensional (2D) B-mode ultrasound yields grayscale images, while the acquisition of serial B-mode images depicting motion over time is referred to as M-mode. Doppler ultrasound uses the Doppler effect to measure blood velocity and is referred to as colour flow Doppler when the measured velocity is shown using a colour scale, usually in combination with B-mode images for visualisation of the surrounding anatomy. M-mode and Doppler ultrasound are the principal modalities used in fetal echocardiography to provide non-invasive views of the fetal heart in standard cardiac planes, shown in Figure 2.8. The four chamber view is commonly acquired during routine obstetric screening to examine the relative size of the chambers and screen for defects of the septa and valves. Outflow tract and three-vessel views are sometimes also used. The use of routine obstetric ultrasound has lead to improved diagnosis of many congenital abnormalities [27] with inclusion of some

basic cardiac screening leading to detection in 10-26% of cases with CHD [26].

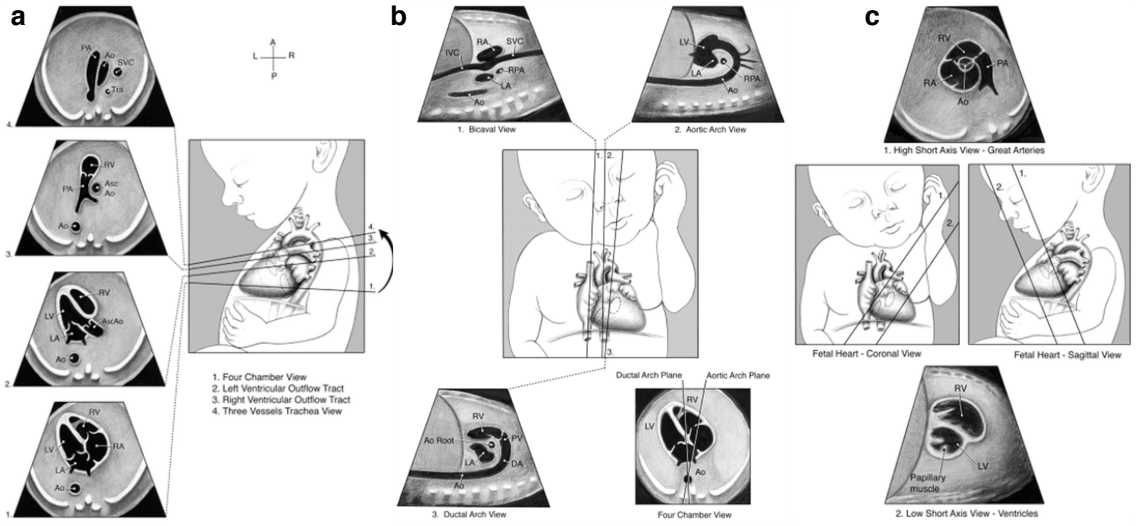


**Figure 2.8:** Standard views of the fetal heart used during echocardiographic examination. (**a**) Transverse scanning planes for fetal echocardiography include an evaluation of the (1) four-chamber view, (2,3) arterial outflow tracts and (4) the three-vessel and trachea view. (**b**) Sagittal views of the (1) superior and inferior vena cava, (2) aortic arch and (3) ductal arch. (**c**) (1) High and (2) low short-axis views. Cardiac anatomy is labelled for reference, including the aorta (Ao), left (LA) and right (RA) atria, left (LV) and right (RV) ventricles, pulmonary artery (PA), trachea (Tra), ductal arch (DA), inferior (IVC) and superior (SVC) venae cavae and the right pulmonary artery (RPA). Diagrams adapted from Figures 1–3 in 'AIUM Practice Guideline for the Performance of Fetal Echocardiography' [28] under license from John Wiley & Sons.

### 2.4.1 Cardiac Evaluation

Suspicion of structural cardiac anomaly on obstetric ultrasound is the leading reason for referral for detailed cardiac evaluation by fetal echocardiography, which consists of a comprehensive imaging of the connections and function of the heart [29]. Imaging is performed using M-mode ultrasound to resolve the dynamics of the heart since static images do not fully demonstrate abnormalities the cardiovascular system. A sequential segmental approach is used to analyse the fetal heart [30, 31], starting with a gross assessment of cardiac position and orientation, and then continuing on to include imaging of the cardiac structures encountered by blood passing through the cardiovascular system. This approach allows for definition of systemic and pulmonary venous connections; atrial and ventricular connections and morphology, including relative chamber size, wall thickness and septal anatomy; valve morphology and size; ventricular arterial connections; great artery size and positions; and arch size relative to each other and position relative to the trachea. Doppler ultrasound is

used to confirm valve function and vessel patency, as well as to assess blood flow patterns and peak velocities and ventricular inflows [26].

A positive diagnosis of CHD is confirmed in 40-50% of cases referred from obstetric ultrasound [26]. Detection rates of up to 90% for cases with severe CHD have been reported for fetal echocardiographic evaluations performed by experienced operators at tertiary care centres [26] and the use of comprehensive, standardised screening protocols have lead to a dramatic increase in detection of all CHD by fetal echocardiography performed in tertiary care centres in the Netherlands [32]. However, in a large study of discordance between fetal and postnatal diagnoses at a leading centre in France, it was found that fetal echocardiography failed to predict the need for immediate neonatal intervention in 1/10 cases [33]. The sensitivity of fetal diagnosis of CHD using echocardiography is also highly dependent on operator experience [34] and acquisition of the desired views can be problematic in cases with unfavourable fetal lie or maternal habitus. The ultrasound signal may be attenuated when imaging deep into the body, while bony structures and oligohydramnios can compromise the the ultrasound images.

### 2.4.2 3D Techniques

Methods for volumetric representation of the fetal heart using ultrasound have been introduced and continue to be developed [27]. These techniques include reconstructed and real-time approaches that allow for offline visualisation in arbitrary planes. Static reconstructions are possible but fail to provide important information about cardiac anatomy that is available in dynamic reconstructions [35].

Cardiac-gated 3D reconstructions are commonly performed using spatio-temporal image correlation (STIC) where multi-planar 2D ultrasound is compounded as a 3D volume with an additional temporal dimension for the cardiac cycle [36]. In the STIC algorithm, each 2D images are rearranged according to the phase in the cardiac cycle at which they were acquired, with cardiac phase based on an initial group-wise estimate of the average heart rate across the acquisition followed by adaptation of beat-to-beat variation of up to $\pm$ 10%. The reconstructed STIC volume is prone to artefact in the through-plane direction due to fetal movement and maternal breathing due to a long acquisition [26]. However a recent extension of the technique, where multiple artefact-free subvolumes are acquired using an electronic probe and compounded as a single volume dataset, has been shown to reduce overall artefact and improve resolution to some degree [37]. Robust methods to reconstruct cardiac-gated volumes from 2D ultrasound in the presence of fetal motion are currently in

early stages of development [38].

Real-time 3D fetal echocardiography acquires a single dynamic 3D dataset, removing the need for cardiac gating and image compounding at the cost of reduced resolution and field-of-view [39]. Though higher sensitivity has been reported for real-time 3D fetal echocardiography compared to the reconstructed technique in a prospective study of 50 mid-gestation fetuses [40], the published use of real-time 3D echocardiography in the fetus remains notably lower than the reconstructed technique.

Currently 3D echocardiography is not standard practice in fetal cardiac evaluation, but these techniques may be used routinely in the future for screening, qualitative assessment of cardiac structure and quantitative assessment of cardiac chamber size and function [26].

## 2.5 Fetal Magnetic Resonance Imaging

The use of fetal MRI was first reported over three decades ago [41, 42], coinciding with the introduction of commercial MRI scanners. Since then, advancement of imaging sequences and reconstruction techniques along with improvements to scanner and receiver coil hardware have expanded the capacities of MRI to image the fetus.

While ultrasound remains the primary modality for prenatal screening, MRI is now used as an adjunct to ultrasound in cases where diagnostic questions remain after ultrasound screening or high-quality ultrasound images cannot be obtained [43, 44]. However, fetal position, rib calcification, maternal obesity, and oligohydramnios may limit ultrasound, particularly at later gestational ages [26]. Compared to ultrasound, MRI allows for imaging of a large field of view, unrestricted by maternal body habitus and fetal presentation, that allows for examination of abnormalities in the context of the entire fetal body. Imaging in true anatomical planes is possible with MRI and multi-planar imaging is straightforward. MRI is also superior to ultrasound for differentiation of soft tissue characteristics and volumetric measurement [44]. Limitations of MRI, compared to ultrasound, include inconvenience and cost of the procedure, availability of scanners, and potential for degraded image quality in the presence of fetal movements due to longer acquisition times.

Currently, fetal MRI is used clinically in assessment of conditions of the central nervous system, pulmonary system and diaphragm, musculoskelatal system, and the

maternal placenta and cervix [44, 45]. Continued technical and research work continues to advance the field, with many developments in fetal brain MRI [46–49] and MRI of other fetal organs [48, 50] including the fetal heart [51].

MRI of the fetal heart is particularly challenging due to the size and complexity of the fetal cardiovascular system, a rapid heart rate, and challenges associated with cardiac gating and fetal movement. Over the past ten years, studies have been performed and techniques have been developed by a variety of international groups that have begun to address these challenges. A recent scientific statement on the diagnosis and treatment of fetal cardiac disease published by the American Heart Association highlights the potential of fetal cardiac MRI [26].

> *If the challenges relating to motion and cardiac gating can be overcome, MRI has the potential to provide high-resolution imaging of the fetal heart in multiple planes and to generate volume data sets with greater resolution than those obtained with ultrasound, offering the potential to provide robust quantitative evaluation of cardiac function and chamber volumes and to provide unique perspectives on venous and arterial anatomy, visceroatrial situs, and thoracic extracardiac malformations affecting fetal cardiovascular structure/function.*

Today, fetal cardiac MRI is recommended in the clinical evaluation of visceroatrial situs, venous returns and associated extracardiac malformations, with potential future use in the assessment of cardiac structure and ventricular volume and function [26]. Active areas of research in fetal cardiac MRI include both morphological and functional techniques. A variety of studies evaluating the utility of static and dynamic MR imaging for morphological assessment of cardiovascular anatomy have been published [52–59]. Non-contrast angiography [60] and tissue characterisation [59] have also been reported. Novel approaches for fetal cardiac gating have been introduced [61–63] leading to techniques for cine imaging [64, 65] and blood flow quantification [63, 66]. Techniques to measure of fetal blood oxygen saturation have also been proposed [67–70].

### 2.5.1 Safety

It is essential that the well-being of the fetus be ensured during MR scanning. Elements of the MR system that may pose a risk to the fetus include include the static magnetic field, time-varying gradient magnetic fields and radio frequency (RF) fields.

MRI is considered safe at 1.5 and 3.0 T in the second and third trimester [43]. It is widely recommended that MRI should be avoided during the first trimester as the fetus is most vulnerable to tetratogenic effects in the first trimester, though there is currently no data on risks of exposure in early gestation [71].

Heat deposition from RF exposure should be managed to ensure global and local heating are within specific absorption rate (SAR) limits associated with a rise in temperature of less than 0.5° C. Studies using models of a pregnant mother and fetus suggest the that fetal SAR and temperature rise will be within international safety limits when the scanner is operated at $<$ 2 W/kg whole body exposure for periods of less than 7.5 minutes [72]. Consequently, it is recommended that MR scanning be performed using a lower whole body SAR limit as a precautionary measure.

Rapid switching of the gradients can cause peripheral nerve stimulation (PNS) and loud acoustic noises. PNS is not of great concern when gradients are kept below mean threshold PNS since the fetus is contained within the maternal body where the induced currents that cause PNS are lower [71].

Gradient-induced acoustic noise is typically measured as A-weighted sound pressure level (SPL) in dB(A) to account for the relative loudness perceived by the human ear [73]. In the MRI environment, SPL can reach 120 dB(A) [74], however some protection is provided by the maternal anatomy surrounding the fetus with attenuation of around 30 dB(A) [75]. The degree of SPL attenuation has been shown to depend on the position of the fetus as well as the frequency of the sound [76, 77]. Though fetal sound exposure during MRI is relatively brief, it has been recommended that fetal exposure to sound during MRI be limited [9, 71], however, no specific limits have been defined. Given the incomplete data on the topic, local group guidelines set a limit of 115 dB(A) SPL exposure based on United Kingdom guidelines issued by the Medicines and Healthcare Products Regulatory Agency that recommend a safe limit of 85 dB(A) with hearing protection [78] and the 30 dB(A) attenuation in utero previously mentioned.

It is recommended that gadolinium-based contrast agents not be used during pregnancy due the potential of toxic effects observed in animal studies, though data in humans is limited [44]. While general anaesthetics have been used in the past to minimise fetal movement [79], direct fetal paralysis or sedation is now strongly discouraged [80].

### 2.5.2 Imaging Techniques

A variety of factors must be considered when imaging the fetus, in general, and the fetal heart, in particular, using MRI. Field strength and scanner performance must be limited to ensure fetal safety (§2.5.1). The imaging field of view should be large enough to cover the maternal anatomy surrounding the fetus to avoid fold-over effects. At the same time, spatial resolution must be sufficient to resolve the small fetal anatomy. Temporal resolution must also be considered when imaging the rapidly-beating fetal heart. Furthermore, short per-image and total scan times should used to reduce the impact of motion on intra- and inter-view image quality. Nearly all fetal MR is performed using 2D techniques as the duration of 3D acquisitions are long compared to fetal and maternal motion.

A range of sequences are used in fetal MRI currently, including single-shot turbo spin echo, spoiled gradient echo, steady state free precession, phase contrast, echo planar imaging and spectroscopy. The key features of these sequence are given below; extensive details of these sequences can be found in an excellent review article on fetal MRI by Gholipour et al. [45].

Single-shot turbo spin echo (ssTSE) is the most commonly used sequence in fetal MRI. The short per-shot duration of ssTSE provides images that 'freeze' the majority of non-cardiac fetal motion. Acquisitions are often accelerated using half-Fourier acquisition, sometimes in combination with parallel imaging, so that k-space for a single 2D image is collected in ~500–1000 ms. The T2-weighting in ssTSE images results in tissue contrast that is particularly beneficial for depicting anatomical detail in the fetal brain, lungs, placenta, fluid-filled cavities and the fetal profile [81]. However, blood flowing through the cardiovascular system has a hypointense intensity in ssTSE images since the movement of blood through the slice is faster than the spin echo used to generate signal. Due to these signal characteristics and the long acquisition time relative to the cardiac cycle, the heart appears as a nearly homogeneous structure with little definition of intra-cardiac features, as shown in Figure 2.9. The same signal characteristics are present in the blood within the extracardiac vasculature, however, due to reduced cardiac-related movement and the contrast provided by the surrounding hyperintense thymus and lung parenchyma, these vessels can be visualised in ssTSE images (Fig. 2.9a). ssTSE is usually acquired using interleaved slices to maximise the distance and time between the acquisition of overlapping or adjacent slices to avoid spin history artefact and minimise slice cross-talk [45].

Balanced steady state free precession (bSSFP) is a gradient echo sequence that

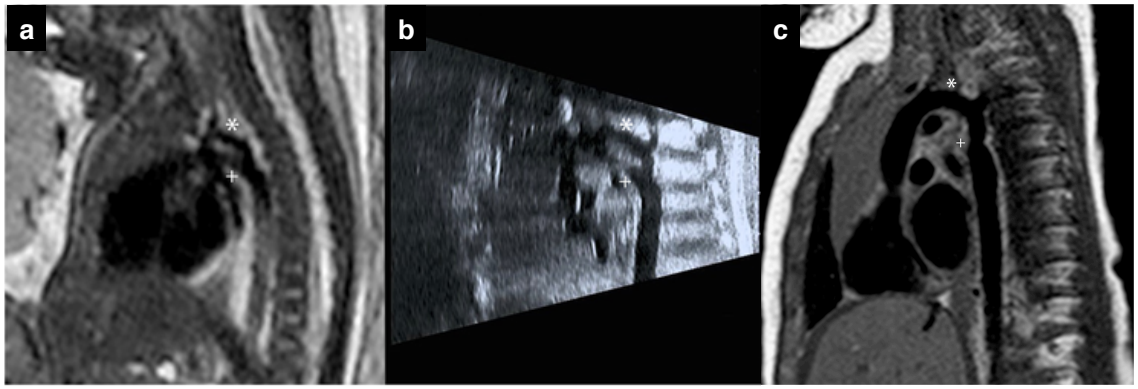


**Figure 2.9:** Single-shot turbo spin echo (ssTSE) image in a 32 week gestational age fetus with suspected coarctation of the aorta. The hypoplastic aortic arch (asterisk) is visualised superior to the dominant ductal arch (cross) on (**a**) fetal MRI, similar to (**b**) prenatal ultrasound. Blood flowing through cardiovascular system has hypointense signal in T2-weighted ssTSE images with the heart appearing as a homogeneous structure and extracardiac vasculature visible against hyperintense thymus and lungs. (**c**) Postnatal MRI of the same patient at 5 months age showing mild coarctation with isthmal hypoplasia and a posterior shelf at the point of insertion of the ductal ligament (cross), a vestige of the fetal arterial duct. Images provided by David FA Lloyd.

employs compensated, or balanced, imaging gradients to so that gradient-induced dephasing is zero at each repetition time (TR) [82] and is often used in postnatal cardiac MRI. Imaging performed in the steady state leads T2/T1-weighted signal with high SNR using short TR. Rapid, repeated acquisition of a 2D slice is possible with bSSFP, allowing for dynamic and cine acquisitions. However, bSSFP is susceptible to banding artefacts resulting from magnetic field inhomogeneity, particularly at 3 T. As shown in Figure 2.10, intracardiac features can be seen in bSSFP images since the signal in blood is hyperintense, while the signal in the myocardium and septa is hypointense. A detailed description of the bSSFP sequence is given in Section 3.2.

The bSSFP sequence is frequently used for static [53–59] and dynamic [52, 55, 59] imaging of the fetal cardiovascular system. Time-resolved cine bSSFP imaging of the fetal heart is also possible [64,65], though image reconstruction requires cardiac synchronisation (§2.5.3) and images may be corrupted by motion due to increased scan duration.

Other sequences used for functional measurements in fetal cardiac MR include phase contrast [63, 66] and time of flight [60] for angiography and T2-prepared steady state free precession for blood oximetry [68–70]. A variety of other imaging sequences have been used in non-cardiac fetal MR, but have found little use in imaging the fetal heart due to the added challenges of fetal cardiac MR . T1-weighted imaging has been performed with spoiled gradient echo and inversion

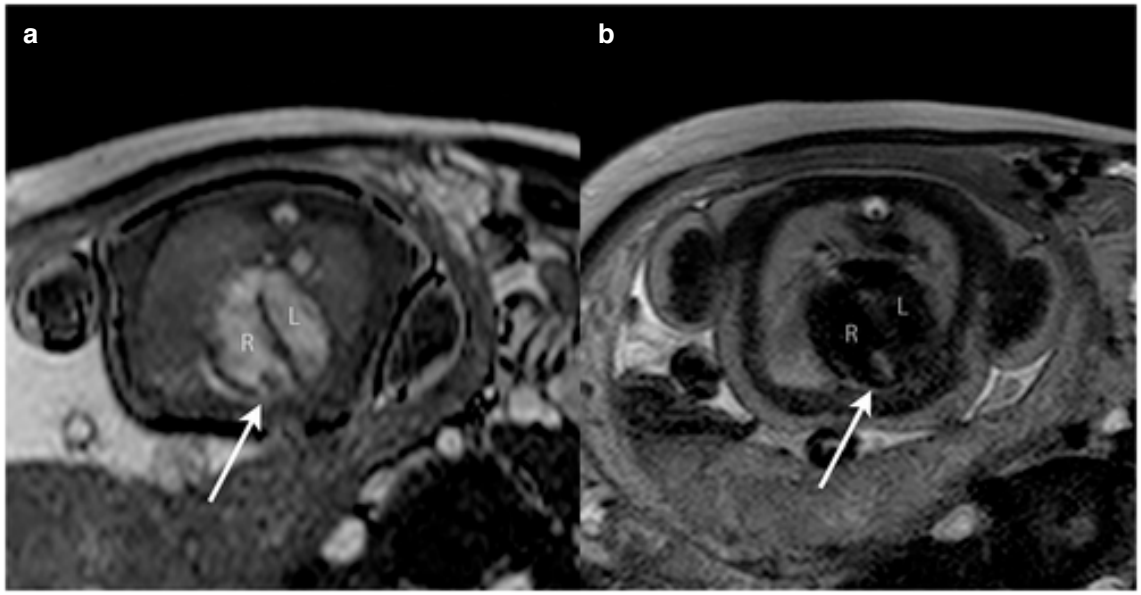


**Figure 2.10:** (**a**) Balanced steady state free precession (bSSFP) and (**b**) single-shot turbo spin echo (ssTSE) images of a 38 week gestational age fetus. Blood has a hyperintense signal in the bSSFP image in (a), while the blood pool is hypointense in the ssTSE image in (b). Based on the size, position and tissue signal on multiple sequences, a solitary ventricular rhabdomyoma (arrow) in the right (R) ventricle was suspected and confirmed postnatally. Images provided by David FA Lloyd.

recovery ssTSE [83, 84]. There is increasing interest in the use of echo planar imaging for diffusion-weighted and function MRI. Published studies have focused on the fetal brain, though postmortem diffusion-weighted MRI of the fetal heart has been reported [85, 86]. Lastly, MR spectroscopy has been used to assess metabolic changes in the fetal brain, lungs and liver, however acquisitions are limited to large single voxel measurements due to limited SNR and long scan duration [46].

### 2.5.3 Cardiac Synchronisation

Postnatal cardiac MR is usually performed while simultaneously measuring an electrocardiogram (ECG) signal so that the acquisition and reconstruction can be synchronised with the cardiac cycle. However, direct measurement of fetal ECG in the MRI scanner environment is not straightforward and preliminary studies [87] have not seen further development.

An MR-compatible Doppler ultrasound device has been proposed as an alternative to ECG and tested in an animal model [61, 62]. This device provides a direct measurement of the fetal cardiac cycle and has been used in a preliminary study of three human fetal subjects [64]. Additional patient preparation is required to set up

the ultrasound probe and mid-exam adjustments may be required if the signal is lost following episodes of general fetal movement.

Retrospective image-based cardiac gating for segmented acquisitions using entropy to measure data consistency was introduced as metric optimised gating, initially for phase contrast MR of fetal cardiopulmonary blood flow [63] and later for cardiac cine imaging [65]. This method relies on an indirect measure of the fetal cardiac cycle and, consequently, is dependent on the data acquired.

Recent work in cardiac-gated fetal cine imaging has seen wider use of the Doppler ultrasound device as well as self-gating methods. These concurrent developments are discussed in Section 6.2.

### 2.5.4 Volume Reconstruction

Volumetric representation may aid interpretation and assessment of the complex features of the fetal heart, however fetal movement and maternal respiration are likely to corrupt 3D MR acquisitions and result in inconsistencies between 2D images in multi-planar acquisitions. Furthermore, even with fast acquisitions, general fetal movements may still corrupt 2D MR images.

Prospective and retrospective motion correction techniques have been employed in fetal MR. Of these approaches, volumetric image reconstruction of static fetal organs from multi-planar ssTSE 2D images, combined with retrospective motion correction, has been the most successful [45]. Image volume reconstruction from 2D MR image was first introduced for volumetric reconstruction of the fetal brain. Initial implementations interleaved scattered data interpolation with 2D-3D image registration to correct for motion to generate volumetric fetal brain images from multi-planar 2D MRI, using either cubic B-spline [88] or Gaussian kernel-based [89] interpolation. An error minimisation (super-resolution) approach was subsequently introduced to reduce the blurring effect from thick-slice 2D MRI in volumes reconstructed using Gaussian kernel-based interpolation [90]. Outlier rejection using robust statistics has been employed to reduce the impact of voxels corrupted by motion and images misaligned to the volume [90, 91], removing the need for manual exclusion of inconsistent data. Inter-image intensity-matching for greater data consistency with improved volume reconstruction has also been shown to improve the reconstruction [91, 92].

Similar motion correction approaches have been used in adult cardiac MRI. Cine

cardiac MRI is usually acquired during a series of breath-holds, resulting in slices that may be misaligned due to differences in respiratory position. Motion correction using 2D-3D registration has been employed to correct between multiple breath-holds and improved ventricular segmentation [93, 94]. Volume reconstruction of the adult heart has also been explored for 2D cine [95] and real-time [96] MRI. At this time, none of these methods have been widely adopted for postnatal cardiac MRI.

# Chapter 3

# Methodology

This chapter reviews the MRI methodologies that form the basis of the work in the following chapters. The first section covers the fundamentals of MRI (§3.1). The following section provides details of the balanced steady state precession imaging sequence (§3.2), commonly used in cardiac MRI. The remaining sections review various aspects of MRI that inform the approach to fetal cardiac MRI in this thesis, including k-space sampling strategies (§3.3), time-resolved acquisition (§3.4), minimisation of image artefacts (§3.5) and techniques for rapid imaging (§3.6).

## 3.1 Magnetic Resonance Imaging Fundamentals

### 3.1.1 MR Physics

The basis of MRI is a phenomenon, that is known as nuclear magnetic resonance (NMR), that describes the effect of external magnetic fields on nuclei that have a nonzero magnetic moment. The NMR effect can be observed in an ensemble of nuclei placed in a strong static magnetic field when an electromagnetic signal is produced by the nuclei in response to being perturbed by a weak oscillating magnetic field.

An NMR experiment consists of three sequential steps. The first step consists of polarisation of the magnetic nuclear spins in a static magnetic field, $B_0$, leading to a small net equilibrium magnetisation, $M_0$, from the ensemble field that is proportional

to the density of nuclei and inversely proportional to temperature. At this point $M_0$ is undetectable as it is aligned with $B_0$ and much smaller in magnitude. In the second step, the ensemble is exposed to a radio-frequency (RF) pulse that generates an oscillating magnetic field, $B_1$, perpendicular to $B_0$, that perturbs the net magnetisation. The $B_1$ magnetic field causes some of the nuclei to resonate and gain energy, tipping the magnetisation away from $B_0$. Lastly, following the RF pulse, the magnetic spins of excited nuclei begin to return to equilibrium, i.e., aligned to $B_0$, and the excited nuclei lose energy as they precess about $B_0$. This energy appears as magnetic flux that can be measured as voltage induced in a receiver coil.

For resonance to occur, the frequency of the RF pulse must match the natural frequency of oscillation of a proton in the constant magnetic field. This is described by the Larmor equation,

$$\omega_0 = \gamma B_0 \ , \tag{3.1}$$

that relates precessional frequency, $\omega_0$, to the constant gyromagnetic ratio of a proton, $\gamma$, and $B_0$. Hydrogen is most often used in MRI as it has a large magnetic moment and is abundant in the human body. Hydrogen has a gyromagnetic ratio of 42.57 MHz/T and a precessional frequency of 63.86 MHz at 1.5 T.

### 3.1.2 Scanner System

In MR imaging, a main superconducting electromagnetic coil is used to produce the static magnetic field. The subject is placed within the bore of the main magnet so that hydrogen protons, and other protons with nonzero magnetic moments, align to $B_0$. Additional shim coils are sometimes used to improve the homogeneity of the magnetic field. A transmit coil produces the RF pulse that excites resonant protons. Three orthogonal gradient coils are used to create small variations, typically linear gradients, in the magnetic field at different times to allow for slice selection and spatial encoding. Lastly, one or more receiver RF coils are used to measure the NMR signal. The receiver coils use quadrature detection in two channels to measure both the magnitude and the phase of the NMR signal by combining the channels as the real and imaginary components of a complex-valued signal. The combination of RF transmit/receive and gradients, referred to as a pulse sequence, is then repeated until enough signals have been measured for the imaging experiment performed.

### 3.1.3 MR Signal Characteristics

The measured MR signal depends on the density of protons and associated relaxation characteristics of the anatomy being measured. The net magnetisation is tipped out of equilibrium due to the RF pulse, resulting in components $M_z$ in the longitudinal direction, parallel to $B_0$, and $M_{xy}$ in the transverse plane, perpendicular to the longitudinal direction. Following the RF pulse, the net magnetisation returns to equilibrium due to spin-lattice and spin-spin interactions.

Spin-lattice relaxation describes the transfer of thermal energy between excited nuclei and the surrounding atomic lattice, resulting in recovery of longitudinal magnetisation that is characterised by time constant $T_1$. The value of $T_1$ is highly dependent on energy transfer and, consequently, molecular motion and the size of the molecule. $T_1$ values of fluids, such as blood, are relatively long, while fat has a short $T_1$.

Spin-spin relaxation describes the decay of transverse magnetisation, perpendicular to $B_0$, due to dephasing, primarily caused by the interaction between the magnetic fields of individual protons. The decay of transverse magnetisation is characterised by time constant $T_2$. The value of $T_2$ tends to be long in free water and tissue containing water.

Additional factors that may impact the MR signal include magnetic field inhomogeneity, diffusion and motion.

### 3.1.4 Spatial Encoding

Point-wise acquisition is possible in NMR, but is time-consuming and provides poor signal [97, 98]. Instead, data is collected in the spatial frequency domain where the entire imaging volume contributes to the received signal, increasing scan efficiency and signal strength. The gradient coils in an MRI system are used to superimpose spatial variation on $B_0$. Since precessional frequency is proportional to magnetic field strength (Eq. 3.1), these gradients cause the precessional frequency to vary with spatial position. This interaction is used in MRI to spatially localise the MR signal by means of spatially-selective excitation, phase-encoding and frequency-encoding.

By convention, x and y are the in-plane directions and z is the through-plane, or slice, direction, for 2D MRI. These directions also correspond to the three gradients

though the gradients themselves may be generated by a combination of the three gradient coils if the imaging axes differ from those of the physical gradient coils.

Spatially selective excitation is accomplished by applying a slice selection gradient at the same time as the RF pulse in order to localise the excitation in one direction. The excitation of nuclei and, consequently, the thickness of the slice, is determined by the interaction between the amplitude of the slice selection gradient and the bandwidth of the RF pulse. Amplitude modulation of the RF pulse by an infinite sinc function in the time domain would result in uniform excitation in the through-plane direction. In practice, a time-apodised or -truncated function, e.g., sinc or Gaussian, is used to modulate the RF pulse, leading to a range of different slice profiles.

Following RF excitation, the measured MR signal is proportional to the rate of change of the net transverse magnetisation of all excited protons in the slice [99]. At this point additional gradients are applied in the in-plane x- and y-directions both before and during signal acquisition.

These time-varying gradients, collectively $\mathbf{G}(t)$, lead to a spatially-varying change in the static magnetic field, $\Delta \mathrm{B}(\mathbf{r}, t) = \mathbf{G}(t) \cdot \mathbf{r}$, where $\mathbf{r}$ is a vector specifying spatial location in three spatial dimensions, and a corresponding change in precessional frequency, $\Delta\omega(\mathbf{r}, t) = \gamma \Delta \mathrm{B}(\mathbf{r}, t)$. The impact on the phase of the transverse magnetisation, $\Delta\phi$, also has a spatial dependence, given by

$$\Delta\phi(\mathbf{r}, t) = \gamma \int_0^t \mathbf{G}(t')\, dt' \cdot \mathbf{r}\ , \tag{3.2}$$

where $t'$ is a dummy variable for integration over time. As a result of the spatially-dependent phase change resulting from Eq. 3.2, the relationship between the MR signal, $m(t)$, and the spatial distribution of the magnetisation resembles the Fourier transform,

$$m(t) = \int \xi\ \mathrm{M}_{\mathrm{xy}}(\mathbf{r}, t)\ e^{j\Delta\phi(\mathbf{r},t)} d\mathbf{r}\ , \tag{3.3}$$

where $\xi$ is a constant that describes the measurement system. This can be interpreted as the gradients modulating the MR signal by a spatial plane-wave function corresponding to a single spatial frequency at any given time [100]. Furthermore, since Eq. 3.3 has the form of a Fourier transform, the relationship between the MR signal and the spatial distribution of $\mathrm{M}_{\mathrm{xy}}$ can be written in terms of spatial frequency dimensions, $\mathbf{k}$, as $m(\mathbf{k}) \equiv m(t)$, or

$$m(\mathbf{k}) = \int \xi\ \mathrm{M}_{xy}(\mathbf{r}, t)\ e^{2\pi i \mathbf{k}(t)\cdot\mathbf{r}} d\mathbf{r}\ , \tag{3.4}$$

where

$$\mathbf{k}(t) = \frac{1}{2\pi}\gamma \int_0^t \mathbf{G}(t')\, dt' \ . \tag{3.5}$$

Thus, spatially-encoded MR data can be collected in a domain called k-space that has dimensions that correspond to spatial frequency in units of 1/distance [101]. Using this gradient encoding strategy, any single sample of the MR signal corresponds to a particular spatial frequency.

Sampling of k-space can be done on a rectilinear Cartesian grid by using frequency- and phase-encoding gradients, applied in the orthogonal x- and y- directions, by convention. In k-space these axes are referred to as $k_x$ and $k_y$. The k-space grid is centred on an origin that represents a zero spatial frequency and extends from $-k_{x,max}$ to $+k_{x,max}$ and $-k_{y,max}$ to $+k_{y,max}$. The centre of k-space, sometimes called the DC component, is proportional to the spatial mean of $M_{xy}(\mathbf{r})$.

Phase-encoding is performed by applying a gradient in the y-direction following the RF pulse to generate a linear relationship between the phase of the MR signal and spatial position. Frequency-encoding is accomplished by applying a gradient while the MR signal is being acquired so that there is a linear relationship between the precession frequency of the spins and spatial location. The timing of the gradients with respect to each other, the RF pulse and data acquisition is described in Section 3.2.1.

The measured data in the Cartesian sampling strategy correspond to a single line of k-space all with the same value of $k_y$. The pulse sequence is repeated with different phase-encoding in order to sample different $k_y$ lines.

The resolution of k-space, $\Delta k_x$ and $\Delta k_y$, is determined by the sampling interval and the strength of the frequency-encoding gradient in the x-direction and by the duration and strength of the phase-encode gradient in the y-direction [102]. If the frequency-encoding gradient amplitude, $G_x$, is constant, then the resolution of $k_x$ is given by

$$\Delta k_x = \frac{1}{2\pi}\gamma G_x \Delta t_x \ , \tag{3.6}$$

where the sampling interval, $\Delta t_x$, is given by

$$\Delta t_x = \frac{1}{\Delta f_{rcv}} \tag{3.7}$$

and $\Delta f_{rcv}$ is the bandwidth of the receiver. Similarly, if the phase-encoding gradient is applied with constant amplitude, $G_y$, for a fixed duration, $\tau_y$, then the resolution of

$k_y$ is given by

$$\Delta k_y = \frac{1}{2\pi}\gamma G_y \tau_y \ . \tag{3.8}$$

The MR signal may contain noise from tissue losses (thermal noise), primarily, and, to a lesser extent, receiver coil losses (e.g., hardware imperfections) [103]. The noise in each of the quadrature receiver channels is uncorrelated and has a Gaussian zero-mean distribution. This additional noise term has been omitted from Eq. 3.4.

### 3.1.5 Image Formation

It is possible to obtain an MR image by inverse Fourier transform of the acquired k-space data. In general both k-space and image data are complex-valued. For 2D MRI, $N_{kx}$ and $N_{ky}$ samples are acquired in the x- and y-directions, respectively. This discrete and finite sampling of k-space, rather than continuous and infinite sampling, has unique consequences on the reconstructed image.

Discrete uniform rectilinear sampling can be expressed as a train of evenly-spaced Dirac delta functions with spacing determined by Eqs. 3.6 and 3.8. This sampling function is known as a Dirac comb function, $\text{III}_{\Delta k}$. Multiplication of $m(\mathbf{k})$ by $\text{III}_{\Delta kx}(\mathbf{k})$ is equivalent to convolution of $\xi M_{xy}(\mathbf{r})$ by $\mathcal{F}^{-1}\{\text{III}_{\Delta kx}(\mathbf{k})\} = \text{III}_{\Delta rx}(\mathbf{r})$, where $\Delta r_x = 1/\Delta k_x$, and an equivalent effect occurs in the y-direction. Consequently, replicas of the imaged anatomy will appear at intervals $1/\Delta k_x$ and $1/\Delta k_y$ in the x- and y-directions, respectively. These distances determine the imaging field of view (FOV), where

$$FOV_x = \frac{1}{\Delta k_x} \quad \text{and} \quad FOV_y = \frac{1}{\Delta k_y} \ . \tag{3.9}$$

For uniformly sampled k-space, the in-plane spatial resolution of the corresponding image is given by

$$\Delta x = \frac{1}{2k_{x,max}} \quad \text{and} \quad \Delta y = \frac{1}{2k_{y,max}} \ . \tag{3.10}$$

For 2D imaging, the nominal resolution in the through-plane direction, $\Delta z$, is given directly from the slice-encoding process as

$$\Delta z = \frac{2\pi \Delta f_{RF}}{\gamma G_z} \ , \tag{3.11}$$

where $G_z$ is the slice-encoding gradient amplitude and $\Delta f_{RF}$ is the RF bandwidth [102].

Finite sampling can be interpreted as multiplication by a rectangular function that is zero for $k > k_{max}$, in k-space. This is equivalent to convolution in image space by $sinc(r_x/\Delta x)$, with zero crossings at intervals of $\Delta x$, in the x-direction and $sinc\left(r_y/\Delta y\right)$ in the y-direction.

Noise in the measured MR signal leads to noise in the reconstructed MR image. MR image noise is commonly described by the signal-to-noise ratio (SNR). For a 2D acquisition, SNR is proportional to the product of the image-space voxel volume and the square root of the total sampling time [99], or

$$\begin{aligned} SNR &\propto \Delta x \Delta y \Delta z \sqrt{N_{kx} N_{ky} \, \Delta t_x} \\ &\propto \Delta x \Delta y \Delta z \sqrt{\frac{N_{ky}}{\Delta f_{rcv}}} \, . \end{aligned} \tag{3.12}$$

The SNR of a 3D acquisition is a factor of $\sqrt{N_{kz}}$ higher than the equivalent 2D acquisition.

The MR signal can be measured using a single large receiver coil or an array of multiple smaller coils. A large coil will have a broad spatial sensitivity but lower peak SNR compared to a small coil. The combination of multiple small coils as a phased array allows for broad spatial coverage with increased SNR [104]. One straightforward way to combine the signals from a phased array is to perform a sum-of-squares combination of the images from each receiver coil [104]. More optimal, but also more complex, coil combinations are possible, allowing for some improvement in SNR and retention of phase information [104, 105].

## 3.2 Balanced Steady State Free Precession MRI

The balanced steady state free precession (bSSFP) MR sequence is widely used in postnatal cardiac MR due to its short repetition time, high SNR and high image intensity contrast between blood and myocardium. The NMR principles of this technique were described sixty years ago [106] and proposed for MRI three decades later, in 1986 [107]. However, the practical application of bSSFP in MRI has only become feasible as the speed, strength and precision of MR gradient systems increased with hardware introduced over the past two decades.

### 3.2.1 Signal Formation

In essence, the bSSFP sequence is an unspoiled gradient echo sequence with all gradients compensated by a gradient of opposite polarity, as shown in Figure 3.1 and described in the following paragraphs.

#### Gradient Echo Signal Formation

The gradient echo (GRE) pulse sequence (Fig.3.1a) starts with RF excitation to tip the net magnetisation by a flip angle, $\alpha$, while the slice selection gradient, $G_z$, is active. Dephasing caused by the slice-selection gradient is reversed, or refocused, by applying a gradient of opposite polarity immediately after the RF pulse. At the same time, the phase-encoding gradient, $G_y$, is applied with a gradient strength determined by the $k_y$ line to be acquired. The signal is intentionally dephased using a frequency-encoding gradient, $G_x$, with negative polarity and then the signal is rephased by a $G_x$ pulse with positive polarity. Consequently a gradient echo signal is formed that is measured by the data acquisition (DAQ) hardware. The $G_x$ gradient is designed to achieve exact rephasing of the signal at a chosen time during the sampling period, typically the centre. Timing of the sequence is described by an echo time (TE), the time between the effective centre of the most recent RF pulse and the point at which the signal is exactly rephased, and a repetition time (TR), the time between RF pulses. Fast gradient echo imaging with short TR is possible using low excitation flip angle and adding a spoiler gradient in just before the slice-select gradient, though the resulting SNR is lower compared to bSSFP [108].

#### Balanced Steady State Free Precession Signal Formation

In the bSSFP sequence (Fig. 3.1b), all gradients are balanced, i.e., $\int_0^{TR} \mathbf{G}(t)dt = 0$, so that gradient-induced dephasing within each repetition is compensated. In addition the polarity of the RF pulse is changed every TR to produce stable results and maximise on resonance signal. The gradient echo signal is measured at TE = TR/2. The transverse magnetisation at the end of the first repetition is non-zero so that the next RF pulse acts on the modified magnetisation. After an initial transient state, where the magnetisation is changing from TR to TR, a steady state of magnetisation will be established, with constant $\alpha$ and TR. For this reason, images are typically reconstructed from data that were collected in the steady state.

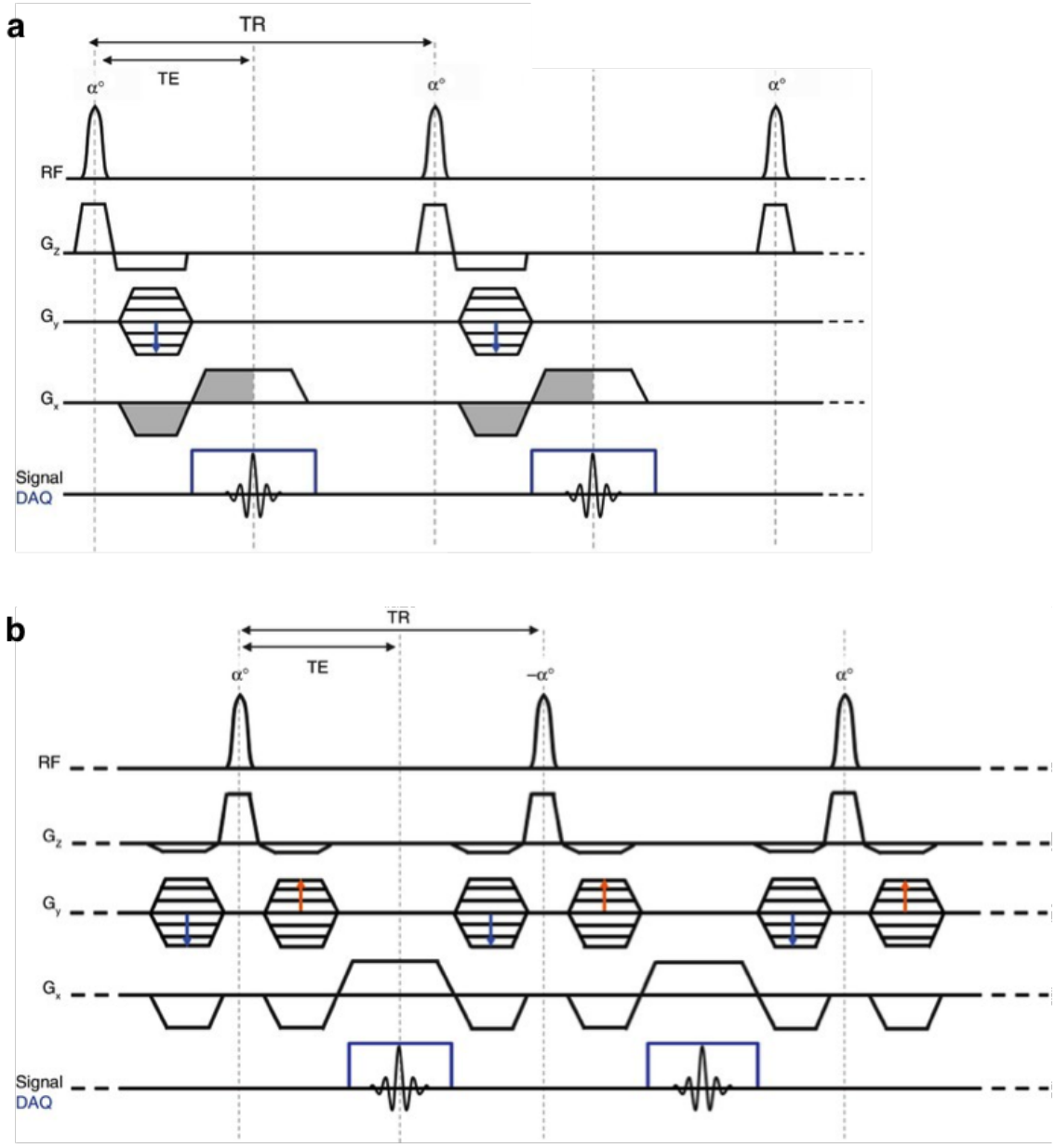


**Figure 3.1:** Pulse sequence diagrams for (**a**) gradient echo(GRE) and (**b**) balanced steady state free precession (bSSFP). Radio frequency (RF) pulses are shown as the amplitude modulation of the RF excitation. Slice-selective ($G_z$), phase-encoding ($G_y$) and frequency-encoding ($G_x$) gradients and data acquisition (DAQ) of MR signal are also shown. Sequence diagrams adapted from Figures 3.7 and 3.11 of 'CMR Pulse Sequences' in 'Basic principles of cardiovascular MRI: Physics and imaging technique' [108] under license from John Wiley & Sons.

### 3.2.2 Signal Contrast

The steady state bSSFP signal for TE = TR/2 and alternating RF polarity, as in Fig.3.1b, is directly proportional to

$$M_{xy} = \frac{(1 - E_1)\sin\alpha}{1 - (E_1 - E_2)\cos\alpha - E_1E_2} M_0 e^{-TE/T_2} , \tag{3.13}$$

and the flip angle, $\alpha^{opt}$, that maximises the magnitude of $M_{xy}$ is given by

$$\alpha^{opt} = \cos^{-1}\left(\frac{E_1 - E_2}{1 - E_1E_2}\right) \tag{3.14}$$

where $E_1 = e^{-TR/T_1}$ and $E_2 = e^{-TR/T_2}$ [102].

For TR $\ll$ T2 $\leq$ T1, Eq. 3.13 simplifies to

$$M_{xy} \approx \frac{\sin\alpha}{(T_1/T_2)(1 - \cos\alpha) + 1 + \cos\alpha} M_0 e^{-TE/T_2} \tag{3.15}$$

and $\alpha^{opt}$ can be approximated as

$$\alpha^{opt} \approx \cos^{-1}\left(\frac{T_1 - T_2}{T_1 + T_2}\right) . \tag{3.16}$$

The maximum bSSFP signal is then $M_{xy}^{opt} \approx \frac{1}{2} M_0 \sqrt{\frac{T_2}{T_1}}$.

Typical relaxation characteristics of adult cardiac tissue at 1.5 T are $T_2$ = 60 ms and $T_1$ = 950 ms in the myocardium [108], while the relaxation of oxygenated blood is around $T_2$ = 300 ms and $T_1$ = 1350 ms [109], with shorter $T_2$ in deoxygenated blood [110]. Consequently, blood has a hyperintense signal in bSSFP images while the myocardium has a much weaker signal. Compared to adult values, fetal blood has a longer $T_2$ (up to 35%) and a slightly shorter $T_1$ (up to 10%) at 1.5 T [111]. This suggests an optimal flip angle in the range of 50–60° to maximise the bSSFP signal from fetal blood, neglecting inflow effects.

### 3.2.3 Transient State

In the transient state the rate of decay towards steady state is a weighted average of $T_1$ and $T_2$, where the weighting is determined by the flip angle [112]. For small flip angles, the decay is mainly dependent on $T_1$, while for large flip angles approaching 180°, the decay is mainly dependent on $T_2$. Since $T_2 \leq T_1$, steady state is reached

earlier for higher flip angles. In the absence of signal preparation, it can take a large number of TRs to reach a true steady state [82]. However, the duration of the transient state can be shortened using an appropriate preparation method. One simple and effective preparation method, called $\alpha/2$-TR$/2$, uses an RF pulse with a flip angle of $+\alpha/2$ applied at TR/2 before the bSSFP sequence, which is shown to bring the magnetisation very near to steady state [113], but can be ineffective for off-resonance spins [112]. Other preparation techniques can be used to reduce the duration of the transient state, including a simple saturation recovery [82] and more complex preparations that use a sequence of RF pulses with different flip angles [114–116].

### 3.2.4 Phase Effects

The bSSFP signal is sensitive to phase effects from off-resonance and flow.

#### Off-Resonance

Deviations in the magnetic field lead to a proportional phase offset in the bSSFP signal with each TR that can lead to strong signal loss in certain regions of the bSSFP image that appear as dark banding image artefacts [112]. The resulting change in the bSSFP signal is relatively small for phase offsets less than $\pm\pi/2$ due to the alternating polarity of the RF excitation. However, phase offsets of $\pm\pi$ results in complete nulling of the bSSFP signal. Fortunately, MR shimming can be used to improve the homogeneity of the magnetic field so that any banding artefacts tend to appear at the edges of the field of view where deviations in the magnetic field may be larger. The amount of dephasing is also proportional to TR, so bSSFP with short TR is less prone to banding artefact. However, the reduction of TR may be constrained by fetal safety limits (§2.5.1). Magnetic field inhomogeneities can be amplified at higher field strengths and, consequently, banding artefacts are more problematic at 3 T compared to 1.5 T.

#### Flow

In addition to off-resonance, the signal generated by the bSSFP sequence is also sensitive to motion. Specifically, the applied gradients induce a spatially-dependent phase accumulation that is proportional to the velocity of motion. This phase accumulation occurs when the the zeroth- or first-order moments of the gradients are

non-zero. In the bSSFP sequence, gradients are balanced within each TR so that the zeroth-order moment is zero, however uncompensated first-order moments will result in an accumulation of phase where there is motion [117, 118]. The signal changes related to fast motion, such as blood flow, are highly acquisition dependent and can be quite complex, particularly when flow effects coincide with off-resonance effects. However, bSSFP is generally quite robust to artefact from flow and motion [82], especially for linear phase-encode ordered acquisitions [118]. Even if a stable steady state is formed, the motion sensitivity of bSSFP can still be observed in the phase of the signal related to the first moments of the gradients between RF excitation and data acquisition. Consequently, the phase of bSSFP images are comprised of a system-dependent background phase and a motion-sensitive phase that is proportional to the product of the gradient first-moment at time TE and the local velocity in the direction of that gradient [119, 120].

## 3.3 K-Space Sampling Strategies

The k-space sampling strategy employed to collect MRI data is relatively flexible [121]. For rapid 2D bSSFP MR, rectilinear Cartesian and radial non-Cartesian sampling are used most often.

### 3.3.1 Cartesian

Cartesian sampling, described previously in Section 3.1.4, samples k-space on a rectilinear grid using a frequency-encoding gradient in the $k_x$ direction and a phase-encoding gradient in the $k_y$ direction. The resulting k-space is rectilinear with uniformly-separated sampling points in $k_x$ and $k_y$. As a result, one particular advantage of Cartesian sampling is the straightforward application of the discrete Fourier transform for image reconstruction.

### 3.3.2 Non-Cartesian

In non-Cartesian sampling, k-space is not acquired on a rectilinear grid. Consequently, image reconstruction is performed using the non-uniform Fourier transform [122] or the sampled data can be interpolated on to a rectilinear grid [123] before applying the faster uniform Fourier transform. Another challenge of non-Cartesian sampling methods is the variety of potentially severe artefacts (spatial

blurring, streaking, uneven image shading) that can arise when there are errors in the locations of k-space samples. This can occur when the actual sampling trajectory differs from the expected trajectory. Exact measurement of the trajectory produced by the gradients or calibration of the gradient system can be used to minimise trajectory errors. Linear radial sampling is frequently used in adult cardiac MRI, while non-linear 2D non-Cartesian sampling strategies, such as spiral [124–126], are not commonly employed for rapid bSSFP MR of the heart due to increased TR.

#### Radial

Radial sampling is accomplished by rotating the frequency- and phase-encoding gradients so that the acquisition occurs along straight lines that pass through the centre of k-space [127]. As a result, k-space coverage is circular, and low spatial frequencies are densely sampled while high spatial frequencies are sparsely sampled. A factor of $\pi/2$ more samples are required for a radial k-space that meets the Nyquist criteria compared to a Cartesian trajectory for the same field of view. However, radial acquisitions are often accelerated by under-sampling of k-space, resulting in streaking artefacts that are fairly well-tolerated for moderate acceleration factors. Reconstruction of under-sampled radial data can be particularly advantageous when the angle between successive spokes is incremented by the golden ratio [128] or a surrogate thereof [129], allowing for flexibility in the trade-off between under-sampling factor, temporal resolution and spatial field of view.

## 3.4 Time-Resolved Acquisition

A time-resolved acquisition can be employed to assess temporal changes in the cardiovascular system using a dynamic or cine imaging approach.

### 3.4.1 Dynamic Imaging

The most straightforward approach, referred to here as dynamic imaging, is to repeatedly acquire a single 2D slice, collecting all k-space data to reconstruct one image frame before proceeding to the next. This results in a time series of images showing the dynamics of the heart in 'real-time' over multiple cardiac cycles. For

fully-sampled 2D dynamic imaging, the temporal resolution, $\Delta t_{dyn}$, is

$$\Delta t_{dyn} = \mathrm{N_{ky}} \mathrm{TR} \ , \tag{3.17}$$

where $\mathrm{N_{ky}}$ is the number of phase-encoding steps.

### 3.4.2 Cine Imaging

If data acquisition is synchronised to the cardiac cycle, a segmented acquisition can be used where a subset of k-space, a segment, is acquired repeatedly for the duration of a cardiac cycle and then other segments are collected during subsequent cardiac cycles. Once all data is collected, a cardiac cine image series can be reconstructed with all data combined as a single cardiac cycle. The temporal resolution of a fully-sampled Cartesian cine acquisition, $\Delta t_{cine}$, is

$$\Delta t_{cine} = \frac{\mathrm{N_{ky}}}{\mathrm{N}_{seg}} \mathrm{TR} \ , \tag{3.18}$$

where $\mathrm{N}_{seg}$ is the number of segments. However all of the data must be collected before any images can be reconstructed. The time required to collect cine data is the total duration of the $\mathrm{N}_{seg}$ consecutive cardiac cycles during which data was acquired.

Clearly, higher temporal resolutions are possible using a cine acquisition, compared to a dynamic acquisition with the same field of view and spatial resolution. However, cine acquisitions can be prone to corruption from any non-cardiac motion that occurs during the acquisition due to the time required to acquire all of the data. For this reason, cine imaging of adult subject is usually performed during breath-hold.

As noted in Section 2.5.3, cine imaging of the fetal heart has been achieved using data-driven and device-based approaches for cardiac gating. The metric optimised gating (MOG) technique was one of the first used for fetal cine phase contrast blood velocity imaging [63] and cardiac cine imaging [65], both using Cartesian sampling. In the MOG technique, a segmented Cartesian acquisition is synchronised to a simulated trigger to ensure the cardiac cycle is over-acquired in each segment and image reconstruction is performed using a model of the fetal heart rate that is adjusted to minimise an entropy-based metric of image quality. At the same time as MOG was introduced, a Doppler ultrasound device was proposed for fetal cardiac gating [61, 62] that provides a direct measurement of the fetal cardiac cycle. Recently published works using MOG or the Doppler ultrasound device for fetal cardiac cine

imaging are discussed in Section 6.2 along with approaches that use self-gating.

## 3.5 Image Artefacts

The major sources of artefact that may degrade fetal cardiac MR image are reviewed in this section.

### 3.5.1 Partial Volume

Partial volume effects occur when an image voxel contains partial contributions from multiple features of interest, such as at the border between the blood pool and the heart wall leading to blurring at tissue boundaries. This effect can be reduced by increasing in-plane resolution and exciting a thinner slice.

### 3.5.2 Aliasing

Spatial image aliasing will occur whenever the imaging FOV is smaller than the imaged anatomy, as discrete sampling leads to replication of imaged anatomy at intervals of $1/\Delta$k, as previously described (§3.1.5). In practice, spatial aliasing in the frequency-encode direction can be avoided by a combination of oversampling, frequency filtering and decimation, as the impact of oversampling on scan time is minimal. However, an oversampling approach is not practical in the phase-encode direction. Ensuring the FOV is large enough to fully cover the imaged anatomy is the only way to avoid aliasing in the phase-encode direction, which can increase scan time substantially. For Cartesian sampling, spatial aliasing appears as straightforward 'wrap-around' of the anatomy outside the field of view in the phase-encode direction. For radial sampling, circular aliasing occurs if the sampling rate along the spokes is too low, while streaking artefacts appear if the spacing between spokes is too large [130]. Imaging of the fetal heart in utero often requires the use of a large FOV to accommodate maternal anatomy.

### 3.5.3 Truncation

Finite k-space sampling is equivalent to image-domain sinc convolution (§3.1.5). As a result, high-frequency oscillations, known as Gibbs ringing artefact, and blur-

ring can occur around sharp intensity changes in reconstructed MR images when $k_{max}$ is not high enough to adequately capture the spatial frequencies in the imaged anatomy. Truncation artefact can be visually prominent when k-space is zero-padded to increase apparent spatial resolution, since the zero-crossings of the sinc kernel are no longer coincident with the centres of neighbouring voxels. Careful apodisation of the sampled k-space when zero-padding can minimise this effect, at the cost of a loss of some high spatial-frequency content.

### 3.5.4 Banding

$B_0$ inhomogeneities can lead dark bands in bSSFP images (§3.2.4). Banding artefacts in bSSFP MR can be reduced by B0 shimming and decreasing TR, and are less problematic a 1.5 T than 3 T.

### 3.5.5 Geometric Distortion

Spatial geometric distortions may appear in MR images when the actual k-space sampling pattern deviates from expected trajectory, as can be the case when there are inhomogeneities in the B0 field or gradient errors occur [99]. Gradient non-linearity increases with distance from isocentre of the MR scanner, leading to spatial distortions [131]. This can be problematic for fetal cardiac MR since the fetal heart in utero is unlikely to be at positioned exactly at isocentre. As previously mentioned, shimming can be used to improve the homogeneity of the magnetic field (§3.1.2). In addition, vendor-implemented processes are available on most scanners that use calibration data to correct for gradient non-linearity [99].

### 3.5.6 Chemical Shift

The difference in resonant frequencies of water and fat, 215 Hz at 1.5 T, can lead to signal nulling when spins are out of phase. For gradient echo sequences at 1.5 T, the signal from water and fat is completely out of phase at TE = $2.2 + n\,4.4$ ms for $n = 0, 1, 2, 3, \ldots$ [132], which will result in nearly complete signal nulling in voxels containing both water and fat. This can be problematic in cardiac MR since there may be fat in and around the heart. In the fetal epicardium, the outer layer of the heart wall, there is normally a layer of fat with a thickness of 1 mm or more [133]. This chemical shift artefact is minimised by avoiding use of the TE values that lead

to water-fat signal nulling. In addition, the signal from fat may be spatially shifted in the frequency-encoding direction, since spatial position is assigned along the frequency-encode direction on the basis of resonant frequency. The amount of spatial shift can be limited by reducing receiver bandwidth.

### 3.5.7 Motion

The process of spatial encoding in MRI is slow and sequential. Movement of the imaged anatomy and the flow of blood and other fluids during the acquisition can corrupt the acquired k-space data in a number of ways. Motion during MR scanning can impact the signal readout process, leading to blurring and ghosting, and the signal generation process, leading to deviations from the expected magnetisation.

The type of motion (e.g., slow non-periodic drift, rapid position change, fast periodic pulsation) have varying consequences that depend on phase-encode ordering in Cartesian sampling. Sequential phase-encode ordering is fairly robust to slow non-periodic motion, but is particularly sensitive to fast periodic motion [134]. Conversely, interleaved phase-encode ordering can lead to severe artefacts due to slow non-periodic motion, but may have fewer artefacts due to fast periodic motion. The impact of a rapid position change is dependent on when the motion happens, with prominent image artefacts resulting from position changes that lead to inconsistencies of central $k_y$ lines, particularly when there is inconsistency over an extended part of k-space either in a block or in a periodic manner. Lastly, a rapid but brief change in position that corrupts the centre of k-space can lead to large artefacts since most of the information in k-space is contained in the lower frequencies.

A variety of maternal and fetal movements can occur within the imaging FOV during an MRI scan of the fetal heart. Some movements are episodic while others are continuous, with various speeds and periodicity. Motion of maternal anatomy can occur due to respiration or bulk movement, as well as cardiac pulsation and blood flow. Various forms of fetal motion may be present as well, including general (§2.2.1) or local (§2.2.2) fetal movements, swallowing of amniotic fluid and fetal breathing movements (§2.2.3), while cardiac pulsation and blood flow (§2.1.2) will certainly be seen. The impact of maternal respiration leads to a corresponding displacement of the fetus, which may be best described as elastic motion since the interface between maternal anatomy and the fetus is made up of soft tissues and amniotic fluid. In the case of general or local fetal movements, the motion can be quite non-rigid and discontinuous from maternal anatomy as the fetus is surrounded be amniotic fluid and can freely move within the uterus to the extent that space allows.

Motion artefacts can be reduced by using rapid imaging techniques (§3.6), motion-insensitive sequences, gradient moment nulling, optimal phase ordering or motion-synchronised acquisitions [134]. Common methods to maintain image quality in adult cardiac MR include cardiac synchronisation, multiple breath-holds or respiratory navigation [135]. Advanced MR image reconstruction techniques have been used in adult cardiac MR to minimise motion artefacts by comparing the data from multiple receiver coils [136] or integrating retrospective motion-correction with image reconstruction [137–139]. In the initial MOG fetal cardiac cine imaging study by Roy *et al.* [65], the scan duration was kept short to limit the chance of fetal movement occurring and maternal breath-hold was used to limit data corruption from maternal respiration where scan duration and maternal compliance allowed. More recently, a golden angle radial trajectory has been used in multiple recent publications on fetal cardiac cine imaging in conjunction with motion detection and compensation (§6.2).

Motion can lead to blurring and ghosting in MR images, as well as effects arising from spin history and prior data mismatch.

#### Blurring

Image-domain blurring occurs when non-central regions of k-space (high spatial-frequencies) are corrupted.

#### Ghosting

Ghosting artefact appears as complete or partial replication of anatomy moving in the phase-encode direction. Perfectly periodic motion leads to coherent ghosts, while deviation from periodic motion leads to incoherent ghosts, such as multiple overlapping replicas or streaks. Pulsatile flow can also lead to ghosting artefacts resulting from periodic modulation of k-space due to flow effects in gradient echo pulse sequences (§3.2.1). For fetal MR using a Cartesian k-space trajectory, it is important to ensure the maternal heart and pulsatile blood vessels, such as the descending aorta, are not aligned with the fetal heart in the phase-encode direction to minimise the overlap of artefact.

#### Spin History

Deviations from the expected MR spin evolution can occur when the anatomy excited by repeated slice-selective RF pulses changes. This may be an issue for 2D bSSFP with the slice-encode direction along the direction of maternal respiration in free-breathing acquisitions.

#### Prior Data Mismatch

A variety of MR image reconstruction techniques use prior data, such as parallel imaging (§3.6.3). Artefacts can arise when the prior data doesn't match the acquired data, e.g., when patient movement shifts the receiver array resulting in misaligned receiver sensitivity maps. Autocalibration may minimise the artefacts that arise in these cases, as prior information is estimated directly from the data rather than a pre-scan, so long as the autocalibrated prior is of sufficient quality for the reconstruction task.

## 3.6 Rapid Imaging

Rapid imaging is essential for fetal cardiac MR in order to resolve the beating fetal heart with adequate image quality and spatial resolution, while also reducing artefacts from motion. The bSSFP pulse sequence already uses a short TR and provides high SNR, however the time required to acquire fully-sampled 2D data is long compared to the fetal heart rate. Sequence parameter optimisation may lead to marginal improvements in temporal resolution and techniques that exploit the inherent spatial and temporal redundancies in the data can be used to achieve further improvement by under-sampling k-space.

### 3.6.1 Sequence Optimisation

Improving the temporal resolution of a 2D acquisition requires reducing the TR or reducing the number of phase-encoding steps, or both. Sequence optimisation requires balancing changes that impact these two parameters with the effect of those changes on image quality, spatial resolution and scan duration. TR can be reduced by increasing gradient amplitudes and slew rates or increasing the amplitude of the RF pulses. However these parameters are constrained by safety factors (§2.5.1)

as increased RF strength and gradient switching may lead to increases in SAR, PNS or SPL. A shorter RF pulse can also be achieved by truncating the RF pulse, leading to a softening of the slice profile, or increasing the excitation bandwidth, $\Delta f_{\mathrm{RF}}$ while leaving $\mathrm{G_z}$ unchanged, leading to a thicker slice. Reducing the number of phase-encode steps can be accomplished by using a lower spatial resolution or smaller field of view. As the orientation of the fetal heart relative to the maternal body is unpredictable, the required spatial coverage is often asymmetric, in which case Cartesian sampling using a square or rectangular FOV with the phase-encode direction along the smaller dimension can be advantageous.

### 3.6.2 Partial Fourier Acquisition

When an MR image has only real values and all imaginary values are zero, the corresponding k-space is Hermitian symmetric such that $m(-\mathbf{k}) = m^*(\mathbf{k})$, where the raised asterisk ($^*$) denotes complex conjugation [99]. In a Partial Fourier acquisition, a fraction of phase-encode lines are acquired and some portion of one half of k-space remains unsampled.

The symmetry of k-space is then used to synthesise the missing samples, either using a homodyne reconstruction if the phase in the MR image is slowly varying [140] or an iterative algorithm for highly variable image phase [141]. Partial Fourier acquisitions of as low as 5/8 of k-space are possible, leading to an acceleration factor of R = 1.6.

### 3.6.3 Parallel Imaging

Fetal MRI is often performed using an array of receiver channels that simultaneously measure the MR signal [142]. As the receiver channels are spatially distributed in the array, they exhibit strongly heterogeneous and mutually distinct spatial sensitivities. The relationship between k-space samples, $\mathrm{d}_c(\mathbf{k})$, in receiver coil $c$ and image voxels, $\mathrm{x}(\mathbf{r})$, can be written as

$$\mathrm{d}_c(\mathbf{k}) = \int \mathrm{x}(\mathbf{r})\mathrm{s}_c(\mathbf{r})e^{2\pi i\mathbf{k}\cdot\mathbf{r}}d\mathbf{r}\ , \tag{3.19}$$

where $\mathrm{s}_c(\mathbf{r})$ is the sensitivity of receiver coil $c$ at spatial location $\mathbf{r}$. Parallel imaging leverages the spatial encoding provided by the receiver sensitivities to facilitate image reconstruction from under-sampled k-space data.

Following the treatment suggested by Pruessmann [100], if data is acquired using a single receiver coil with uniform sensitivity, a discretised form of the MR acquisition in Eq. 3.19 can be expressed as

$$\mathbf{d} = \mathbf{F}\mathbf{x} \,, \tag{3.20}$$

where **d** and **x** are vectors collecting all k-space and image values, respectively, and **F** is a diagonal matrix with the appropriate Fourier encoding for each voxel in **x**.

Similarly, a general expression for parallel imaging can be written as a linear system in the form

$$\mathbf{d} = \mathbf{E}\mathbf{x} \,, \tag{3.21}$$

where **d** collects the k-space data sampled by all receiver coils and **E** is an encoding matrix. In Eq. 3.21, **E** = **AFS** so that **x** is encoded by the spatially-varying receiver sensitivities, **S**, as well as the the Fourier transform, **F**, and **A** is a logical array that indicates which samples were acquired. **A** will be entirely filled with ones if the data is fully-sampled, however if **A** has any zero entries, the data is under-sampled. Solving the inverse problem requires inverting **E**. Since direct inversion is likely not possible, in practice an estimate, $\widehat{\mathbf{x}}$, can be obtained by minimising the residual between **Ex** and **d**,

$$\widehat{\mathbf{x}} = \underset{\mathbf{x}}{\operatorname{argmin}} \, \|\mathbf{E}\mathbf{x} - \mathbf{d}\|_2 \,. \tag{3.22}$$

Taking the Moore-Penrose psuedo-inverse of **E** and adjusting for noise correlations between the receivers, gives

$$\widehat{\mathbf{x}} = (\mathbf{E}^H \Psi^{-1} \mathbf{E})^{-1} \mathbf{E}^H \Psi^{-1} \, \mathbf{d} \,, \tag{3.23}$$

where $\Psi$ is a square matrix of receiver coil noise covariance and the raised $H$ indicates the transposed complex conjugate [143]. For fully-sampled k-space, i.e., **A** has no zero entries, Eq. 3.23 is equivalent to coil-wise Fourier reconstruction and maximum SNR least-squares coil combination [100,104]. However, the scanner gradients and receiver sensitivities provide independent spatial encoding that can be leveraged to reconstruct images from under-sampled k-space data. This is particularly evident for regular under-sampling of Cartesian $k_y$ lines, as periodic modulation in k-space leads to predictable aliasing (§3.1.5).

The two most common parallel imaging techniques for uniformly under-sampled Cartesian acquisitions are SENSitivity Encoding (SENSE) and GeneRalized Autocalibrating Partially Parallel Acquisition (GRAPPA) [144], which operate in the image and k-space domains, respectively. Non-Cartesian trajectories can also be under-sampled and reconstructed using techniques such as conjugate gradient

SENSE [145] and non-Cartesian GRAPPA [146]. Assuming accurate calibration data is available, SENSE provides slightly higher image quality than GRAPPA in highly-accelerated applications [147]. Arbitrary k-space sampling trajectories can be reconstructed using iterative self-consistent parallel imaging reconstruction (SPIRiT) [148], which includes regularisation to minimise noise propagation and facilitate convergence. Parallel imaging is common in adult cardiac MR using SENSE and GRAPPA with acceleration factors of R = 2–4 [149].

When required, sensitivity maps can be generated from full FOV pre-scan images acquired using the receiver array coil and body coil. Division of each receiver coil image by the body coil image yields the corresponding complex-valued sensitivity map. A sum-of-squares coil-combined image can be used as the divisor if a body coil image is unavailable [143].

### SENSE

A full-FOV image can be produced by separating under-sampling aliases in the image-domain using SENSE [143]. The SENSE reconstruction for regularly under-sampled $k_y$ lines in a Cartesian trajectory is similar to Eq. 3.23 and is given by

$$\mathbf{x} = (\mathbf{S}^H \Psi^{-1} \mathbf{S})^{-1} \mathbf{S}^H \Psi^{-1} \, \mathbf{x}_{alias} \, , \tag{3.24}$$

for an acquisition using $N_c$ receiver coils and an acceleration factor of R leading to $N_R$ overlapping aliases, where $\mathbf{x}_{\text{alias}}$ is an $N_c \times 1$ vector of complex image values for a single voxel in the reduced-FOV single-coil images and $\mathbf{S}$ is the corresponding $N_c \times N_R$ matrix of receiver sensitivities at the $N_R$ unaliased voxel positions in $N_R \times 1$ vector $\mathbf{x}$. Eq. 3.24 is the solution to a set of $N_c$ linear equations in $N_R$ unknowns.

The SNR of resulting image, $SNR_{PI}$, will be

$$SNR_{PI}(\mathbf{r}) = \frac{SNR_{full}}{g(\mathbf{r})\sqrt{R}} \tag{3.25}$$

which is reduced because of under-sampling by factor R and can be spatially non-uniform as it is dependent on a geometry factor, $g(\mathbf{r})$, that represents spatially-varying noise amplification [102, 143]. Aliasing in the full FOV can lead to localised errors in the reconstructed images when receiver sensitivity maps do no accurately represent the acquired data [147]. In time-resolved acquisitions, a time-interleaved $k_y$ under-sampling pattern can be used so that k-space data can be shared between successive image frames to allow for receiver sensitivities to be calculated from low

temporal resolution images reconstructed from a fully-sampled k-space; this technique is called temporal SENSE (TSENSE) [150].

#### GRAPPA

An alternative approach to SENSE is to compute the missing k-space data from weighted combinations of the sampled k-space data using GRAPPA [144]. The GRAPPA reconstruction requires a small part of k-space to be fully-sampled for use as an auto-calibration signal from which to determine the weights, but does not require explicit image domain receiver sensitivity maps. The GRAPPA acquisition may be slightly longer compared to SENSE, when auto-calibration signal phase-encoding lines are interleaved with the under-sampled acquisition. Aliasing in the reconstructed full FOV is not a challenge with GRAPPA, however inaccuracies in the auto-calibration signal will result in errors that are distributed across the reconstructed image [147]. Temporal GRAPPA (TGRAPPA) [151] is an extension of GRAPPA analogous to TSENSE.

### 3.6.4 Temporal Acceleration

Time-resolved imaging allows for the use of acceleration techniques that exploit the redundancy in the temporal dimension. Dynamic acquisitions can be thought of as sampling data in k-t space, where each dynamic image frame is represented by a unique time point. Data acquisition can then be used to under-sample k-t space in k-space and temporal dimensions. Such an approach is used in TSENSE and TGRAPPA (§3.6.3), where a large time window is used to generate calibration data prior to resolving spatial under-sampling using SENSE or GRAPPA. However, accounting for both spatial and temporal under-sampling jointly can allow for increased acceleration [152].

One such technique, k-t SENSE [153], leverages the spatio-temporal sparsity in the image and temporal frequency domain, called x-f space. Another technique, k-t GRAPPA [154], follows from GRAPPA much in the same way that k-t SENSE follows from SENSE.

Applying an inverse Fourier transform in the k-space dimensions followed by a Fourier transform along the temporal dimension results in a compact signal in x-f in applications where only a small region of the FOV has high frequency temporal information and the remainder of the FOV is slowly varying. Including the temporal

Fourier transform in Eq. 3.21, leads to

$$\mathbf{d} = \mathbf{E}\boldsymbol{\rho} \,, \tag{3.26}$$

where $\boldsymbol{\rho}$ is the reconstructed dynamic image series in x-f space and the encoding matrix is adapted as $\mathbf{E} = \mathbf{A}\mathbf{F}_{x\to k}\mathbf{S}\mathbf{F}_{f\to t}$, where $\mathbf{F}_{x\to k}$ applies spatial Fourier encoding as in Eqs. 3.20 and 3.21 and $\mathbf{F}_{f\to t}$ applies the inverse Fourier transform in time [153]. Employing receiver sensitivity encoding in Eq. 3.26 improves aliasing artefact removal.

A variety of other techniques have been proposed beyond k-t SENSE and k-t GRAPPA that simultaneously exploit spatial and temporal resolution by reconstructing following a temporal transformation using principal components (k-t PCA [155]), using data-driven auto-calibration in x-f space (x-f Choice [156]) or employing compressed sensing techniques (§3.6.5) with pseudo-random k-t sampling patterns (k-t SPARSE [157], k-t FOCUSS [158]).

#### k-t SENSE

Eq. 3.26 can be simplified considerably if k-t space is sampled on a rectilinear grid with sheared grid under-sampling pattern and reconstruction is performed in the x-f domain. As described by Tsao *et al.* [153], a regularised k-t SENSE reconstruction for uniform Cartesian under-sampling is given by

$$\boldsymbol{\rho} = \bar{\boldsymbol{\rho}} + \Theta\mathbf{S}^H(\mathbf{S}\Theta\mathbf{S}^H + \Psi)^{-1}(\boldsymbol{\rho}_{alias} - \mathbf{S}\bar{\boldsymbol{\rho}}) \,, \tag{3.27}$$

where noise characteristics are incorporated as in SENSE (Eq. 3.24), $\bar{\boldsymbol{\rho}}$ is the baseline temporal mean signal and $\Theta$ is a prior estimate of the distribution of signal in x-f space. In practice, the level of regularisation in the k-t SENSE reconstruction (Eq. 3.27) is controlled by scaling $\Psi$.

The x-f prior, $\Theta$, can be generated from training data, with low spatial resolution and equivalent temporal resolution compared to $\rho$, that is acquired in a separate training stage or interleaved in the under-sampled k-t acquisition. However the interleaved acquisition decreases the temporal resolution of the scan. Auto-calibration techniques have been proposed that use TSENSE on the k-t under-sampled data generate training data, removing the need for separate training data [159].

The position of aliased replicas in x-f space is determined by the k-t sampling pattern used to acquire the data. Consequently, an optimal k-t sampling pattern can be used

to minimise signal overlap in x-f space, which can be particularly beneficial at higher acceleration factors [160].

The application of k-t SENSE for temporal acceleration in fetal cardiac MRI is described in Sections 4.2 and 4.5.

#### k-t GRAPPA

The k-t GRAPPA reconstruction [144] is applied directly in k-t space and shares many of the characteristics of GRAPPA in that no prior knowledge of receiver sensitivities is required and the reconstructed images are dependent on the auto-calibration signal used to derive k-t interpolation weights. A strategy similar to TGRAPPA can be used to obtain the spatio-temporal auto-calibration signal.

### 3.6.5 Compressed Sensing

Another approach to accelerate MRI is to use the inherent sparsity of the imaged anatomy to constrain the reconstruction [161]. This is possible when the image signal can be compressed via a sparsifying transform such that it is prominent against the under-sampling artefact. For this reason, random under-sampling of k-space is used so that aliasing artefacts are diffuse and incoherent. Care must be taken in designing compressed sensing algorithms as the choice of sparsifying transformation combined with level of regularisation can lead to loss of image features in compressed sensing reconstructions [149]. Compressed sensing is compatible with parallel imaging and temporal acceleration, and has been recently employed for fetal cardiac cine MR imaging, as discussed in Section 6.2.

# Chapter 4

# 2D Cine Reconstruction from Single-Slice Dynamic MRI

## 4.1 Introduction

Magnetic resonance imaging has unique potential for anatomical mapping of the fetal heart and great vessels. Advancements in MRI over the last decade have brought an increased interest in the use of MRI as an adjunct to ultrasound in the diagnosis of congenital cardiac abnormalities in utero [51]. However, clinical studies evaluating the feasibility of MRI for assessment of the fetal heart have noted moderate sensitivity and data corruption due to fetal motion as current limitations [53, 57, 162]. Synchronisation with the fetal cardiac cycle also poses a challenge (§2.5.3). Segmented cine acquisitions have been achieved using self-consistency in reconstruction to infer a gating signal [65] or MR-compatible Doppler ultrasound-based triggering [64], though these methods are prone to corruption from fetal and maternal motion (§3.4.2). An alternative approach is to use rapid dynamic ('real-time') imaging with high temporal resolution to obtain serial 'snapshots' of the fetal heart and surrounding anatomy that can be motion-corrected and reassembled by compounding images from several cardiac cycles.

The aims of this work were to establish a MR protocol for highly-accelerated two-dimensional dynamic imaging of the heart in utero, and to develop methods for cine reconstruction that compensate for fetal and maternal motion. Preliminary work is described in the following sections (§4.2–4.4) leading up to a final 2D cine recon-

struction framework, presented as published in the journal Magnetic Resonance in Medicine (§4.5) including additional details of the fetal heart rate simulation used to evaluate timing errors associated with the use of a constant heart rate (§4.6). A conclusions section (§4.7) closes the chapter. Links to the preliminary work referenced in Sections 4.2–4.5 can be found in the list of conference presentations in the Publications and Software section at the end of this thesis.

## 4.2 Accelerated Dynamic MR Imaging

Direct measurement of postnatal cardiac morphology is typically obtained from dark blood sequences that have long TR making them inadequate for dynamic imaging of the fetal heart. The balanced steady state free precession (bSSFP) sequence provides good blood-tissue contrast, thereby achieving an indirect measure of cardiac anatomy (§3.2) and has been shown to be effective for imaging the fetal heart [56, 65]. A field strength of 1.5 T was selected over 3 T for lower RF exposure and to reduce $B_0$ inhomogeneity to minimise bSSFP banding artefact (§3.5.4).

Parameter selection was constrained by anatomical geometry (§2.1.1) and physiology (§2.1.2), as well as safety factors (§2.5.1). Guidelines for cardiac ventriculography in infants were also used to inform parameter selection, though it should be noted that functional assessment was not the aim of this work. These guidelines suggest 2D cine MR imaging with 1.2×1.2×4.0 mm voxels and 15 cardiac phases [163]. In fetal MRI, the FOV should be at least 300 mm to fully cover maternal anatomy, while the k-space matrix size should provide sufficient spatial resolution to depict the features of the fetal cardiovascular system. As shown in Section 2.1.1, the ductal arch and inferior vena cava measure ~3 mm in diameter at the end of the second trimester. Clearly a voxel size of less than 3 mm should be used to resolve these features. Ideally the scan duration should be kept as short as possible to minimise the chance of fetal movements (§2.2) occurring. A temporal resolution equivalent to $>$5 cardiac phases may be sufficient to resolve the cardiac cycle so that the heart can be depicted without blurring at end-systole and mid-diastole, based on suggested image acquisition windows for triggered 3D bSSFP in infants [163].

Temporal resolution can be improved by using rapid imaging techniques (§3.6), such as decreasing TR or under-sampling k-space, though SNR will be decreased as a consequence. An excitation flip angle of 60° can be used to maximise the bSSFP signal from fetal blood (3.2.2). A Cartesian trajectory was used to efficiently sample

the entirety of k-space (§3.3).

The minimum TR was found to be limited by sound level safety limits in adherence with local group guidelines (§2.5.1). As scanner predicted sound pressures were unreliable, tests were conducted in a phantom set-up to establish safe sequence parameters. Sound pressure level was measured at isocentre with an OptiSLM100 system and fibre-optic microphones (Optoacoustics, Mazor, Israel) for Cartesian bSSFP MRI acquisitions in scanner transverse, sagittal and coronal orientations with varying repetition time, revealing overall high sound pressure levels with a drop to acceptable levels at TR = 3.8 ms in all slice orientations, as shown in Figure 4.1. Acceptable sound pressure levels were also measured in oblique orientations in the phantom set-up at this TR and as well as in initial fetal examinations confirming that no measurements exceeded the limit.

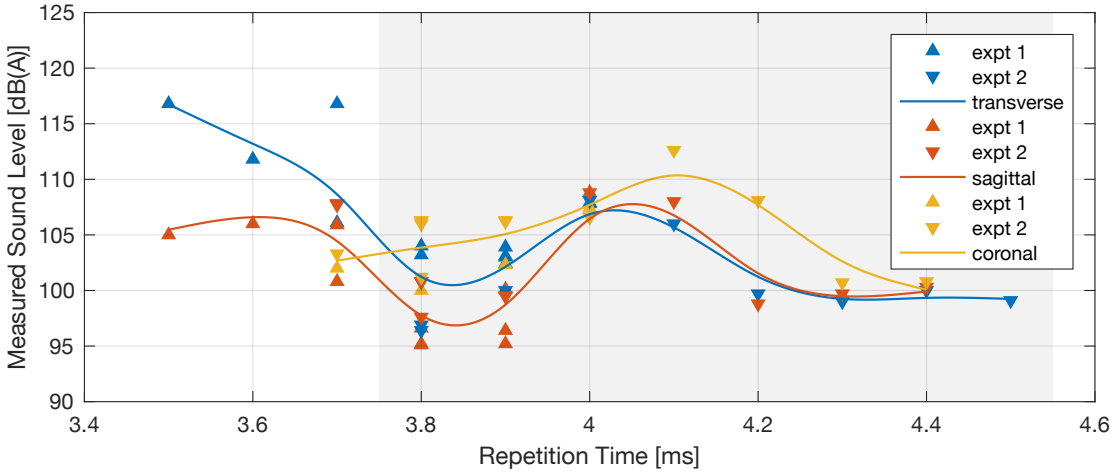


**Figure 4.1:** Sound pressure level assessment of dynamic Cartesian bSSFP MRI measured by MR-compatible microphone in a phantom set-up. Measurements were made on two separate occasions, experiment 1 (upper triangles) and 2 (lower triangles) with spline fit (solid lines), in scanner transverse (blue), sagittal (red) and coronal (yellow) orientations. A drop in sound level to acceptable levels was measured in all scan plan orientations at a repetition time of 3.8 ms and above (grey shaded region).

A preliminary protocol for dynamic bSSFP, presented in 2015 [164], was implemented with parameters based on the criteria above as well as previous applications of bSSFP for cine [65] and dynamic [56] fetal cardiac MRI. SENSE (§3.6.3) was used in combination with partial Fourier acquisition (3.6.2) to improve temporal resolution, with a combined under-sampling factor of R = 3–5. Sequence parameters used in the preliminary exploration were as follows: TR/TE 3.8/1.9 ms, flip angle 60°, FOV 400×300 mm, spatial resolution 1.8×2.3×6.0-8.0 mm, partial Fourier acquisition 5/8, SENSE R = 2–4, temporal resolution 83-170 ms and $\geqslant$ 40 dynamic image frames. Increased SENSE acceleration resulted in improved temporal resolution but decreased SNR, as shown in Figure 4.2. The prevalence of noise with

increased acceleration was clearly observed, though large anatomical features remained visible in the resulting images.

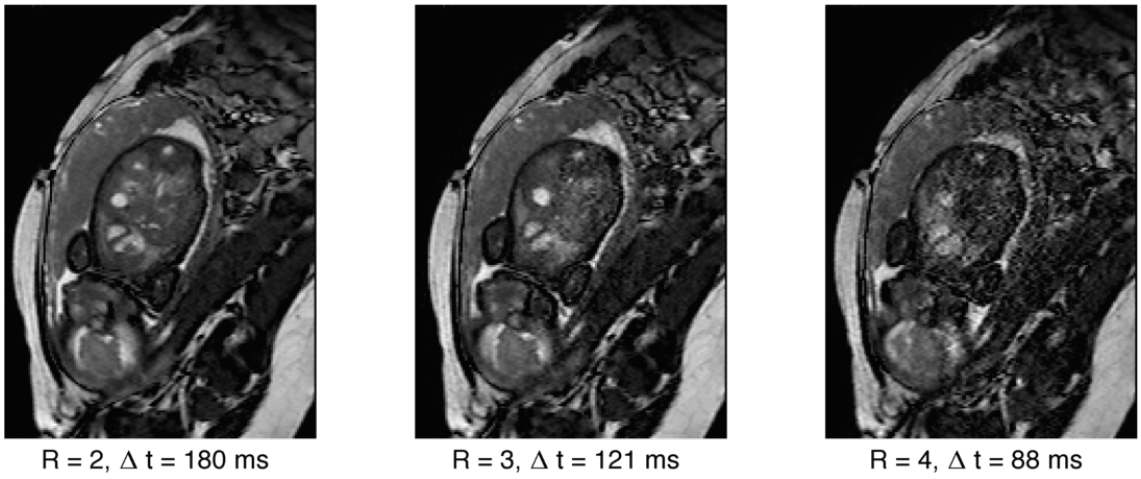


**Figure 4.2:** Dynamic images from a short-axis view of the fetal heart obtained with increasing SENSE reduction factors, R, and improved temporal resolution, $\triangle$t.

Subsequently, dynamic imaging with k-t SENSE (§3.6.4) was employed to improve temporal resolution while preserving SNR, taking advantage of the fact that the highly-dynamic fetal heart occupies only a small fraction of the field of view, as presented in 2016 [165]. Data was acquired using a 2D bSSFP sequence with regular Cartesian k-t under-sampling, a FOV of 400×300 mm and a spatial resolution of 1.8×2.3×6.0 mm. A spatio-temporally optimal sampling pattern [160] was used to minimise the overlap of aliases in x-f space, as shown in Figure 4.3, enabling acceleration of R = 8 to achieve a temporal resolution of 68-80 ms. This acceleration factor corresponds to the ratio of the width of the fetal heart to the FOV in the phase-encoding direction, thus ensuring minimal overlap of x-f aliases (Fig. 4.3b).

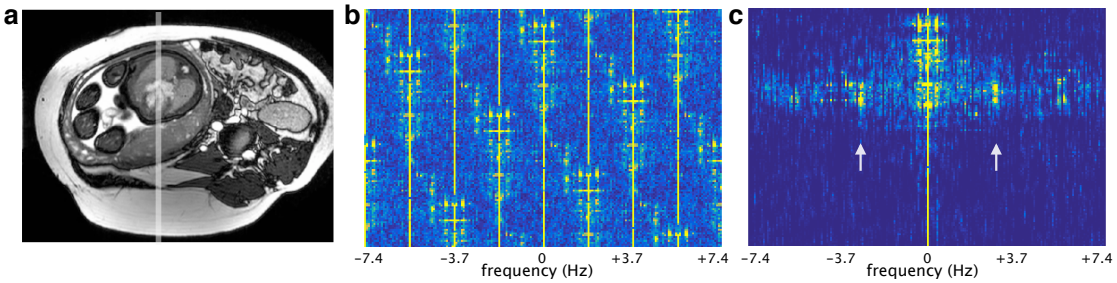


**Figure 4.3:** Accelerated k-t SENSE dynamic MR imaging of the fetal heart. (**a**) Dynamic image frame, reconstructed using k-t SENSE, with associated x-f space, corresponding to vertical grey line in (a), shown for (**b**) aliased, under-sampled x-f data, and (**c**) k-t SENSE reconstructed x-f data, revealing fundamental frequency of the fetal heart rate (arrows).

Later, data was acquired with 2.0×2.0×6.0 mm voxels to maintain isotropic in-plane resolution, as presented in 2017 [166]. Additional details of the dynamic k-t bSSFP acquisition are given in Section 4.5.

## 4.3 Motion Compensation

In a preliminary motion compensation framework [164], visual assessment was used to reject images in which the fetus was actively moving and an image-based navigator was used to select frames at end expiration of the maternal breathing cycle. The fetal heart rate was identified by temporally reordering dynamic image frames to minimise the temporal total variation between image frames in the region of the fetal heart.

A subsequent framework reduced the manual input required to user-specified target image frame and fetal heart region of interest [165]. The fetal heart rate was then identified in x-f space based on the conspicuous peaks in the fetal heart region of interest (ROI) in the range of expected fundamental frequencies (Fig. 4.3c). Spatial displacement of the fetal heart was compensated by employing self-gating, using per-frame sum of squared difference with the target frame calculated across the full maternal FOV to gate the through-plane displacement of the fetal heart due to maternal respiration, and rigid registration to the target image frame to correct for in-plane motion.

In the final 2D framework (§4.5), image-based maternal respiratory gating was replaced by an outlier rejection approach as systematic rejection of data based on a surrogate marker may be inaccurate and inefficient.

## 4.4 Cine Reconstruction

In early work, dynamic images were compounded by binning and averaging images with similar cardiac phase [164]. This was later changed to a temporal interpolation to improve the image quality of the densely-sampled data [165] and further refined to preserve the full temporal resolution of the undersampled acquisition [167], as presented in the following section (§4.5). It should be noted that as a consequence of verbatim inclusion of a published article, the symbols used here to denote acquired dynamic MR images and reconstructed cine images differs from those used in the following chapter.

# 4.5 Fetal Cardiac Cine Imaging Using Dynamic MRI

Magnetic Resonance in Medicine 79:327–338 (2018)

## Fetal Cardiac Cine Imaging Using Highly Accelerated Dynamic MRI With Retrospective Motion Correction and Outlier Rejection

Joshua F.P. van Amerom,[1] David F.A. Lloyd,[1,2] Anthony N. Price,[1] Maria Kuklisova Murgasova,[1] Paul Aljabar,[3] Shaihan J. Malik,[1] Maelene Lohezic,[1] Mary A. Rutherford,[1,3] Kuberan Pushparajah,[1,2] Reza Razavi,[1,2] and Joseph V. Hajnal[1]

**Purpose:** Development of a MRI acquisition and reconstruction strategy to depict fetal cardiac anatomy in the presence of maternal and fetal motion.
**Methods:** The proposed strategy involves i) acquisition and reconstruction of highly accelerated dynamic MRI, followed by image-based ii) cardiac synchronization, iii) motion correction, iv) outlier rejection, and finally v) cardiac cine reconstruction. Postprocessing entirely was automated, aside from a user-defined region of interest delineating the fetal heart. The method was evaluated in 30 mid- to late gestational age singleton pregnancies scanned without maternal breath-hold.
**Results:** The combination of complementary acquisition/reconstruction and correction/rejection steps in the pipeline served to improve the quality of the reconstructed 2D cine images, resulting in increased visibility of small, dynamic anatomical features. Artifact-free cine images successfully were produced in 36 of 39 acquired data sets; prolonged general fetal movements precluded processing of the remaining three data sets.
**Conclusions:** The proposed method shows promise as a motion-tolerant framework to enable further detail in MRI studies of the fetal heart and great vessels. Processing data in image-space allowed for spatial and temporal operations to be applied to the fetal heart in isolation, separate from extraneous changes elsewhere in the field of view. **Magn Reson Med 79:327–338, 2018. © 2017 The Authors Magnetic Resonance in Medicine published by Wiley Periodicals, Inc. on behalf of International Society for Magnetic Resonance in Medicine. This is an open access article under the terms of the Creative Commons Attribution License, which permits use, distribution and reproduction in any medium, provided the original work is properly cited.**

**Key words:** magnetic resonance imaging; fetal heart; cardiac cine; motion correction; congenital heart disease

### INTRODUCTION

Magnetic resonance imaging increasingly is being used as an adjunct to ultrasound to assess the developing fetus. Motion, however, remains a key limiting factor to the use of MRI to depict the fetal heart and great vessels in utero (1–3). The challenges are numerous when imaging a small, rapidly beating heart that is subject to various regular and spontaneous movements within the context of the maternal torso.

The fetal heart has a complex structure and is a relatively small and dynamic target for MRI. The ventricles are each only 15 mm in diameter in late gestation (4), and the normal fetal heart rate is 120 to 160 beats per minute (5), with low variation compared to adults (6) and no significant change in heart rate pattern during MRI (7). Gas exchange to the fetus occurs through the placenta, but episodic fetal respiratory movements still occur, causing displacement of the fetal diaphragm and chest wall (8). The fetus also can move freely, and general fetal movements occur at irregular intervals. Overall mobility is reduced with increased occupancy of the uterus at later gestational ages, although movement of the fetal trunk is present throughout gestation (9,10). Maternal respiration also is a factor because movement of the maternal anatomy leads to potentially large displacements of the entire fetal body. Although these sources of motion can be minimized during scanning, for example by maternal breath-hold or fetal sedation, such approaches can be both impractical and unacceptable and are likely to cause maternal discomfort and anxiety.

Synchronization with the fetal cardiac cycle during MRI data acquisition also poses a challenge. Electrocardiogram (ECG) gating of the fetal heart is unreliable (11), but segmented cine acquisitions have been achieved using self-consistency in reconstruction to infer a gating signal (12,13) or MR-compatible Doppler ultrasound-based triggering (14,15). However, with these methods, both regular and spontaneous motion may still corrupt the data.

[1]Division of Imaging Sciences and Biomedical Engineering, King's College London, London, United Kingdom.
[2]Department of Congenital Heart Disease, Evelina Children's Hospital, London, United Kingdom.
[3]Centre for the Developing Brain, King's College London, London, United Kingdom.

*Correspondence to: Joshua F.P. van Amerom, Division of Imaging Sciences & Biomedical Engineering, King's College London, St Thomas' Hospital, London SE1 7EH, United Kingdom. joshua.vanamerom@kcl.ac.uk; Twitter: @jfpvanamerom

This work was supported by the Engineering and Physical Sciences Research Council [grant no. EP/H046410/1]; the Medical Research Council Strategic Fund [grant no. MR/K0006355/1]; the Wellcome Trust [award no. 102431]; and the National Institute of Health Research [Biomedical Research Centre based at Guy's and St Thomas' National Health Services Foundation Trust and King's College London].

Funded by the EPSRC Programme, MRC Strategic Fund, Wellcome Trust, and NIHR BRC.

Received 6 December 2016; revised 1 March 2017; accepted 3 March 2017

DOI 10.1002/mrm.26686
Published online 3 April 2017 in Wiley Online Library (wileyonlinelibrary.com).

In this work, we aim to develop a MRI acquisition and reconstruction strategy to depict fetal cardiac anatomy in the presence of maternal and fetal motion. Retrospective reconstruction of cine images from a series of dynamic (real-time) images acquired without breath-hold or ECG triggering has been investigated in adult cardiac MRI (16). In the context of fetal cardiac imaging, a dynamic acquisition may provide serial views of the fetal heart and surrounding anatomy fast enough to freeze the various types of expected motion with the potential for retrospective processing to detect movement and correct for its effects. However, for in utero examinations, real-time imaging cannot achieve the same resolution as a segmented cine reconstruction (when cardiac gating is feasible), resulting in compromised signal-to-noise ratio (SNR) and resolution. To overcome these limitations, we explored an imaging strategy that favors both spatial and temporal fidelity at acquisition and initial reconstruction, resulting in noisy real-time images that then can be compounded to recover SNR while generating a cine image series representing a single cardiac cycle (17). In this work, we have developed the idea further, producing a pipeline approach that starts with highly accelerated dynamic MRI of the fetal heart and uses retrospective, image-based techniques to provide cardiac synchronization, motion correction, and outlier rejection to generate a fully corrected 2D cine image series. The method has been evaluated on 30 fetuses.

## METHODS

The proposed strategy involves 1) acquisition and reconstruction of highly accelerated dynamic MRI, followed by 2) cardiac synchronization, 3) motion correction, 4) outlier rejection, and finally 5) cardiac cine reconstruction. Processing of this data was performed sequentially and iteratively, as depicted in Figure 1. The entire reconstruction pipeline was implemented in MatLab R2016a (Mathworks, Natick, USA) using methods of the signal processing, image processing, and statistics toolboxes. A repository of source code is available: https://github.com/jfpva/fetal_cmr_cine_2d (SHA-1:556b9646bf).

Thirty singleton pregnancies (25–35 weeks gestational age) were scanned on a 1.5 Tesla Ingenia system (Philips, Best, Netherlands), including seven volunteers and 23 cases with congenital heart disease and related conditions. Scans were performed in one or more views of the fetal heart, typically short- and long-axis orientations without maternal breath-hold. Expectant mothers were scanned in a left lateral tilt position using an anterior torso coil array in combination with a posterior spine coil array to measure signal in 28 receiver channels. Studies were conducted with the approval of the local research ethics committee, and all participants gave written informed consent prior to enrollment. Reconstruction methods were established using data from five cases collected early in the study. Reconstruction parameters were refined further, once all cases were scanned using an additional five data sets selected at random.

The following sections outline the conceptual framework of this approach, beginning with a description of the acquisition and reconstruction of highly accelerated dynamic MRI and subsequent kernel-weighted interpolation to reconstruct cine images, followed by the details of cardiac synchronization, motion correction, and outlier rejection.

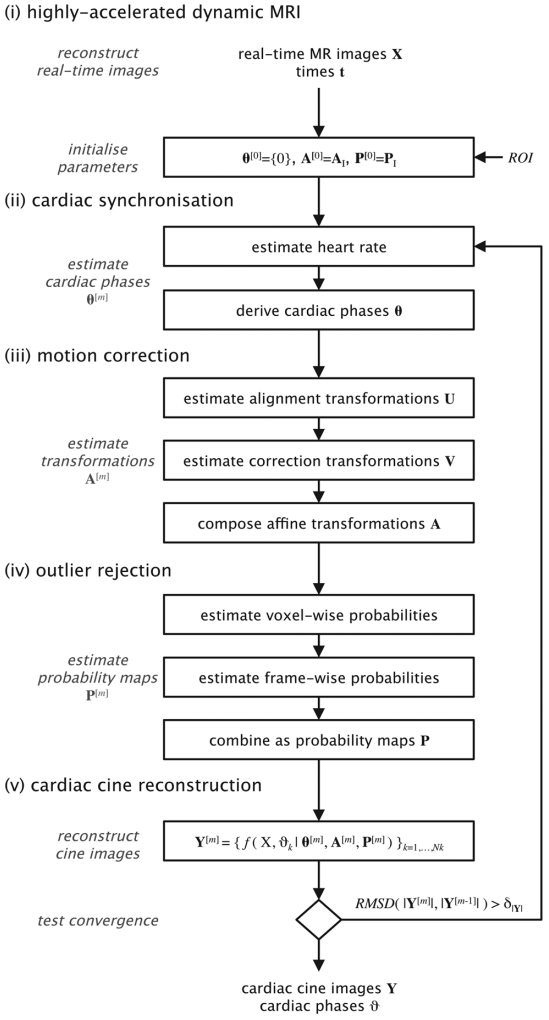


FIG. 1. Proposed method for motion-tolerant fetal cardiac cine imaging. The steps comprise (**i**) data acquisition and image reconstruction of time series of highly accelerated dynamic (real-time) MR images, **X**, followed by retrospective, image-based (**ii**) cardiac synchronization, (**iii**) motion correction, and (**iv**) outlier rejection, before a final (**v**) cardiac cine reconstruction. Steps (ii)–(v) were repeated using updated parameters, **θ**, **A**, and P, until the RMSD of the signal intensity in the region of interest of successive cardiac cine reconstructions, Y, was below the tolerance $\delta_{|Y|}$. ROI, region of interest; RMSD, root mean square difference.

### Highly Accelerated Dynamic MRI

The fetal body in utero is surrounded by the maternal uterus and torso. The discrepancy in size and temporal dynamics of the fetal heart and surrounding anatomy leads to highly complementary signal properties in space

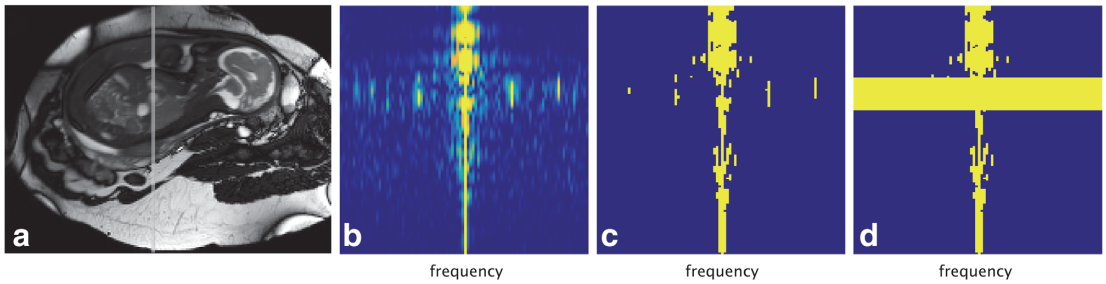


FIG. 2. A 33-week gestational age fetus in utero surrounded by maternal anatomy in (**a**) the signal intensity of the time-averaged baseline estimate, $\bar{\rho}$, of the *k-t* sampled dynamic data. (**b**) The *x-f* prior, $\Theta$, at the location of the gray vertical line in (a) reveals spatiotemporal sparsity in the x-f domain. Regions of the *x-f* prior above the regularization term (ie, $\Theta > \Lambda S \Psi S^H (S S^H)^{-2}$) are shown for (**c**) spatially uniform regularization with $\Lambda = \lambda_0 I$, and (**d**) spatially adaptive regularization, in which $\Lambda$ has diagonal elements $\lambda_{j \notin ROI} = \lambda_0$ and $\lambda_{j \in ROI} = \lambda_{ROI}$, with $\lambda_0 > \lambda_{ROI}$.

and time, with the fetal heart occupying only a small fraction of the spatial field of view but exhibiting a large range of temporal frequencies, *f*, whereas the surrounding anatomy is much more slowly varying. Consequently, when a dynamic sequence designed with time resolution suitable to capture the pulsation of the fetal heart is Fourier-transformed in time to create a *x-f* representation, the resulting space has sparse signal content, as shown in Figure 2b. Real-time imaging with *k-t* undersampling can take advantage of this spatiotemporal sparsity to achieve high acceleration factors in which k-space is undersampled with a sheared grid pattern, resulting in aliasing of the *x-f* support with minimal overlap between aliases.

The *k-t* sensitivity encoding (SENSE) reconstruction aims to recover a vector of complex-valued *x-f* signals, $\rho$, for voxels aliased to $\rho_{alias}$ using prior knowledge of the spatiotemporal distribution of the unaliased signals, $\Theta$, and receiver array sensitivities, S (18). The closed-form *k-t* SENSE reconstruction problem in *x-f* space is given by

$$\rho = \bar{\rho} + \Theta S^H (S \Theta S^H + \lambda \Psi)^{-1} (\rho_{alias} - S\bar{\rho}), \qquad [1]$$

where $\bar{\rho}$ is a time-averaged baseline estimate of $\rho$, and $\lambda\Psi$ is a regularization term comprised of controlling parameter $\lambda$ and noise covariance matrix $\Psi$. Baseline subtraction in Equation [1] aids the reconstruction by removing the contribution of voxels dominated by static signal, reducing the number of voxels contributing aliased signal.

The priors in $\Theta$ can be determined from full field of view, low spatial-resolution training data that is acquired interleaved with the undersampled scan or during a separate acquisition phase (18). The latter approach was adopted for this study because maximizing temporal resolution in the final images was key. The choice of $\lambda$ balances content revealed by $\Theta$, with noise properties specified in $\Psi$ such that reducing $\lambda$ recovers more dynamic content but increases the noise in the final reconstruction. In the fetal cardiac case, most of the spatial field of view contains regions of static or slowly moving anatomy, with an easily identified and highly localized region of interest (ROI) for which there are higher temporal frequencies to recover. This situation was exploited by adopting spatially adaptive regularization in which $\lambda$ was preferentially reduced in regions of highly dynamic anatomy, leading to

$$\rho = \bar{\rho} + \Lambda^{-1} \Theta S^H (S \Lambda^{-1} \Theta S^H + \Psi)^{-1} (\rho_{alias} - S\bar{\rho}), \qquad [2]$$

where $\Lambda$ is a diagonal matrix of spatially adaptive regularization-controlling parameters. In this work, the elements of $\Lambda$ were assigned a base value, $\lambda_0$, for voxels outside the ROI and a much lower value, $\lambda_{ROI}$, for voxels inside the ROI, as shown in Figures 2c through d. Using data collected in preparation for this study, a regularization level of $\lambda_0 = 0.0014$ was found to capture the dynamics of the maternal anatomy and limit noise in the reconstructed real-time images. A highly permissive regularization level of $\lambda_{ROI} = 0.01\,\lambda_0$ was used to preserve the full temporal resolution of the accelerated acquisition, as indicated in Figure 2d. In this application, reduction of $\lambda$ was well tolerated because noise in the real-time images was reduced when those images were combined to generate the final cine images.

MRI is generally considered safe at 1.5 T in the second and third trimester (19), but caution should be exercised to limit RF exposure (20) and acoustic noise levels (21). Imaging was performed with a 2D Cartesian balanced steady-state free precession (bSSFP) sequence, as it is the standard for postnatal cardiac cine MR, and the combination of short acquisition and high signal has been shown to be effective for imaging the fetal heart (22). Uniform-density *k-t* sampling with an optimal spatiotemporal grid pattern (23) was used to minimize the overlap of aliases in *x-f* space. Coil calibration data was acquired in a prescan, and low spatial-resolution training data was acquired immediately following the undersampled data. Minimal overlap between aliases of the *x-f* support was maintained by setting the time taken to phase-encode a field of view just large enough to encompass the fetal heart, $t_{enc}$, as the maximum frame rate. When viewed from the perspective of acceleration by undersampling, the upper limit on the acceleration factor was set by the ratio of the full maternal field of view in the phase-encode direction to the size of the fetal heart. Imaging parameters were selected with reference to previous MRI studies of the fetal heart using segmented cine (12) and real-time (24) bSSFP, and were optimized to yield adequate signal and contrast to depict the fetal heart and surrounding anatomy with sufficient

temporal resolution to capture cardiac pulsation during preliminary pilot cases not included in this report (25). Single-slice imaging was performed with the following sequence parameters: repetition time (TR)/echo time (TE) 3.8/1.9 ms; flip angle 60°; field of view 400 × 304 mm; voxels 2 × 2 × 6 mm; acceleration factor 8; and temporal resolution 72 ms. Operation was constrained to 2 W/kg or less whole body-specific absorption rate, and low peripheral nerve stimulation and gradient-induced acoustic noise settings were used. This limited scanner performance resulting in variations in timing, with TR ranging from 3.8 to 4.4 ms (median 4.2 ms) and temporal resolutions ranging from 72 to 83 ms (median 81 ms). In five cases, the field of view was increased to accommodate maternal anatomy, leading to temporal resolutions 1 or 2 TR longer.

In initial cases, a scan duration of 16 to 20 seconds was used to establish the amount of data typically required for robust real-time and cine reconstructions. This data was reconstructed at full and reduced durations, showing increased image quality with increased scan duration but at the same time a higher chance of motion corruption. A scan duration of approximately eight seconds was determined to balance the benefits and risks. All fetal real-time images were reconstructed with an equivalent scan duration of approximately 8 seconds.

An initial *k-t* SENSE reconstruction with spatially uniform regularization ($\lambda = \lambda_0$ in Equation 1) was used as a reference to specify the static ROI delineating the margin of the fetal heart. This was the only manual intervention required for the complete postprocessing pipeline. Real-time images were then reconstructed using Equation [2], following the process described in the original *k-t* SENSE method (18).

### Cine Reconstruction from Dynamic MRI

Acquisition and reconstruction of highly accelerated dynamic MRI results in a time series of real-time images $\mathbf{X} = \{\mathrm{X}_i\}_{i=1,\ldots,N_i}$ at times $\mathbf{t} = \{t_i\}_{i=1,\ldots,N_i}$, where $i$ indexes real-time frame number from 1 to $N_i = 96$, and frame $\mathrm{X}_i$ has elements $x_{\mathrm{j},i}$ at 2D spatial coordinates j.

If the heart rate is known, retrospective cardiac synchronization can be performed by mapping times $\mathbf{t}$ to cardiac phases $\boldsymbol{\theta} = \{\theta_i\}_{i=1,\ldots,N_i}$, where the values of $\theta_i$ fall on the cyclic interval $[0, 2\pi]$. Reordering the real-time image series according to $\theta_i$ leads to a densely sampled set of images for a single cardiac cycle. Real-time images were kept as complex valued data arrays to facilitate further processing.

Kernel-weighted interpolation can be used to reconstruct a cine image, $\mathrm{Y}_\vartheta$, at cardiac phase $\vartheta$ from a combination of $\mathrm{X}_i$ as:

$$\mathrm{Y}_\vartheta = \frac{\sum_i d_i \mathrm{X}_i}{\sum_i d_i}, \qquad [3]$$

where weights $d_i$ are obtained from a kernel function $d(\vartheta, \theta_i)$ that acts as a temporal point spread function, distributing the values of $\mathbf{X}$ to $\mathrm{Y}_\vartheta$. In the *k-t* SENSE method, $\mathbf{X}$ is obtained by inverse Fourier transform of the reconstructed temporal frequency spectrum, which strictly is band-limited by the sampled frame rate; and data for a single frame are considered acquired simultaneously, which suggests that the appropriate kernel function is a sinc. However, the cyclic nature of the cardiac phase requires that the kernel width does not exceed 2 $\pi$ and that the kernel weight should be smoothly varying at $\pm\pi$. In this work, a Tukey window was used to taper the kernel near $\pm\pi$, leading to a kernel-weighting function of the form

$$d(\vartheta, \theta_i) = sinc\left(\pi\left(\frac{\angle(\vartheta, \theta_i)}{\theta_{enc}}\right)\right) win_{Tukey}\left(\angle(\vartheta, \theta_i)|\alpha\right), \qquad [4]$$

where $\angle(\vartheta, \theta_i)$ is the angular difference between $\vartheta$ and $\theta_i$ wrapped on the interval $[-\pi, +\pi]$; the temporal resolution of the acquisition is given by $\theta_{enc} = 2\pi\, t_{enc}/t_{RR}$ in units of cardiac phase, using the cardiac period $t_{RR}$ to normalize $t_{enc}$; and $\alpha$ is the proportion of the outer edge of the window with tapered cosine lobes.

Motion correction and outlier rejection were included in the reconstruction of $\mathrm{Y}_\vartheta$ to improve image quality in the presence of fetal and maternal motion. The aim of motion-correction was to align the position of the fetal heart across all $\mathrm{X}_i$. A set of spatial transformations, $\mathbf{A} = \{\mathrm{A}_i\}_{i=1,\ldots,N_i}$, was estimated using image registration techniques, with transformation of real-time image frame $\mathrm{X}_i$ by $\mathrm{A}_i$ denoted as $\mathrm{X}_i^{(\mathrm{A})}$. Outlier rejection was used to reduce the influence of corrupted data, such as voxels with motion artifact or frames with inconsistent anatomical views. Posterior probability maps, $\mathbf{P} = \{\mathrm{P}_i\}_{i=1,\ldots,N_i}$, were generated to indicate the probability, $p_{\mathrm{j},i}$, that each voxel in $\mathbf{X}$ was an inlier, and were used in the cine reconstruction as a robust statistic in the kernel-weighting function.

Including motion correction and outlier rejection in Equation [3] lead to a kernel-weighted interpolation of $\mathrm{X}_i$ at cardiac phase $\vartheta$, given estimates of cardiac phases $\boldsymbol{\theta}$, spatial transformations $\mathbf{A}$, and posterior probability maps $\mathbf{P}$, of the form

$$\begin{aligned} \mathrm{Y}_\vartheta &= f(\mathbf{X}, \vartheta|\boldsymbol{\theta}, \mathbf{A}, \mathbf{P}) \\ &= \sum\nolimits_i \mathrm{W}_i \circ \mathrm{X}_i^{(\mathrm{A})} \end{aligned}, \qquad [5]$$

with kernel-weighting and normalization combined in weighting maps $\mathbf{W} = \{\mathrm{W}_i\}_{i=1,\ldots,N_i}$, where $\circ$ indicates Hadamard (element-wise) matrix multiplication, and superscript (A) denotes spatial transformation by A. The weighting map for real-time image frame $i$ is then given by

$$\mathrm{W}_i = \left(d_i \mathrm{P}_i^{(\mathrm{A})}\right) \oslash \left(\sum_{i'=1}^{N_i} d_{i'} \mathrm{P}_{i'}^{(\mathrm{A})}\right), \qquad [6]$$

where $\oslash$ indicates element-wise matrix division.

Cardiac synchronization, motion correction, and outlier rejection steps were performed iteratively. Parameters were initialized for iteration $m = 0$ such that cardiac phase was zero for all real-time image frames, $\boldsymbol{\theta}^{[0]} = \{0\}_{i=1,\ldots,N_i}$; spatial transformations were set to an identity transformation, $\mathbf{A}^{[0]} = \mathbf{A}_\mathrm{I}$, such that $\mathbf{X} = \mathbf{X}^{(\mathrm{A}_\mathrm{I})}$; and probability maps had all voxels as full inliers, $\mathbf{P}^{[0]} = \mathbf{P}_\mathrm{I}$ with $p_{\mathrm{j},i} = 1$ for all j and $i$.

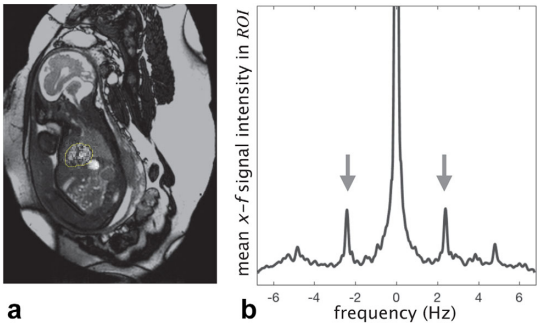


FIG. 3. (**a**) Image frame from real-time series reconstructed using Equation [2] corresponding to fetus shown in Figure 2a, with region of interest over the fetal heart (yellow dotted line), rotated so the fetus is in radiographic image orientation. (**b**) The fetal heart rate (arrows) appears as local maxima in the range of fundamental frequencies (1.8–2.7 Hz) of the mean *x-f* signal intensity in the region of interest.

### Cardiac Synchronization

Synchronization with the cardiac cycle was required to resolve the beating of the fetal heart. One advantage of the high temporal resolution acquisition was that the fetal heart rate could be estimated directly from the real-time image series because the periodicity of the fetal heart was revealed as conspicuous peaks in the temporal frequency spectrum.

An estimate of the fetal cardiac period, $t_{RR}$, was obtained from the spatially transformed real-time images, $\mathbf{X}^{(\mathrm{A})}$. The temporal frequency spectrum of the fetal heart was calculated by taking the spatial mean in *x-f* space over the ROI after interpolation to a resolution of 0.1 beats per minute by zero-padding in time before Fourier transformation. The local maxima in this signal in the range of fundamental frequencies (1.8–2.7 Hz) was identified as the fetal heart rate corresponding to $t_{RR}$, as shown in Figure 3b. This estimate of the fetal heart rate was used to map each $t_i$ to an associated cardiac phase, $\theta_i = 2\pi(t_i \mathrm{mod} t_{RR})/t_{RR}$.

### Motion Correction

Rigid body in-plane image registration was used to estimate a set of affine transformation matrices $\mathbf{A} = \{\mathrm{A}_i\}_{i=1,\ldots,N_i}$ that align the position of the fetal heart across the real-time image series. Image registration was performed using the Matlab imregtform function (MathWorks) between pairs of source and matched target images by minimizing a sum of squares differences cost function. Confounding fetal and maternal anatomy was masked out using the ROI, which was doubled in area for image registration as inclusion of some fetal chest anatomy was found to improve results. The origin of coordinates was defined as the centroid of the ROI, and three iterations with decreasing Gaussian spatial blurring ($\sigma = 1.6,\ 1.2,\ 0.8$ mm) of the source images were used to facilitate convergence. Spatial transformations were applied to $\mathbf{X}$ using cubic interpolation to yield $\mathbf{X}^{(\mathrm{A})}$, whereas linear interpolation was used for $\mathbf{P}^{(\mathrm{A})}$ to maintain discontinuities in the probability maps.

In some cases, an initial image registration was found to include some overfitting manifest by a periodic twisting of the cine sequence along the long axis of the heart as it beats. Thus, two image registration steps were performed for each $\mathrm{X}_i$: the first registration resulted in spatial transformations $\mathbf{U}$ that provided most of the spatial alignment, and the second resulted in spatial transformations $\mathbf{V}$ that compensated for any residual twisting of the heart. These two sets of spatial transformations were then composed as $\mathrm{A}_i = \mathrm{U}_i\mathrm{V}_i$.

Spatial transformations $\mathbf{U}$ were obtained from image registration of the native images $\mathrm{X}_i$ to target images $\hat{\mathrm{X}}_i$, calculated using Equation [5] at $\theta_i$ given current estimates of $\boldsymbol{\theta}$, $\mathbf{A}$, and $\mathbf{P}$, but excluding the source image frame, $\mathrm{X}_i$, so that

$$\begin{aligned}\hat{\mathrm{X}}_i &= \hat{f}(\mathbf{X}, \theta_i | \boldsymbol{\theta}, \mathbf{A}, \mathbf{P}) \\ &= \textstyle\sum_{i' \neq i} \hat{\mathrm{W}}_{i'} \circ \mathrm{X}_{i'}^{(\mathrm{A})}\end{aligned}, \qquad [7]$$

where $i$ was also omitted from the summation in Equation [6] to calculate $\hat{\mathrm{W}}_{i'}$.

Spatial transformations $\mathbf{V}$ were obtained from image registration between pairs of source and target images calculated using Equation [5] and differing only in input spatial transformation. Source images were calculated as $\{f(\mathbf{X}, \theta_i | \boldsymbol{\theta}, \mathbf{U}, \mathbf{P})\}_{i=1,\ldots,N_i}$ using $\mathbf{U}$ as input, whereas target images were calculated as $\{f(\mathbf{X}, \theta_i | \boldsymbol{\theta}, \mathbf{A}_\mathrm{I}, \mathbf{P})\}_{i=1,\ldots,N_i}$ using the null transformation $\mathbf{A}_\mathbf{I}$ to capture the average position of the fetal heart during the whole acquisition.

### Outlier Rejection

Robust statistics were employed to exclude inconsistent data using an approach that has been shown to be effective for reconstruction of volumetric fetal MRI from 2D images (26). Each voxel and frame was classified as an inlier or outlier using mixture models of the two classes, with parameters estimated using expectation maximization. In this way, the weighting of voxels that were corrupted by motion artifact and frames that were misaligned or contained inconsistent anatomical views could be reduced or rejected completely. The elements of probability maps $\mathrm{P}_i$ were calculated as the product of voxel- and frame-wise probabilities, $p_{\mathrm{j},i} = p_{\mathrm{j},i}^{voxel}\, p_i^{frame}$. Figure 4 depicts the voxel- and frame-wise outlier rejection process.

Voxel-wise classification was based on voxel-wise error maps $\mathbf{E} = \{\mathrm{E}_i\}_{i=1,\ldots,N_i}$, calculated as

$$\mathrm{E}_i = \mathrm{X}_i - \hat{\mathrm{X}}_i^{(\mathrm{A}^{-1})}, \qquad [8]$$

where the inverse spatial transformation, $\mathrm{A}^{-1}$, was used to align the voxels in each reference image frame $\hat{\mathrm{X}}_i$ with the acquired data in $\mathrm{X}_i$ (Fig. 4 a-c).

The likelihood of observing error $e_{\mathrm{j},i}$ was modeled as

$$\mathbb{P}(e_{\mathrm{j},i} | \sigma_e, c_e) = G(e_{\mathrm{j},i} | \sigma_e) c_e + b_e(1 - c_e) \qquad [9]$$

using a mixture of a bivariate Gaussian inlier distribution $G(e_{\mathrm{j},i} | \sigma_e)$ with zero mean and variance $\sigma_e$ in both real and imaginary components (Fig. 4e), and a uniform outlier distribution of density $b_e$ with a mixing proportion

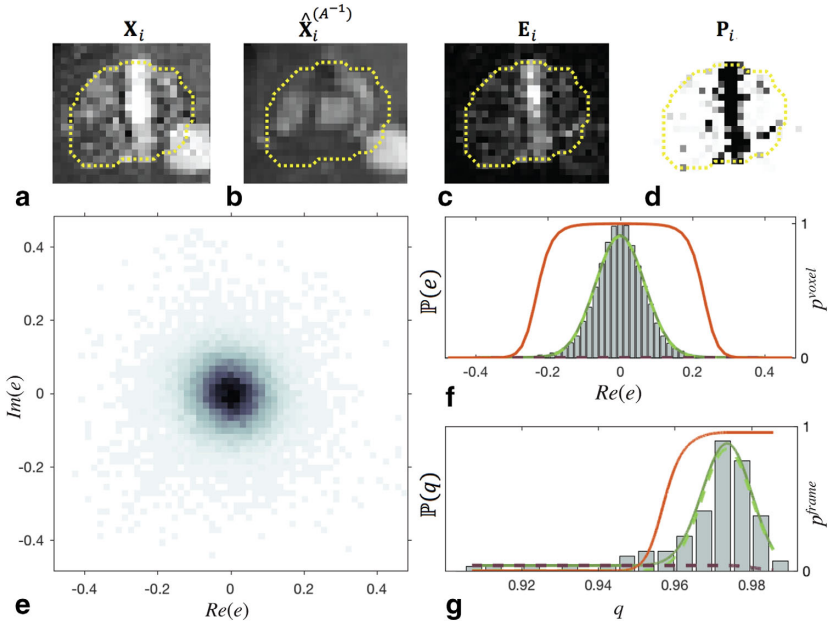


FIG. 4. Cropped views of the heart of the fetus shown in full field of view in Figure 3a in (**a**) real-time image frame, $X_i$, and (**b**) matched reference image, $\hat{X}_i^{(A^{-1})}$. The difference between these two images yields (**c**) an error map, $E_i$, from which (**d**) a probability map, $P_i$, is generated. Voxel-wise probabilities are determined from (**e**) the distribution of complex error values in the region of interest (dotted line) in (c) for all image frames, for which (**f**) a cross-section with Im(e) = 0 is shown to aid interpretation. The voxel-wise likelihood of observing errors $\mathbb{P}(e)$ (solid green line) is modeled using a mixture of a Gaussian inlier distribution (dashed green line) and uniform outlier distribution (dashed purple line), to give voxel-wise posterior probability weighting $p^{voxel}$ (red line). Frame-wise probabilities are determined in a similar manner based on (**g**) the distribution of frame potentials, $q_i$, using a mixture of a Rician inlier distribution (dashed green line), $R(1-q_i)$, and a uniform outlier distribution (dashed purple line), resulting in frame-wise posterior probability weighting $p^{frame}$ (red line). Signal intensities of complex-valued voxels are shown in (a), (b), and (c) for visualization. The gray scale of the probability map in (**d**) varies from 0 (black) to 1 (white).

given by $c_e$ (Fig. 4f). These distribution parameters were estimated by maximizing the log-likelihood $\sum_{j\in ROI}\sum_i log\,\mathbb{P}(e_{j,i}|\sigma_e, c_e)$, resulting in an estimate of the voxel-wise posterior probability given by

$$p_{j,i}^{voxel} = \frac{G(e_{j,i}|\sigma_e)c_e}{G(e_{j,i}|\sigma_e)c_e + b_e(1-c_e)} \quad [10]$$

Frame-wise posterior probability was used to further reduce the weighting of frames containing many voxels with low voxel-wise posterior probability. The frame-wise potential, $q_i$, of each real-time image $X_i$ was calculated as $q_i = \sqrt{\sum_{j\in ROI}(p_{j,i}^{voxel})^2/N_{j\in ROI}}$, where $N_{j\in ROI}$ is the number of voxels in the ROI. The likelihood of observing $q_i$ was modeled as the mixture of a Rician inlier distribution, $R(1-q_i|1-\nu_q,\sigma_q)$ with noncentrality $\nu_q$ and scale $\sigma_q$, and uniform outlier distribution with density $b_q$, given by

$$\mathbb{P}(q_i|\nu_q,\sigma_q,c_q) = R(1-q_i|1-\nu_q,\sigma_q)c_q + b_q(1-c_q), \quad [11]$$

with mixing proportion given by $c_q$ (Fig. 4g). In practice, the right tail of the frame-wise outlier class was tapered to ensure $p_i^{frame}$ was nondecreasing. As with voxel-wise outlier rejection, distribution parameters were estimated by log-likelihood maximization to give frame-wise posterior probability

$$p_i^{frame} = \frac{R(1-q_i|1-\nu_q,\sigma_q)c_q}{R(1-q_i|1-\nu_q,\sigma_q)c_q + b_q(1-c_q)} \quad [12]$$

### Cardiac Cine Reconstruction

For each iteration, $m$, of the full pipeline (Fig. 1), a cine image series, $\mathbf{Y}^{[m]} = \{Y_{\vartheta_k}^{[m]}\}_{k=1,\ldots,N_k}$, was generated for $N_k = 25$ uniformly distributed cardiac phases using Equation [5]. To aid visualization of subtle features, reconstructed spatial resolution was increased in $Y_{\vartheta_k}$ by first increasing the spatial resolution of real-time images $X_i$ and probability maps $P_i$. Real-time images were zero-padded in k-space to an apparent resolution of $1.25 \times 1.25$ mm to improve visualization of small structures (27). No k-space apodization was applied to preserve spatial resolution. Gibbs ringing effects were reduced when combining spatially transformed real-time images with subvoxel displacements. Probability maps were scaled to the same resolution using linear interpolation to maintain discontinuities.

Processing continued iteratively until the algorithm converged or $N_m = 5$ iterations were reached.

Convergence was measured as the root mean square difference (RMSD) of the signal intensity in the ROI of successive cardiac cine reconstructions, $RMSD(|\mathbf{Y}^{[m]}|, |\mathbf{Y}^{[m-1]}|)_{j\in ROI} < \delta_{|\mathbf{Y}|}$. After some experimentation, the convergence tolerance, $\delta_{|\mathbf{Y}|}$, was set to 0.1% of the maximum signal intensity in the real-time images within the ROI.

### Evaluation

Line profiles in *x-t*, drawn across the cardiac anatomy, were used to visualize the signal evolution during the cardiac cycle of the real-time and cine images series, and to assess the effect of motion correction and outlier rejection. Voxel- and frame-wise probabilities used for outlier rejection were visualized and inspected in the real-time images for correspondence between outlier classification and visually inconsistent voxels and frames. The effect of *k-t* SENSE regularization was assessed by comparing cine image series generated from real-time images reconstructed using spatially uniform (Eq. [1]) and spatially adaptive (Eq. [2]) regularization.

Image quality was assessed by two fetal cardiologists (D.L., K.P.). Cine image series reconstructed using the proposed method were scored on a 5-point scale for both gross and fine features of the fetal heart and great vessels—score 4: high contrast between blood and myocardium, distinct appearance of fine structural details, and no noteworthy artifacts; score 3: adequate image quality to determine most intracardiac structures, some insignificant artifacts; score 2: sufficient image quality to determine some intracardiac structures, despite some significant artifacts; score 1: some significant artifacts, adequate image quality to determine general ventricular morphology only; and score 0: inadequate image quality to visualize global cardiac structure. The two reviewers' assessments were combined as an average score.

The utility of each step in the pipeline was evaluated by comparing the results of the full pipeline with those from reduced pipelines that excluded one or more steps. An entropy-based image quality metric was used to compare the resulting cine image series. The entropy metric favors high contrast and has been shown to be sensitive to motion artifacts in MRI (28). The entropy, $H$, of cine image series

$$H(\mathbf{Y}) = \sum_{j\in ROI}\sum_{k}\frac{|y_{j,\vartheta_k}|}{y_{max}} ln\left(\frac{|y_{j,\vartheta_k}|}{y_{max}}\right) \qquad [13]$$

where signal intensities $|y_{j,\vartheta_k}|$ were normalized by $y_{max} = \sqrt{\sum_{j\in ROI}\sum_k |y_{j,\vartheta_k}|^2}$. Relative entropy was used for comparison between data sets, where entropy values were normalized by dividing by the entropy of the cine generated from initial parameter values, $H(\mathbf{Y}^{[0]})$.

## RESULTS

Data was acquired in 30 singleton pregnancies, including nine cases with two scans in different orientations in the same fetus. Of these 39 data sets, three were acquired during periods of general fetal movement, when the fetus was in motion during most of the scan, precluding further processing. The remaining 36 data sets were successfully reconstructed using the method depicted in Figure 1. An example reconstruction is shown in Figures 5 and 6.

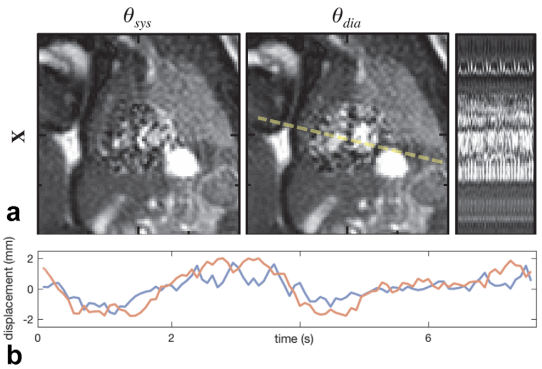


FIG. 5. Reconstructed real-time image series for fetus shown in full field-of-view image in Figure 3a. (**a**) Reconstructed real-time images, $\mathbf{X}$, showing cropped views of the fetal heart at end-ventricular systole, $\theta_{sys}$, and diastole, $\theta_{dia}$, with line profile across ventricles (dashed line) showing real-time frames ordered based on estimated cardiac phase. (**b**) Mean in-plane displacement of voxels $j \in$ region of interest of $\mathbf{X}^{(A)}$ in vertical (red line) and horizontal (blue line) directions showing a pattern of displacement consistent with the effects of maternal respiration. Cropped views cover 100 mm in each direction, with 25-mm markers shown for reference.

Spatiotemporal sparsity similar to the pattern shown in Figure 2 was evident in all data sets. An example real-time image frame, acquired without maternal breath-hold, is shown in Figure 3a, in which a high level of noise can be observed within the ROI. In all cases, the estimated heart rate resulted in a cardiac phase reordering that revealed the pulsatility of the fetal heart in a combined cardiac cycle, similar to the *x-t* profile shown to the right of Figure 5a. In three of the cases with the

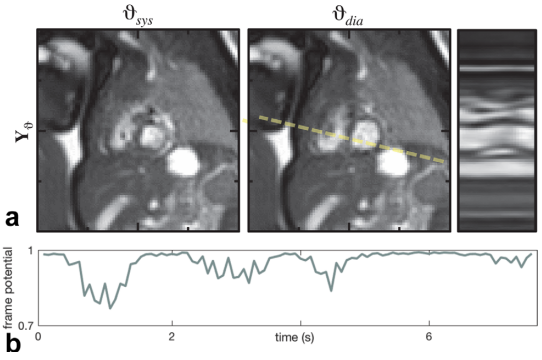


FIG. 6. Cine image series, $\mathbf{Y}$, reconstructed from real-time image series shown in Figure 5a. (**a**) Cropped views of the fetal heart in cine image frames at systole, $\vartheta_{sys}$, and diastole, $\vartheta_{dia}$, with line profile across the ventricles (dashed line) showing the temporal dynamics of the cardiac anatomy. (**b**) Frame potential, $q_i$, of real-time image frame $X_i$ was reduced during periods of large displacement, shown in Figure 5b, as the fetal heart was also displaced through-plane. Cropped views cover 100 mm in each direction, with 25- mm markers shown for reference.

two data sets in the same fetus, the scans were performed in quick succession such that little change in heart rate was anticipated between them. In these cases, the estimated heart rates differed by 1.4, 1.5, and 2.0% of the mean estimated heart rate, respectively, providing support for the use of a single heart rate for cardiac synchronization of data from each short acquisition. In most of the data sets, the estimated heart rate did not change between iterations of the pipeline. However, the alignment of the fetal heart across real-time images resulting from motion correction had the effect of making the peaks in the *x-f* signal more prominent, and in two data sets a difference of more than 1% of the final heart rate was observed between initial and final iterations.

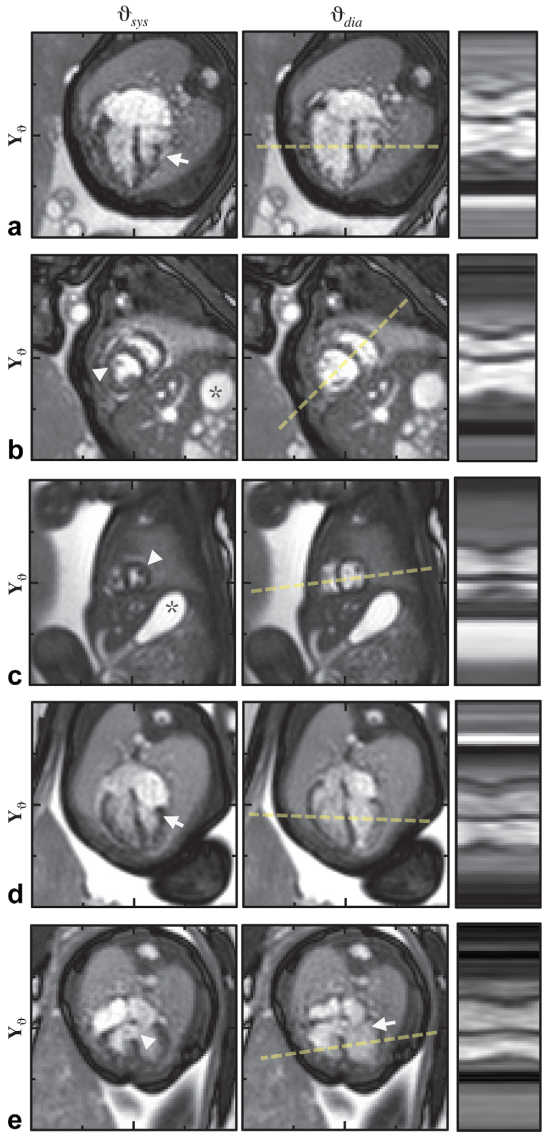


Figure 5b shows mean in-plane displacement in $X_i^{(A)}$ for voxels $j \in ROI$ plotted against time with a pattern of displacement consistent with the effects of maternal respiration. The frame potential, shown in Figure 6b, was reduced during periods of large displacement because the fetal heart was also displaced through-plane. The maximum in-plane displacement in this data set was 2.1 mm, and 27% of voxels were considered outliers ($p_{j\in ROI,i} < 0.5$). The maximum in-plane displacement in all data sets ranged from 0.5 to 2.3 mm, with a median of 1.8 mm, whereas a median of 13% of voxels were considered outliers, ranging from 2% to 63%. Frames classified as outliers were typically those misaligned or heavily corrupted due to motion. The final reconstructed cine series (Fig. 6a) shows clear depiction of the cardiac anatomy.

Expert image evaluation resulted in a median combined score of 2.5 out of 4. No individual cine image series was given a score of 4, although 89% of combined scores were higher than 1, indicating that intracardiac structures as well as general ventricular morphology could be determined in most of the cases. Abnormalities suspected from echocardiographic examination prior to MRI were confirmed when appropriate imaging planes were acquired, as shown in the cine reconstructions in Figure 7.

The utility of each step in the full method was evaluated by comparing the cine image series reconstructed using the full pipeline with those reconstructed leaving out one or more steps. Figure 8 illustrates how the adaptive regularization in the *k-t* SENSE reconstruction allows additional details of the cardiac motion to be depicted. An example is shown in Figure 9, in which the cine image series reconstructed using the full pipeline had improved anatomical depiction compared to those reconstructed using a subset of the pipeline. Figure 10 presents the quantitative results for all cases, showing that each step in the reconstruction served to improve image quality. Of the two main correction steps, the largest reduction in relative entropy was due to motion correction in 67% of the reconstructions and due to outlier rejection in the other 33%.

FIG. 7. Reconstructed cine image series, **Y**, with heart shown at systolic, $\vartheta_{sys}$, and diastolic, $\vartheta_{dia}$, cardiac phases and line profile time plots corresponding to dashed line across the ventricles. Cropped views cover 100 mm in each direction, with 25-mm markers shown for reference. The heart of a 33-week gestational-age fetus with atrioventricular and ventriculoarterial discordance is shown in (**a**) long- and (**b**) short-axis orientations revealing transposed morphological left and right ventricles. The moderator band (arrow) can be seen on the morphological right ventricle in the anatomical left/anterior position in four-chamber view of the heart with apex to the left in (a), whereas mitral-valve papillary muscles (arrowhead) can be seen on the morphological left ventricle on the anatomical right side opposite the stomach (asterisk) in short axis view in (b). (**c**) Short axis view in 27-week gestational age fetus with normal situs, for comparison with (b), in which papillary muscles (arrowhead) are seen on the morphological left ventricle on the anatomical left side with the stomach (asterisk) for reference. (**d**) Four-chamber view in a 33-week gestational age fetus with coarctation of the aorta. (**e**) Long-axis view in a 30-week gestational age fetus with a ventricular septal defect (arrowhead). Atrioventricular valves (arrows) can be seen in (d) and (e).

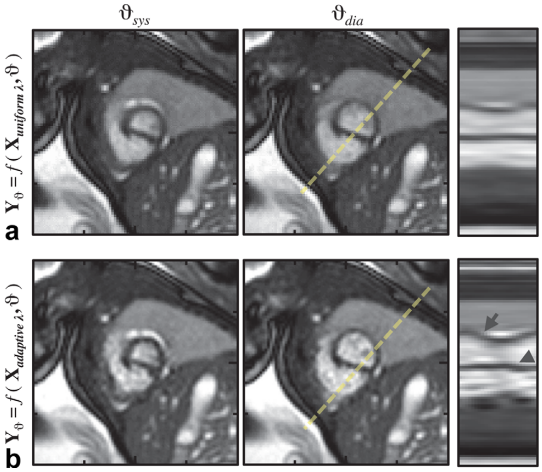


FIG. 8. Comparison of (**a**) cine images, $Y_\vartheta$, reconstructed from real-time image series, $\mathbf{X}_{uniform\lambda}$, generated using spatially uniform regularization (Eq. [1]) with $\lambda = \lambda_0$, and (**b**) cine images reconstructed from real-time image series, $\mathbf{X}_{adaptive\lambda}$, generated using spatially adaptive regularization (Eq. [2]), in 33-week gestational age fetus. The impact of *k-t* SENSE regularization on reconstructed cine images can be seen in the additional high-frequency temporal dynamics in the line profiles (dashed lines), including pulsatility (arrow) and end-systolic torsion (arrowhead). Cropped views cover 100 mm in each direction, with 25-mm markers shown for reference.

Videos of the real-time and cine image series shown in Figures 7 to 9 are available as Supporting Videos S1 to S3.

## DISCUSSION

Highly accelerated real-time imaging was able to capture the motion of the fetal heart as well as the surrounding anatomy, allowing for direct estimation of, and correction for, cardiac pulsation and motion—as well as rejection of data that could not be made consistent both at the individual voxel and frame level. Cine reconstruction effectively combined the data as a single cardiac cycle, increasing the visibility of small, dynamic anatomical features, and enabled visualization of congenital abnormalities in the clinical cases. The use of robust statistics enabled the reconstruction to effectively deal with inconsistencies in the data that could not be resolved by in-plane motion correction, such as due to maternal respiration, motion artifact, and short episodes of general fetal movement. The full pipeline was found to be highly effective, with successful reconstructions in all but three data sets in which there was fetal motion, such that there were few frames depicting a single consistent cardiac cross-sectional slice.

The reordered real-time images produced cine sequences that were sampled far more densely in cardiac phase than the temporal resolution of the individual image frames. This allowed images to be compounded without sacrificing temporal resolution by using a tuned weighting function that respected sequence timing and cardiac period. Because image-compounding recovered SNR, it

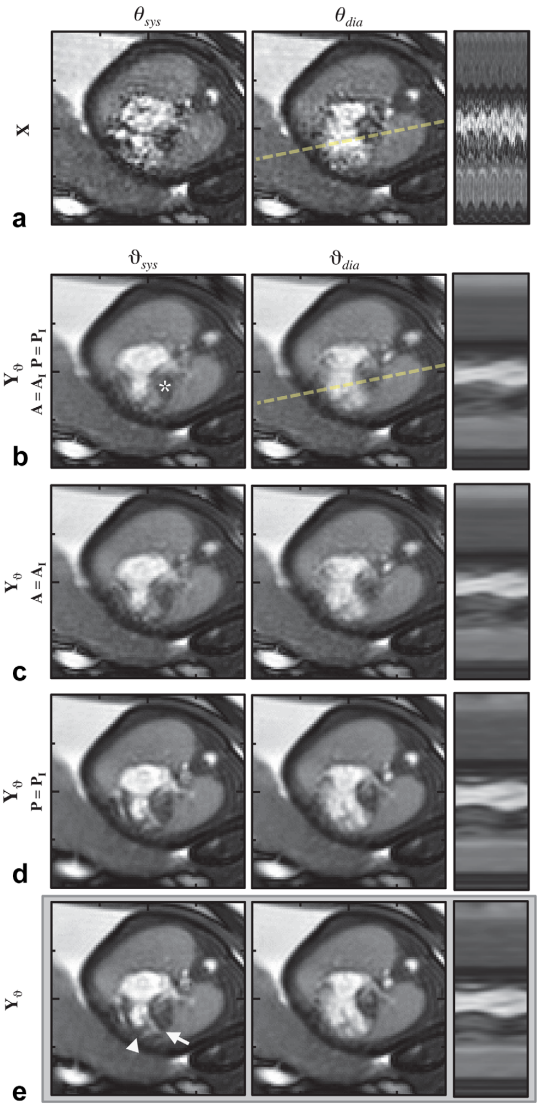


FIG. 9. Comparison of cine image series reconstructed using some or all steps in the proposed pipeline. Cropped views of the heart of a 30-week gestational age fetus with hypoplastic left-heart syndrome at systole and diastole reveal contraction and dilation of the right ventricle in a line-profile time plot corresponding to the dashed line across the ventricles for (**a**) reconstructed real-time images $\mathbf{X}$ reordered based on cardiac phase. Cine image series, $\mathbf{Y}$, reconstructed using (**b**) cardiac synchronization only, with $\mathbf{A} = \mathbf{A}_I$ and $\mathbf{P} = \mathbf{P}_I$, (**c**) cardiac synchronization and outlier rejection, with $\mathbf{A} = \mathbf{A}_I$, (**d**) cardiac synchronization and motion correction, with $\mathbf{P} = \mathbf{P}_I$, and (**e**) the full pipeline show the heart, including underdeveloped left ventricle (asterisk), with added detail. Each step included in the pipeline increased the clarity of blood–tissue boundaries in the resulting reconstructed cine images, improving depiction of small anatomical features such as the interventricular septum (arrow) and moderator band (arrowhead). Cropped views cover 100 mm in each direction, with 25-mm markers shown for reference.

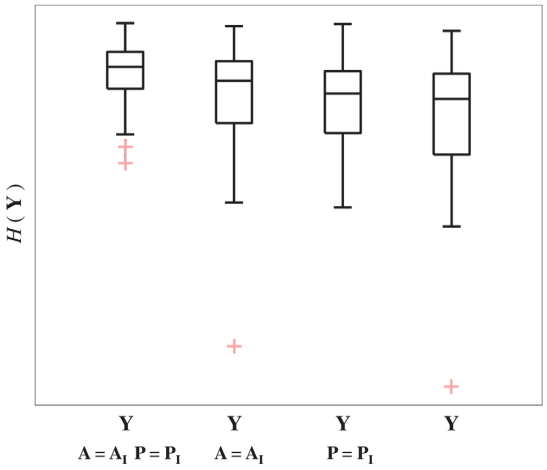


FIG. 10. Comparison of image quality in cine image series, $\mathbf{Y}$, reconstructed using cardiac synchronization only ($\mathbf{A} = \mathbf{A}_I$, $\mathbf{P} = \mathbf{P}_I$), cardiac synchronization and outlier rejection ($\mathbf{A} = \mathbf{A}_I$), cardiac synchronization and motion correction ($\mathbf{P} = \mathbf{P}_I$), and the full pipeline. The greatest improvement in image quality, that is, reduction in relative entropy $H(\mathbf{Y})$, in all 36 data sets was achieved using the combination of steps in the proposed pipeline. Boxes span the first to third quartiles with a band at the median. Whiskers extend to the furthest value within 1.5 interquartile range.

was feasible to preserve the full temporal resolution of the undersampled acquisition by selectively regularizing the *k-t* SENSE reconstruction to favor temporal fidelity in the fetal heart. This was achieved using Equation [2], exploiting the disparity in dynamic content between the fetal heart and the rest of the imaged scene. Despite the low SNR of the resulting time series of real-time images, heart rate estimation, motion correction, and outlier rejection steps all were found to perform reliably, with no failures. The resulting postprocessing pipeline is fully automatic, except for a single manual step in which a region of interest covering the fetal heart is defined. It may be possible to identify an appropriate ROI using an image segmentation approach, resulting in a fully automatic reconstruction pipeline, although this was outside the scope of the present study.

The spatial and temporal resolution achieved in this work improves on the resolution in previous studies of the fetal heart using dynamic MRI (24,29). The proposed method preserves temporal fidelity at the acquired resolution because there effectively is no regularization in the region of the fetal heart in the spatially adaptive *k-t* SENSE reconstruction. Cardiac anatomy and motion is clearly depicted in the resulting cine images such that it may be possible to characterize the myocardium and relative chamber sizes at the current resolution; however, a higher resolution would be desirable for accurate functional assessment based on guidelines for ventriculography in infants: $1.2 \times 1.2 \times 4.0\,\text{mm}$, $t_{RR}/15$ (30). Fetal cardiac imaging using compressed sensing reconstruction of undersampled segmented cine data to achieve high resolution and short scan times has recently been reported (13), although the regularized reconstruction can impact spatial and temporal resolution at high acceleration rates. Thus, a direct comparison with the results reported here is not simple. Radial sampling is compatible with the proposed framework but is less well matched to image-domain processing with locally reduced regularization at the heart, as used in this study, because it results in a less sparse *x-f* alias distribution and is less efficient than Cartesian coverage due to dense sampling around the k-space origin. Functional assessment using the proposed method remains to be explored, likely in combination with further development and optimization of the acquisition and reconstruction strategy to improve resolution and include multislice data to allow for volumetric reconstruction.

It is a challenge to prospectively account for each source of motion effecting the position of the fetal heart. Although segmented cine acquisition potentially can achieve both higher spatial and cardiac phase resolution, the use of a dynamic acquisition offers potential advantages for addressing both motion and artifacts. The ability to process data in image-space allowed for spatial and temporal operations to be applied to the fetal heart in isolation so that incidental changes in other parts of the field of view, such as due to movement of the mother or peripheral parts of the fetal anatomy, did not influence the result.

The focus of this work was to demonstrate that dynamic fetal cardiac MRI can form the basis of an effective imaging approach in the presence of maternal and fetal motion, and to develop the required processing pipeline. The starting point was the concept of adaptive reconstruction of undersampled dynamic imaging, required to achieve a temporal resolution fast enough to freeze the fetal heart. In this study, low-resolution training data was acquired to guide the reconstruction, effectively doubling the acquisition time, which is both inefficient and increases the possibility of data corruption due to general fetal movement. In the future, several improvements could be investigated. Integration of autocalibrated (ie, reference-less) dynamic image reconstruction (31,32) with the proposed method could improve motion robustness because it reduces scan duration and ensures that the priors used in reconstruction are consistent with the target data, but it is likely to reduce temporal resolution. A calibration-free (33) reconstruction, leveraging knowledge of the spatial location of dynamic regions and expected bandwidths, also may be possible. Additional temporal filtering effects may be reduced by appropriate filtering of the subtracted baseline signal (34), which will also be of benefit if coil sensitivities are autocalibrated instead of derived from a prescan, as they are currently. In this work, one set of adaptive regularization parameters was used to reconstruct real-time images using Equation [2] for all data sets because these parameters are independent of signal level. A better balance of tradeoffs between noise suppression and temporal fidelity potentially could be achieved by tuning these parameters case by case, such as by an automated L-curve analysis.

The use of a constant heart rate for cardiac synchronization leads to timing errors because the true heart rate varies from beat to beat. In this study, a small number of cases were used to check that mean fetal heart rate is stable over the duration of the acquisition by acquiring

multiple data sets in quick succession. However, timing errors within a data set would still be expected. To explore the potential magnitude of this effect, Monte Carlo simulations of fetal heart rate traces were generated using a previously established model (35), with expected distribution of baseline fetal heart rate (5) and beat-to-beat variation (6). Based on 500 runs, each simulating approximately 8 seconds with measurements every 71 ms to 88 ms (96 measurements total), cardiac phase errors, $\Delta\theta_i$, are expected to be within $\pm 0.10\, t_{RR}$ 95% of the time and within $\pm 0.05\, t_{RR}$ 75% of the time. These errors are small in comparison to the image acquisition time. A refinement of the method could be to incorporate an appropriate self-gating technique (36,37) to accommodate beat-to-beat variation, thus reducing timing error. This might become important if longer acquisition durations are used.

Motion correction and outlier rejection steps were shown to improve the image quality of the final reconstructed cine images in all cases. In two-thirds of the datasets, reconstructed motion correction alone provided more improvement in image quality than outlier rejection alone. However, the two processes proved to be complementary, with the combination of the two providing more improvement in image quality than either process alone.

The proposed method shows promise as a framework for comprehensive fetal cardiac MRI. Working in the image domain allowed separation of fetal cardiac pulsation from other extraneous changes elsewhere in the field of view, which get mixed together when processing is done in k-space. In the future, this work may be extended to multislice acquisition to reconstruct volumetric data, offering the potential for fully motion-compensated 3D assessment of dynamic features of the fetal heart and great vessels.

## ACKNOWLEDGMENT

Thank you to Matthew Fox, Joanna Allsop, and Ana Gomes for oversight during the scanning of volunteers and patients.

## REFERENCES

1. Votino C, Jani J, Damry N, Dessy H, Kang X, Cos T, Divano L, Foulon W, De Mey J, Cannie M. Magnetic resonance imaging in the normal fetal heart and in congenital heart disease. Ultrasound Obstet Gynecol 2012;39:322–329.
2. Loomba RS, Chandrasekar S, Shah PH, Sanan P. The developing role of fetal magnetic resonance imaging in the diagnosis of congenital cardiac anomalies: a systematic review. Ann Pediatr Cardiol 2011;4: 172–176.
3. Dong S-Z, Zhu M, Li F. Preliminary experience with cardiovascular magnetic resonance in evaluation of fetal cardiovascular anomalies. J Cardiovasc Magn Reson 2013;15:40.
4. Schneider C, McCrindle BW, Carvalho JS, Hornberger LK, McCarthy KP, Daubeney PEF. Development of Z-scores for fetal cardiac dimensions from echocardiography. Ultrasound Obstet Gynecol 2005;26: 599–605.
5. Pildner von Steinburg S, Boulesteix A-L, Lederer C, Grunow S, Schiermeier S, Hatzmann W, Schneider K-TM, Daumer M. What is the "normal" fetal heart rate? PeerJ 2013;1:e82.
6. Ortiz MR, Aguilar SD, Alvarez-Ramirez J, Martínez A, Vargas-Garcia C, González-Camarena R, Echeverría JC. Prenatal RR fluctuations dynamics: detecting fetal short-range fractal correlations. Prenat Diagn 2006;26:1241–1247.
7. Vadeyar SH, Moore RJ, Strachan BK, Gowland PA, Shakespeare SA, James DK, Johnson IR, Baker PN. Effect of fetal magnetic resonance imaging on fetal heart rate patterns. Am J Obstet Gynecol 2000;182: 666–669.
8. Patrick J, Challis J. Measurement of human fetal breathing movements in healthy pregnancies using a real-time scanner. Semin Perinatol 1980;4:275–286.
9. Hayat TTA, Nihat A, Martinez-Biarge M, McGuinness A, Allsop JM, Hajnal JV, Rutherford MA. Optimization and initial experience of a multisection balanced steady-state free precession cine sequence for the assessment of fetal behavior in utero. Am J Neuroradiol 2011;32: 331–338.
10. Piontelli A. Development of Normal Fetal Movements. Milan, Italy: Springer Milan; 2015.
11. Paley MNJ, Morris JE, Jarvis D, Griffiths PD. Fetal electrocardiogram (fECG) gated MRI. Sensors (Basel) 2013;13:11271–11279.
12. Roy CW, Seed M, van Amerom JF, Al Nafisi B, Grosse-Wortmann L, Yoo SJ, Macgowan CK. Dynamic imaging of the fetal heart using metric optimized gating. Magn Reson Med 2013;70:1598–1607.
13. Roy CW, Seed M, Macgowan CK. Accelerated MRI of the fetal heart using compressed sensing and metric optimized gating. Magn Reson Med 2016:1–11.
14. Yamamura J, Kopp I, Frisch M, Fischer R, Valett K, Hecher K, Adam G, Wedegärtner U. Cardiac MRI of the fetal heart using a novel triggering method: initial results in an animal model. J Magn Reson Imaging 2012;35:1071–1076.
15. Yamamura J, Schönnagel B, Tavares De Sousa M, Much C, Ueberle F, Adam G, Kording F. Fetal cardiac MRI and left ventricular function assessment using a new gating strategy based on Doppler Ultrasound: Preliminary results. In Proceedings of the 23rd Annual Meeting of ISMRM, Toronto, Canada, 2015. p. 0632.
16. Kellman P, Chefd'hotel C, Lorenz CH, Mancini C, Arai AE, McVeigh ER. Fully automatic, retrospective enhancement of real-time acquired cardiac cine MR images using image-based navigators and respiratory motion-corrected averaging. Magn Reson Med 2008;59:771–778.
17. van Amerom JFP, Kuklisova Murgasova M, Price AN, et al. Fetal cardiac cine imaging from super-resolution reconstruction of highly-accelerated real-time MRI. In Proceedings of the 24th Annual Meeting of ISMRM, Singapore, 2016. p. 458.
18. Tsao J, Boesiger P, Pruessmann KP. k-t BLAST and k-t SENSE: dynamic MRI with high frame rate exploiting spatiotemporal correlations. Magn Reson Med 2003;50:1031–1042.
19. Patenaude Y, Pugash D, Lim K, et al. The use of magnetic resonance imaging in the obstetric patient. J Obstet Gynaecol Can 2014;36:349–355.
20. Hand JW, Li Y, Hajnal JV. Numerical study of RF exposure and the resulting temperature rise in the foetus during a magnetic resonance procedure. Phys Med Biol 2010;55:913–930.
21. De Wilde JP, Rivers AW, Price DL. A review of the current use of magnetic resonance imaging in pregnancy and safety implications for the fetus. Prog Biophys Mol Biol 2005;87:335–353.
22. Saleem SN. Feasibility of MRI of the fetal heart with balanced steady-state free precession sequence along fetal body and cardiac planes. AJR Am J Roentgenol 2008;191:1208–1215.
23. Tsao J, Kozerke S, Boesiger P, Pruessmann KP. Optimizing spatiotemporal sampling for k-t BLAST and k-t SENSE: application to high-resolution real-time cardiac steady-state free precession. Magn Reson Med 2005;53:1372–1382.
24. Brugger PC. MRI of the fetal heart. In: Prayer D, ed. Fetal MRI. Medical Radiology. Berlin, Germany: Springer; 2011; 247–258.
25. Lloyd DFA, Amerom JFP van, Pushparajah K, et al. An exploration of the potential utility of fetal cardiovascular MRI as an adjunct to fetal echocardiography. Prenat Diagn 2016;36:1–10.
26. Kuklisova-Murgasova M, Quaghebeur G, Rutherford MA, Hajnal JV, Schnabel JA. Reconstruction of fetal brain MRI with intensity matching and complete outlier removal. Med Image Anal 2012;16:1550–1564.
27. Bernstein MA, Fain SB, Riederer SJ. Effect of windowing and zero-filled reconstruction of MRI data on spatial resolution and acquisition strategy. J Magn Reson Imaging 2001;14:270–280.
28. Atkinson D, Hill DL, Stoyle PN, Summers PE, Keevil SF. Automatic correction of motion artifacts in magnetic resonance images using an entropy focus criterion. IEEE Trans Med Imaging 1997;16:903–910.
29. Fogel MA, Wilson RD, Flake A, Johnson M, Cohen D, McNeal G, Tian Z-YY, Rychik J. Preliminary investigations into a new method of functional

assessment of the fetal heart using a novel application of 'real-time' cardiac magnetic resonance imaging. Fetal Diagn Ther 2005;20:475–480.
30. Fratz S, Chung T, Greil GF, Samyn MM, Taylor AM, Valsangiacomo Buechel ER, Yoo S-J, Powell AJ. Guidelines and protocols for cardiovascular magnetic resonance in children and adults with congenital heart disease: SCMR expert consensus group on congenital heart disease. J Cardiovasc Magn Reson 2013;15:51.
31. Malik SJ, Schmitz S, O'Regan D, Larkman DJ, Hajnal JV. x-f Choice: reconstruction of undersampled dynamic MRI by data-driven alias rejection applied to contrast-enhanced angiography. Magnetic Resonance in Medicine 2006;56:811–823.
32. Ponce IP, Blaimer M, Breuer FA, Griswold MA, Jakob PM, Kellman P. Auto-calibration approach for k-t SENSE. Magn Reson Med 2014; 71:1123–1129.
33. Madore B, Glover GH, Pelc NJ. Unaliasing by Fourier-encoding the overlaps using the temporal dimension (unfold), applied to cardiac imaging and fMRI. Magn Reson Med 1999;42:813–828.
34. Blaimer M, Ponce IP, Breuer FA, Jakob PM, Griswold MA, Kellman P. Temporal filtering effects in dynamic parallel MRI. Magn Reson Med 2011;66:192–198.
35. Jansz MS, Seed M, van Amerom JFP, Wong D, Grosse-Wortmann L, Yoo S-J, Macgowan CK. Metric optimized gating for fetal cardiac MRI. Magn Reson Med 2010;64:1304–1314.
36. Larson AC, White RD, Laub G, McVeigh ER, Li D, Simonetti OP. Self-gated cardiac cine MRI. Magn Reson Med 2004;51:93–102.
37. Nijm GM, Sahakian AV, Swiryn S, Carr JC, Sheehan JJ, Larson AC. Comparison of self-gated cine MRI retrospective cardiac synchronization algorithms. J Magn Reson Imaging 2008;28:767–772.

## SUPPORTING INFORMATION

Additional supporting information may be found in the online version of this article.

**Video S1.** Videos of dynamic and cine image series shown in Figure 7. Real-time images are shown in full field of view (left) and cropped view (center) at acquired frame rate, with cropped view of cine image series (right) looped for duration of video. The full field of view is $400 \times 304$ mm and cropped views are $100 \times 100$ mm. Images are oriented with the fetus in radiographic image orientation.
(**a**) Thirty-three week gestational age fetus with atrioventricular and ventriculoarterial discordance shown in Figure 7a. (**b**) Thirty-three week gestational age fetus with atrioventricular and ventriculoarterial discordance shown in Figure 7b. (**c**) Twenty-seven week gestational age fetus shown in Figure 7c. (**d**) Thirty-three week gestational age fetus shown in Figure 7d.(e) Thirty week gestational age fetus with ventricular septal defect shown in Figure 7e.

**Video S2.** Videos of dynamic and cine image series shown in Figure 8 showing impact of *k-t* SENSE regularization in 33 week gestational age fetus. Real-time image series (left) reconstructed with spatially-uniform (top) and spatially-adaptive regularization (bottom) are shown at acquired frame rate. Additional high-frequency temporal dynamics can be seen between resulting cine image series (right). Cropped views are $100 \times 100$ mm, and images are oriented with the fetus in radiographic image orientation.

**Video S3.** Videos of dynamic and cine image series shown in Figure 9 comparing cine images reconstructed using some or all steps in the proposed pipeline in a 30 week gestational age fetus with hypoplastic left heart syndrome. Real-time image series (left) was used to generate cines using (left to right) cardiac synchronization only; cardiac synchronization and outlier rejection; cardiac synchronization and motion correction; and the full pipeline. Cropped views are $100 \times 100$ mm, and images are oriented with the fetus in radiographic image orientation.

## 4.6 Fetal Heart Rate Simulation

The fetal heart rate varies from beat to beat. Fetal heart rates were simulated in order to evaluate timing errors resulting from the use of a constant heart rate for cardiac synchronisation.

Short-term beat-to-beat variation is low in the fetus according to a previous study of fetal ECG recordings [8] and the mean estimated heart rate was shown to be stable (4.5) with 2% or less difference between successively acquired data sets. Though heart rate variation could result in a broadening of the temporal frequency spectrum (§4.5 Fig. 3 b), no problems were encountered during cardiac synchronisation as data were acquired over a short time window (8 seconds). The effect of using a constant heart rate estimate to represent the varying fetal heart rate was assessed using simulated fetal heart rate traces. The fetal heart rate was modelled as a bounded walk superimposed on a constant baseline [63] for the expected distribution of fetal heart rate [7] and short-term beat-to-beat variation [8], as shown in Figure 4.4. Timing errors, $\Delta\theta_i = \theta_i^{true} - \theta_i^{estimated}$, for the range of sampling rates of the dynamic acquisition used in this work were calculated for 500 simulated heart rate traces. It was found that approximately 95% of all timing errors were within $\pm\frac{2\pi}{10}$ ($\pm\,0.10\,t_{RR}$) and approximately 75% of all timing errors were within $\pm\frac{2\pi}{20}$ ($\pm\,0.05\,t_{RR}$). Thus, for a fetal heart rate of 135 bpm, around the 50$^{th}$ percentile (§2.1.2), $t_{RR}$ = 445 ms and the timing error of any single dynamic frame is expected to be well below 45 ms.

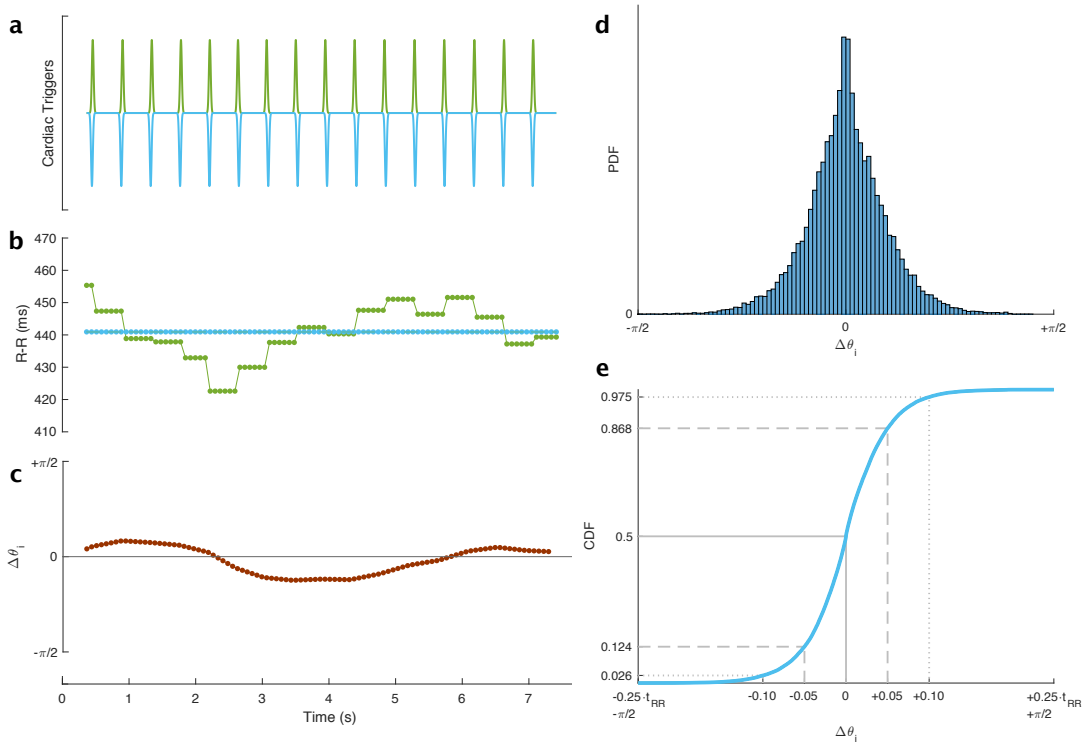


**Figure 4.4:** Results of Monte Carlo assessment of simulated fetal heart rate traces. (**a**) Cardiac trigger times for one of 500 simulated heart rate traces in the simulation (green) with an R-R interval of 441 $\pm$ 7.8 ms, compared to evenly spaced cardiac triggers using constant R-R interval estimate (blue). (**b**) R-R interval plotted against time with dynamic image frame timing indicated by dot markers and (**c**) timing error ($\Delta\theta_i = \theta_i^{true} - \theta_i^{estimated}$). (**d**) Distribution and (**e**) cumulative distribution of the aggregate of all timing errors in 500 simulations.

## 4.7 Conclusions

The aims of this work were to establish a protocol for rapid dynamic MR imaging to acquire serial 'snapshots' of the fetal heart and surrounding anatomy, and to develop methods for motion corrected cine reconstruction. A k-t SENSE acquisition was established, exploiting the disparity in dynamic content between the fetal heart and the rest of the imaged scene to achieve 8-fold under-sampling. Motion-compensation was performed in the image domain to allow for separation of fetal cardiac pulsation from other extraneous changes elsewhere in the field of view, which get mixed together when processing is done in k-space. Robust statistics were used to reduce the influence of data effected by maternal respiration, motion artefact and short episodes of general fetal movement that could not be resolved by in-plane motion correction. These points were discussed in greater detail in Section 4.5. This 2D framework could not, however, deal with large through-plane motion, motivating further work using a multi-planar acquisition and volumetric reconstruction.

# Chapter 5

# 3D Whole-Heart Cine Reconstruction from Multi-Planar Dynamic MRI

## 5.1 Introduction

This work builds on the motion-tolerant framework previously described for 2D cine reconstruction of single slice dynamic MRI (§ 4.5), with the aim of developing an acquisition and reconstruction approach to generate a three-dimensional cine representation of fetal cardiovascular anatomy in utero from multi-planar dynamic MR images without the need for maternal breath-hold or significant manual processing. Cine fetal cardiac imaging with whole heart coverage presents numerous challenges due to maternal and fetal motion as well as the rapid fetal heart rate and cardiac synchronisation. In this work, 3D capability was achieved using a mulit-planar dynamic acquisition combined with retrospective image-domain techniques for motion correction, cardiac synchronisation and outlier rejection.

A hybrid framework was initially implemented to explore the possibility of 3D whole heart cine reconstruction from 2D dynamic MRI [166]. In this approach, several parallel slices of 2D dynamic MRI were acquired in long and short axis orientations and each slice was independently reconstructed as a 2D cine (§4.5). Synchronisation of the cardiac cycle was performed using cross-correlation of the 2D cine signal intensities in the fetal heart, first between pairs of parallel slices and then between the slices of the acquired orientations. A 3D volume was then reconstructed as described by Kuklisova *et al.* [91] separately for each cardiac phase in the 2D cine

image series. The 3D volumes were then concatenated in the fourth dimension resulting in a 3D cine volume. This initial approach yielded promising results in a pilot study of five fetal subjects suggesting the potential of volumetric cine reconstruction directly from the acquired dynamic images to accommodate a wider range of fetal motion with greater detail of the fetal cardiovascular system.

To achieve a fully volumetric cine reconstruction, the volume reconstruction software developed by Kuklisova *et al.* [91] was extended to include a temporal component. With additional improvements to the multi-planar acquisition, motion correction and cardiac synchronisation, this framework was capable of reconstructing 3D cine volumes that allowed for multiple planes to be visualised, from MR images acquired without maternal breath-hold without requiring precise scan plane prescription during acquisition [168].

Links to the preliminary work referenced above can be found in the list of conference presentations in the Publications and Software section at the end of this thesis.

The current implementation of the proposed framework, presented here in Section 5.2, has been further refined, and was validated using a numerical phantom simulation and evaluated in a study of eleven human fetal subjects.

## 5.2 Methods

The proposed strategy for whole-heart 3D cine reconstruction of the fetal heart from multi-planar dynamic MRI is illustrated in Figure 5.1 and consists of the following steps:

1. acquisition and k-t SENSE reconstruction of multi-planar dynamic MRI in multiple scan plane orientations (§5.2.1);
2. an initial motion correction stage to achieve rough spatial alignment of the fetal heart (§5.2.3);
3. heart rate estimation and slice-slice cardiac cycle alignment (§5.2.4); and
4. 3D cine reconstruction (§5.2.2), including outlier rejection, interleaved with;
5. further spatial alignment of individual image frames (§5.2.3).

The methods developed and implemented for each of these steps are described below in the sections indicated above in brackets.

Notation changed between chapters 4 and 5: Please note that the symbols used in this chapter to denote acquired dynamic MR images and reconstructed cine images, $\mathbf{Y}$ and $\mathbf{X}$ respectively, differ from those introduced previously in Section 4.5. This

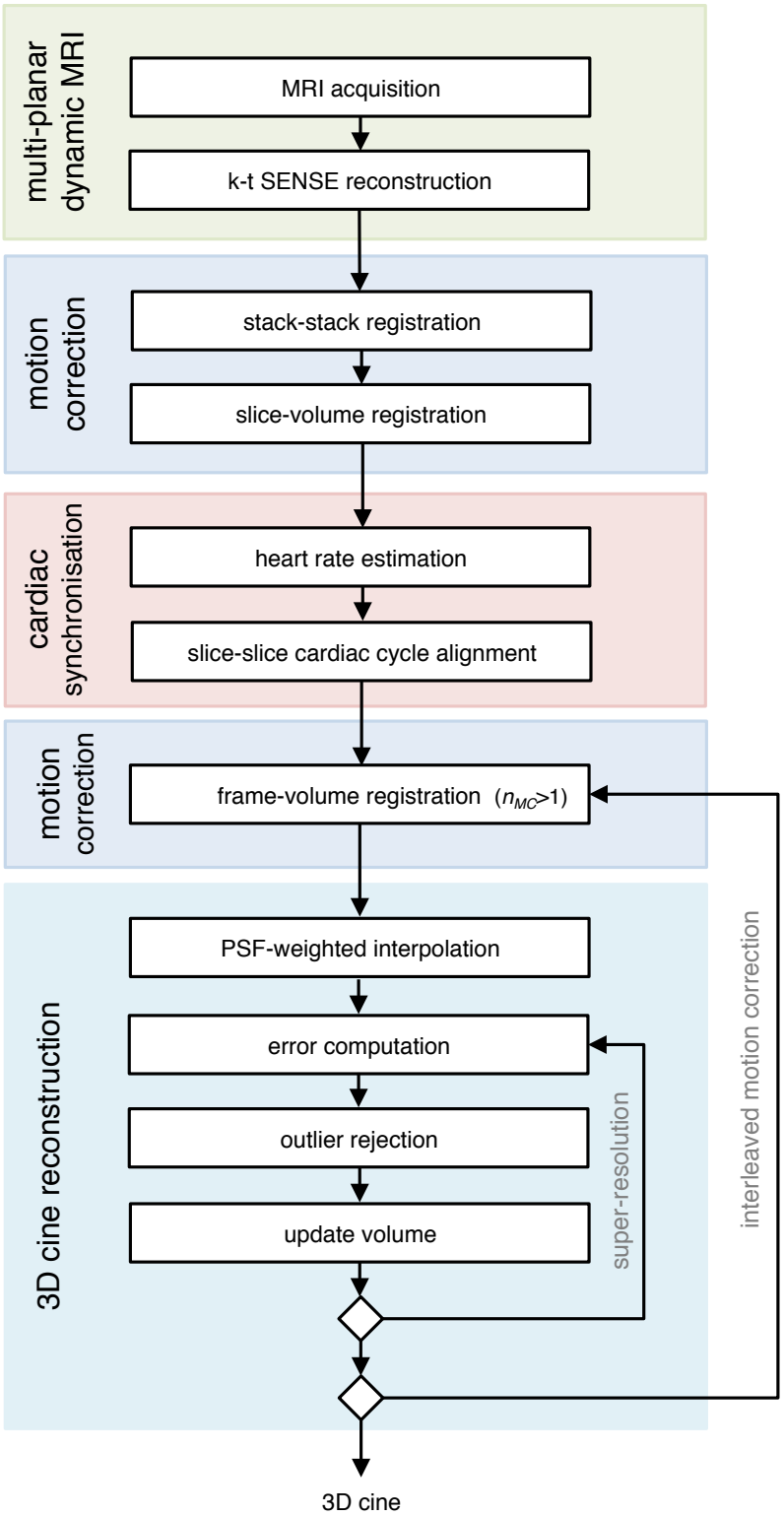


**Figure 5.1:** Method for 3D cine reconstruction of 2D dynamic MR images, including multi-planar dynamic MRI acquisition and k-t SENSE reconstruction, an initial motion correction stage, cardiac synchronisation and, finally, 3D cine reconstruction, including outlier rejection, interleaved with frame-volume registration. User-specified fetal heart and chest regions of interest, and identification of a target stack for initial motion correction are the only manual preparations required for reconstruction.

has been done to align with the symbols commonly used by other authors in related presentations of 2D-3D MRI methods. A notation section that lists the symbols relevant to these methods has been included at the end of this chapter (page 119).

### 5.2.1 Multi-Planar Dynamic MRI

Highly-accelerated dynamic MRI was acquired using regular Cartesian k-t undersampling and reconstructed using k-t SENSE, as described in Section (§4.5. Parallel slices were acquired as in previous 2D-3D MRI reconstruction studies [91], with $\frac{1}{3}$ to $\frac{1}{2}$ overlap between slices and all dynamic data collected for one slice before proceeding to the next slice in the stack. This acquisition scheme increased the likelihood of complete and repeated sampling of the fetal heart to facilitate volumetric reconstruction, as fetal and maternal movement was expected to shift the fetal heart relative to the imaging field of view. Acquisition of three stacks of slices with orthogonal slice orientations ensured full coverage of the fetal heart, with additional stacks acquired in oblique orientations as examination time permitted. This resulted in a set of $N_k$ dynamic MR images, $\mathbf{Y} = \{\mathrm{Y}_k\}_{k=1,\ldots,N_k}$, with acquisition times $t = \{t_k\}_{k=1,\ldots,N_k}$ and elements $y_{jk}$ at 2D spatial coordinates indexed by $j$. Subsets of $\mathbf{Y}$ for a single slice are defined as $\mathbf{Y}_l = \{\mathrm{Y}_k\}_{k \in slice_l}$, where the temporal mean, $\overline{\mathrm{Y}}_l$, is equivalent to the inverse temporal Fourier transform of $\overline{\rho}$ in the k-t SENSE reconstruction (§4.5, Eq. 1).

In the 2D framework, single-slice dynamic MR images were reconstructed using k-t SENSE with spatially-adaptive regularisation (§4.5, Eq. 2) to preserve the full temporal resolution of the accelerated acquisition. These complex-valued dynamic images were then combined as cine image series using robust statistics based on complex-valued errors to suppress voxels corrupted by artefact. This was possible because the phase of the complex-valued dynamic images was fairly consistent in a single slice. However, in this 3D framework, the phase of the dynamic images is inconsistent due to changes in slice orientation and position. As a result, these complex-valued images cannot be directly combined as a coherent complex-valued volume. Consequently, spatially-uniform k-t SENSE regularisation and magnitude-valued images were used in this work to simplify volume reconstruction methods and focus on the key challenge of locating slices in 3D space and time to reconstruct cine volumetric representations of the fetal cardiovascular system. The use of the phase information of the acquired dynamic MR images for cine volume reconstruction is discussed further in Section 5.4.1.

Motion correction, cardiac synchronisation and volume reconstruction were all per-

formed on a regions of interest centred on the fetal heart. While it may be possible identify these regions using automated segmentation techniques [169, 170], in this work masks identifying fetal cardiac anatomy, $R_l$, were manually prescribed for each $\overline{Y}_l$. These masks included the chambers of the heart, as well as the great vessels and arterial arches. These user-specified fetal heart masks were the only manual preparation required, aside from a user-specified fetal chest volume of interest and identification of a target stack used for motion correction.

### 5.2.2 Volume Reconstruction

Reconstruction of a 3D cine volume from 2D MR images requires information about the spatial and temporal position of the heart in each acquired 2D image frame. While the slice position and acquisition times are known, the relative spatial displacement due to fetal-maternal motion and the cardiac phase are not. However, if the spatial and temporal positions can be accurately estimated, the spatial location of images can be transformed using rigid transformation matrices $\mathbf{A} = \{A_k\}_{k=1,\ldots,N_k}$, assuming rigid-body displacement, and acquisition times can be mapped to cardiac phases, $\boldsymbol{\theta} = \{\theta_k\}_{k=1,\ldots,N_k}$, with $\theta_k$ defined on a cyclic interval $[0, 2\pi]$.

#### MR Image Acquisition Model

In practice, MR image intensities are affected by intensity scaling caused by system gain and receiver coil sensitivities. At 1.5T, RF transmit magnetic field inhomogeneities are generally not severe and in this work any residual transmit effects are treated as part of an overall multiplicative correction. One way to achieve intensity-corrected images, $Y_k^*$, is to apply a scaling to each image, $s_k$, and a multiplicative bias field, $B_k$, to the voxels in each image, resulting in $y_{jk}^* = s_k exp(-b_{jk})$, as previously described [91].

Image domain super-resolution reconstruction is based on forward modelling of the image acquisition process, with volume reconstruction formulated as the solution to the inverse problem. In this work the aim was to recover a volumetric representation of the beating fetal heart. The MR image acquisition model previously used for static anatomy [91] was modified to include a temporal component, assuming the periodic motion of the cardiac anatomy can be characterised by a cardiac phase so that all acquired dynamic images can be combined as a single cardiac cycle. This MR image acquisition model describes the relationship between intensity-corrected MR images, $Y_k^*$, and a high resolution cine volume with three spatial dimensions and a

fourth periodic temporal dimension, $\mathbf{X} = \{\mathrm{X}_h\}_{h=1,\ldots,N_h}$, with elements $x_{ih}$ for a spatial index $i$ and a temporal index $h$ corresponding to cardiac phases $\vartheta = \{\vartheta_h\}_{h=1,\ldots,N_h}$. A matrix of spatio-temporal weights, $\mathbf{W}^{hk}$, relates $\mathrm{Y}_k^*$ and $\mathbf{X}$, in a image acquisition model given by

$$\mathrm{Y}_k^* = \sum_h \mathbf{W}^{hk}\mathrm{X}_h \tag{5.1}$$

where $\mathbf{W}^{hk}$ functions as a global transformation operator between the volume and images, including geometric transformation, blurring and down-sampling. Matrices $\mathbf{W}^{hk}$ are the product of a spatial weight, $\mathbf{M}^k$, and a temporal weight, $d^{hk}$, so that $w_{ij}^{hk} = d^{hk}m_{ij}^k$. Each row of $\mathbf{M}_k$ is made of of coefficients $\{m_{ij}^k\}_{i=1,\ldots,N_i}$ that relate the spatial locations of cine volume $\mathbf{X}$ and MR image $\mathrm{Y}_k^*$ taking in to account spatial blurring and down-sampling, as well as the movement defined by spatial transformation $\mathrm{A}_k$. A spatial point spread function (PSF) forms the basis for $\mathbf{M}_k$ and is determined by the MR acquisition. The in-plane point spread is a sinc distribution, but is here approximated by a Gaussian distribution with full width at half maximum equal (FWHM) to 1.2 times the in-plane voxel size, where $\sigma_{\mathrm{PSF}} = \mathrm{FWHM}_{\mathrm{PSF}}/2\sqrt{2\ln 2}$. In the through-plane direction, the point spread has previously been measured to be approximately Gaussian with full width at half maximum equal to the slice thickness [88]. The temporal PSF for the band-limited k-t SENSE reconstruction is a sinc with periodicity equal to the sampled frame rate, as described for 2D cine reconstruction (§4.5). The key change from the methods used for 2D cine reconstruction is the inclusion of spatial weights as a function of 3D spatial coordinates in the image acquisition model.

An initial estimate of $\mathbf{X}$ can be obtained by PSF-weighted interpolation of the scattered data in $\mathbf{Y}^*$,

$$x_{ih}^{[0]} = \frac{\sum_j \sum_k w_{ij}^{hk} y_{jk}^*}{\sum_j \sum_k w_{ij}^{hk}} \tag{5.2}$$

with initial estimates of scale $s_k = 1$ and bias $b_{jk} = 0$ for all $j$ and $k$. Simulated intensity-corrected images, $\widehat{\mathrm{Y}}_k$, can be obtained using Eq. 5.1, and error, $\mathrm{E}_k$, can be calculated as

$$\mathrm{E}_k = \mathrm{Y}_k^* - \widehat{\mathrm{Y}}_k \tag{5.3}$$

for subsequent outlier detection and super-resolution reconstruction.

### Outlier Rejection

Some of the acquired image frames in $\mathbf{Y}$ may be corrupted by artefact, or misplaced in space or time. Robust statistics were employed to reduce the impact of

inconsistent data, on both a voxel- and image frame-wise basis, as implemented by Kuklisova *et al.* [91]. Both voxels and image frames were classified as inliers or outliers using expectation maximisation to estimate the distribution parameters of mixture model of the two classes. The posterior probabilities of a voxel, $p_{jk}^{voxel}$, or image frame, $p_k^{frame}$, belonging to the inlier class were combined as probability maps $\mathrm{P}_k$, with elements $p_{jk} = p_{jk}^{voxel} p_k^{frame}$, and used to down-weight data belonging to the outlier classes.

*Voxel-Wise Robust Statistics*

The likelihood of observing error, $e_{jk}$, for voxel $y_{jk}$ was modelled as

$$\mathbb{P}(e_{jk}|\sigma_e, c_e) = G(e_{jk}|\sigma_e)c_e + b_e(1 - c_e) \tag{5.4}$$

using a Gaussian inlier distribution, $G(e_{jk}|\sigma_e)$, with zero mean and variance $\sigma_e^2$, and a uniform outlier distribution of density $b_e$, and a mixing proportion $c_e$. Parameters $\sigma_e$, $b_e$, and $c_e$ were estimated by maximising the log-likelihood of Eq. 5.4, $\sum_j \sum_k log\ \mathbb{P}(e_{jk}|\sigma_e, c_e)$, and the posterior probability that voxel $y_{jk}$ was an inlier was calculated as

$$p_{jk}^{voxel} = \frac{G(e_{jk}|\sigma_e)c_e}{G(e_{jk}|0, \sigma_e)c_e + b_e(1 - c_e)} \ . \tag{5.5}$$

*Frame-Wise Robust Statistics*

The root mean square of the voxel-wise posterior probability in a frame was used as an indication of the frame-wise potential, $q_k$ of $\mathrm{Y}_k$ as an inlier,

$$q_k = \sqrt{\sum_j (1 - p_{jk}^{voxel})^2 / N_j} \ , \tag{5.6}$$

where $N_j$ is the number of voxels in $\mathrm{Y}_k$. The likelihood of observing $q_k$ was modelled as the mixture of a Gaussian inlier distribution with mean $\mu_{in}$ and variance $\sigma_{in}^2$ and a Gaussian outlier distribution with mean $\mu_{out}$ and variance $\sigma_{out}^2$,

$$\mathbb{P}(q_k|\mu_{in}, \sigma_{in}, \mu_{out}, \sigma_{out}, c_q) = G(q_k|\mu_{in}, \sigma_{in})c_q + G(q_k|\mu_{out}, \sigma_{out})(1 - c_q) \tag{5.7}$$

with mixing proportion $c_q$. This mixture of classes was found to be suitable for frame-wise classification, rather than the mixture used for voxel-wise classification, due to the effects of averaging in Eq. 5.6 [91].

The log-likehood of Eq. 5.7 was maximised to estimate the frame-wise distribution

parameters and the posterior probability that $Y_k$ was an inlier was calculated as

$$p_k^{frame} = \frac{G(q_k|\mu_{in},\sigma_{in})c_q}{G(q_k|\mu_{in},\sigma_{in})c_q + G(q_k|\mu_{out},\sigma_{out})(1-c_q)} \ . \tag{5.8}$$

In practice, $p_k^{frame}$ was set to 1 for image frames with $q_k < \mu_{in}$ and to 0 for image frames with $q_k > \mu_{out}$ to ensure $p_k^{frame}$ is a non-increasing function of $q_k$.

### Super-Resolution

The PSF-weighted interpolation in Eq. 5.2 leads to blurring in the reconstructed volume due to the thick slices of the acquired images. However, super-resolution methods [90,91] can be used to recover a high-resolution volume. This was accomplished by iteratively minimising the sum of squared differences of the error, with objective function, $F_{SR}(\mathbf{X})$, given by

$$F_{SR}(\mathbf{X}) = \sum_j \sum_k p_{jk} e_{jk}^2 + \lambda R(\mathbf{X}) \tag{5.9}$$

that includes an adaptive regularisation term, $R(\mathbf{X})$, to stabilise the reconstruction while preserving edge features, and a regularisation controlling parameter, $\lambda$. The adaptive regularisation term was previously proposed [171] and successfully applied to volume reconstruction of fetal MRI [91,172] as

$$R(\mathbf{X}) = \sum_i \sum_{\mathbf{d}} \varphi\left(\frac{x_{i+\mathbf{d}} - x_i}{\delta|\mathbf{d}|}\right) \tag{5.10}$$

with potential function $\varphi(z) = 2\sqrt{1+z^2} - 2$, and where $\mathbf{d}$ represents a vector between $i$ and one of 26 spatially-neighbouring voxels and $\delta$ is a scaling parameter that defines the value of the gradient above which an edge is detected. Note that no regularisation is applied in the temporal dimension.

Applying gradient descent to Eq. 5.9 yields the following updating equation

$$\mathbf{X}^{[n_{SR}]} = \mathbf{X}^{[n_{SR}-1]} + \alpha \nabla F_{SR}(\mathbf{X}^{[n]}) \ , \text{ or} \tag{5.11a}$$

$$x_{ih}^{[n_{SR}]} = x_{ih}^{[n_{SR}-1]} + \alpha \sum_j \sum_k p_{jk} w_{ij}^{hk} e_{jk} + \alpha\lambda \frac{\partial}{\partial x_{ih}} R(\mathbf{X}^{[n_{SR}-1]}) \tag{5.11b}$$

for super-resolution iteration $n_{SR}$, where

$$\frac{\partial}{\partial x_{ih}} R(\mathbf{X}) \frac{1}{\delta^2} = \sum_{\mathbf{d}} \frac{x_{i+\mathbf{d}} - x_i}{|\mathbf{d}|\sqrt{1 + \frac{x_{i+\mathbf{d}} - x_i}{\delta|\mathbf{d}|^2}}} \ , \tag{5.12}$$

and $\lambda$ balances the effects of regularisation with the *a priori* volume $\mathbf{X}^{[n_{SR}-1]}$ and step size $\alpha = min(\frac{1}{20\lambda}, 1)$.

Intensity matching and bias correction were performed as described by Kuklisova *et al.* [91]. Scales were initialised as 1 and bias fields as 0, and then recovered by minimising $\sum_j \sum_k p_{jk} e_{jk}^2$. Scaling values were calculated as

$$s_k = \frac{\sum_j p_{jk}^{voxel} exp(-b_{jk}) y_{jk} \widehat{y}_{jk}}{\sum_j p_{jk}^{voxel} \left(exp(-b_{jk}) y_{jk}\right)^2}. \tag{5.13}$$

and bias fields were updated as

$$\mathbf{B}^{[n_{SR}]} = \mathbf{B}^{[n_{SR}-1]} + \grave{\mathbf{B}}^{[n_{SR}]} \tag{5.14}$$

where differential bias field, $\grave{\mathbf{B}}$, is given by

$$\grave{b}_{jk} = \frac{\sum_{j'} p_{j'k}^{voxel} y_{j'k}^{*} G_{\sigma_B}(dist(y_{jk}, y_{j'k})) log(y_{jk}^{*} / \widehat{y}_{jk})}{\sum_{j'} p_{j'k}^{voxel} y_{j'k}^{*[n_S R]} G_{\sigma_B}(dist(y_{jk}, y_{j'k}))} \tag{5.15}$$

with an amount of Gaussian smoothing specified by $\sigma_B$, and where $dist(y_{jk}, y_{j'k})$ represents the Euclidean distance between the spatial locations of $y_{jk}$ and $y_{j'k}$, as in Kuklisova *et al.* [91].

Algorithm 5.1 below describes the steps involved in super-resolution volume reconstruction of 2D images.

A volume of interest, R, was used to specify the spatial coverage for reconstruction of **X**. Optional inputs allow for motion correction, if transformations **A** are specified, and reconstruction of a cine volume rather than a static volume, if cardiac phases $\theta$ and $N_h > 1$ are specified. If no transformations are specified, the identity transform `I` is used. The algorithm starts with an initial estimate **X** using Eq. 5.2 and attempts to improve **X** using Eq. 5.11a with updated estimates of robust statistics and intensity corrections over $N_{SR}$ iterations.

### 5.2.3 Motion Correction

The position of the fetal heart will change from image frame to frame due to maternal and fetal movements. To achieve the spatial coherence required for volume reconstruction, rigid body image registration was used to estimate transformations $\mathbf{A} = \{A_k\}_{k=1,\ldots,N_k}$ that align $Y_k$ with **X**. Registration was performed in three stages to facilitate convergence, as depicted in Figure 5.1. The temporal mean of all dynamic

**Algorithm 5.1:** volume reconstruction

**Input:** $\mathbf{Y}$, R
**Input:** (optional) $\theta$, $\mathbf{A}$, $N_h$,
**Output:** $\mathbf{X}$
**Initialise:** (if unspecified) $\theta \leftarrow \{0\}$, $\mathbf{A} \leftarrow \{\mathrm{I}\}$, $N_h \leftarrow 1$

// initialise isotropic reconstructed volume voxel lattice
$i \leftarrow$ prescribed by R;
$\vartheta_h = \frac{h-1}{N_h} 2\pi, \quad \forall\ h = 1, \ldots, N_h$;

// calculate spatio-temporal mapping
$w_{ij}^{hk} \leftarrow d^{hk} m_{ij}^{k} \quad \forall$ pairs $i, j$ and $h, k$;

// initialise scale and bias
$s_k \leftarrow 1 \quad \forall\ k$;
$b_{jk} \leftarrow 0 \quad \forall\ j, k$

// initialise volume
$x_{ih}^{[0]} \leftarrow \frac{\sum_j \sum_k w_{ij}^{hk} y_{jk}^{*}}{\sum_j \sum_k w_{ij}^{hk}} \quad \forall\ i$ and $h$

**for** $n_{SR} \leftarrow 1$ **to** $N_{SR}$ **;** // super-resolution (SR) iterations
**do**

  // simulate images
  $\widehat{\mathrm{Y}}_k \leftarrow \mathbf{W}_k \mathbf{X}^{[n_{SR}-1]} \quad \forall\ k$ ; // Eq. 5.1

  // calculate error
  $\mathbf{E} \leftarrow \mathbf{Y}^{*} - \widehat{\mathbf{Y}}$ ; // Eq. 5.3

  // estimate robust statistics
  $\mathbf{P} \leftarrow$ *robuststatistics*($\mathbf{E}$) ; // Eqs. 5.4--5.8

  // estimate intensity scaling and bias correction
  $\mathbf{B} \leftarrow \mathbf{B}^{[n_{SR}-1]} + \grave{\mathbf{B}}^{[n_{SR}]}$ ; // Eq. 5.14
  $s_k \leftarrow \underset{\mathbf{s}}{\operatorname{argmin}} \sum_j \sum_k p_{jk} e_{jk}^2 \quad \forall\ k$ ; // Eq. 5.13

  // update volume
  $\mathbf{X}^{[n_{SR}]} \leftarrow \mathbf{X}^{[n_{SR}-1]} + \alpha \nabla F_{SR}(\mathbf{X}^{[n_{SR}-1]})$ ; // Eq. 5.11a

**end**

images in a slice, $\overline{\mathrm{Y}}_l$, was used as a reference free from from cardiac pulsation. Use of temporal mean images $\overline{\mathbf{Y}}$ for the initial stages of motion correction allowed for gross spatial alignment, facilitating cardiac synchronisation between slices and providing an initial estimate of $\mathbf{A}$ prior to motion correction of individual image frames.

Displacement, $disp(\,)$, was used to assess the change in position of the voxels in $\mathbf{Y}$ subject to estimated transformations $\mathbf{A}$. The displacement of individual image frames, $disp(\mathrm{A}_k)$, and global displacement, $disp(\mathbf{A})$, were calculated as

$$disp(\mathrm{A}_k) = \frac{\sum_j dist\left(y_{jk}, \mathrm{A}_k(y_{jk})\right)}{N_j}, \quad \text{and} \tag{5.16a}$$

$$disp(\mathbf{A}) = \frac{\sum_k \sum_j dist\left(y_{jk}, \mathrm{A}_k(y_{jk})\right)}{\sum_k N_j} \tag{5.16b}$$

respectively, where $dist\left(y_{jk}, \mathrm{A}_k(y_{jk})\right)$ is the spatial distance between the position of voxel $y_{jk}$ as acquired and the position of $y_{jk}$ transformed by $\mathrm{A}_k$.

Similarly, deviation from the average slice transformation, $dev()$, was used to assess the dispersion of estimated transformations. Deviation for an image frame, $dev(\mathrm{A}_k)$, slice, $dev(\mathbf{A}_l)$, and all frames, $dev(\mathbf{A})$, were measured as

$$dev(\mathrm{A}_k) = \frac{\sum_j dist\left(\mathrm{A}_l(y_{jk}), \mathrm{A}_k(y_{jk})\right)}{N_j}, \tag{5.17a}$$

$$dev(\mathbf{A}_l) = \frac{\sum_{k\in l} \sum_j dist\left(\mathrm{A}_l(y_{jk}), \mathrm{A}_k(y_{jk})\right)}{\sum_{k\in l} N_j}, \quad \text{and} \tag{5.17b}$$

$$dev(\mathbf{A}) = \frac{\sum_k \sum_j dist\left(\mathrm{A}_l(y_{jk}), \mathrm{A}_k(y_{jk})\right)}{\sum_k N_j} \tag{5.17c}$$

respectively, where $\mathrm{A}_l$ is the average probability-weighted slice transformation, calculated as

$$A_l = expm\left(\frac{\sum_{k\in l} p_k^{frame}\, logm(A_k)}{\sum_{k\in l} p_k^{frame}}\right) \tag{5.18}$$

using the matrix exponential, $expm(\,)$, and matrix logarithm, $logm(\,)$, to perform addition and scalar multiplication of the transformation matrices [173] to find the Frechét mean of $\mathbf{A}_l$ [174].

### Stack-Stack Registration

Stacks were first aligned by volumetric registration as in other volume reconstruction work [88, 89, 91], using $\overline{\mathbf{Y}}$, to provide an initial estimate of $\mathbf{A}$. The displacement between stacks of temporal mean images were estimated by registration of all stacks

with a nominated target stack.

#### Slice-Volume Registration

Using the transformations estimated by stack-stack registration, an initial volume was reconstructed with $\overline{\mathbf{Y}}$ and stack-stack transformations **A** as input to Algorithm 5.1. Subsequently, interleaved slice-volume motion correction (MC) and volume reconstruction was performed for $N_{MC}$ iterations to establish slice-wise alignment of $\overline{\mathbf{Y}}$. A volume of interest, $\mathrm{R}_{\mathrm{chest}}$, containing the entire fetal chest was used for slice-volume registration, making use of the anatomy surrounding the heart to aid the registration process.

#### Frame-Volume Registration

Finally, following cardiac synchronisation (§5.2.4) individual image frames, $\mathrm{Y}_k$, were spatially aligned using slice-wise transformations as a starting point. Similar to slice-volume registration, an initial cine volume was reconstructed using **Y**, $\theta$, $N_h = 25$ and slice-wise transformations **A** as inputs, followed by $N_{MC}$ iterations of interleaved frame-volume motion correction and cine volume reconstruction, resulting in cine volume **X**. A volume of interest, $\mathrm{R}_{\mathrm{heart}}$, containing only fetal cardiac anatomy was used for frame-volume registration. The overfitting found in dynamic image to 2D cine registration (§4.5), where the resulting transformations included some erroneous rotation following the torsion of the cardiac chambers along the long axis as the heart beats, was not observed in reconstructed cine volumes.

### 5.2.4 Cardiac Synchronisation

The temporal position in the cardiac cycle must be known for each image frame so that images can be combined as a single cardiac cycle. The heart rate was first estimated independently for each acquired slice time-series and then the cardiac cycle synchronised between slices.

#### Heart Rate Estimation

A heart rate was estimated for each slice using the approach previously described for the reconstruction of a 2D cine from single slice dynamic MRI (§4.5), as shown

in Figure 5.2. A temporal frequency spectrum was measured from the x-f signal in slice $l$, by taking the temporal Fourier transform of $\mathbf{Y}_l$ and then calculating the spatial mean over $R_l$. The fetal heart rate was identified as the temporal frequency at local maxima in this signal within a range of expected heart rates (105-180 bpm). Reciprocation of these heart rates resulted in estimated R-R intervals, $t_l^{RR}$, for each slice location and cardiac phases were calculated as $\theta_k = 2\pi \left(t_k \; mod \; t_l^{RR}\right) / t_l^{RR}$, where *mod* is the modulus operator.

Displacement of the heart and variation of the fetal heart rate resulted in diminished peaks in the temporal frequency maxima. Examples of heart rate estimation in the presence of motion are shown in Figure 5.2 for a slice with little motion (Fig. 5.2a and b) and a slice a high degree of motion (Fig. 5.2c and d) with a lower and broader peak compared to the slice with little motion. These peak characteristics were measured as peak height, the prominence of the peak relative to surrounding minima, and peak width, the full width at half prominence of the peak. Unreliable heart rate estimates were identified as those with peak characteristics more than three normal standard deviations from the median, where the standard deviation was estimated as the median absolute deviation scaled by $1/Q(3/4) \approx 1.4826$ and $Q()$ is the quantile function [175]. This was done first using peak height to exclude estimates from maxima with low peaks, and then using peak width to exclude maxima with broad peaks. Excluded estimates were replaced by the linear interpolation of heart rate estimates in temporally adjacent slices within the same stack.

### Slice-Slice Synchronisation

In the initial hybrid framework synchronisation of the cardiac cycle between slices was performed using the cross-correlation of the signal intensities in the 2D cine images to estimate the temporal offset between pairs of adjacent slices and between pairs of stacks of slices [166]. This approach did not account for movement and was, consequently, prone to error when some slices were corrupted by motion. An improved approach that was robust to motion was subsequently implemented, based on the group-wise intersection of slices.

To determine the overlap between slices, dynamic MR images were cast as cines in volume space by performing a volume reconstruction for each slice using estimated heart rates and slice-wise transformations. Specifically, a cine volume, $\mathbf{X}_l$, was reconstructed for each slice, $l$, from the dynamic images in that slice, $\mathbf{Y}_l$, using estimated cardiac phases $\theta_l$ and slice-volume transformations $\mathbf{A}_l$. A volume of interest containing only fetal cardiac anatomy was used for all volume reconstructions.

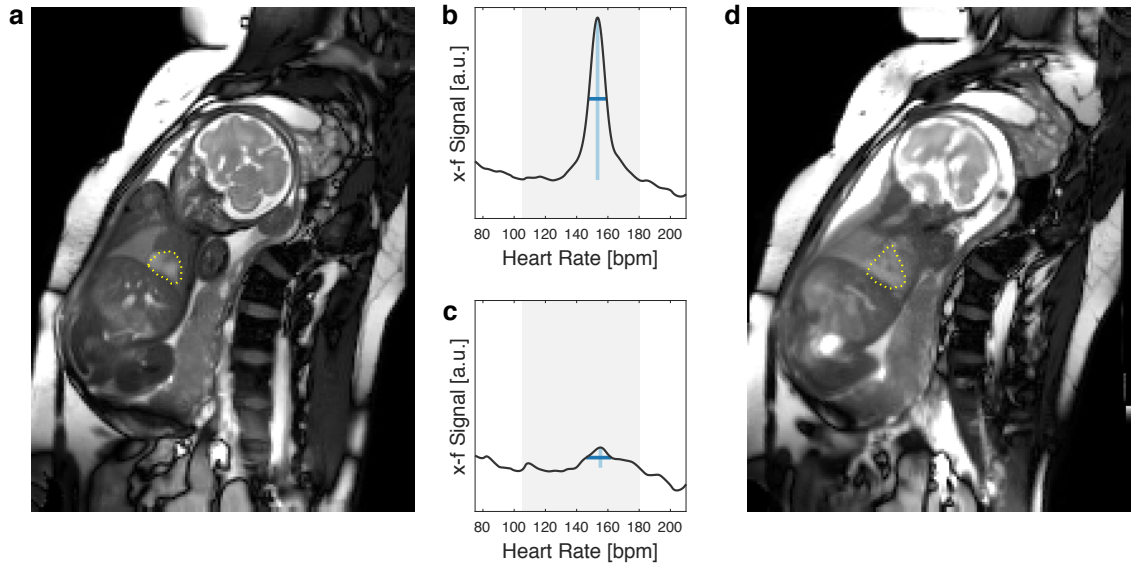


**Figure 5.2:** Heart rate estimation in the presence of motion. (**a**) Temporal mean image for a slice with little motion ($dev(\mathbf{A}_l)$ = 1.5 mm) with region of interest over the fetal heart (dotted yellow line), rotated to show the fetus in radiographic orientation in acquired field of view (304×400 mm). (**b**) Temporal frequency spectrum (magnitude of the spatial mean *x-f* signal in the region of the fetal heart) shows a clear maxima in the range of expected heart rates (grey band, 1.75-3.00 Hz). Peak height (light blue vertical line) and width (dark blue horizontal line) are shown. Fetal movement ($dev(\mathbf{A}_l)$ = 9.4 mm) during the acquisition of a different slice from the same stack leads to (**c**) a lower and broader peak in the temporal frequency spectrum and (**d**) blurring in the fetal heart (dotted yellow line) and surrounding anatomy in the temporal mean image .

Volume weights, $\mathbf{V}_l$, representing the weighted contribution of slice $l$ in volume space as $v_{ihl} = \sum_j \sum_{k \in l} w_{ij}^{hk}$, were used to determine the spatial intersection of slices. The overlap between slice $l$ and slice $l'$ could then be calculated as $\sum_i \sum_h v_{ihl} v_{ihl'}$, as shown in Figure 5.3.

The temporal offset between slices was represented as $\theta_l^{offset}$. Applying offset $\theta_l^{offset}$ to $\mathbf{X}_l$ and $\mathbf{V}_l$ was achieved by applying a cyclic Fourier time shift, $\phi_\theta(\,)$, i.e., addition of a linear phase in the temporal frequency domain, to get $\phi_{\theta_l^{offset}}(\mathbf{X}_l)$ and $\phi_{\theta_l^{offset}}(\mathbf{V}_l)$. Aligning the cardiac cycles of all the slices was equivalent to determining the offsets that maximised the overlap-weighted similarity between $\phi_{\theta_l^{offset}}(\mathbf{X}_l)$, i.e.,

$$\underset{\theta_l^{offset}}{\operatorname{argmin}} \; -\sum_l \sum_{l'} \frac{\sum_i \sum_h \widetilde{v}_{ihl} \widetilde{v}_{ihl'} \; cc\left(\phi_{\theta_l^{offset}}(\mathbf{X}_l), \phi_{\theta_{l'}^{offset}}(\mathbf{X}_{l'})\right)}{\sum_i \sum_h \widetilde{v}_{ihl} \widetilde{v}_{ihl'}}, \tag{5.19}$$

where $cc(\,)$ is Pearson's correlation coefficient and $\widetilde{v}_{ihl}$ is an element of $\phi_{\theta_l^{offset}}(\mathbf{V}_l)$. A fully group-wise optimisation was computationally intensive in practice, so a bootstrap approach was adopted instead, where one temporal offset was estimated at

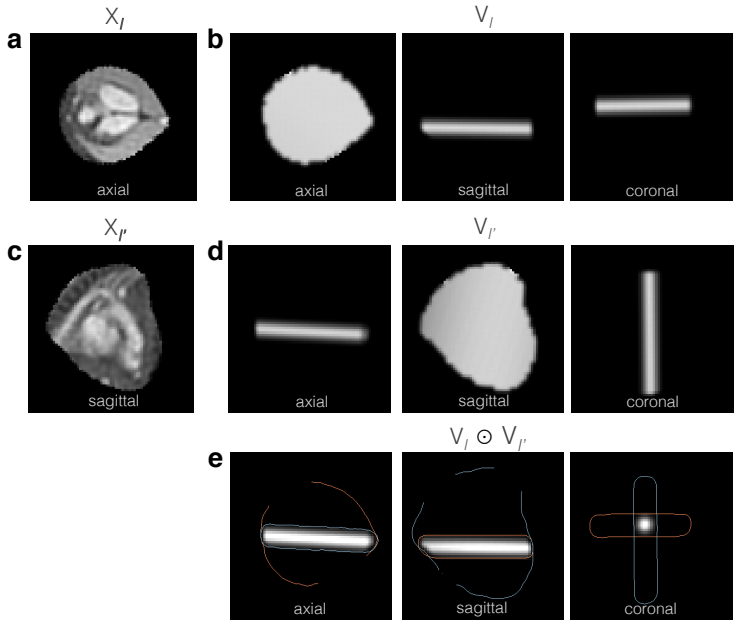


**Figure 5.3:** Slice-slice cardiac synchronisation of multi-planar dynamic MRI was performed by temporally aligning the cardiac cycles between cine volumes, $\mathbf{X}_l$, constructed from $\mathbf{Y}_l$ while using volume weights, $\mathbf{V}_l$, to determine the overlap between slices. The volumes for one slice are shown as (**a**) cine volume, $X_l$, shown in acquired axial plane, and (**b**) volume weights, $V_l$. A different slice, $l'$, from a stack acquired approximately orthogonal to the slice in (a) is shown as (**c**) cine volume, in sagittal plane, and (**d**) volume weights in same planes as (b). (**e**) The element-wise product of the two volume weights, $\mathbf{V}_l \odot \mathbf{V}_{l'}$. The overlap between slice $l$ and $l'$ was calculated as the sum of this element-wise product, i.e., $\sum_i \sum_h v_{ihl} v_{ihl'}$. The outline of $\mathbf{V}_l$ (orange line) and $\mathbf{V}_{l'}$ (blue line) are shown for reference.

each iteration using the objective function,

$$F_\theta\left(\theta_l^{offset}\right) = -\sum_{l' \in \{l''\}} \frac{\sum_i \sum_h \widetilde{v}_{ihl} \widetilde{v}_{ihl'} \; cc\left(\phi_{\theta_l^{offset}}\left(\mathbf{X}_l\right), \phi_{\theta_{l'}^{offset}}\left(\mathbf{X}_{l'}\right)\right)}{\sum_i \sum_h \widetilde{v}_{ihl} \widetilde{v}_{ihl'}} \,. \tag{5.20}$$

The slice $l'$ with the greatest overlap with all other slices was assigned $\theta_{l'}^{offset} = 0$, and used as an initial target slice. A different slice with the greatest overlap with $l'$ was then identified and an offset was estimated by finding $\theta_l^{offset}$ that minimised Eq. 5.20. This slice was then added to the set of fixed target slices $\{l''\}$ and the process was continued using the next slice with the greatest overlap with $\{l''\}$. This continued until all $\theta_l^{offset}$ were estimated. Upon completion, cardiac phases were adjusted as $\theta_k = (\theta_k + \theta_l^{offset}) \; mod \; 2\pi$, where *mod* is the modulus operator.

**Table 5.1:** Fetal study subjects.

| ID | GA | Reason for Scan | No. Stacks | No. Slices | US |
|---|---|---|---|---|---|
| 01 | $32^{+1}$ | dilated aortic root | 5 | 37 | * |
| 02 | $30^{+3}$ | volunteer | 5 | 37 | * |
| 03 | $24^{+6}$ | volunteer | 5 | 45 | * |
| 04 | $29^{+6}$ | right aortic arch | 6 | 54 | |
| 05 | $31^{+0}$ | ventricular diverticulum | 6 | 55 | * |
| 06 | $32^{+3}$ | right aortic arch | 6 | 75 | |
| 07 | $31^{+4}$ | double aortic arch | 4 | 44 | |
| 08 | $32^{+2}$ | right aortic arch | 4 | 42 | * |
| 09 | $28^{+0}$ | volunteer | 5 | 51 | * |
| 10 | $31^{+4}$ | double aortic arch | 3 | 35 | * |
| 11 | $33^{+2}$ | cardiac tumour | 4 | 42 | |

ID: Fetal case number. GA: gestational age in weeks$^{+\text{days}}$. No. Stacks: number of multi-planar dynamic MRI stacks acquired. No. Slices: number of slices acquired across all stacks. US: asterisk indicates matched 2D and STIC ultrasound data acquired.

### 5.2.5 Fetal Study

Imaging was performed as part of a larger research project [176]. Multi-planar dynamic MR imaging was acquired in eleven consecutive singleton pregnancies when examination time permitted acquisition of a minimum of three stacks with a combined total of at least thirty slices to ensure good coverage of cardiovascular anatomy. Fetal subjects ranged from 24 to 34 weeks gestational age. Details of the eleven cases, comprising three volunteers and eight subjects with cardiac anomalies, are listed in Table 5.1. All participants gave written informed consent prior to enrolment in the study.

#### Imaging

*Magnetic Resonance Imaging*

A research pulse sequence was implemented to collect multi-planar dynamic data using a regular Cartesian k-t under-sampling pattern. In the vendor software release (R5.1.7, Philips, Best, Netherlands), the acquisition order was prescribed by a slice loop inside a dynamic loop. Changes were made to the sequence software to allow for collection of all dynamic k-t data for one slice at a time before proceeding to the next slice, with appropriate preparation and dummy excitations preceding the acquisition of k-t data for each slice and not interleaved between excitations. All

sequence changes were reviewed by experienced sequence programmers for functional utility, safety compliance and image quality according to local standard operating procedures, and passed both phantom and adult volunteer tests prior to use in the fetal study. The sequence code was version controlled, tracking all changes from the vendor software release (R5.1.7), and distributed to a remote server-based repository (see software list at the end of this thesis for details).

Scanner operation was constrained to ensure fetal and maternal safety with respect to specific absorption rate (SAR), peripheral nerve stimulation(PNS), and sound pressure level (SPL). Whole body SAR was limited to a maximum of 1.2 W/kg, thereby also limiting expected local SAR in the fetus as suggested by fetomaternal simulations [72]. Gradient output was limited to 60% of the mean threshold PNS (50 T/s), typically measuring 22.7-28.2 T/s for multi-planar dynamic MRI. Sound pressures were limited to maximum A-weighted level of 115 dB(A), to maintain acceptable exposure, limiting the TR to 3.8 ms (§4.2). While necessary, safety constraints placed a limit on scanner performance and, consequently, achievable image quality and resolution.

Stacks of multi-planar dynamic images were acquired in three to six scan planes covering the fetal heart using the multi-planar 2D balanced steady state free precession (bSSFP) sequence. Highly-precise scan plane prescription was not required, as specific views could be later obtained from the reconstructed 3D cine. However, to achieve a good distribution of scan plane orientations, the first three stacks were prescribed roughly transverse, sagittal and coronal to the fetal trunk, with additional stacks prescribed in scanner transverse, sagittal, or coronal planes. In-plane rotation was used to reduce the size of the field of view in the phase encode direction while avoiding alignment of pulsatile maternal anatomy, e.g., maternal descending aorta, with the fetal heart in the phase encode direction to avoid complications in the k-t SENSE reconstruction.

Sequence parameters were based on those used in the 2D cine work (§4.6), and were selected to balance competing goals of good signal and contrast, high spatio-temporal resolution with full coverage of the fetomaternal anatomy in the field of view, and minimal scan time. multi-planar k-t under-sampled bSSFP data were collected with the following default parameters: TR/TE 3.8/1.9 ms, flip angle 60°, field of view 400×304 mm, imaging matrix 200×152, voxel size 2.0×2.0×6.0 mm, 8× acceleration, 72 ms temporal resolution, 96 images per slice, slice overlap 2–3 mm, 5–20 slices per stack. A steady state was established using an $\alpha$/2-TR/2 preparation pulse [113] followed by a series of twenty four dummy excitations prior to the acquisition of each slice, established experimentally prior to the fetal study. Coil

calibration data were acquired in a scan immediately preceding the multi-planar acquisition, and low spatial-resolution training data was acquired immediately following the under-sampled data. In some cases the default field of view did not fully accommodate the maternal anatomy in the prescribed image plane and was either decreased (ID03: 2 stacks, ID09: 3 stacks, ID11: 2 stacks) or increased (ID01: 1 stack, ID05: 2 stacks, ID06: 4 stacks, ID07: 3 stacks, ID08: 2 stacks, ID09: 1 stack, ID10: 2 stacks, ID11: 1 stack) in the phase encode direction. This resulted in a proportional change in the temporal resolution of the acquired data, with a median decrease of 7.6 ms and median increase of 3.8 ms. Stack coverage in the through-plane direction ranged from 22 to 63 mm (median 38 mm), with a median of nine slices acquired per stack.

*Echocardiography*

Ultrasound (US) examinations were performed in seven cases on the same day or three days prior to the MRI examination as part of a standard research protocol (ID01–03, ID07–10). The echocardiography protocol included comprehensive 2D M-mode imaging in standard views of all cardiovascular structures as well as B-mode sweeps covering the fetal trunk that were used to produce 4D Spatio-Temporal Image Correlation (STIC) volumes [36]. An EPIQ V7G system (Philips, Best, Netherlands) was used with a C9-2 curved array, V6-2 curved volume and X6-1 matrix array transducers (Philips, Best, Netherlands).

### Reconstruction

Multi-planar dynamic MR images were reconstructed using published methods [167] described in Chapter 4. Additional functionality was added using ReconFrame 3.0.535 (GyroTools, Zurich, Switzerland) to load raw k-space data, prepare receiver sensitivity maps, apply k-space and image-space corrections (e.g., phase and geometry corrections), extract temporal and spatial information, and to place k-t SENSE reconstructed images in a common world coordinate space. All k-t SENSE reconstructions were performed using spatially-uniform regularisation, i.e., $\lambda_0 = \lambda_{ROI} = 0.0014$ in §4.5 Eq. 2. Code to perform multi-planar k-t SENSE reconstruction was implemented in MATLAB (Mathworks, Natick, USA).

The volume reconstruction described in Algorithm 5.1 was implemented using the Image Registration Toolkit (IXICO, London, United Kingdom), building on the framework for reconstruction of fetal brain volumes from 2D MRI implemented by Kuklisova *et al.* [91], with additional methods for 3D cine volume reconstruction (§5.2.2).

A volume mask for 3D cine reconstruction was created by combining all fetal heart masks, $R_l$, transformed by estimated slice-volume transformations, $A_l$, with a small amount of blur ($\sigma$ = 10 mm in most cases, increased to 18 mm in some instances) to smooth the edges of volume of interest. The resulting mask was intersected with the fetal chest mask, $\mathbf{R}_{\text{chest}}$, to ensure no anatomy outside the fetus was included. Reconstruction parameters were based on those previously described [91], and validated for this work by numerical simulation experiments (§5.2.6, §5.3.1). Kuklisova *et al.* use an edge definition parameter, $\delta$, of half the difference between intensities along edges of interest, or approximately $\frac{3}{14}$ the mean signal in all $y_{jk}$, and a regularisation controlling parameter $\lambda$ = 0.08 for $n_{MC}$ = 1 decreasing geometrically to a value of $\widetilde{\lambda}$ = 0.01 for reconstruction of the final volume. Total number of iterations suggested by previous work are $N_{MC} = 6 - 9$ motion correction iterations and $N_{SR}$ = 10 super-resolution iterations for motion correction target volumes ($n_{MC} < N_{MC}$) and $\widetilde{N}_{SR}$ = 30 for reconstruction of the final volume, based on empirical assessment [91]. These parameter values were used as a starting point for volume reconstruction and further investigated via numerical simulation. Parameter space optimisation for 3D volume reconstruction by Kainz *et al.* suggest $N_{MC}$ = 3, $N_{SR}$ = 4 and $\widetilde{N}_{SR}$ = 13, while also noting improved image quality of the reconstructed volume with using 4 stacks as input to the reconstruction and the presence of a low amount of motion as exhibited by typical fetal MRI multi-planar data [172]. Volume reconstruction was performed at a spatial resolution of 1.25 mm, equivalent to $\frac{5}{8}$ the acquired in-plane resolution, similar to the ratio used for reconstruction of fetal brain MRI [91], and a temporal resolution corresponding to $N_h$ = 25 cardiac phases, to provide motion correction targets across the entire cardiac cycle.

Stack-stack registration was performed using a volumetric mask created by combining all slice-wise fetal heart masks, $R_l$, and applying a Gaussian blurring ($\sigma$ = 35 mm) followed by morphological closing to smooth the edges of the volume mask. Using the estimated transforms, a larger volumetric mask was created in a similar manner, but with $\sigma$ = 80 mm to ensure large coverage, and an initial baseline volume, $\overline{X}$, was reconstructed as a reference for a user-specified fetal chest volume of interest, $R_X^{ches}$. Slice-volume alignment was then performed by interleaving volume reconstruction, using $R_X^{ches}$, with slice-volume registration for $N_{MC}$ iterations.

All cardiac synchronisation functionality was developed in MATLAB (Mathworks, Natick, USA). The code for heart rate estimation was based on the implementation used in the 2D cine work (§4.5). Cine volumes, $\mathbf{X}_l$, for slice-slice synchronisation (§5.2.4) were reconstructed using estimated slice-volume transformations and estimated heart rates, while limiting the volume reconstruction input to the images from a single slice, $l$, at a time. Slice-slice cardiac synchronisation was performed

using constrained non-linear multivariate minimisation using the interior point approach implemented in the MATLAB Optimisation Toolbox.

All reconstruction software was version controlled on remote code repositories. Details can be found in the Software list included at the end of this thesis.

### Evaluation

Whole-heart 3D cine volumes were assessed by expert cardiac MRI readers to establish the quality of the reconstruction method. Three observers (seven, six, and three years experience reading cardiac MRI, respectively) were asked to independently navigate the reconstructed volumes using the Medical Image Interaction Toolkit Workbench (German Cancer Research Center Division of Medical Image Computing, Heidelberg, Germany) and score them in eleven categories based on the segmental approach to defining cardiac anatomy and pathology [26, 30, 31] as listed in Table 5.2.

**Table 5.2:** Evaluation categories based on segmental approach to defining cardiac anatomy and pathology.

| Category |
|---|
| Abdominal Position |
| Cardiac Position |
| Systemic Venous Connection |
| Pulmonary Venous Connection |
| Atrial Morphology |
| Atrioventricular Connection |
| Ventricular Arrangement |
| Ventricular Morphology |
| Ventriculo-Arterial Connection |
| Great Vessel Arrangement |
| Aortic and Ductal Arch Anatomy |

Data was presented without context, though the reviewers may have been present at the time of individual fetal examinations and could have recalled unique cases, e.g., the subject scanned for a cardiac tumour (ID11).

A five-point scale was used for scoring, as described in Table 5.3.

The median, mean and range of scores were calculated by category and by fetal case, for individual reviewers and collectively, to assess the quality of the reconstructed volumes and agreement between readers with respect to the categories in

**Table 5.3:** Description of five-point scale used for expert scoring.

| Score | Description |
|---|---|
| 4 | high image quality and distinct appearance of cardiac structures |
| 3 | adequate image quality to determine most details |
| 2 | sufficient image quality to determine some details |
| 1 | poor image quality with significant lack of detail |
| 0 | inadequate image quality to visualise any cardiac structure |

question and the fetal cases studied.

Ultrasound images acquired during the broader research project were used for qualitative comparison with 3D cine volumes in cases where matched data was available.

### 5.2.6 Simulation

A numerically simulated phantom was used to optimise and evaluate the proposed methods under controlled conditions. The Magnetic Resonance eXtended CArdiac-Torso (MRXCAT) phantom [177] was used as the basis for the simulation. MRXCAT is a framework for numerical simulation of cardiac MRI based on the eXtended CArdiac Torso (XCAT) [178] that defines anatomical tissue masks based on high-resolution segmented adult cadaver images [179] at 0.33×0.33×1.00 mm spatial resolution, with pulsatile cardiac movement modelled on in vivo 4D tagged MRI. These tools were used to simulate a high spatio-temporal resolution cine volume, $\chi$, with tissue properties adapted to the in utero environment, i.e., the signal of air in the lungs, trachea and the space surrounding the body in the postnatal simulation were replaced with the signal characteristics of amniotic fluid. The spatial and temporal dimensions of $\chi$ were scaled to match the fetal heart, resulting in a resolution of 0.44×0.44×0.44 mm and 20 ms.

The image acquisition model (Eq. 5.1) was used with $\chi$ as input to generate dynamic images from with 0.5 mm in-plane resolution and 6 mm through-plane resolution. These images were further down-sampled to 2 mm in-plane resolution by truncating k-space while adding noise at a level equivalent to that observed in the fetal images ($\sigma_{noise}$ = 0.07). Heart rates and displacements were based on in utero measurements of the fetal heart made during the fetal study. Gaussian kernel regression ($\sigma_{motion}$ = 200 ms) was applied to spatial transformation parameters, i.e. translations and rotations, relative to the centre of the heart to ensure smooth displacement from image frame to frame. True cardiac phases and transformations

were denoted $\theta^*$ and $\mathbf{A}^*$, respectively. Transformations were scaled to change the amount of displacement by a factor $c$ as $c \odot \mathrm{A}_k^* = expm(c\ logm(\mathrm{A}_k^*))$ [173], where $expm(\,)$ denotes the matrix exponential and $logm(\,)$ the matrix logarithm. Example simulated data is shown in Figure 5.4.

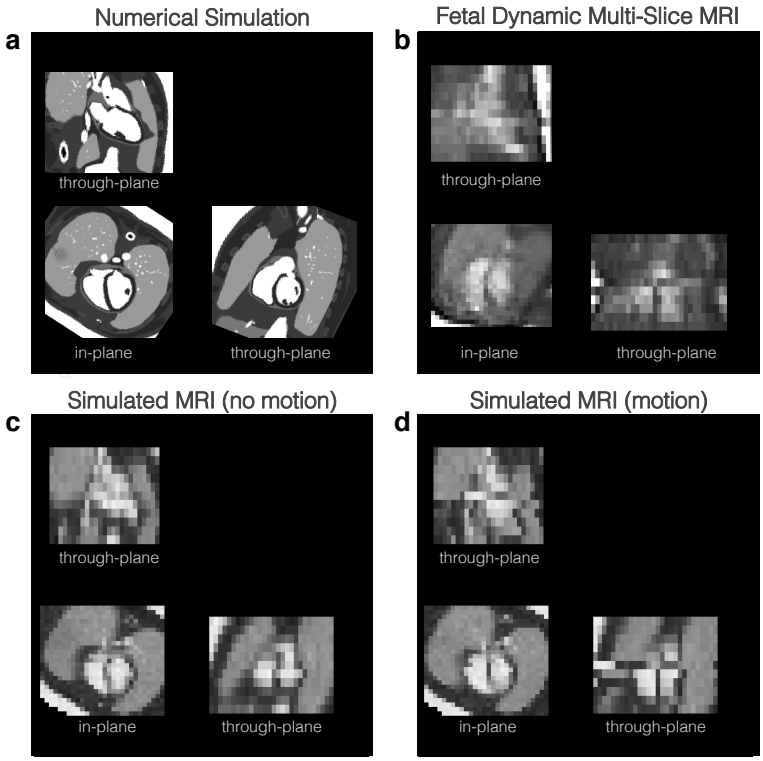


**Figure 5.4:** Numerical simulation of multi-planar dynamic MR images based on (**a**) high resolution numerical simulation of beating heart with no other fetal or maternal movement, using motion and cardiac pulsation extracted from (**b**) dynamic MR images acquired during the fetal study, showing misalignment of slices due to fetal movement. Simulated dynamic images are shown with (**c**) no motion and (**d**) motion.

Cine volumes were reconstructed from simulated dynamic MR images and the results were compared with the ground truth data using error metrics to assess various aspects of the 3D cine reconstruction framework. As motion-related imaging artefact was not simulated, outlier rejection was not used during volume reconstruction of the simulated images. In the following metrics, $\mathbf{X}^*$ denotes a cine volume reconstructed from simulated MRI data using $\mathbf{A}^*$ and $\theta^*$, while $\chi^*$ represents the high-resolution ground truth linearly resampled to the resolution of $\mathbf{X}$.

Image quality was assessed by normalised root mean square error (*NRMSE*) as

$$NRMSE\,(\mathbf{X}, \mathbf{X}^*) = \frac{\sqrt{\sum_i \sum_h (x_{ih} - x_{ih}^*)/ \sum_h N_i}}{\sum_i \sum_h x_{ih}^* / \sum_h N_i}. \tag{5.21}$$

The accuracy of motion correction was quantified as target registration error (*TRE*),

defined as

$$TRE\left(\mathbf{A},\mathbf{A}^{*}\right)=\frac{\sum_{j}\sum_{k}dist\left(\mathsf{A}_{k}(y_{jk}),\mathsf{A}_{k}^{*}(y_{jk})\right)}{\sum_{k}N_{j}} \tag{5.22}$$

where $dist\left(\mathsf{A}_{k}(y_{jk}),\mathsf{A}_{k}^{*}(y_{jk})\right)$ is the spatial distance between the position of voxel $y_{jk}$ transformed by $\mathsf{A}_{k}$ and $\mathsf{A}_{k}^{*}$. Lastly, cardiac synchronisation error was calculated as the root mean square error (RMSE),

$$RMSE\left(\boldsymbol{\theta},\boldsymbol{\theta}^{*}\right)=\sqrt{\sum_{k}(\theta_{k}-\theta_{k}^{*})/N_{k}}, \tag{5.23}$$

between estimated $\theta_{k}$ and true $\theta_{k}^{*}$, using $\mathsf{A}_{k}^{*}$ to ensure correct alignment of slices.

## 5.3 Results

The results of simulation experiments (§5.3.1) were used to evaluate the proposed method and select appropriate reconstruction parameters. Subsequently, data acquired during the fetal study were reconstructed using the selected parameters and evaluated as described in Section 5.3.2.

### 5.3.1 Simulation

*Volume Reconstruction Parameters*

Reconstruction parameter space was assessed by reconstructing cine volumes for a range of values of regularisation controlling parameter $\widetilde{\lambda}$ and edge scaling parameter $\delta$ using true transformation and cardiac phases, and calculating the error between the resulting cine volume, $\mathbf{X}^{*}$, and the numerically simulated cine volume, $\boldsymbol{\chi}^{*}$. Five stacks of simulated multi-planar dynamic MRI were generated with no motion scaling ($disp(\mathbf{A})$ = 3.7 mm) and used to reconstruct cine volumes with combinations of $\widetilde{\lambda}$ ranging from 0.005 to 0.015 and $\delta$ ranging from $\frac{1}{14}$ to $\frac{9}{14}$ of the mean signal intensity, $\overline{y}_{jk}$, for $N_{SR}$ = 30 super-resolution iterations. The resulting $NRMSE(\mathbf{X}^{*},\boldsymbol{\chi}^{*}$ contour maps, Figure 5.5, showed increasing image quality as super-resolution iteration $n_{SR}$ increased, with the lowest error occurring in the region of previously recommended parameter values, $\widetilde{\lambda}$ = 0.01 and $\delta=\frac{3}{14}\overline{y}_{jk}$. These parameter values were used in all subsequent volume reconstructions of simulated and fetal MR images. The volume reconstructed with these parameters showed cardiac anatomy and pulsation matching the numerically simulated cine volume, as shown in Figure 5.6,

providing evidence of geometric accuracy. However, there was some blurring in all reconstructed $\mathbf{X}^*$ compared to the high resolution $\chi^*$, due to the low spatio-temporal resolution sampling of the dynamic images, resulting in a high baseline *NRMSE* across all reconstruction parameter values. There was also some signal inhomogeneity within the blood pool in the heart in reconstructed $\mathbf{X}^*$, with an appearance similar to Gibbs ringing, e.g., Fig. 5.6f.

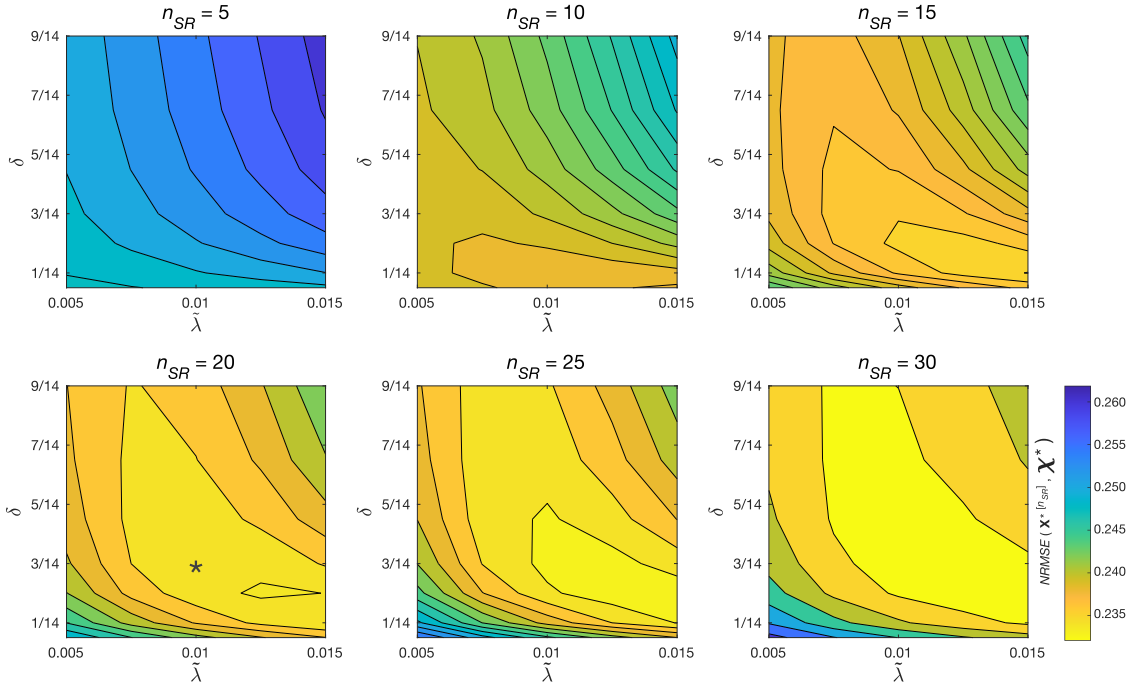


**Figure 5.5:** Normalised root mean square error (*NRMSE*) between 3D cine volume, $\mathbf{X}^*$, reconstructed from simulated MR images using known transformations and cardiac phases, and the ground truth cine volume, $\chi^*$. Error contour maps are shown for $\mathbf{X}^{*[n_{SR}]}$ after $n_{SR} = 5$ to 30 super-resolution iterations for a range of values for regularisation controlling parameter, $\widetilde{\lambda}$, and edge definition parameter, $\delta$. Values of $\delta$ are given relative to mean signal intensity $\overline{y}_{jk}$. The asterisk indicates the selected reconstruction parameter values.

### *Super-Resolution Iterations*

The relationship between number of super-resolution iterations and image quality in these results was investigated further by plotting the change in error against $n_{SR}$ for a cine volume reconstructed using the established values of $\lambda$ and $\delta$. As shown in Figure 5.7a, improvement in image quality levelled off with increasing $n_{SR}$. Based on these results, $\widetilde{N}_{SR} = 20$ iterations were used for the final volume reconstruction iteration when reconstructing fetal data.

### *Number of Stacks*

Reconstructions were also performed using fewer than the total number of simulated

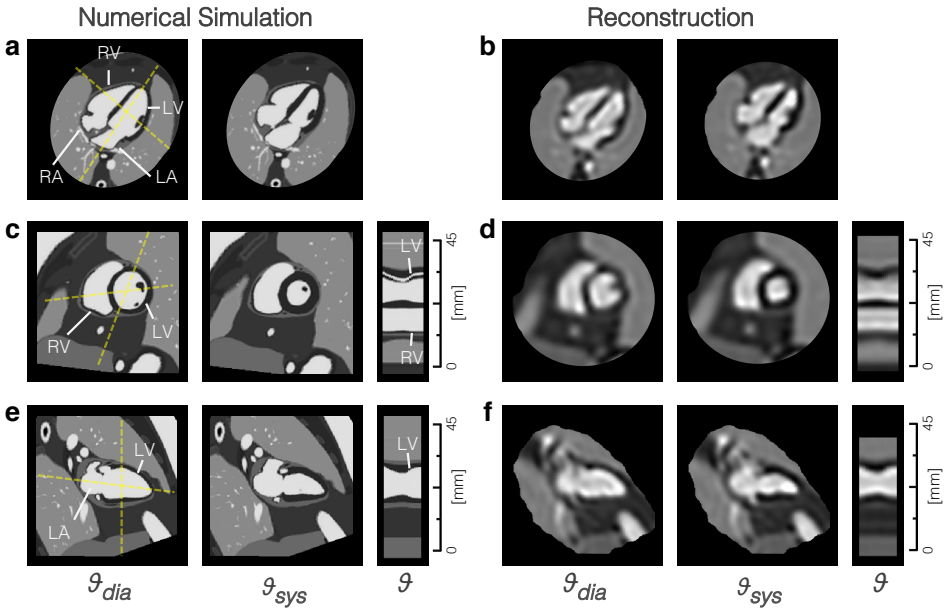


**Figure 5.6:** Simulated 3D cine volumes of the heart, matched to the size of an early third trimester fetus, re-sliced in the long and short axes of the heart. Reference cine volume (left) was created by numerical simulation with high spatio-temporal resolution (0.44 mm isotropic, 20 ms) and used to generated simulated dynamic MRI with reduced spatio-temporal resolution (2×2×6 mm, 69-76 ms), receiver noise ($\sigma_{noise}$ = 0.07) and moderate fetal motion ($disp(\mathbf{A}^*)$ = 3.7 mm). These simulated MR image were used to reconstruct a cine volume (right) using the known cardiac phase and spatial transformation of each frame. The heart is shown in (**a**) and (**b**) four chamber, (**c**) and (**d**) mid-short axis and (**e**) and (**f**) left two chamber views at diastole ($\vartheta_{dia}$) and systole ($\vartheta_{dia}$). Line profiles show contraction and dilation of the ventricles across the cardiac cycle ($\vartheta$) at the intersection of the short axis with (c) and (d) the horizontal long axis or (e) and (f) the vertical long axis (dashed yellow lines). The left (LV) and right (RV) ventricles and left (LA) and right (RA) atria are labelled for reference. All boxes bounding the views measure 55×55 mm. The fetal heart is shown in radiological orientation, i.e., image axes towards top and right of the page correspond to left, anterior and/or superior anatomical directions. Double-oblique planes are shown using spatial B-spline interpolation to avoid voxel distortion.

stacks of multi-planar dynamic MRI to assess the impact on resulting cine volumes. Cine volumes were reconstructed using three and four of the simulated stacks and compared with $\chi^*$, as Fig. 5.7a, . The results of this test, Figure 5.7b, showed a small decrease in error with increasing number of stacks, if transformations and cardiac phases are known. This suggests that all stacks available be used in the reconstruction. While not tested in this simulation experiment, it would seem to be a reasonable assumption that the inclusion of additional data from unique imaging planes in the reconstruction would improve motion correction and cardiac synchronisation estimates, thereby further improving the reconstruction.

*Cardiac Synchronisation*

To assess the impact of motion on the accuracy of cardiac synchronisation, the same five stacks of simulated multi-planar dynamic MRI were generated with motion scaled from $disp(\mathbf{A}^*)$ = 0 mm to 15 mm, and the method previously described for slice-slice cardiac synchronisation (§5.2.4) was applied with $A_l$ set to the average of all $A_k^*$ for $k \in l$. As shown in Figure 5.7c, the lowest errors occurred for $disp(\mathbf{A}^*)$ in the range of 2.3 to 9.3 mm with $RMSE(\boldsymbol{\theta}, \boldsymbol{\theta}^*) < \frac{3}{32}\pi$, or approximately 0.05 $t^{RR}$. The lowest $RMSE(\boldsymbol{\theta}, \boldsymbol{\theta}^*)$ was $\frac{1}{20}\pi$, for simulated MR images with a $disp(\mathbf{A}^*)$ = 5.6 mm,, equivalent to 10 ms for a the mean R-R interval measured in the fetal study (404 ms). For reference, the median $disp(\mathbf{A})$ measured in the eleven fetal cases was 5.8 $\pm$ 1.8 mm. Very low levels of movement resulted in reduced overlap between slices and, consequently, misalignment of the cardiac cycle in slices that had very little overlap with all other slices. Conversely, the overlap between slices increased with some movement, resulting in an improvement in cardiac synchronisation. However, large displacements lead to blurring in $\mathbf{X}_l$ and an increase in the cardiac synchronisation error for all slices.

*Motion Correction*

Lastly, the entire motion correction framework was used without any knowledge of the true transformations to access the accuracy of spatial alignment using the same five stacks of simulated multi-planar dynamic MRI used to assess reconstruction parameters (Fig. 5.5) and $N_{SR}$ (Fig. 5.7a). Volume reconstructions were performed with established parameters, i.e., $\lambda$ = 0.01, $\delta = \frac{3}{14}\overline{y}_{jk}$ and $N_{SR}$ = 20. Target registration error, shown in Figure 5.7d, improved across the registration stages resulting in a final $TRE(\mathbf{A}, \mathbf{A}^*)$ = 1.34 mm, equivalent to 2/3 the acquired in-plane resolution, after $N_{MC}$ = 3 frame-volume registration iterations, similar to the $TRE$ measured previously for fetal brain volume reconstruction 0.72 mm for 1 mm in-plane resolution images [91]. A similar decrease in $NRMSE$ was observed between cine volumes reconstructed with estimated transformations and ground truth transformations. No clear improvement was observed for higher number of motion correction iterations, suggesting that $N_{MC}$ = 3 is sufficient, as previously noted.

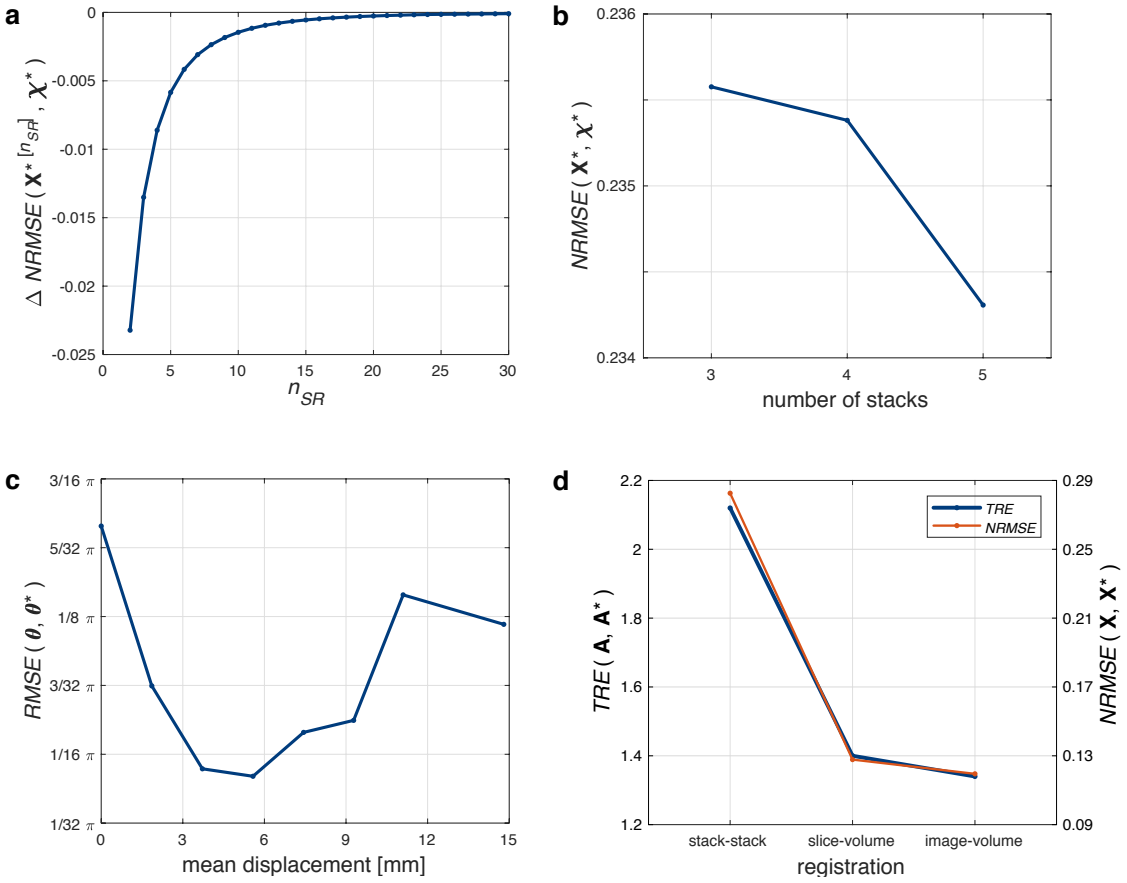


**Figure 5.7:** Assessment of 3D cine reconstruction using MR images simulated from numerical phantom. (**a**) Change in normalised root mean square error (*NRMSE*) between cine volume reconstructed using known transformations and cardiac phases, $\mathbf{X}^{*\,[n_{SR}]}$, and ground truth, $\mathcal{X}^*$, with number of number of super-resolution iterations, $n_{SR}$. (**b**) *NRMSE* versus number of stacks used in reconstruction. (**c**) Root mean square error (*RMSE*) of estimated cardiac phases after slice-slice cardiac synchronisation using ground truth transformations of $\mathbf{A}^*$ versus mean displacement of $\mathbf{A}^*$. (**d**) Target registration error (TRE) of estimated transformations for stack-stack, slice-volume, and frame-volume registrations (blue line), with *NRMSE* between 3D cine volumes reconstructed using estimated transformations and ground truth transformations using $N_{SR}$ = 20 iterations (red line). All assessments shown were based on volume reconstructions using reconstruction parameters established in the preceding simulation experiment ($\widetilde{\lambda}$ = 0.01, $\delta = \frac{3}{14}\overline{y}_{jk}$, Fig. 5.5).

### 5.3.2 Fetal Study

Cine volumes were successfully reconstructed in all eleven fetal cases. Reconstructed 3D cine volumes could be viewed in any arbitrary plane and at any phase in the cardiac cycle to examine cardiovascular morphology and connectivity. An example is shown in Figure 5.8 where the 3D cine volume is viewed in double-oblique cardiac imaging planes along the long and short axes of the heart and other standard views. The relative size of the chambers of the heart can be seen in horizontal long axis (four chamber) and mid-short axis views, with dilation and contraction of the left (LV) and right (RV) ventricles and left (LA) and right (RA) atria as the heart beats. Outflow tract and other off-axis views reveal arterial and venous connections of the aorta (Ao), pulmonary artery (PA), superior (SVC) and inferior (IVC) vena cava, as well as the positions of the Ao and ductal arch (DA).

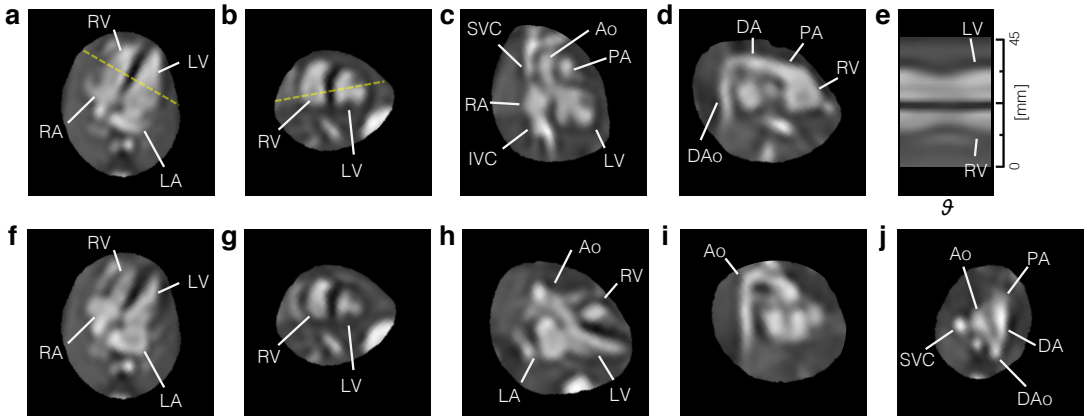


**Figure 5.8:** 3D cine MRI volume of the heart of a healthy $28^{+0}$ week gestational age fetus (ID09) re-sliced in standard views of the heart. The heart is shown in diastole (top row) in (**a**) four chamber, (**b**) mid-short axis, (**c**) left ventricular outflow tract, and (**d**) right ventricular outflow tract views. In diastole, both left (LV) and right (RV) ventricles are dilated, while both left (LA) and right (RA) atria are compressed. Ventriculo-arterial connections can be seen in outflow tract views with the aorta (Ao) arising from the LV in (c) and the pulmonary artery (PA) from the RV in (d). Systemic venous connections of the superior (SVC) and inferior (IVC) vena cava with the RA can also be seen in (c). (**e**) A line profile at the intersection of the four chamber and mid-short axis views (dashed yellow lines) shows the contraction and dilation of the ventricles with cardiac phase ($\vartheta$). The heart is also shown in systole (bottom row) in (**f**) four chamber and (**g**) mid-short axis views, corresponding to (a) and (b), with dilated atria and contracted ventricles, as well as (**h**) left three chamber, (**i**) aortic arch, and (**j**) three vessel views. The ductal arch (DA) can be seen in both (d) and (j), connecting the PA to the descending aorta (DAo), while the the Ao arch can be seen in (i) and (j). All boxes bounding the views measure 65×65 mm. The fetal heart is shown in radiological orientation, i.e., image axes up and right relative to the page correspond to left, anterior and/or superior anatomical directions. Views are shown using spatial B-spline interpolation to avoid voxel distortion in double-oblique planes.

Fetal results are summarised in Table 5.4, including mean and standard deviation of

**Table 5.4:** Summary of fetal results.

| ID | Expert Score [0–4] | Heart Rate [bpm] | Transformations $disp(\mathbf{A})$ [mm] | $dev(\mathbf{A})$ [mm] | Outliers $p^{voxel}$ [% $p < 0.5$] | $p^{frame}$ [% $p < 0.5$] | No. Images Inside Volume |
|---|---|---|---|---|---|---|---|
| 01 | 3.52 [2,4] | $147 \pm 5$ | 4.6 | 1.1 | 0.4 | 5.7 | 3552 |
| 02 | 3.55 [1,4] | $155 \pm 7$ | 5.2 | 1.7 | 0.5 | 9.4 | 3552 |
| 03 | 3.42 [1,4] | $147 \pm 6$ | 7.7 | 1.3 | 1.1 | 7.4 | 3936 |
| 04 | 3.12 [0,4] | $143 \pm 7$ | 11.2 | 1.8 | 0.4 | 21.6 | 3163 |
| 05 | 3.39 [1,4] | $148 \pm 11$ | 12.2 | 2.3 | 0.4 | 10.4 | 5280 |
| 06 | 3.58 [2,4] | $139 \pm 4$ | 7.6 | 1.3 | 0.5 | 15.6 | 6719 |
| 07 | 3.06 [1,4] | $153 \pm 8$ | 8.4 | 2.3 | 0.5 | 28.3 | 3072 |
| 08 | 3.48 [2,4] | $151 \pm 5$ | 4.9 | 1.2 | 0.4 | 20.2 | 3525 |
| 09 | 3.39 [2,4] | $150 \pm 5$ | 2.8 | 1.0 | 1.0 | 7.7 | 4887 |
| 10 | 3.55 [1,4] | $150 \pm 3$ | 4.7 | 1.3 | 0.8 | 4.6 | 3072 |
| 11 | 3.15 [1,4] | $153 \pm 7$ | 5.8 | 2.0 | 1.5 | 43.7 | 4032 |
| median | 3.42 | $150 \pm 6$ | 5.8 | 1.3 | 0.5 | 10.4 | 3552 |

ID: Fetal case number. Expert Score: mean and range of scores assigned by all reviewers across all categories. Heart Rate: mean and standard deviation of estimated fetal heart rates. Transformations: global displacement, $disp(\mathrm{A})$, and deviation from average slice transformation, $dev(\mathbf{A})$. Outliers: percent of voxel, $p^{voxel}$, and image frame, $p^{frame}$, posterior probabilities below 0.5. No. Images Inside Volume: number of image frames contributing to volume reconstruction, prior to outlier rejection. Images at the edges of the volume, i.e., those contributing fewer than $\frac{1}{10} median(N_j)$ voxels, were excluded from these summary statistics as they had minimal impact on the reconstructed volume but were more likely to be misaligned in space or time.

estimated heart rates, as well as estimated displacements and outliers. Mean expert scores are also listed, as an indication of overall quality. Image frames at the outer edges of the volume, i.e., those contributing fewer than $\frac{1}{10} median(N_j)$ voxels to the reconstruction, were excluded from heart rate, displacement and outlier statistics as they had minimal impact on the reconstructed volume but were more likely to be misaligned in space or time as a result of having a very small overlap with the volume.

The median estimated heart rate across all cases was 150 bpm (400 ms), ranging from 139 bpm (431 ms) to 155 bpm (387 ms), similar to the heart rates estimated in thirty fetuses of similar gestational age assessed for the 2D cine experiments (§4.5), as well as the heart rates estimated by Doppler ultrasound during MRI in a recent study of fifteen fetuses [180]. Estimated heart rates tended to vary slowly between slices acquired consecutively in a stack, as shown in Figure 5.9, with a pattern in keeping with the bounded walk superimposed on a constant baseline used to model the fetal heart rate [63] (§4.6). The simple approach for identification and

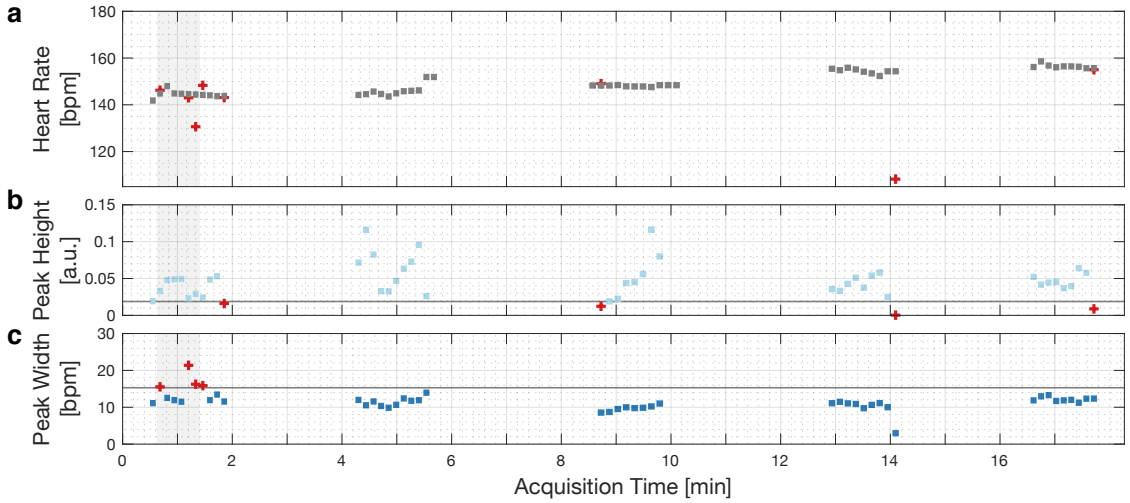


**Figure 5.9:** (**a**) Estimated heart rate for each slice acquired in a healthy $28^{+0}$ week gestational age fetus (ID09), with mean heart rate 150±5 bpm (401±13 ms). Unreliable heart rate estimates (red crosses) were identified using the (**b**) height and (**c**) width of the peak in the temporal frequency spectrum used to estimate the heart rate, as shown in Fig. 5.2. Threshold limits (horizontal lines, peak height 0.02, peak width 15.5 bpm) were calculated as three scaled median absolute deviations from the median. The heart rates for slices with peak heights less than the threshold were replaced with values linearly interpolated from temporally adjacent slices. Subsequently, heart rates for slices with peak widths above the threshold were replaced in a similar manner. Motion correction and outlier rejection results are shown in Fig. 5.10 for the all image frames acquired in the time window indicated by the grey vertical band (38 to 83 seconds).

replacement of unreliable heart rate estimates was able to deal with qualitatively discernible outliers (Fig. 5.9b and c) and did not appear to corrupt the estimated heart rates in any of the eleven cases.

Displacement, $disp\,(\mathbf{A})$, ranged from 2.8 to 12.2 mm, with a median of 5.8±1.8 mm median absolute deviation across all fetal cases. Displacements estimated in the 3D cine framework were much higher compared to the in-plane displacements estimated for in the 2D cine work (§4.5) since motion was also corrected in the through-plane direction in this 3D work, and a larger amount of data was acquired over a longer period of time. Estimated transformations for six consecutive slices in one stack acquired in a healthy fetus (ID09) are shown in Figure 5.10. An episode of fetal movement can be seen from acquisition time 72-78 s in the fifth and sixth slices shown. In the slices shown, $dev(\mathbf{A}_l)$ = 0.8, 1.4, 0.6, 1.0, 2.8 and 1.6 mm. Deviation from average slice transformation, $dev\,(\mathbf{A})$, ranged from 1.0 to 2.3 mm across all fetal cases, with a median of 1.3±0.3 mm median absolute deviation.

The dispersion of estimated transformations, $dev\,(\mathbf{A})$, was correlated with slice-wise heart rate variation ($r$ = 0.84, $p$ = 0.001). A similar correlation was found between displacement, $disp(\mathbf{A})$, and slice-wise heart rate variation ($r$ = 0.70, $p$ = 0.016),

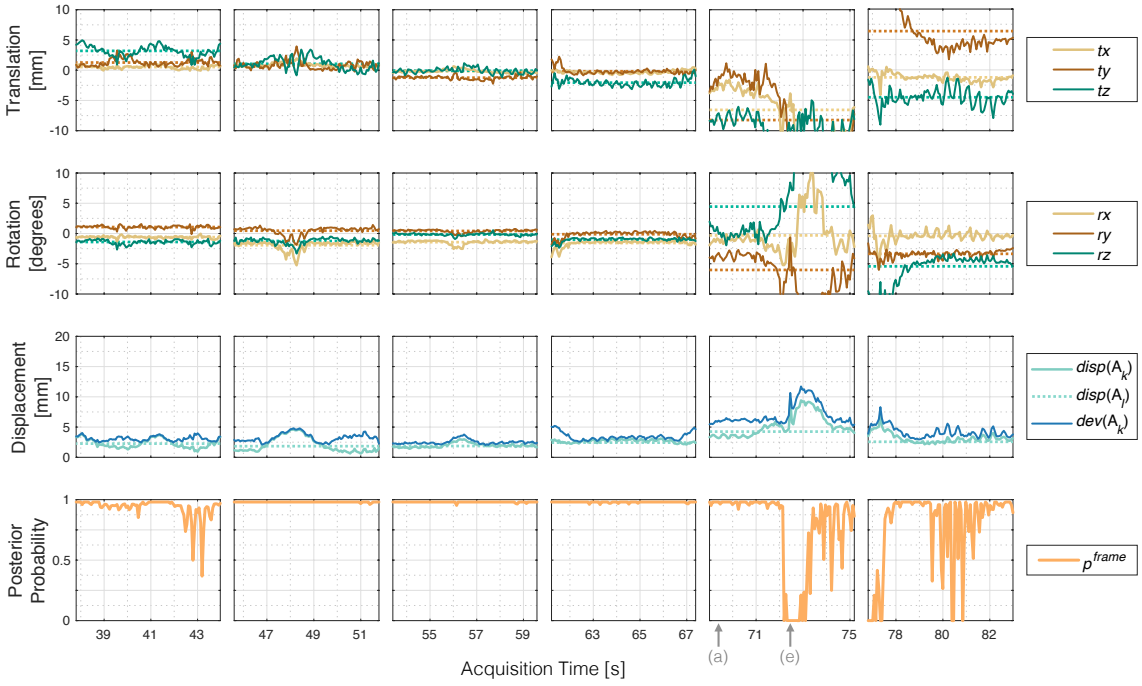


**Figure 5.10:** Estimated transformations, displacements and image frame-wise posterior probabilities for six consecutive slices in one stack of multi-planar dynamic MR images acquired in a $28^{+0}$ week gestational age fetus (ID09), corresponding to time window marked in Fig. 5.9. Translations *tx*, *ty* and *tz* are with respect to scanner right-left, anterior-posterior and superior-inferior directions, respectively. Rotations *rx*, *ry* and *rz* are about scanner y-z, x-z and x-y axes, respectively. Translation and rotation of the average slice transformation (Eq. 5.18) are plotted as dotted lines. Displacement of image frame-wise transformations, $disp(\mathrm{A}_k)$, and average slice transformations, $disp(\mathrm{A}_l)$, are plotted as solid and dotted lines, respectively. Deviation from the average slice transformation, $dev(\mathrm{A}_k)$, is shown relative to $disp(\mathrm{A}_l)$. Arrows on the time axis of the fifth slice indicate the image frames shown in Fig. 5.12a and e.

suggesting that the fetal heart rate may vary more while the fetus is active and moving. However, this trend may also point to increased variation in heart rate due to errors in heart rate estimation in the presence of motion.

The robust statistics approach to outlier rejection during volume reconstruction resulted in a median of 0.5% of voxels with $p_{jk}^{voxel} < 0.5$ and a median of 10.4% of image frames with $p_k^{frame} < 0.5$. Frame-wise posterior probability, $p^{frame}$, in the example previously shown (Fig. 5.10) was reduced during periods of large displacements and remains high during periods with little movement. The distribution of voxel-wise errors and image frame potentials are shown for this case in Figure 5.11 along with inlier-outlier class distributions and posterior probabilities. A small negative skew was observed in voxel-wise error distributions of fetal data, resulting in a non-zero median error. No skew was observed in the voxel-wise error distributions in the simulation experiment or in reconstructions using $\widehat{\mathbf{Y}}$ generated from fetal cine volumes (Eq. 5.1).

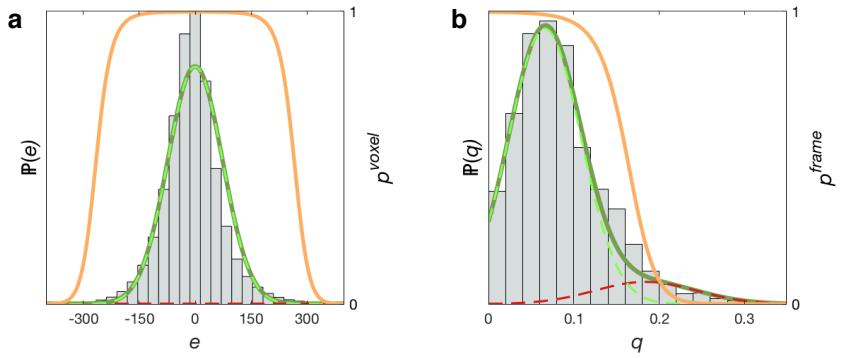


**Figure 5.11:** Outlier rejection using voxel- and image frame-wise robust statistics in a $28^{+0}$ week gestational age fetus (ID09) at completion of 3D cine reconstruction. (**a**) Voxel-wise error distribution (grey bars) with likelihood, $\mathbb{P}(e)$ (solid green line, Eq. 5.4), of observing error, $e$, modelled as the mixture of a Gaussian-distributed inlier class (dashed green line) and uniformly-distributed outlier class (dashed red line). Distribution parameters were estimated by maximising the log-likelihood of $\mathbb{P}(e)$ and used to map error to voxel-wise posterior probability, $p^{voxel}$ (solid orange line, Eq. 5.5). (**b**) Distribution of image frame potentials, $q$ (grey bars), with likelihood, $\mathbb{P}(q)$ (solid green line, Eq. 5.7), modelled as the mixture of Gaussian-distributed inlier (dashed green line) and outlier (dashed red line) classes, with expectation maximisation of $\mathbb{P}(q)$ resulting in frame-wise posterior probability weighting, $p^{frame}$ (solid orange line, Eq. 5.8).

On inspection of the results of individual image frames, Figure 5.12, the robust statistics were shown to effectively reduce the influence of voxels and frames corrupted by motion artefact. In general, cases with large $dev(\mathbf{A})$ had a higher percentage of image frames classified as outliers than those with small $dev(\mathbf{A})$, though a non-significant correlation ($p = 0.08$) was measured. However, this trend, in combination with the examples shown in Figs. 5.10 and 5.12, demonstrated that frames

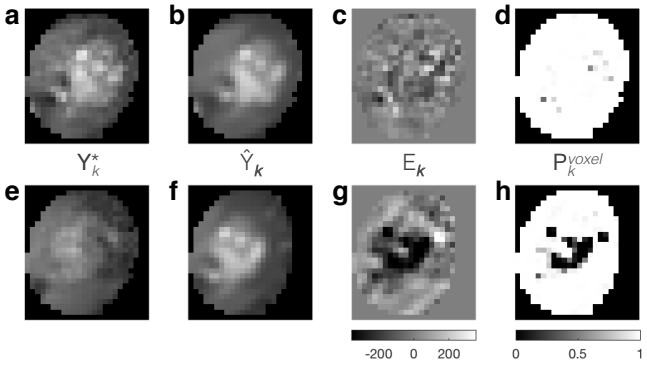


**Figure 5.12:** Voxel-wise error and probability maps for two image frames from the same slice acquired in high transverse plane in a $28^{+0}$ week gestational age fetus (ID09) at completion of 3D cine reconstruction. Image frames correspond to markers in Fig. 5.10, with one frame acquired during a period of no fetal movement (top row) and the other acquired during a period of fetal movement (bottom row). Cropped views of the fetal heart show (**a**) and (**e**) intensity-corrected images, $\mathrm{Y}^{*}_{k}$, (**b**) and (**f**) simulated images, $\widehat{\mathrm{Y}}_{k}$, (**c**) and (**g**) calculated error maps, $\mathrm{E}_{k}$, and (**d**) and (**h**) voxel-wise posterior probability probability maps, $\mathrm{P}^{voxel}_{k}$.

acquired during periods of fetal motion tended to be classified as outliers.

A particularly large outlier class was estimated in one case (ID11), shown in Figure 5.13. This fetus had a large mass in the heart that was determined to be a fibroma involving the myocardial free wall of the right ventricle based on this cine volume, as well as tissue characterisation from supplementary prenatal MR imaging [181]. Postnatal MRI findings were felt to be unclear, though the mass was thought to be a possible angiosarcoma based on its appearance on perfusion imaging. The baby passed at nineteen days age at which point the mass was confirmed to be a fibroma on post-mortem autopsy.

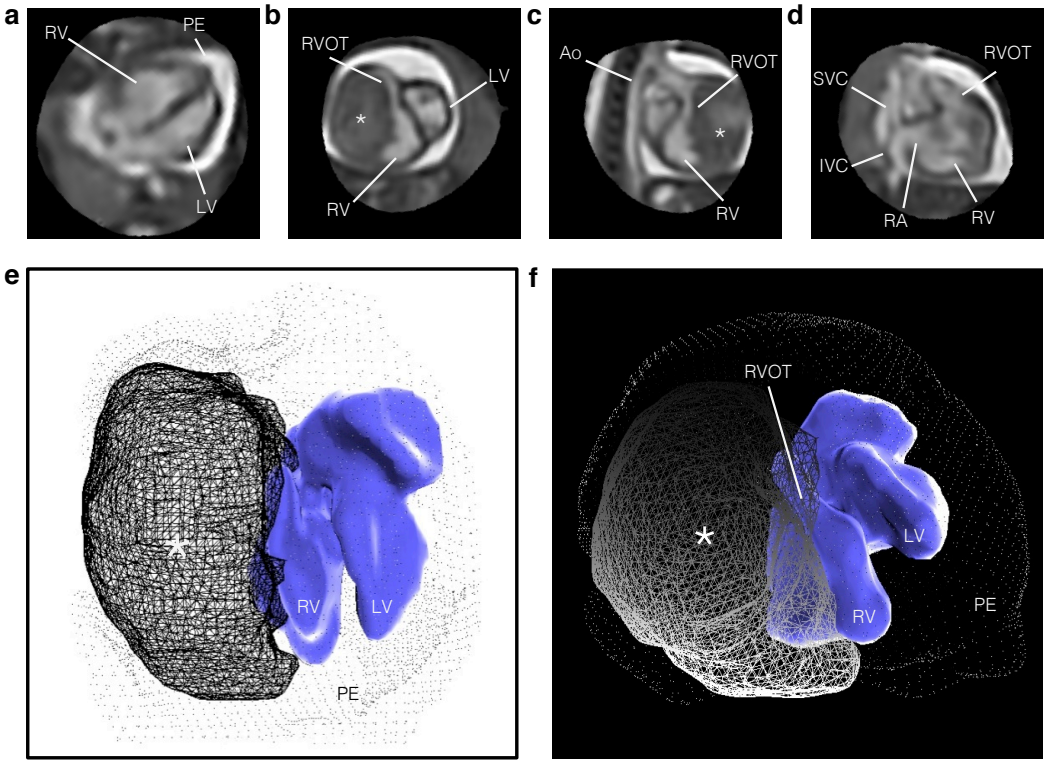


**Figure 5.13:** Cine volume of the heart of a $33^{+3}$ week gestational age fetus (ID11) with large fibroma, measuring 24×24×37 mm, involving the lateral wall of the right ventricle. The 3D cine volume is shown in diastolic cardiac phase in (**a**) four chamber, (**b**) short axis, (**c**) right ventricular outflow tract and (**d**) right three chamber view. Extensive associated pericardial effusion (PE) can be seen as bright signal surrounding the heart. A segmented volume rendering is shown in (**e**) superior and (**f**) anterior views, for reference of relative shape and position of the heart (blue surface), fibroma (lined mesh) and pericardial effusion (dotted mesh). The fibroma (asterisk) is encapsulated within myocardial tissue and confined to the margin of the right ventricular (RV) cavity, causing external compression of the right side of the heart, including the RV, right atrium (RA) and right ventricular outflow tract (RVOT), while the left ventricle (LV), aorta (Ao), and both the superior (SVC) and inferior (IVC) vena cava appear normal. All boxes bounding the cine volume views in (a-d) measure 80×80 mm. The fetal heart is shown in radiological orientation, i.e., image axes towards the top and right of the page correspond to left, anterior and superior anatomical directions. Views are shown using spatial B-spline interpolation to avoid voxel distortions in double-oblique planes.

The ability to visualise the relationship of the tumour to the myocardium in three dimensions and in time was particularly useful to help narrow down the differential diagnosis by fetal MRI. Despite rejection of nearly 44% of image frames, the reconstructed cine volume still showed a clear depiction of the fibroma and pericardial effusion, as well as smaller anatomical features such as compression of the right ventricular outflow tract. Upon inspection of the reconstruction results, no readily apparent cause was found for the large outlier class. However, due to the large fibroma, measuring 21 $cm^3$, and extensive pericardial effusion, this particular heart was grossly different in shape and appearance compared to the other fetal cases. It may be that the current implementation of outlier rejection is better suited to fine, high-contrast anatomy, such as the normal fetal brain and heart, than to anatomy containing large, homogeneous regions of very high or low signal. All other cases in the fetal study were healthy or had localised cardiac anomalies. Fetal cases less affected by fetal movement, i.e., those in the lower half of mean intra-slice variation in displacements, had smaller outlier classes, ranging from 4.5% to 20.2% of included image frames.

All steps of the proposed method were performed as described, with the exception of two cases that required some motion-corrupted slices to be manually excluded during volume reconstruction. Prior to excluding motion-corrupted slices, these two cases had $dev(\mathbf{A})$ = 3.8 mm (ID04) and 2.5 mm (ID07), larger than all other cases. An example of a motion-corrupted slice is shown in Figure 5.14 for a case where, of 54 total slices, one entire stack of nine slices and ten additional individual slices in other stacks were visually identified and excluded (ID04). In the other case (ID07), twelve of 44 slices were visually identified and excluded. Excluded slices, $I'$, had a high degree of motion in the original reconstructions, with median $dev(\mathbf{A}_{I'})$ = 8.7 mm (ID04) and 2.9 mm (ID07). In the case with the greatest motion (ID04), manual landmark-based registration was needed to align the stacks prior to any motion correction. In addition, an initial target for slice-slice cardiac synchronisation was manually defined in those two cases and one other (ID03), as the automatically selected target slice was visually determined to be motion corrupted.

Manual intervention yielded visually improved 3D cine reconstructions in the two cases where motion-corrupted slices were excluded, though they still received the lowest mean reviewer scores in the study. Large outlier classes were estimated in both cases, as expected. Comparing the views of the most motion-corrupted case (ID04) in Figure 5.15, good depiction of the cardiac anatomy can be seen in the reconstruction after manual intervention, with sharper chamber and vessel boundaries and coherent cardiac pulsation, that is absent in the original. Importantly, there is greater clarity of the arch vessels, of particular interest in this case with isolated

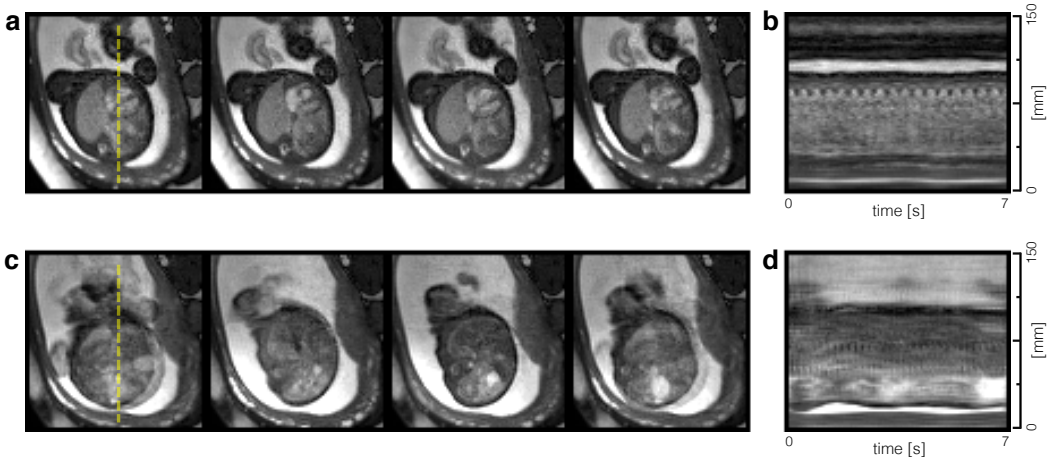


**Figure 5.14:** Dynamic MR images acquired in $29^{+6}$ week gestational age fetus (ID04). (**a**) Cropped views of $1^{st}$, $33^{rd}$, $64^{th}$, and $96^{th}$ image frames in a slice with little fetal movement, $dev(\mathbf{A}_l)$ = 0.9 mm, and (**b**) line profile across the fetal heart and chest corresponding to yellow dashed line in (a) for all frames in the slice. The same (**c**) image frame numbers and (**d**) line profile in a slice from the same stack, acquired eight seconds after the slice in (a), with large fetal movements, $dev(\mathbf{A}_l)$ = 10.1 mm. The slice shown in (c) was manually excluded from the 3D cine reconstruction. Manual exclusion of data was required in two of eleven cases (ID04,ID07) where the fetus was moving frequently throughout the acquisition. All images are shown at acquired in-plane resolution, cropped to 150×150 mm.

right aortic arch, which were obscured in the original cine volume (Fig. 5.15e), but could be seen in the cine volume reconstructed with manual intervention (Fig. 5.15j).

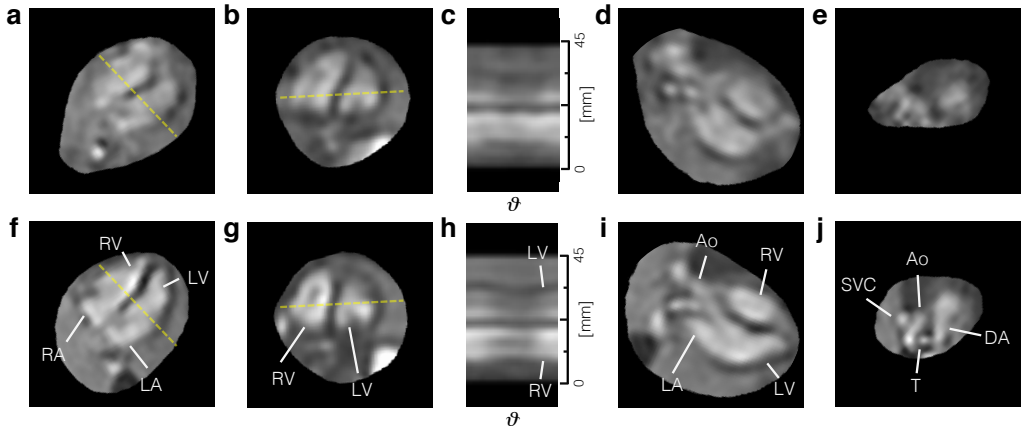


**Figure 5.15:** Reconstructed 3D cine volume of the heart of a $29^{+6}$ week gestational age fetus with isolated right aortic arch (ID04). Fetal movement was a challenge in this case, with large fetal movements occurring throughout the acquisition, as depicted in Fig. 5.14. These data were originally reconstructed using all acquired dynamic images resulting in a 3D cine volume corrupted by motion (top row). Exclusion of 19 of 54 total slices, including one entire stack of nine slice, resulted in a 3D cine reconstruction of improved quality (bottom row), particularly in the definition and detail of the arch anatomy in question. The heart is shown at end-ventricular diastole in (**a**) four chamber and (**b**) short axis views, with (**c**) a line profile at the intersection of the two views (dashed yellow lines) showing a cross section of the ventricles across cardiac phases ($\vartheta$). The heart is also shown in (**d**) three chamber view and (**e**) a high transverse view, similar to a three vessel view. Normal intracardiac anatomy is seen more clearly in matched (**f**) four chamber and (**g**) short axis views, as well as (**i**) a three chamber view showing the aortic (Ao) arch emerging from the left ventricle (LV), and then passing between the left atrium (LA) and right ventricle (RV). The vascular ring can be seen in (**j**) a high transverse view, with the superior vena cava (SVC) at right and the duct arch (AD) passing to the left of the trachea (T), as normal, while the aorta (Ao) passes to the right. The fetal heart is shown in radiological orientation, with bounding boxes measuring 65×65 mm. Double-oblique views are shown using spatial B-spline interpolation to avoid voxel distortion.

### *Evaluation*

The outcome of the expert scoring using the coding scheme in Tables 5.3 and 5.2 is shown in Figure 5.16 and summarised in Table 5.5. Scores were generally high in all categories suggesting a potential utility for the 3D cine reconstructions to assess a range of cardiac anatomy. Mean scores were between 3 and 4 for all fetal cases (median 3.4), as summarised in Table 5.4, indicating that all 3D cine volumes were of adequate quality to determine most anatomical details. The lowest mean scores across all reviewers were assigned for pulmonary venous connections, atrioventricular connections, and arch anatomy, indicating that small, complex anatomical features were the most challenging for the reviewers. The low mean score for atrial morphology can be largely attributed to the low scores assigned by reviewer 3. Scores assigned by more experienced reviewers (reviewers 1 and 2) were higher than the less experienced reviewer. A non-parametric assessment of

inter-rater agreement revealed no scoring bias between reviewers 1 and 2, and a median difference of -1 between scores assigned by reviewer 3 and the scores assigned by each of the two more experienced reviewers.

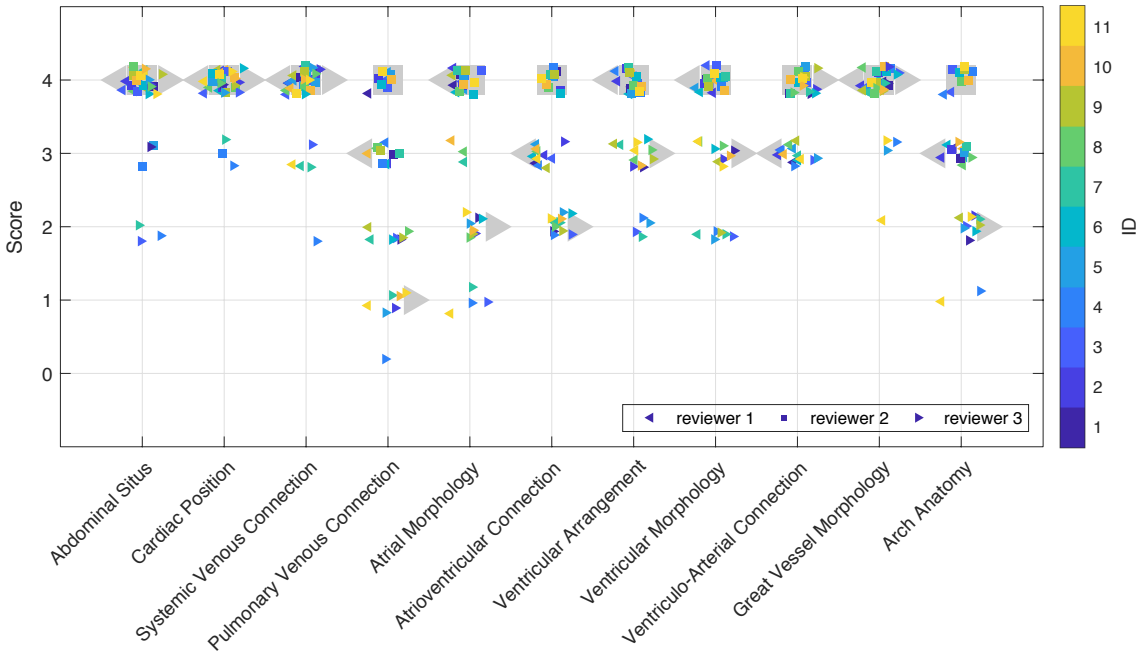


**Figure 5.16:** Reviewer score by evaluation category. Scores are shown for reviewer 1 (left-pointing triangles), reviewer 2 (squares), and reviewer 3 (right-pointing triangles), with six, seven, and three years experience reading cardiac MRI, respectively. Median reviewer scores are shown as large grey markers while coloured markers denote fetal case identification number.

**Table 5.5:** Reviewer score by evaluation category.

| Evaluation Category | Score | | | |
|---|---|---|---|---|
| | All Reviewers | Reviewer 1 | Reviewer 2 | Reviewer 3 |
| Abdominal Situs | 3.7 [2,4] | 4.0 [4,4] | 3.8 [3,4] | 3.4 [2,4] |
| Cardiac Position | 3.9 [3,4] | 4.0 [4,4] | 3.9 [3,4] | 3.8 [3,4] |
| Systemic Venous Connection | 3.8 [2,4] | 3.8 [3,4] | 4.0 [4,4] | 3.6 [2,4] |
| Pulmonary Venous Connection | 2.6 [0,4] | 2.9 [1,4] | 3.5 [3,4] | 1.4 [0,2] |
| Atrial Morphology | 3.1 [1,4] | 3.5 [1,4] | 4.0 [4,4] | 1.7 [1,2] |
| Atrioventricular Connection | 3.0 [2,4] | 2.9 [2,3] | 4.0 [4,4] | 2.1 [2,3] |
| Ventricular Arrangement | 3.4 [2,4] | 3.6 [3,4] | 4.0 [4,4] | 2.6 [2,3] |
| Ventricular Morphology | 3.4 [2,4] | 3.5 [2,4] | 4.0 [4,4] | 2.5 [2,3] |
| Ventriculo-Arterial Connection | 3.6 [3,4] | 3.0 [3,3] | 4.0 [4,4] | 3.7 [3,4] |
| Great Vessel Morphology | 3.8 [2,4] | 3.8 [2,4] | 4.0 [4,4] | 3.7 [3,4] |
| Arch Anatomy | 2.9 [1,4] | 2.9 [1,4] | 3.6 [3,4] | 2.1 [1,3] |

Mean and range of scores by evaluation category for all reviewers combined, as well as separately for each of three reviewers with six, seven, and three years experience reading cardiac MRI, respectively.

Cine volumes were compared with 2D and STIC ultrasound in the seven fetal cases where matched data was acquired. An example is shown in Figure 5.17 for a fetus with a dilated ascending aorta (ID01) where the three imaging methods are compared in matched views. Though STIC quality has been reported to be reduced in fetuses in the third trimester [182], the STIC volume of this $32^{+1}$ week gestational age fetus was the best of those acquired. In the other six fetal cases with matched ultrasound data, 2D echocardiography images were of comparable quality to those shown in Figure 5.17. However STIC volumes in four cases were clearly of poor quality (ID03,ID08–10), particularly in the through-plane direction, presumably due to fetal motion.

Both 2D echo and STIC showed clear definition of vessel and chamber boundaries, including valves, with high spatial and temporal resolution. Reconstructed cine MRI volumes had good contrast between blood and surrounding tissue. However, visualisation of valves and other small and rapidly moving anatomy was limited due to the spatio-temporal resolution of the acquisition. While the real-time aspect of 2D echo made it robust to fetal motion, interpretation of complex anatomy was limited to the views acquired by the operator during the examination. By contrast, both STIC and MRI cine volumes allowed for offline analysis in arbitrary imaging planes with full coverage of the heart and great vessels, facilitating understanding of spatial relationships between cardiovascular structures.

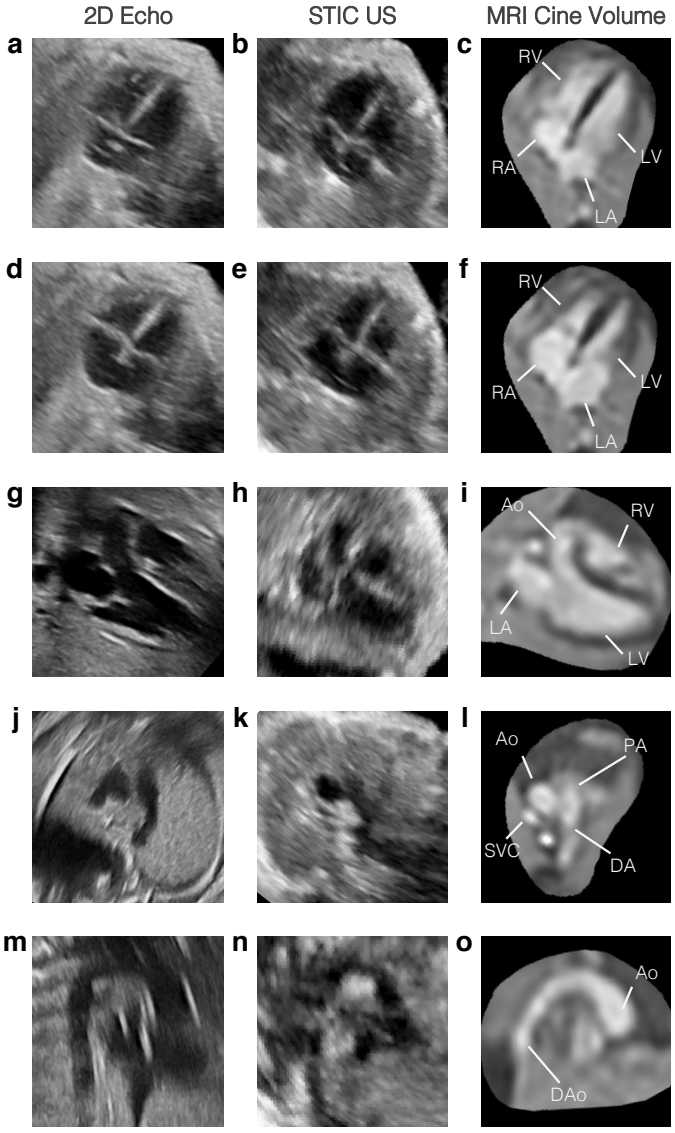


**Figure 5.17:** Comparison of ultrasound and MRI in a $32^{+1}$ week gestational age fetus (ID01) with moderate dilation of the ascending aortic root and rightward tortuosity of the proximal ascending aorta. The fetal heart is shown in matched views in 2D echocardiogram (left column), 4D spatio-temporal image correlation (STIC) ultrasound (centre column) and 3D cine MRI (right column). Four chamber views at (**a**)-(**c**) end-ventricular diastole and (**d**)-(**f**) end-ventricular systole show the alternating contraction and expansion of the ventricles (LV,RV) and atria (LA,RA), with balanced chambers. (**g**)-(**i**) Left three chamber view, (**j**)-(**l**) three vessel view and (**m**)-(**o**) aortic arch in sagittal view revealing a dilated aorta (Ao) at the sino-tubular junction, compared to the pulmonary artery (PA), ductal arch (DA) and descending aorta (DAo). All bounding boxes measuring 65×65 mm and the fetal heart is shown in radiological orientation. The MRI volume is shown using spatial B-spline interpolation to avoid voxel distortions in double-oblique planes.

Some artefacts were seen in 2D ultrasound images and STIC volumes, occasionally obscuring cardiac anatomy. Acoustic shadowing appeared as dark areas, as in Fig. 5.17g, j, k and m. Blurring and image misalignment appeared in STIC volumes, such as blurring in the through-plane direction in Fig. 5.17h and discontinuities in the descending aorta in 5.17n. These effects likely occurred due to fetal movement, though reduced sensitivity in anatomy distant from the transducer may also have an impact. MRI had good signal coverage of the entire cardiovascular system in all fetal cases.

## 5.4 Discussion

Whole-heart 3D cine reconstruction of the fetal heart from multi-planar dynamic MRI was successful in all eleven fetal cases using the proposed framework. These reconstructed volumes could be visualised in any 2D plane without the need for highly-specific scan plane prescription prior to acquisition or maternal breath hold to minimise motion. The three dimensional aspect of these volumes allowed for interpretation of the complex connections of the cardiac chambers and vessels, while the temporal aspect improved the depiction of pulsatile anatomy.

Reconstructions of simulated MR images confirmed that spatial and temporal features could be reliably recovered, within the limits of the resolution of the acquisition. There was some blurring in the cine volumes reconstructed from simulated MR images compared to the high resolution ground truth, which can be attributed to the low spatio-temporal resolution sampling of the simulated MR images. There was also a ringing-like signal intensity effect in cine volumes that was apparent in the simulation results (Fig. 5.6), and may also impact the cine volume reconstructions in the fetal study, though the effect was more subtle. It is not readily apparent where the effect originates from, but further investigation of spatial point spread functions and edge-preserving regularisation may be informative.

Overall high scores were assigned by three expert readers in an evaluation based on the segmental approach to defining cardiac anatomy and pathology. The lowest scores were assigned in categories focused on small, complex anatomical features, such as pulmonary venous connections and arch anatomy, where spatio-temporal resolution limited the depiction of fine details, as was also the case for small septal defects and all atrioventricular and ventriculo-arterial valves. Though a category such as ventricular morphology received high scores in this evaluation, as there was enough other information to give the reviewers high confidence, particular ab-

normalities, such as valvular defects, were more visible in ultrasound images. However, some cardiac anatomy was obscured by artefact in the ultrasound images due to acoustic shadowing and, in the case of STIC volumes, blurring and misalignment. The results of the expert evaluation suggest that there is potential utility of the method to generate 3D cine volumes that can be used for a comprehensive assessment of the fetal heart, either as an adjunct to ultrasound or in combination with other MRI techniques. For example, while aortic and ductal arch branching patterns may be difficult to determine in the 3D cine volume, a static volume reconstruction of $T_2$-weighted single shot fast spin echo images [183] may more clearly depict the details of the arch anatomy.

The focus of this work was on 3D depiction of the whole fetal heart and, consequently, the acquisition and reconstruction of k-t SENSE MRI was not fundamentally changed from the implementation in Section 4. Many of the potential improvements previously suggested (§4.5) still apply. Low spatial resolution training data was collected following k-t under-sampled multi-planar data and used to reconstruct the dynamic images. However, training data could be estimated directly from the under-sampled data [156, 159] to reduce acquisition duration and motion-tolerance. Similarly, static or dynamic receiver coil sensitivities could estimated from the under-sampled data rather than a separate pre-scan [184] to further reduce scan time and improve motion tolerance. Spatially-uniform k-t SENSE regularisation was used in this work. Temporal fidelity will likely improve if dynamic images are reconstructed using spatially-adaptive regularisation [167] to preserve the full temporal resolution of the under-sampled acquisition and baseline images are processed to reduce temporal filtering effects [185].

Simultaneous multi-planar techniques [186] could be incorporated to reduce scan time and increase data consistency as motion correction and cardiac synchronisation could be performed using groups of slices acquired simultaneously. In addition, a single- or multi-band acquisition could be performed with 2D imaging planes that are swept smoothly across the anatomy of interest to preserve steady state conditions and coverage, thereby increasing the efficiency of the acquisition [187].

The methods proposed in this chapter are fully automated aside for user-specified masks of the fetal heart and chest and selection of a target stack for stack-stack registration. While these user-interactions are not particularly labourious, they could be automated to achieve a fully automatic reconstruction pipeline. The target stack for stack-stack registration could be identified using a measure of slice alignment [172], while masks could be generated using automated segmentation techniques [169, 170]. A minimal motion criteria would also improve selection of the initial target

slice for slice-slice cardiac synchronisation (5.2.4), as manual selection was required in three of eleven fetal cases where the initial target slice was motion corrupted. In two cases, manual intervention was required to exclude data with significant motion. The anatomy was blurred and inconsistent in the original cine volumes reconstructed using these motion-corrupted data (Fig. 5.15) as errors in stack-stack and slice-volume registrations lead to slice-slice cardiac synchronisation errors, and the reconstruction could not converge on a good depiction of the underlying fetal heart. An initial motion detection stage could serve to identify those slices with significant motion prior to any motion correction or cardiac synchronisation without need for intervention. Even if all slices are used in a final reconstruction, exclusion of slices corrupted by motion in a preliminary cine volume reconstruction may allow for reconstruction of a good quality volume to use as a registration target in a final motion correction stage using all slices.

Simulated dynamic multi-planar MR images were used to assess the proposed motion correction methods against known spatial transformations. These experiments resulted in a registration error 1.34 mm after all three stages of motion correction were performed, equivalent to 2/3 the acquired in-plane resolution, similar to the error reported by Kuklisova *et al.* [91]. Rigid body image registration was used in this work, but many postnatal approaches to cardiac MR motion correction use non-rigid registration methods to adapt to the deformation of the heart. However, it is unclear if non-rigid registration is of value for fetal cardiac MRI as the lungs are water-laden and less compressible than air-filled lungs, which is likely to impact the interaction of heart shape and chest motion.

The use of a constant heart rate for each slice does not accommodate beat-to-beat variation resulting in small timing errors (§4.6). Image-based self-gating methods [170,188,189] could be used to reduce these timing errors, either in combination with or in replacement of the current approach.

Simulation experiments showed slice-slice cardiac synchronisation error of less than 5% of the cardiac cycle for the range of displacements measured in the majority of fetal cases, suggesting the proposed method provided reliable results. However, the position of each image frame in the cardiac cycle, $\theta$, are estimated prior to cine volume reconstruction. Cardiac synchronisation may be improved if $\theta$ is updated during volume reconstruction by comparison of dynamic images, $\mathbf{Y}$, with reconstructed cine volume, $\mathbf{X}$, for example, by minimising RMSE between $\mathbf{Y}$ and $\widehat{\mathbf{Y}}$ generated from $\mathbf{X}$ with respect to $\theta$ constrained by an appropriate model of heart rate variation, i.e., $\underset{\theta}{\operatorname{argmin}}\, RMSE(\mathbf{Y}, \widehat{\mathbf{Y}})$.

Outlier rejection was performed as implemented by Kuklisova *et al.* [91], with robust statistics shown to effectively reduce the influence of inconsistent data. As magnitude-valued images were used, sensitivity to image artefacts that manifest in the phase of complex-valued images was reduced compared to the complex-valued outlier rejection approach employed in the 2D framework (§4.5). However, this did not appear to have a dramatic effect as dynamic images were reconstructed using spatially-uniform k-t SENSE regularisation, thereby suppressing image artefact to some extent.

There was a small negative skew in voxel-wise error distributions in the fetal data. This is may be the result of blurring in the reconstructed cine volumes compared to the acquired dynamic images as no skew was observed in the error distributions in the simulation experiments or in cine volume reconstructions using dynamic images generated from fetal cine volumes themselves. A more appropriate choice of the spatio-temporal PSF used for volume reconstruction, such as a continuous sinc in the in-plane direction [172], may resolve this issue.

In the 2D framework (§4.5), the distribution of frame potentials was modelled as the mixture of a Rician inlier and uniform outlier class. This may also be an effective model for the 3D framework, but has not yet been implemented. Similarly, a fixed number of motion correction and super-resolution iterations was used for cine volume reconstruction. A convergence criteria may save computation time, as was utilised in the 2D cine framework.

The proposed framework for 3D cine reconstruction may not generalise to cases with dramatic non-localised differences from normal fetal cardiac anatomy, such as large homogeneous regions of very high or low signal in cardiac tumours and pericardial effusion (Fig. 5.13). Outlier rejection may be particularly sensitive to these differences, as a large number of frames were rejected as outliers in this fetal case, though a good quality cine volume was still reconstructed.

### 5.4.1 Potential for Simultaneous 3D Cine Reconstruction and Velocity Mapping

Phase information in the acquired dynamic images was ignored in the current cine volume reconstruction framework. Volume reconstruction from complex-valued dynamic images is not a straightforward extension of the current framework, but has the potential to simultaneously generate 4D velocity maps, i.e., cine velocity volumes, from the same data. Phase contrast SSFP methods have been proposed

[120], using the flow sensitivity of the bSSFP sequence to encode velocity in the phase images [117]. By relating the phase in the dynamic images to the encoded velocity, it may be possible to simultaneously reconstruct cine velocity maps in addition to a magnitude-valued cine volume representing the fetal heart.

For complex-valued **Y**, the phase in an acquired voxel, $\angle y_{jk}$, is the sum a velocity-encoded phase, $\phi_{jk}$, and a background phase. The smoothly varying background phase can be estimated by fitting a low-order 2D or 3D polynomial to the phase in static tissues and subtracted from $\angle y_{jk}$ so that only the velocity-encoded phase remains [190]. The velocity-encoded phase can then be related to the underlying velocity as

$$\phi = \gamma \upsilon_{read} M_{1,read} + \gamma \upsilon_{phase} M_{1,phase} + \gamma \upsilon_{slice} M_{1,slice} \tag{5.24}$$

where $\gamma$ is the gyromagnetic ratio, and $\upsilon$ and $M_1$ are the velocity and first moments of the gradient waveforms, respectively, in the readout, phase-encode and slice directions [120].

To fully integrate complex-valued **Y** and reconstruct volumetric velocity maps, the velocity-encoded phase would need to be related to three-dimensional space, and the image acquisition model (Eq. 5.1) would have to be adjusted to include velocity terms, precipitating a number of changes to the framework. Instead, as a proof of principle, the framework was modified to reconstruct complex-valued **X**. Background phase has removed from complex-valued **Y** by subtracting a third-order 3D polynomial fit to the phase in static amniotic fluid and tissue in each acquired stack and a phase sign correction was applied to improve phase consistency, so that the signs of all $\phi_{jk}$ were aligned with $\phi_{jk}$ of the target stack. All steps in the framework were performed as described earlier in this chapter, with the modification that real- and imaginary-valued volumes were also generated from the real and imaginary components of **Y** after the final motion correction iteration. Initial estimates of the real and imaginary components of **X** were generated by PSF-weighted interpolation (Eq. 5.2) and then updated at each super-resolution iteration (Eq. 5.11) using the magnitude-valued **X** in the adaptive regularisation term. An example of a reconstructed complex-valued 3D cine volume is shown in Figure 5.18 with the velocity-encoded phase most sensitive to velocities in the fetal superior-inferior direction, perpendicular to the target stack acquired transverse to the fetal trunk, and the magnitude-valued volume shown as an anatomical reference. Peak velocities can be seen in the great vessels in systole, with reduced velocity in diastole.

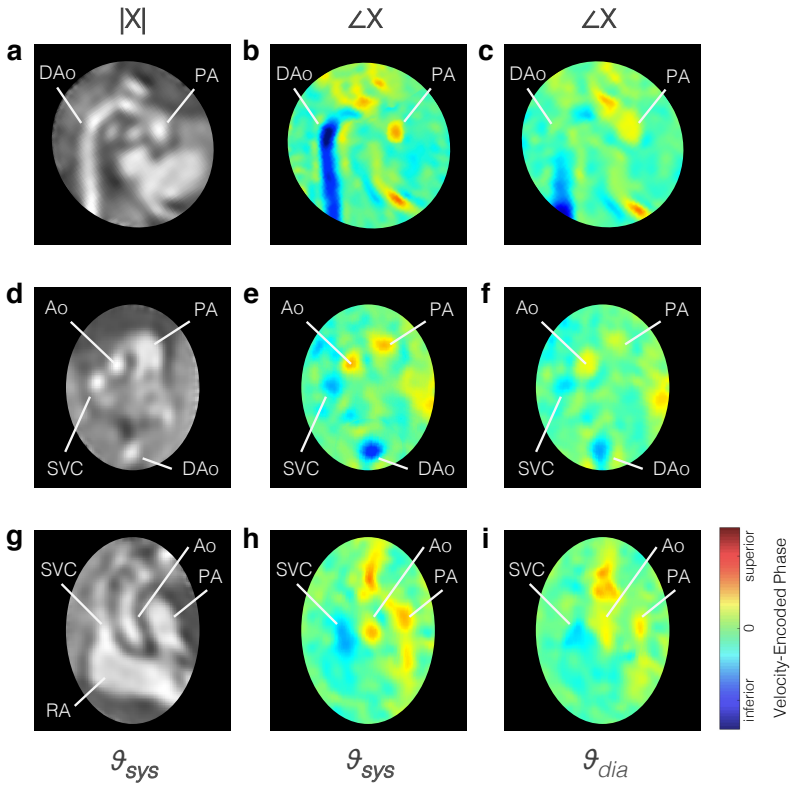


**Figure 5.18:** Pseudo 4D velocity mapping in a healthy $30^{+3}$ week gestational age fetus (ID02). Complex-valued cine volume magnitude, $|\mathbf{X}|$, and velocity-encoded phase, $\angle\mathbf{X}$, are shown in (**a**)-(**c**) sagittal aortic arch plane, (**d**)-(**f**) three vessel view and (**g**)-(**i**) coronal plane perpendicular to three vessel view. The phase of the reconstructed cine volume was most sensitive to velocities in the fetal superior-inferior direction, perpendicular to the target stack acquired transverse to the fetal trunk. Flow in the inferior direction (blue), is seen in the descending aorta (DAo) and superior vena cava (SVC), while flow in the superior direction (red) is seen in the ascending aorta (Ao) and pulmonary artery (PA). Peak flows can be seen in systole, $\vartheta_{sys}$, with reduced flow during diastole, $\vartheta_{dia}$. The right atrium (RA) is labelled in (g) for reference. The fetal heart is oriented in radiological convention with double-oblique planes shown using spatial B-spline interpolation to avoid voxel distortion.

## 5.5 Conclusions

Fetal cardiac MRI is a challenge due to the small size of the fetal heart, the rapid heart beat, and motion. The aim of this work was to develop an acquisition and reconstruction framework to generate a three-dimensional representation of the fetal cardiovascular system in utero using MRI. This was achieved using a highly-accelerated multi-planar dynamic acquisition combined with retrospective motion correction, cardiac synchronisation, outlier rejection and volumetric cine reconstruction in the image domain. The motion-tolerant framework did not require maternal breath-hold or precise scan planning during acquisition, and reconstruction was fully automated aside from user-specified masks of the fetal heart and chest. The framework proved to be robust when used on fetal data and successfully generated good quality cine volumes in all eleven fetal cases studied. The use of image-domain motion correction methods conferred significant advantages in terms of outlier rejection and the ability to accommodate quite large fetal motion, but had the downside of presenting major challenges for increasing the spatial and temporal resolution of the dynamic MR acquisition. Reconstructions from simulated MR images confirmed that correct spatial and temporal features could be reliably recovered, though there was some blurring due to the spatio-temporal resolution of the acquired dynamic images and a subtle signal intensity ringing effect at the blood-myocardium boundary of unknown origin.

Experts had an overall high confidence in a comprehensive evaluation of the fetal heart using reconstructed cine volumes. There was sufficient potential for diagnostic value that, in the three months following the fetal cases presented in this study, data was collected for clinical rather than research purposes in 8 of 30 fetal cardiac cases scanned. These included seven fetal singletons and one fetal twin (gestational age $23^{+5}$ to $32^{+1}$) with a variety of cardiac conditions including abnormal arch anatomy, cardiac tumour, common arterial trunk, septal defects, stenoses, congenitally-corrected transposition of the great arteries and dextrocardia.

A preliminary assessment of a velocity-sensitive volume reconstruction using the velocity information encoded in the phase of dynamic bSSFP acquisitions yielded promising initial results, suggesting the potential for simultaneous reconstruction of a three-dimensional cine and fully-encoded velocity maps from multi-planar dynamic MRI. The proposed methods show promise as a framework for fully-motion compensated 3D assessment of the fetal heart and great vessels.

# Notation

### Indices

| | |
|---|---|
| $j$ | image voxel spatial coordinates |
| $k$ | image frame |
| $l$ | slice, i.e., set of image frames at one slice location $\{k\}_{k\in l}$ |
| $i$ | volume voxel spatial coordinates |
| $h$ | cine cardiac phase |
| $N_j$ | number of voxels in image frame $k$ |
| $N_k$ | number of image frames |
| $N_i$ | number of voxels in volume |
| $N_h$ | number of cardiac phases in cine volume |

### Multi-Planar Dynamic MRI

| | |
|---|---|
| $\mathrm{Y}_k$ | dynamic MR image |
| $y_{jk}$ | voxel in $\mathrm{Y}_k$ |
| $\mathrm{t}_k$ | acquisition time of image frame $k$ |
| $\mathbf{Y}$ | set of all $\mathrm{Y}_k$, i.e., $\{\mathrm{Y}_k\}_{k=1,\ldots,N_k}$ |
| $\mathbf{Y}_l$ | set of all $\mathrm{Y}_k$ at slice location $l$, i.e., $\{\mathrm{Y}_k\}_{k\in l}$ |
| $\overline{\mathrm{Y}}_l$ | temporal mean of all $\mathrm{Y}_k$ at slice location $l$ |

### Cine Volume Reconstruction

| | |
|---|---|
| $\mathsf{X}_h$ | 3D volume |
| $x_{ih}$ | voxel in $\mathsf{X}_h$ |
| $\mathbf{X}$ | cine volume, i.e., $\{\mathsf{X}_h\}_{h=1,\ldots,N_h}$ |
| $\vartheta_h$ | cardiac phase of volume $h$ |
| $\mathsf{Y}_k^*$ | intensity corrected dynamic image frame |
| $\widehat{\mathsf{Y}}_k$ | dynamic image frame simulated from $\mathbf{X}$ |
| $\mathsf{E}_k$ | error between $\mathsf{Y}_k^*$ and $\widehat{\mathsf{Y}}_k$ |
| $e_{jk}$ | voxel-wise error |
| $w_{ij}^{hk}$ | spatio-temporal weight relating $y_{jk}^*$ and $x_{ih}$ |
| $m_{ij}^{k}$ | spatial weight |
| $d^{hk}$ | temporal weight |
| $\mathsf{R}_l$ | 2D mask of fetal heart in slice $l$ |
| $\mathsf{R}_{\text{heart}}$ | 3D mask of fetal heart |
| $\mathsf{R}_{\text{chest}}$ | 3D mask of fetal chest |
| $\lambda$ | adaptive regularisation controlling parameter |
| $\delta$ | adaptive regularisation edge scaling parameter |
| $n_{MC}$ | motion correction iteration |
| $N_{MC}$ | number of motion correction iterations |
| $n_{SR}$ | super-resolution iteration |
| $N_{SR}$ | number of super-resolution iterations |

### Outlier Rejection

| | |
|---|---|
| $\mathbb{P}(e)$ | likelihood of observing error $e$ |
| $p_{jk}^{voxel}$ | posterior probability that $y_{jk}$ is an inlier |
| $\mathsf{P}_k^{voxel}$ | image map of voxel-wise probabilities |
| $q_k$ | potential of $\mathbf{Y}_k$ |
| $\mathbb{P}(q)$ | likelihood of observing potential $q$ |
| $p_k^{frame}$ | posterior probability that $\mathsf{Y}_k$ is an inlier |
| $\mathsf{P}_k$ | 2D probability map with $p_{jk} = p_{jk}^{voxel} p_k^{frame}$ |

**Motion Correction**

| | |
|---|---|
| $A_k$ | rigid transformation matrix aligning $Y_k$ with $\mathbf{X}$ |
| $\mathbf{A}$ | set of all transformations, i.e., $\{A_k\}_{k=1,\ldots,N_k}$ |
| $\mathbf{A}_l$ | set of all $A_k$ for slice location $l$, i.e., $\{A_k\}_{k\in l}$ |
| $A_l$ | probability-weighted average slice transformation |

**Cardiac Synchronisation**

| | |
|---|---|
| $t_l^{RR}$ | estimated R-R interval for slice $l$ |
| $\theta_k$ | cardiac phase of $\mathbf{Y}_k$ |
| $\boldsymbol{\theta}$ | set of all $\theta_k$, i.e., $\{\theta_k\}_{k=1,\ldots,N_k}$ |
| $\mathbf{X}_l$ | cine volume reconstructed using $\mathbf{Y}_l = \{Y_k\}_{k\in l}$ |
| $\mathbf{V}_l$ | volume weights, i.e., weighted contribution of $\mathbf{Y}_l$ in volume space |

**Simulation**

| | |
|---|---|
| $\chi$ | numerically simulated cine volume with high spatio-temporal resolution |
| $\boldsymbol{\theta}^*$ | true cardiac phases of $\mathbf{Y}$ simulated from $\chi$ |
| $\mathbf{A}^*$ | true transformation of $\mathbf{Y}$ simulated from $\chi$ |
| $\mathbf{X}^*$ | cine volume reconstructed using $\boldsymbol{\theta}^*$ and $\mathbf{A}^*$ |
| $\chi^*$ | $\chi$ resampled to the resolution of $\mathbf{X}$ |

# Chapter 6

# Conclusions

This chapter concludes the thesis with a summary of the research presented in previous chapters (§6.1), followed by a discussion of concurrent developments in fetal cardiac MR imaging (§6.2) and potential future directions of the work in this thesis (§6.3), and closes with some concluding remarks (§6.4).

## 6.1 Summary

Fetal cardiac MRI is particularly challenging due to the size and complexity of the heart, rapid heart beat and fetal motion. If these challenges can be overcome, MRI has the potential to provide multi-planar and volumetric images, allowing for unique perspectives of the anatomy of the fetal heart and an increased role in clinical screening for structural anomalies as an adjunct to ultrasound.

This thesis explored the use of motion-corrected MRI to visualise the fetal heart and great vessels in utero. The aim of this work was to develop a dynamic MRI acquisition and image-domain cine reconstruction strategy to depict the fetal heart in the presence of maternal and fetal motion. Rapid dynamic imaging was performed with a balanced steady state free precession sequence using a 2D Cartesian trajectory and uniform k-t under-sampling, with k-t SENSE reconstruction. Retrospective image-based methods for cardiac synchronisation and motion correction were used to align dynamic images according to cardiac phase and spatial position. Dynamic images were then combined to generate a cine image series. Outlier rejection was integrated with cine reconstruction to reduce the influence of inconsistent data and

image artefacts arising from pronounced fetal movements.

### 2D Cine Reconstruction from Single-Slice Dynamic MRI

This approach was first established for 2D cine reconstruction from single-slice dynamic MRI, as described in Chapter 4. The implemented 2D framework was entirely automated, aside from a user-defined region of interest delineating the fetal heart. Cardiac synchronisation, motion correction and outlier rejection steps were performed followed by cine reconstruction. The entire sequence of steps was repeated a number of times until the process converged. The nominal resolution of the resulting cine images was the same as the acquired dynamic images, 2×2×6 mm and ~72 ms.

The framework was evaluated in 30 mid- to late-gestational age singleton fetuses, including 23 cases with congenital heart disease, scanned without maternal breath-hold in one or more planes. Artefact-free cine images were successfully produced in 36 of 39 acquired data sets, while prolonged fetal movements precluded processing of the remaining three. Image quality was assessed by two expert reviewers on a five point scale, from 0 to 4, resulting in a median combined score of 2.5 across all cases. The combination of complementary acquisition/reconstruction and correction/rejection steps in the framework served to improve the quality of the reconstructed 2D cine images, resulting in increased visibility of small, dynamic anatomic features compared to reconstructions that omitted one or both of the motion correction or outlier rejection steps. The 2D framework corrected for in-plane displacement of the fetal heart, but could only deal with through-plane motion by rejecting data.

### 3D Whole-Heart Cine Reconstruction from Multi-Planar Dynamic MRI

In Chapter 5, a 3D framework was developed, building on the 2D work, to accommodate motion in three dimensions and generate volumetric cine images from multi-planar 2D dynamic MRI acquired in a 3–6 different scan plane orientations. The 3D framework used an initial motion correction stage for rough spatial alignment between 2D slices, followed by cardiac synchronisation, first within each slice and then between slices. Subsequently, 3D cine reconstruction including outlier rejection was interleaved with further motion correction and repeated a number of times to ensure convergence. No maternal breath-hold or precise scan planning was required during acquisition, and the reconstruction process was fully automated aside from user-specified masks of the fetal heart and chest. The nominal resolution of

the resulting cine volumes was 2×2×2 mm and ~72 ms.

The 3D framework was optimised and validated using a numerical phantom simulation and evaluated in a study of eleven mid- to late-gestational age singleton fetuses, including 8 cases with structural cardiac anomalies. The framework proved to be robust when used on fetal data and successfully generated good quality cine volumes from all fetal data. Displacements estimated in the 3D framework (11 data sets, median displacement 5.8 mm, range 2.8–12.2 mm) were much higher compared to the in-plane displacements estimated in the 2D work (36 data sets, maximum displacement 2.3 mm) since motion was also corrected in the through-plane direction. The 3D cine data could be visualised in any 2D plane with full coverage of the heart and great vessels, allowing for optimal views of complex anatomy and facilitating understanding of spatial relationships between cardiovascular structures. A comprehensive evaluation of the features of the fetal heart depicted in the reconstructed cine volumes was performed by three experienced reviewers on a five point scale, from 0 to 4. Scores were high for all fetal cases (median combined score 3.4), indicating that the 3D cine images were of adequate quality to determine most anatomical details, though lower scores were given for small, complex anatomical features such as pulmonary venous connections (mean combined score 2.6) and arch anatomy (mean combined score 2.9).

MRI cine volumes were compared with matched prenatal 2D and 3D ultrasound images, acquired within three days of MRI examination, confirming accurate anatomic representation based on visual assessment. While valves and other small and rapidly moving anatomy were more visible in the ultrasound images, cardiac anatomy was occasionally obscured by artefact from acoustic shadowing and motion. By contrast, the MRI volumes provided artefact-free coverage of the entire heart with good contrast between blood and myocardium, but lacked detail in valves and other very small, rapidly moving anatomy.

A preliminary evaluation of complex-valued volume reconstruction using the velocity information encoded in the phase of dynamic bSSFP acquisitions yielded promising initial results, suggesting the potential for simultaneous reconstruction of a three-dimensional cine and multi-dimensional velocity maps.

## 6.2 Concurrent Developments

There have been a number developments in fetal cardiac MR imaging in the past three years, most notably the commercial availability of a Doppler ultrasound gating device and the use of compressed sensing reconstruction and continuous golden-angle radial sampling. This section discusses these and other developments concurrent with work produced in this thesis.

### Doppler Ultrasound Cardiac Gating

There has been increased use of the Doppler ultrasound device for fetal cardiac gating in recent years following from improvements in the hardware and safety testing [191]. Doppler ultrasound gating has been used in a cine imaging study of fifteen human fetal subjects [180]. A device is now available commercially (northh medical GmbH, Hamburg, Germany) and has been used by other groups in studies of cardiac-gated fetal MR [192, 193].

### Compressed Sensing

Compressed sensing (§3.6.5) has been used to achieve increased acceleration in time-resolved cine imaging techniques.

In the initial application of metric optimised gating (MOG) for fetal cardiac cine imaging by Roy *et al.* [65], regular Cartesian under-sampling was used with GRAPPA cine image reconstruction to accelerate the acquisition by R = 2. Building on that initial work, they employed a random Cartesian sampling strategy in combination with compressed sensing cine image reconstruction to achieve acceleration factors as high as R = 2–4 [194], with some temporal blurring noted at R = 4. The joint compressed sensing reconstruction enforces the sparsity of the spatial total variation and the temporal Fourier transform of the cine image series as well as the MOG entropy metric.

## Continuous Golden-Angle Radial Sampling

Unlike a segmented Cartesian cine acquisition, data acquired with a continuous golden-angle radial trajectory (§3.3.2) can be used to reconstruct both a dynamic image series and a cine image series from the same data. This can be advantageous in fetal cardiac cine MR imaging, as information about periodic and spontaneous motion can be obtained from the dynamic images and then used to reconstruct the cine images, as has been done in adult cardiac MRI [138]. This trajectory has been employed in studies from three separate groups; Roy *et al.* [195], Haris *et al.* [192, 196] and Chaptinel *et al.* [197]. In all three studies, image reconstruction was performed using compressed sensing, enforcing spatial and temporal total variation in combination with additional sparsifying transformations.

### Cardiac Synchronisation

MOG [63] and self-gating [188] techniques were adopted in these studies using continuous golden-angle radial sampling. In each case, the cardiac phase of each radial k-space spoke was estimated and then spokes were grouped according to cardiac phase to allow reconstruction of a cine image series.

Roy *et al.* [195] acquired 3000 spokes (~15 s) and reconstructed dynamic images with a temporal resolution of ~74 ms. MOG was applied directly to the dynamic images to estimate the cardiac phase of each spoke.

Haris *et al.* [196] acquired 4000 spokes (~16 s) using a tiny golden angle increment and used the $k_0$ value of each spoke as a zero-dimensional cardiac self-gating signal. No dynamic images were reconstructed. The cardiac phase of each spoke was derived from a principal component analysis of the signal.

Chaptinel *et al.* [197] acquired 1600 spokes (~7 s) and reconstructed dynamic images with a temporal resolution of ~62 ms. Cross-correlation between dynamic images was then used to establish cardiac synchronisation.

### Motion Compensation

Various strategies were used in these studies to minimise, estimate and compensate for motion.

Maternal breath-hold was used by Haris *et al.* [196] and Chaptinel *et al.* [197] to

mitigate displacement of the fetal heart due to maternal respiration.

In the methods proposed by Roy *et al.* [195] and Chaptinel *et al.* [197], the dynamic image series was used to manually identify periods of significant fetal motion so that data acquired during those periods could be rejected, an improvement on the common strategy in fetal MRI of monitoring image quality during the MR scanning session and repeating an entire sequence when motion corruption is observed.

Roy *et al.* [195] performed scans during maternal free-breathing and used the dynamic image series to estimate the rigid in-plane displacement of the fetal heart and compensate for the displacement in k-space using the Fourier shift theorem. In follow-up work presented by Haris *et al.* [192] using Doppler ultrasound gating and maternal free-breathing, a similar approach to motion-compensation was adopted where rigid in-plane displacement was estimated from low temporal resolution dynamic images. Spokes with displacements that were approximately translation were corrected in k-space, while the remainder were rejected.

The results of these studies are impressive, particularly the flexibility of continuous golden angle radial sampling and the resolution achieved, however characterising and compensating for fetal and maternal motion remains a significant challenge as motion across the entire FOV must be dealt with prior to or during cine MR image reconstruction.

## Evaluation

In addition to methodological developments, recent studies have included evaluation of the proposed techniques against other imaging modalities and techniques.

In the work by Chaptinel *et al.* [197], MRI was compared with echocardiography in six fetal subjects. Anatomical measurements were made in the four chamber, short axis and three vessel views. Good agreement between the modalities and low inter- and intra-observer variability was found.

In a precursor to the published method using MOG and radial sampling, Roy *et al.* presented a comparison of cine imaging using the same technique with static images reconstructed from the same data to evaluate the utility of cine imaging in the assessment of congenital heart disease [198]. A stack of ten parallel slices spanning the heart were acquired in four late-gestational age fetuses with congenital heart disease. Cine and static images were scored by an expert reviewer in terms of various cardiac structures, resulting in higher scores overall for cine images, par-

ticularly when static images were corrupted by fetal motion.

Haris *et al.* [196] compared their golden-angle radial cine imaging method with Cartesian sampled MOG [65]. Data was acquired in five healthy third-trimester fetuses and cine images were assessed by two expert reviewers in terms of qualitative scores and quantitative measurements showing some marginal, but non-significant, improvement using the radial approach.

In the work presented in this thesis, results were evaluated qualitatively by expert scoring of 2D and 3D cine images was performed and comparison with ultrasound. It would have been satisfying to also include a comparison with one or more of the 2D cine imaging methods mentioned above, however, the incompatible acquisition strategies precluded direct comparison, particularly in the case of radial sampling. That being said, it may be possible to use the regularly under-sampled Cartesian k-t data acquired for the studies presented in Chapters 4 or 5 in a compressed sensing MOG reconstruction [194] if the periodicity of the fetal heart and k-t sampling are asynchronous to result in a sufficiently random sampling of k-space. However, this has not been investigated since radial sampling appears to be the leading approach at this time. While data acquired in separate scans could be used for comparison, motion between scans will likely lead to unique differences between the two sets of data. Furthermore, there are currently no fetal volumetric cine MR imaging methods or 3D motion correction techniques for comparison.

## Phase Contrast Flow Imaging

Lastly, it's worth noting recent development in fetal cine phase contrast MRI. The utility of the compressed sensing methods used for Cartesian cine imaging with MOG [194] to accelerate cine phase contrast MRI [199], showing accurate flow measurements for retrospective under-sampling up to $R = 6$. The golden-angle radial work of Roy *et al.* [195] was combined with 3D velocity-encoded cine phase contrast MRI to assess mutli-dimensional flow in a single slice in two fetal subjects [200]. More conventional 4D flow has also been presented, both in a phantom setup and two fetal subjects using Doppler ultrasound gating [201], though the data is prone to motion artefact as the scan duration is long (~150 s) and no motion compensation was used.

## 6.3 Future Directions

There are three areas where future work could be focused to build on the framework for volumetric cine imaging of the heart presented in this thesis: improvement of the current methods, extension to include phase-velocity in the framework and application of the method in postnatal subjects.

A variety of potential improvements to the methods proposed in this thesis have been discussed in detail in Sections 4.5 and 5.4, with potential gains in resolution and fidelity, as well as reduced scan duration and decreased reliance on prior data and manual input. In addition, it would be interesting to see if new fetal-specific receiver coil arrays [202, 203] and the cardiac signal from a Doppler ultrasound gating device (§6.2) would be of benefit.

Extending the cine volume reconstruction framework to include phase information may allow for simultaneous reconstruction of cine volumes and multi-dimensional velocity maps, as noted in Secion 5.4.1. This would require the framework to take complex-valued dynamic images as input and produce a cine volume with four components for each voxel (i.e., velocity in three orthogonal directions, in addition to a magnitude), similar to 4D flow MRI data. Even if the velocity results are not of interest, the use of phase information may increase the quality of reconstructed cine volumes and improve the ability of outlier detection to identify inconsistent data.

The methods presented in this thesis may have potential applications in postnatal cardiac MRI. The motion-tolerant framework may be particularly beneficial in neonatal and paediatric patients where involuntary movements and breathing can be problematic. In adult patients, retrospective volumetric reconstruction from 2D MRI could be used as an alternative to 3D acquisition as 3D spin echo black-blood imaging can suffer from motion and susceptibility artefact while 3D bSSFP bright-blood imaging has reduced signal contrast compared to 2D bSSFP.

## 6.4 Concluding Remarks

This thesis described the unique challenges of fetal cardiac imaging and explored the potential of MRI to depict the fetal heart in utero as an adjunct to ultrasound for screening of structural cardiac anomalies. Targeted solutions to these challenges were developed that take advantage of the strengths of MRI while addressing the limitations of the modality in the context of fetal imaging, culminating in a motion-

tolerant framework for volumetric representation of the fetal cardiovascular system. This framework combined rapid dynamic acquisition with retrospective cardiac synchronisation and motion correction. A dynamic Cartesian k-t SENSE acquisition was used to maximise the temporal resolution of the acquisition while minimising spatiotemporal regularisation in the reconstructed images. Image space volume reconstruction made it possible to correct for movement of the fetal heart in isolation, separate from extraneous motion elsewhere in the field of view. The impact of motion-corrupted data on the reconstructed volume was limited by weighting all data according to a robust statistic that effectively rejected data acquired corrupted by motion.

The framework was applied in eleven mid- to late-gestational age fetuses, with successful results in all cases. This is the first time that volumetric depiction of the fetal heart and great vessels in utero has been achieved using motion-corrected MRI. The three dimensional aspect of these volumes allowed for interpretation of the arrangement and complex connections of the cardiac chambers and vessels, while the temporal cine aspect improved the depiction of pulsatile anatomy. In the future it may be possible to simultaneously reconstruct velocity maps from these same data, yielding volumes similar to 4D flow MRI. These preliminary results suggest this is a promising framework for fully-motion compensated 3D whole-heart cine fetal MRI.

# Publications and Software

## Publications

### Journal Articles

Lloyd DFA, van Amerom JFP, Pushparajah K, Simpson JM, Zidere V, Miller O, Sharland G, Allsop JM, Fox MJ, Lohezic M, Murgasova M, Malamateniou C, Hajnal JV, Rutherford MA, Razavi R. **An exploration of the potential utility of fetal cardiovascular MRI as an adjunct to fetal echocardiography**. Prenatal Diagnosis. 2016;36:916–925. doi: 10.1002/pd.4912.

van Amerom JFP, Lloyd DFA, Price AN, Kuklisova Murgasova M, Aljabar P, Malik SJ, Lohezic M, Rutherford MA, Pushparajah K, Razavi R, Hajnal JV. **Fetal cardiac cine imaging using highly accelerated dynamic MRI with retrospective motion correction and outlier rejection**. Magnetic Resonance in Medicine. 2018;79:327–338. doi: 10.1002/mrm.26686.

van Amerom JFP, Lloyd DFA, Murgasova MK, Price AN, Malik SJ, Schneider T, Van Poppel M, Pushparajah K, Rutherford MA, Razavi R, Hajnal JV. **Fetal whole-heart 3D cine reconstruction from motion-corrected 2D dynamic imaging**. 2018. *in preparation*.

Lloyd DFA, Pushparajah K, Simpson JM, van Amerom JFP, Van Poppel M, Schulz A, Kainz B, Kuklosova-Murgasova M, Lohezic M, Allsop JM, Mathur S, Bellsham-REvell H, Vigneswaran T, Charakida M, Miller O, Zidere V, Sharland G, Rutherford MA, Hajnal JV, Razavi R. **High-resolution 3D visualisation of fetal congenital heart disease using prenatal MRI with motion corrected slice-volume registration**. The Lancet. 2018. *in submission*.

## Conference Presentations

van Amerom JFP, Price AN, Aljabar P, Malik SJ, Malamateniou C, Pushparajah K, Allsop JM, Fox MJ, Rutherford MA, Razavi R, Hajnal JV, **Fetal cardiac cine imaging using realtime MRI and image-based spatiotemporal motion-correction**. Proceedings of The European Society for Magnetic Resonance in Medicine and Biology Congress, 2015;S85–86.
doi: 10.1007/s10334-015-0487-2.

van Amerom JFP, Kuklisova Murgasova M, Price AN, Malik SJ, Aljabar P, Lloyd DFA, Pushparajah K, Lohezic M, Fox MJ, Allsop JM, Rutherford MA, Razavi R, Hajnal JV. **Fetal cardiac cine imaging from motion-corrected super-resolution reconstruction of highly-accelerated real-time MRI**. Proceedings of The International Society for Magnetic Resonance in Medicine Annual Meeting. 2016;0458. *Summa Cum Laude* merit award.
url: cds.ismrm.org/ protected/16MPresentations/ abstracts/0458.html.

Lloyd DFA, Kainz B, van Amerom JFP , Pushparajah K, Lloyd, Simpson JM, Zidere V, Miller O, Sharland GK, Zhang T, Lohezic M, Allsop JM, Fox JM, Malamateniou C, Rutherford MA, Hajnal JV, Razavi R. **Three-Dimensional Modelling of the Fetal Vasculature from Prenatal MRI using Motion-Corrected Slice-to-Volume Registration**. Proceedings of The International Society for Magnetic Resonance in Medicine Annual Meeting. 2016;1677.
url: cds.ismrm.org/ protected/16MPresentations/ abstracts/1677.html.

Lohezic M, van Amerom JFP, Pegoretti K, McCabe L, Malamateniou C, Carney O, Fox M, Allsop J, Hajnal JV. **A reasoned approach to explore single shot FSE acquisition for fetal MRI**. Proceedings of The International Society for Magnetic Resonance in Medicine Annual Meeting. 2016;3888.
url: cds.ismrm.org/protected/16MPresentations/abstracts/3888.html.

van Amerom JFP, Lloyd DA, Murgasova MK, Price AN, Malik J, Aljabar P, Allsop JM, Gomes A, Rutherford MA, Pushparajah K, Razavi R, Hajnal JV. **Fetal cardiac volume reconstruction from motion-corrected multi-slice dynamic MRI**. Proceedings of The International Society for Magnetic Resonance in Medicine Annual Meeting. 2017;3263.
url: cds.ismrm.org/protected/17MPresentations/abstracts/3263.html.

Lloyd DFA, van Amerom JFP, Murgasova M, Kainz B, Pushparajah K, Rutherford M, Hajnal JV, Razavi R. **Insights from comprehensive fetal cardiovascular MRI assessment using 3D motion-correction and metric-optimised gated phase contrast in cases of suspected coarctation of the aorta**. Proceedings of The International Society for Magnetic Resonance in Medicine Annual Meeting. 2017;3261.
url: cds.ismrm.org/protected/17MPresentations/abstracts/3261.html.

Ruijsink B, Puyol-Antón E, Usman M, van Amerom JFP, Duong P, Forte MNV, Pushparajah K, Frigiola A, Nordsletten DA, King AP, Razavi R. **Semi-automatic Cardiac and Respiratory Gated MRI for Cardiac Assessment During Exercise**. Proceedings of the International Workshop on Reconstruction and Analysis of Moving Body Organs. 2017;86–95.
doi: 10.1007/978-3-319-67564-0_9.11.

van Amerom JFP, Lloyd DFA, Murgasova MK, Price AN, Malik SJ, Van Poppel M, Pushparajah K, Rutherford MA, Razavi R, Hajnal JV. **Fetal whole-heart 3D cine reconstruction using motion-corrected multi-slice dynamic imaging**. Proceedings of The International Society for Magnetic Resonance in Medicine Annual Meeting. 2018;1052. *Summa Cum Laude* merit award.
url: cds.ismrm.org/protected/18MPresentations/abstracts/1052.html.

Jackson LH, Price AN, Hutter J, Cordero-Grande L, Ho A, Slator PJ, Santo A, van Amerom JFP, Murgasova M, McCabe L, Rutherford MA, Hajnal JV. **Respiration resolved imaging using continuous steady state multiband excitation with linear frequency sweeps**. Proceedings of The International Society for Magnetic Resonance in Medicine Annual Meeting. 2018;4134.
url: cds.ismrm.org/protected/18MPresentations/abstracts/4134.html.

# Software

**fetal_cmr_cine_2d** 2D cine reconstruction from single-slice dynamic MRI (§4.5) implemented in MATLAB (Mathworks, Natick, USA). Includes methods for k-t SENSE MR image reconstruction, cardiac synchronisation, motion correction, outlier rejection and cine image series reconstruction.
repository: github.com/jfpva/fetal_cmr_cine_2d

**m2d_dyn_interleaved** Pulse sequence modifications of Philips R5.1.7 software (Philips, Best, Netherlands) to perform multi-2D k-t acquisition (§5.2.5).
repository: dhcpgit.isd.kcl.ac.uk:philips-ppe-R5.

**ktrecon** K-t SENSE reconstruction for Philips multi-2D dynamic MRI data (§5.2.5), implemented in MATLAB (Mathworks, Natick, USA) using some of the functionality of ReconFrame 3.0.535 (GyroTools, Zurich, Switzerland).
repository: github.com/jfpva/ktrecon.git.

**fetal_cmr_cine_3d** Heart rate estimation and slice-slice cardiac synchronisation (§5.2.4) implemented in MATLAB (Mathworks, Natick, USA).
repository: github.com/jfpva/fetal_cmr_cine_3d.git.

**IRTK** 3D motion correction (§5.2.3), cine volume reconstruction and outlier rejection (§5.2.2), implemented in C++ with the Image Registration Toolkit (IXICO, London, United Kingdom), building on the frame-work for reconstruction of fetal brain volumes from 2D MRI implemented by Kuklisova *et al* [91].
repository: gitlab.com/mariadeprez/irtk.git.

# Bibliography


[1] A. Moorman, S. Webb, N. A. Brown, W. Lamers, and R. H. Anderson, “Development of the heart: (1) formation of the cardiac chambers and arterial trunks.,” *Heart (British Cardiac Society)*, vol. 89, pp. 806–14, 7 2003.

[2] A. C. Cook, R. W. Yates, and R. H. Anderson, “Normal and abnormal fetal cardiac anatomy,” *Prenatal Diagnosis*, vol. 24, no. 13, pp. 1032–1048, 2004.

[3] D. T. Ginat, M. W. Fong, D. J. Tuttle, S. K. Hobbs, and R. C. Vyas, “Cardiac Imaging: Part 1, MR Pulse Sequences, Imaging Planes, and Basic Anatomy,” *American Journal of Roentgenology*, vol. 197, pp. 808–815, 10 2011.

[4] O. Uzun, B. K. Balcı, G. Goynumer, and O. Uzun, “Recognition of Normal Fetal Cardiac Structures,” *Journal of Fetal Medicine*, vol. 3, pp. 109–119, 9 2016.

[5] R. Oberhoffer, J. Högel, and D. Lang, “Normal characteristics of cardiac dimensions and function in the fetus,” *European Journal of Ultrasound*, vol. 2, pp. 93–106, 4 1995.

[6] C. Schneider, B. W. McCrindle, J. S. Carvalho, L. K. Hornberger, K. P. McCarthy, and P. E. F. Daubeney, “Development of Z-scores for fetal cardiac dimensions from echocardiography.,” *Ultrasound in Obstetrics & Gynecology*, vol. 26, pp. 599–605, 11 2005.

[7] S. Pildner von Steinburg, A.-L. Boulesteix, C. Lederer, S. Grunow, S. Schiermeier, W. Hatzmann, K.-T. M. Schneider, and M. Daumer, “What is the ”normal” fetal heart rate?,” *PeerJ*, vol. 1, p. e82, 2013.

[8] M. R. Ortiz, S. D. Aguilar, J. Alvarez-Ramirez, A. Martínez, C. Vargas-Garcia, R. González-Camarena, and J. C. Echeverría, “Prenatal RR fluctuations dynamics: detecting fetal short-range fractal correlations,” *Prenatal Diagnosis*, vol. 26, pp. 1241–1247, 12 2006.

[9] J. P. De Wilde, A. W. Rivers, and D. L. Price, “A review of the current use of magnetic resonance imaging in pregnancy and safety implications for the fetus.,” *Progress in biophysics and molecular biology*, vol. 87, pp. 335–53, 1 2005.

[10] A. Piontelli, *Development of Normal Fetal Movements*. Milano: Springer Milan, 2015.

[11] T. T. a. Hayat, A. Nihat, M. Martinez-Biarge, A. McGuinness, J. M. Allsop, J. V. Hajnal, and M. a. Rutherford, “Optimization and initial experience of a multisection balanced steady-state free precession cine sequence for the assessment of fetal behavior in utero.,” *American Journal of Neuroradiology*, vol. 32, pp. 331–8, 2 2011.

[12] S. C. Mitchell, S. B. Korones, and H. W. Berendes, “Congenital heart disease in 56,109 births. Incidence and natural history.,” *Circulation*, vol. 43, pp. 323–32, 3 1971.

[13] D. van der Linde, E. E. Konings, M. A. Slager, M. Witsenburg, W. A. Helbing, J. J. Takkenberg, and J. W. Roos-Hesselink, “Birth Prevalence of Congenital Heart Disease Worldwide: A Systematic Review and Meta-Analysis,” *Journal of the American College of Cardiology*, vol. 58, pp. 2241–2247, 11 2011.

[14] B. G. Bruneau, “The developmental genetics of congenital heart disease.,” *Nature*, vol. 451, pp. 943–8, 2 2008.

[15] L. Allan, B. Benacerraf, J. a. Copel, J. S. Carvalho, R. Chaoui, S. H. Eik-Nes, E. Tegnander, U. Gembruch, J. C. Huhta, G. Pilu, J. Wladimiroff, and S. Yagel, “Isolated major congenital heart disease.,” *Ultrasound in Obstetrics & Gynecology*, vol. 17, pp. 370–9, 5 2001.

[16] C. Wren, Z. Reinhardt, and K. Khawaja, “Twenty-year trends in diagnosis of life-threatening neonatal cardiovascular malformations.,” *Archives of disease in childhood. Fetal and neonatal edition*, vol. 93, pp. 33–5, 1 2008.

[17] S. P. Miller, P. S. McQuillen, S. Hamrick, D. Xu, D. V. Glidden, N. Charlton, T. Karl, A. Azakie, D. M. Ferriero, a. J. Barkovich, and D. B. Vigneron, “Abnormal brain development in newborns with congenital heart disease.,” *The New England Journal of Medicine*, vol. 357, pp. 1928–38, 11 2007.

[18] J. I. E. Hoffman, “Congenital Heart Disease,” in *Essential Cardiology*, pp. 393–406, Totowa, NJ: Humana Press, 2005.

[19] J. I. Hoffman and S. Kaplan, “The incidence of congenital heart disease,” *Journal of the American College of Cardiology*, vol. 39, pp. 1890–1900, 6 2002.

[20] H. Isaacs, “Fetal and Neonatal Cardiac Tumors,” *Pediatric Cardiology*, vol. 25, pp. 252–273, 6 2004.

[21] M. C. Carrilho, G. Tonni, E. Araujo Júnior, and Júnior, “Fetal cardiac tumors: prenatal diagnosis and outcomes.,” *Revista Brasileira de Cirurgia Cardiovascular*, vol. 30, no. 1, pp. VI–VII, 2015.

[22] R. Freedom, K.-J. Lee, C. MacDonald, and G. Taylor, “Selected Aspects of Cardiac Tumors in Infancy and Childhood,” *Pediatric Cardiology*, vol. 21, pp. 299–316, 7 2000.

[23] C. Mady, “Left Ventricular Diverticulum: Analysis of Two Operated Cases and Review of the Literature,” *Angiology*, vol. 33, pp. 280–286, 4 1982.

[24] M. Sklansky, “New dimensions and directions in fetal cardiology.,” *Current opinion in pediatrics*, vol. 15, pp. 463–71, 10 2003.

[25] L. D. Allan and I. C. Huggon, “Counselling following a diagnosis of congenital heart disease,” *Prenatal Diagnosis*, vol. 24, pp. 1136–1142, 12 2004.

[26] M. T. Donofrio, A. J. Moon-Grady, L. K. Hornberger, J. a. Copel, M. S. Sklansky, A. Abuhamad, B. F. Cuneo, J. C. Huhta, R. a. Jonas, A. Krishnan, S. Lacey, W. Lee, E. C. Michelfelder, G. R. Rempel, N. H. Silverman, T. L. Spray, J. F. Strasburger, W. Tworetzky, and J. Rychik, “Diagnosis and Treatment of Fetal Cardiac Disease: A Scientific Statement From the American Heart Association.,” *Circulation*, 4 2014.

[27] S. L. Collins and L. Impey, “Prenatal diagnosis: types and techniques.,” *Early human development*, vol. 88, pp. 3–8, 1 2012.

[28] AIUM, “Practice Guideline for the Performance of Fetal Echocardiography,” *Journal of Ultrasound in Medicine*, vol. 30, pp. 127–136, 1 2011.

[29] L. E. Hunter and J. M. Simpson, “Prenatal screening for structural congenital heart disease.,” *Nature Reviews. Cardiology*, vol. 11, pp. 323–34, 6 2014.

[30] S. J. Yoo, Y. H. Lee, K. S. Cho, and D. Y. Kim, “Sequential segmental approach to fetal congenital heart disease.,” *Cardiology in the young*, vol. 9, pp. 430–44, 7 1999.

[31] J. S. Carvalho, S. Y. Ho, and E. A. Shinebourne, “Sequential segmental analysis in complex fetal cardiac abnormalities: a logical approach to diagnosis,” *Ultrasound in Obstetrics and Gynecology*, vol. 26, pp. 105–111, 8 2005.

[32] C. van Velzen, S. Clur, M. Rijlaarsdam, C. Bax, E. Pajkrt, M. Heymans, M. Bekker, J. Hruda, C. de Groot, N. Blom, and M. Haak, “Prenatal detection of congenital heart disease-results of a national screening programme,” *BJOG: An International Journal of Obstetrics & Gynaecology*, vol. 123, pp. 400–407, 2 2016.

[33] M. Bensemlali, J. Stirnemann, J. Le Bidois, M. Lévy, F. Raimondi, E. Hery, B. Stos, B. Bessières, Y. Boudjemline, and D. Bonnet, “Discordances Between Pre-Natal and Post-Natal Diagnoses of Congenital Heart Diseases and Impact on Care Strategies,” *Journal of the American College of Cardiology*, vol. 68, pp. 921–930, 8 2016.

[34] U. M. Reddy, R. A. Filly, and J. A. Copel, “Prenatal imaging: ultrasonography and magnetic resonance imaging.,” *Obstetrics and gynecology*, vol. 112, pp. 145–57, 7 2008.

[35] M. S. Sklansky, T. R. Nelson, and D. H. Pretorius, “Three-dimensional fetal echocardiography: gated versus nongated techniques.,” *Journal of Ultrasound in Medicine*, vol. 17, pp. 451–457, 7 1998.

[36] G. R. DeVore, P. Falkensammer, M. S. Sklansky, and L. D. Platt, “Spatio-temporal image correlation (STIC): new technology for evaluation of the fetal heart.,” *Ultrasound in Obstetrics and Gynecology*, vol. 22, pp. 380–7, 10 2003.

[37] F. Guasina, F. Bellussi, G. Morganelli, G. Salsi, G. Pilu, and G. Simonazzi, “Electronic spatiotemporal image correlation improves four-dimensional fetal echocardiography,” *Ultrasound in Obstetrics & Gynecology*, vol. 51, pp. 357–360, 3 2018.

[38] C. Tanner, B. Flach, C. Eggenberger, O. Mattausch, M. Bajka, and O. Goksel, “Consistent reconstruction of 4D fetal heart ultrasound images to cope with fetal motion,” *International Journal of Computer Assisted Radiology and Surgery*, pp. 1–11, 6 2017.

[39] D. Maulik, N. C. Nanda, D. Maulik, and G. Vilchez, “A brief history of fetal echocardiography and its impact on the management of congenital heart disease,” *Echocardiography*, vol. 34, no. 12, pp. 1760–1767, 2017.

[40] U. Herberg, B. Steinweg, C. Berg, and J. Breuer, "Echocardiography in the Fetus – A Systematic Comparative Analysis of Standard Cardiac Views with 2D, 3D Reconstructive and 3D Real-Time Echocardiography," *Ultraschall in der Medizin - European Journal of Ultrasound*, vol. 32, pp. 293–301, 4 2010.

[41] F. Smith, F. MacLennan, D. Abramovich, I. MacGilivray, and J. Hutchison, "NMR imaging in human pregnancy: A preliminary study," *Magnetic Resonance Imaging*, vol. 2, pp. 57–64, 1 1984.

[42] S. M. McCarthy, R. A. Filly, D. D. Stark, P. W. Callen, M. S. Golbus, and H. Hricak, "Magnetic resonance imaging of fetal anomalies in utero: early experience.," *American Journal of Roentgenology*, vol. 145, pp. 677–82, 10 1985.

[43] Y. Patenaude, D. Pugash, K. Lim, L. Morin, S. Bly, K. Butt, Y. Cargill, G. Davies, N. Denis, G. Hazlitt, K. Naud, A. Ouellet, and S. Salem, "The use of magnetic resonance imaging in the obstetric patient.," *Journal of Obstetrics and Gynaecology Canada*, vol. 36, pp. 349–55, 4 2014.

[44] T. Wataganara, A. Ebrashy, L. D. Aliyu, R. A. Moreira de Sa, R. Pooh, A. Kurjak, C. Sen, A. Adra, and M. Stanojevic, "Fetal magnetic resonance imaging and ultrasound: report of the Working Group on Ultrasound in Obstetrics of the World Association of Perinatal Medicine," *Journal of Perinatal Medicine*, 1 2016.

[45] A. Gholipour, J. A. Estroff, C. E. Barnewolt, R. L. Robertson, P. E. Grant, B. Gagoski, S. K. Warfield, O. Afacan, S. A. Connolly, J. J. Neil, A. Wolfberg, and R. V. Mulkern, "Fetal MRI: A technical update with educational aspirations," *Concepts in Magnetic Resonance Part A*, 3 2015.

[46] M. Rutherford, S. Jiang, J. Allsop, L. Perkins, L. Srinivasan, T. Hayat, S. Kumar, and J. Hajnal, "MR imaging methods for assessing fetal brain development.," *Developmental neurobiology*, vol. 68, pp. 700–11, 5 2008.

[47] O. A. Glenn, "MR imaging of the fetal brain," *Pediatric Radiology*, vol. 40, pp. 68–81, 1 2010.

[48] U. M. Reddy, A. Z. Abuhamad, D. Levine, and G. R. Saade, "Fetal imaging: Executive Summary of a Joint Eunice Kennedy Shriver National Institute of Child Health and Human Development, Society for Maternal-Fetal Medicine, American Institute of Ultrasound in Medicine, American College of Obstetricians and Gynecolog," *American Journal of Obstetrics and Gynecology*, vol. 210, pp. 387–397, 5 2014.

[49] M. R. Plunk and T. Chapman, “The Fundamentals of Fetal MR Imaging: Part 1,” *Current Problems in Diagnostic Radiology*, pp. 1–16, 7 2014.

[50] M. R Plunk and T. Chapman, “The Fundamentals of Fetal Magnetic Resonance Imaging: Part 2.,” *Current problems in diagnostic radiology*, pp. 1–9, 6 2014.

[51] R. S. Loomba, S. Chandrasekar, P. H. Shah, and P. Sanan, “The developing role of fetal magnetic resonance imaging in the diagnosis of congenital cardiac anomalies: A systematic review,” *Annals of Pediatric Cardiology*, vol. 4, pp. 172–176, 7 2011.

[52] M. A. Fogel, R. D. Wilson, A. Flake, M. Johnson, D. Cohen, G. McNeal, Z.-Y. Y. Tian, and J. Rychik, “Preliminary investigations into a new method of functional assessment of the fetal heart using a novel application of ’real-time’ cardiac magnetic resonance imaging,” *Fetal Diagnosis and Therapy*, vol. 20, pp. 475–480, 1 2005.

[53] L. Manganaro, S. Savelli, M. Di Maurizio, A. Perrone, A. Francioso, L. La Barbera, P. Totaro, F. Fierro, A. Tomei, F. Coratella, A. Giancotti, L. Ballesio, and F. Ventriglia, “Assessment of congenital heart disease (CHD): is there a role for fetal magnetic resonance imaging (MRI)?,” *European Journal of Radiology*, vol. 72, pp. 172–80, 10 2009.

[54] G. Gorincour, B. Bourlière-Najean, B. Bonello, A. Fraisse, N. Philip, A. Potier, B. Kreitmann, and P. Petit, “Feasibility of fetal cardiac magnetic resonance imaging: preliminary experience.,” *Ultrasound in Obstetrics & Gynecology*, vol. 29, pp. 105–8, 1 2007.

[55] L. Manganaro, S. Savelli, M. Di Maurizio, A. Perrone, J. Tesei, A. Francioso, M. Angeletti, F. Coratella, D. Irimia, F. Fierro, F. Ventriglia, and L. Ballesio, “Potential role of fetal cardiac evaluation with magnetic resonance imaging: preliminary experience.,” *Prenatal diagnosis*, vol. 28, pp. 148–56, 2 2008.

[56] S. N. Saleem, “Feasibility of MRI of the fetal heart with balanced steady-state free precession sequence along fetal body and cardiac planes.,” *American Journal of Roentgenology*, vol. 191, pp. 1208–15, 10 2008.

[57] C. Votino, J. Jani, N. Damry, H. Dessy, X. Kang, T. Cos, L. Divano, W. Foulon, J. De Mey, and M. Cannie, “Magnetic resonance imaging in the normal fetal heart and in congenital heart disease.,” *Ultrasound in Obstetrics & Gynecology*, vol. 39, pp. 322–9, 3 2012.

[58] L. Gaur, L. Talemal, D. Bulas, and M. T. Donofrio, “Utility of fetal magnetic resonance imaging in assessing the fetus with cardiac malposition,” *Prenatal Diagnosis*, vol. 36, pp. 752–759, 8 2016.

[59] D. F. A. Lloyd, J. F. P. van Amerom, K. Pushparajah, J. M. Simpson, V. Zidere, O. Miller, G. Sharland, J. Allsop, M. Fox, M. Lohezic, M. Murgasova, C. Malamateniou, J. V. Hajnal, M. Rutherford, and R. Razavi, “An exploration of the potential utility of fetal cardiovascular MRI as an adjunct to fetal echocardiography,” *Prenatal Diagnosis*, vol. 36, no. 10, pp. 916–925, 2016.

[60] J. Neelavalli, U. Krishnamurthy, P. K. Jella, S. S. Mody, B. K. Yadav, K. Hendershot, E. Hernandez-Andrade, L. Yeo, M. D. Cabrera, E. M. Haacke, S. S. Hassan, and R. Romero, “Magnetic resonance angiography of fetal vasculature at 3.0 T.,” *European Radiology*, 5 2016.

[61] J. Yamamura, B. Schnackenburg, H. Kooijmann, M. Frisch, K. Hecher, G. Adam, and U. Wedegärtner, “High resolution MR imaging of the fetal heart with cardiac triggering: a feasibility study in the sheep fetus.,” *European Radiology*, vol. 19, pp. 2383–90, 10 2009.

[62] J. Yamamura, I. Kopp, M. Frisch, R. Fischer, K. Valett, K. Hecher, G. Adam, and U. Wedegärtner, “Cardiac MRI of the fetal heart using a novel triggering method: initial results in an animal model.,” *Journal of Magnetic Resonance Imaging*, vol. 35, pp. 1071–6, 5 2012.

[63] M. S. Jansz, M. Seed, J. F. P. van Amerom, D. Wong, L. Grosse-Wortmann, S.-J. Yoo, and C. K. Macgowan, “Metric optimized gating for fetal cardiac MRI,” *Magnetic Resonance in Medicine*, vol. 64, pp. 1304–14, 11 2010.

[64] J. Yamamura, B. Schönnagel, M. Tavares De Sousa, C. Much, F. Ueberle, G. Adam, and F. Kording, “Fetal cardiac MRI and left ventricular function assessment using a new gating strategy based on Doppler Ultrasound: Preliminary results,” in *Proceedings of the International Society for Magnetic Resonance in Medicine*, p. 0632, 2015.

[65] C. W. Roy, M. Seed, J. F. P. van Amerom, B. Al Nafisi, L. Grosse-Wortmann, S.-J. Yoo, and C. K. Macgowan, “Dynamic imaging of the fetal heart using metric optimized gating.,” *Magnetic Resonance in Medicine*, vol. 70, pp. 1598–607, 12 2013.

[66] M. Seed, J. F. P. van Amerom, S.-J. Yoo, B. Al Nafisi, L. Grosse-Wortmann, E. Jaeggi, M. S. Jansz, and C. K. Macgowan, “Feasibility of quantification of the distribution of blood flow in the normal human fetal circulation using

CMR: a cross-sectional study.," *Journal of Cardiovascular Magnetic Resonance*, vol. 14, p. 79, 1 2012.

[67] U. Wedegärtner, H. Kooijman, J. Yamamura, M. Frisch, C. Weber, R. Buchert, A. Huff, K. Hecher, and G. Adam, "In vivo MRI measurement of fetal blood oxygen saturation in cardiac ventricles of fetal sheep: a feasibility study.," *Magnetic Resonance in Medicine*, vol. 64, pp. 32–41, 7 2010.

[68] L. Sun, C. K. Macgowan, J. G. Sled, S.-J. Yoo, C. Manlhiot, P. Porayette, L. Grosse-Wortmann, E. Jaeggi, B. W. McCrindle, J. Kingdom, E. Hickey, S. Miller, and M. Seed, "Reduced Fetal Cerebral Oxygen Consumption is Associated With Smaller Brain Size in Fetuses With Congenital Heart Disease," *Circulation*, vol. 131, pp. 1313–1323, 3 2015.

[69] M. Seed, "Fetal Cardiovascular Magnetic Resonance," in *MRI of Fetal and Maternal Diseases in Pregnancy* (G. Masselli, ed.), pp. 183–204, Cham: Springer International Publishing, 2016.

[70] S. Portnoy, M. Seed, J. G. Sled, and C. K. Macgowan, "Non-invasive evaluation of blood oxygen saturation and hematocrit from T 1 and T 2 relaxation times: In-vitro validation in fetal blood," *Magnetic Resonance in Medicine*, vol. 78, pp. 2352–2359, 2 2017.

[71] P. Gowland, "Safety of Fetal MRI Scanning," in *Fetal MRI*, pp. 49–54, Springer, Berlin, Heidelberg, 2011.

[72] J. W. Hand, Y. Li, and J. V. Hajnal, "Numerical study of RF exposure and the resulting temperature rise in the foetus during a magnetic resonance procedure.," *Physics in Medicine and Biology*, vol. 55, pp. 913–30, 2 2010.

[73] International Electrotechnical Commission, "International Electrotechnical Commission 61672-1:2013 Electroacoustics - Sound level meters - Part 1: Specifications," tech. rep., International Electrotechnical Commission, 2013.

[74] D. L. Price, J. P. De Wilde, A. M. Papadaki, J. S. Curran, and R. I. Kitney, "Investigation of acoustic noise on 15 MRI scanners from 0.2 T to 3 T," *Journal of Magnetic Resonance Imaging*, vol. 13, pp. 288–293, 2 2001.

[75] P. Glover, J. Hykin, P. Gowland, J. Wright, I. Johnson, and P. Mansfield, "An assessment of the intrauterine sound intensity level during obstetric echo-planar magnetic resonance imaging.," *The British journal of radiology*, vol. 68, pp. 1090–4, 10 1995.

[76] J.-P. Lecanuet, B. Gautheron, A. Locatelli, B. Schaal, A.-Y. Jacquet, and M.-C. Busnel, "What sounds reach fetuses: Biological and nonbiological modeling of the transmission of pure tones," *Developmental Psychobiology*, vol. 33, pp. 203–219, 11 1998.

[77] K. J. Gerhardt and R. M. Abrams, "Fetal Exposures to Sound and Vibroacoustic Stimulation," *Journal of Perinatology*, vol. 20, pp. S20–S29, 12 2000.

[78] D. Grainger, "Safety Guidelines for Magnetic Resonance Imaging Equipment in Clinical Use," tech. rep., United Kingdom Medicines and Healthcare Products Regulatory Agency, 2015.

[79] F. Daffos, F. Forestier, J. Mac Aleese, C. Aufrant, L. Mandelbrot, E. A. Cabanis, M. T. Iba-Zizen, J. M. Alfonso, and J. Tamraz, "Fetal curarization for prenatal magnetic resonance imaging," *Prenatal Diagnosis*, vol. 8, pp. 311–314, 5 1988.

[80] W. Sepulveda, R. Ximenes, A. E. Wong, F. Sepulveda, P. Martinez-Ten, and R. Ximenes, "Fetal magnetic resonance imaging and three-dimensional ultrasound in clinical practice: applications in prenatal diagnosis.," *Best practice & research. Clinical obstetrics & gynaecology*, vol. 26, pp. 593–624, 10 2012.

[81] P. C. Brugger, "MRI of the Fetal Heart," in *Fetal MRI* (D. Prayer, ed.), Medical Radiology, pp. 247–258, Berlin, Heidelberg: Springer Berlin Heidelberg, 2011.

[82] O. Bieri and K. Scheffler, "Fundamentals of balanced steady state free precession MRI," *Journal of Magnetic Resonance Imaging*, vol. 38, pp. 2–11, 7 2013.

[83] P. C. Brugger, F. Stuhr, C. Lindner, and D. Prayer, "Methods of fetal MR: beyond T2-weighted imaging.," *European Journal of Radiology*, vol. 57, pp. 172–81, 2 2006.

[84] C. Malamateniou, A. K. McGuinness, J. M. Allsop, D. P. O'Regan, M. A. Rutherford, and J. V. Hajnal, "Snapshot Inversion Recovery: An Optimized Single-Shot T1-weighted Inversion-Recovery Sequence for Improved Fetal Brain Anatomic Delineation," *Radiology*, vol. 258, pp. 229–235, 1 2011.

[85] C. Mekkaoui, P. Porayette, M. P. Jackowski, W. J. Kostis, G. Dai, S. Sanders, and D. E. Sosnovik, "Diffusion MRI tractography of the developing human fetal heart.," *PloS one*, vol. 8, p. e72795, 1 2013.

[86] E. Pervolaraki, R. A. Anderson, A. P. Benson, B. Hayes-Gill, A. V. Holden, B. J. R. Moore, M. N. Paley, and H. Zhang, "Antenatal architecture and activity of the human heart.," *Interface focus*, vol. 3, 4 2013.

[87] M. N. J. Paley, J. E. Morris, D. Jarvis, and P. D. Griffiths, "Fetal electrocardiogram (fECG) gated MRI.," *Sensors (Basel, Switzerland)*, vol. 13, pp. 11271–9, 1 2013.

[88] S. Jiang, S. Member, H. Xue, A. Glover, M. Rutherford, D. Rueckert, and J. V. Hajnal, "MRI of moving subjects using multislice Snapshot images with Volume Reconstruction (SVR): Application to fetal, neonatal, and adult brain studies," *IEEE Transactions on Medical Imaging*, vol. 26, no. 7, pp. 967–980, 2007.

[89] F. Rousseau, O. A. Glenn, B. Iordanova, C. Rodriguez-Carranza, D. B. Vigneron, J. A. Barkovich, and C. Studholme, "Registration-based approach for reconstruction of high-resolution in utero fetal MR brain images.," *Academic Radiology*, vol. 13, pp. 1072–81, 9 2006.

[90] A. Gholipour, J. a. Estroff, and S. K. Warfield, "Robust super-resolution volume reconstruction from slice acquisitions: application to fetal brain MRI.," *IEEE Transactions on Medical Imaging*, vol. 29, pp. 1739–58, 10 2010.

[91] M. Kuklisova-Murgasova, G. Quaghebeur, M. A. Rutherford, J. V. Hajnal, and J. A. Schnabel, "Reconstruction of fetal brain MRI with intensity matching and complete outlier removal.," *Medical Image Analysis*, vol. 16, pp. 1550–64, 12 2012.

[92] K. Kim, P. A. Habas, V. Rajagopalan, J. A. Scott, J. M. Corbett-Detig, F. Rousseau, A. J. Barkovich, O. A. Glenn, and C. Studholme, "Bias field inconsistency correction of motion-scattered multislice MRI for improved 3D image reconstruction.," *IEEE Transactions on Medical Imaging*, vol. 30, pp. 1704–12, 9 2011.

[93] A. G. Chandler, R. J. Pinder, T. Netsch, J. A. Schnabel, D. J. Hawkes, D. L. G. Hill, and R. Razavi, "Correction of misaligned slices in multi-slice cardiovascular magnetic resonance using slice-to-volume registration.," *Journal of Cardiovascular Magnetic Resonance*, vol. 10, p. 13, 2008.

[94] A. Elen, J. Hermans, J. Ganame, D. Loeckx, J. Bogaert, F. Maes, and P. Suetens, "Automatic 3-D Breath-Hold Related Motion Correction of Dynamic Multislice MRI," *IEEE Transactions on Medical Imaging*, vol. 29, pp. 868–878, 3 2010.

[95] F. Odille, A. Bustin, B. Chen, P.-a. Vuissoz, and J. Felblinger, "Motion-Corrected, Super-Resolution Reconstruction for High-Resolution 3D Cardiac Cine MRI," in *Medical Image Computing and Computer-Assisted Intervention – MICCAI*, vol. 9351, pp. 435–442, 2015.

[96] M. Jantsch, D. Rueckert, A. N. Price, and J. V. Hajnal, "3D cardiac cine reconstruction from free-breathing 2D real-time image acquisitions using iterative motion correction," in *IEEE International Symposium on Biomedical Imaging*, pp. 812–815, 2013.

[97] M. A. Syed, S. V. Raman, and O. P. Simonetti, eds., *Basic principles of cardiovascular MRI: Physics and imaging technique*. Cham: Springer International Publishing, 2015.

[98] M. Loecher and O. Wieben, "k-Space," in *Basic Principles of Cardiovascular MRI*, pp. 13–23, Cham: Springer International Publishing, 2015.

[99] V. Kuperman, *Magnetic resonance imaging : physical principles and applications*. Academic Press, 2000.

[100] K. P. Pruessmann, "Encoding and reconstruction in parallel MRI," *NMR in Biomedicine*, vol. 19, pp. 288–299, 5 2006.

[101] D. B. Twieg, "The k-trajectory formulation of the NMR imaging process with applications in analysis and synthesis of imaging methods," *Medical Physics*, vol. 10, pp. 610–621, 9 1983.

[102] M. A. Bernstein, K. F. King, and X. J. Zhou, *Handbook of MRI Pulse Sequences*. Elsevier, 2004.

[103] C. E. Hayes and L. Axel, "Noise performance of surface coils for magnetic resonance imaging at 1.5 T," *Medical Physics*, vol. 12, pp. 604–607, 9 1985.

[104] P. B. Roemer, W. A. Edelstein, C. E. Hayes, S. P. Souza, and O. M. Mueller, "The NMR phased array.," *Magnetic Resonance in Medicine*, vol. 16, pp. 192–225, 11 1990.

[105] D. O. Walsh, A. F. Gmitro, and M. W. Marcellin, "Adaptive reconstruction of phased array MR imagery.," *Magnetic Resonance in Medicine*, vol. 43, pp. 682–90, 5 2000.

[106] H. Y. Carr, "Steady-State Free Precession in Nuclear Magnetic Resonance," *Physical Review*, vol. 112, pp. 1693–1701, 12 1958.

[107] A. Oppelt, R. Graumann, H. Barfuss, H. Fischer, W. Hartl, and W. Schajor, "FISP - a new fast MRI sequence," *Electromedia*, vol. 54, pp. 15–18, 1986.

[108] R. Dharmakumar, B. Sharif, and H.-J. Yang, "CMR Pulse Sequences," in *Basic Principles of Cardiovascular MRI*, pp. 25–40, Cham: Springer International Publishing, 2015.

[109] G. J. Stanisz, E. E. Odrobina, J. Pun, M. Escaravage, S. J. Graham, M. J. Bronskill, and R. M. Henkelman, "T1, T2 relaxation and magnetization transfer in tissue at 3T," *Magnetic Resonance in Medicine*, vol. 54, pp. 507–512, 9 2005.

[110] G. A. Wright, B. S. Hu, and A. Macovski, "Estimating oxygen saturation of blood in vivo with MR imaging at 1.5 T," *Journal of Magnetic Resonance Imaging*, vol. 1, pp. 275–283, 5 1991.

[111] S. Portnoy, M. Osmond, M. Y. Zhu, M. Seed, J. G. Sled, and C. K. Macgowan, "Relaxation properties of human umbilical cord blood at 1.5 Tesla.," *Magnetic Resonance in Medicine*, 4 2016.

[112] K. Scheffler and S. Lehnhardt, "Principles and applications of balanced SSFP techniques.," *European Radiology*, vol. 13, pp. 2409–18, 11 2003.

[113] M. Deimling and O. Heid, "Magnetization Prepared True FISP Imaging," in *International Society for Magnetic Resonance in Medicine*, vol. 22, p. 495, 1994.

[114] D. G. Nishimura and S. Vasanawala, "Analysis and Reduction of the Transient Response in SSFP Imaging," in *Proceedings of the International Society for Magnetic Resonance in Medicine*, p. 301, 2000.

[115] J. Hennig, O. Speck, and K. Scheffler, "Optimization of signal behavior in the transition to driven equilibrium in steady-state free precession sequences," *Magnetic Resonance in Medicine*, vol. 48, pp. 801–809, 11 2002.

[116] P. Le Roux, "Simplified model and stabilization of SSFP sequences," *Journal of Magnetic Resonance*, vol. 163, pp. 23–37, 7 2003.

[117] M. Markl and N. J. Pelc, "On flow effects in balanced steady-state free precession imaging: Pictorial description, parameter dependence, and clinical implications," *Journal of Magnetic Resonance Imaging*, vol. 20, pp. 697–705, 10 2004.

[118] O. Bieri and K. Scheffler, "Flow compensation in balanced SSFP sequences," *Magnetic Resonance in Medicine*, vol. 54, pp. 901–907, 10 2005.

[119] W. R. Overall, D. G. Nishimura, and B. S. Hu, “Fast phase-contrast velocity measurement in the steady state,” *Magnetic Resonance in Medicine*, vol. 48, pp. 890–898, 11 2002.

[120] M. Markl, M. Alley, and N. Pelc, “Balanced phase-contrast steady-state free precession (PC-SSFP): A novel technique for velocity encoding by gradient inversion,” *Magnetic Resonance in Medicine*, vol. 49, pp. 945–952, 5 2003.

[121] J. Hennig, “K-space sampling strategies.,” *European Radiology*, vol. 9, pp. 1020–31, 1 1999.

[122] J. Fessler and B. Sutton, “Nonuniform fast fourier transforms using min-max interpolation,” *IEEE Transactions on Signal Processing*, vol. 51, pp. 560–574, 2 2003.

[123] V. Rasche, R. Proksa, R. Sinkus, P. Bornert, and H. Eggers, “Resampling of data between arbitrary grids using convolution interpolation,” *IEEE Transactions on Medical Imaging*, vol. 18, pp. 385–392, 5 1999.

[124] C. B. Ahn, J. H. Kim, and Z. H. Cho, “High-Speed Spiral-Scan Echo Planar NMR Imaging-I,” *IEEE Transactions on Medical Imaging*, vol. 5, no. 1, pp. 2–7, 1986.

[125] C. H. Meyer, B. S. Hu, D. G. Nishimura, and A. Macovski, “Fast Spiral Coronary Artery Imaging,” *Magnetic Resonance in Medicine*, vol. 28, pp. 202–213, 12 1992.

[126] X. Feng, M. Salerno, C. M. Kramer, and C. H. Meyer, “Non-Cartesian balanced steady-state free precession pulse sequences for real-time cardiac MRI,” *Magnetic Resonance in Medicine*, vol. 75, pp. 1546–1555, 4 2016.

[127] P. C. Lauterbur, “Image Formation by Induced Local Interactions: Examples Employing Nuclear Magnetic Resonance,” *Nature*, vol. 242, pp. 190–191, 3 1973.

[128] S. Winkelmann, T. Schaeffter, T. Koehler, H. Eggers, and O. Doessel, “An optimal radial profile order based on the Golden Ratio for time-resolved MRI.,” *IEEE Transactions on Medical Imaging*, vol. 26, pp. 68–76, 1 2007.

[129] S. Wundrak, J. Paul, J. Ulrici, E. Hell, M.-A. Geibel, P. Bernhardt, W. Rottbauer, and V. Rasche, “Golden ratio sparse MRI using tiny golden angles,” *Magnetic Resonance in Medicine*, vol. 75, pp. 2372–2378, 6 2016.

[130] K. Scheffler and J. Hennig, “Reduced circular field-of-view imaging,” *Magnetic Resonance in Medicine*, vol. 40, pp. 474–480, 9 1998.

[131] D. Wang, W. Strugnell, G. Cowin, D. M. Doddrell, and R. Slaughter, "Geometric distortion in clinical MRI systems: Part I: evaluation using a 3D phantom," *Magnetic Resonance Imaging*, vol. 22, pp. 1211–1221, 11 2004.

[132] F. W. Wehrli, T. G. Perkins, A. Shimakawa, and F. Roberts, "Chemical shift-induced amplitude modulations in images obtained with gradient refocusing," *Magnetic Resonance Imaging*, vol. 5, pp. 157–158, 1 1987.

[133] G. Iacobellis and H. J. Willens, "Echocardiographic epicardial fat: a review of research and clinical applications.," *Journal of the American Society of Echocardiography*, vol. 22, pp. 1311–9, 12 2009.

[134] M. Zaitsev, J. Maclaren, and M. Herbst, "Motion artifacts in MRI: A complex problem with many partial solutions.," *Journal of Magnetic Resonance Imaging*, vol. 42, pp. 887–901, 10 2015.

[135] A. D. Scott, J. Keegan, and D. N. Firmin, "Motion in Cardiovascular MR," *Radiology*, vol. 250, no. 2, pp. 331–351, 2009.

[136] D. Atkinson, D. J. Larkman, P. G. Batchelor, D. L. G. Hill, and J. V. Hajnal, "Coil-based artifact reduction.," *Magnetic Resonance in Medicine*, vol. 52, pp. 825–30, 10 2004.

[137] F. Odille, S. Uribe, P. G. Batchelor, C. Prieto, T. Schaeffter, and D. Atkinson, "Model-based reconstruction for cardiac cine MRI without ECG or breath holding.," *Magnetic Resonance in Medicine*, vol. 63, pp. 1247–57, 5 2010.

[138] M. S. Hansen, T. S. Sørensen, A. E. Arai, and P. Kellman, "Retrospective reconstruction of high temporal resolution cine images from real-time MRI using iterative motion correction.," *Magnetic Resonance in Medicine*, vol. 68, pp. 741–50, 9 2012.

[139] L. Feng, L. Axel, H. Chandarana, K. T. Block, D. K. Sodickson, and R. Otazo, "XD-GRASP: Golden-angle radial MRI with reconstruction of extra motion-state dimensions using compressed sensing," *Magnetic Resonance in Medicine*, vol. 75, pp. 775–788, 2 2016.

[140] D. Noll, D. Nishimura, and A. Macovski, "Homodyne detection in magnetic resonance imaging," *IEEE Transactions on Medical Imaging*, vol. 10, pp. 154–163, 6 1991.

[141] E. Haacke, E. Lindskogj, and W. Lin, "A fast, iterative, partial-fourier technique capable of local phase recovery," *Journal of Magnetic Resonance*, vol. 92, pp. 126–145, 3 1991.

[142] S. D. Serai, A. C. Merrow, and B. M. Kline-Fath, "Fetal MRI on a multi-element digital coil platform.," *Pediatric radiology*, vol. 43, pp. 1213–7, 9 2013.

[143] K. P. Pruessmann, M. Weiger, M. B. Scheidegger, and P. Boesiger, "SENSE: sensitivity encoding for fast MRI.," *Magnetic Resonance in Medicine*, vol. 42, pp. 952–62, 11 1999.

[144] M. A. Griswold, P. M. Jakob, R. M. Heidemann, M. Nittka, V. Jellus, J. Wang, B. Kiefer, and A. Haase, "Generalized autocalibrating partially parallel acquisitions (GRAPPA)," *Magnetic Resonance in Medicine*, vol. 47, pp. 1202–1210, 6 2002.

[145] K. P. Pruessmann, M. Weiger, P. Börnert, and P. Boesiger, "Advances in sensitivity encoding with arbitrary k-space trajectories.," *Magnetic resonance in medicine*, vol. 46, pp. 638–51, 10 2001.

[146] N. Seiberlich, P. Ehses, J. Duerk, R. Gilkeson, and M. Griswold, "Improved radial GRAPPA calibration for real-time free-breathing cardiac imaging," *Magnetic Resonance in Medicine*, vol. 65, pp. 492–505, 2 2011.

[147] M. Blaimer, F. Breuer, M. Mueller, R. M. Heidemann, M. a. Griswold, and P. M. Jakob, "Smash, Sense, Pils, Grappa," *Topics in Magnetic Resonance Imaging*, vol. 15, pp. 223–236, 8 2004.

[148] M. Lustig and J. M. Pauly, "SPIRiT: Iterative self-consistent parallel imaging reconstruction from arbitrary k-space.," *Magnetic Resonance in Medicine*, vol. 64, pp. 457–71, 8 2010.

[149] J. Tran-Gia, H. Köstler, and N. Seiberlich, "Fast Imaging," in *Basic Principles of Cardiovascular MRI*, pp. 63–86, Cham: Springer International Publishing, 2015.

[150] P. Kellman, F. H. Epstein, and E. R. McVeigh, "Adaptive sensitivity encoding incorporating temporal filtering (TSENSE).," *Magnetic Resonance in Medicine*, vol. 45, pp. 846–52, 5 2001.

[151] F. a. Breuer, P. Kellman, M. a. Griswold, and P. M. Jakob, "Dynamic autocalibrated parallel imaging using temporal GRAPPA (TGRAPPA).," *Magnetic Resonance in Medicine*, vol. 53, pp. 981–5, 4 2005.

[152] J. Tsao and S. Kozerke, "MRI temporal acceleration techniques," *Journal of Magnetic Resonance Imaging*, vol. 36, pp. 543–60, 9 2012.

[153] J. Tsao, P. Boesiger, and K. P. Pruessmann, “k-t BLAST and k-t SENSE: dynamic MRI with high frame rate exploiting spatiotemporal correlations,” *Magnetic Resonance in Medicine*, vol. 50, pp. 1031–42, 11 2003.

[154] F. Huang, J. Akao, S. Vijayakumar, G. R. Duensing, and M. Limkeman, “k-t GRAPPA: a k-space implementation for dynamic MRI with high reduction factor.,” *Magnetic resonance in medicine*, vol. 54, pp. 1172–84, 11 2005.

[155] H. Pedersen, S. Kozerke, S. Ringgaard, K. Nehrke, and W. Y. Kim, “k-t PCA: temporally constrained k-t BLAST reconstruction using principal component analysis.,” *Magnetic resonance in medicine*, vol. 62, pp. 706–16, 9 2009.

[156] S. J. Malik, S. Schmitz, D. O’Regan, D. J. Larkman, and J. V. Hajnal, “x-f Choice: reconstruction of undersampled dynamic MRI by data-driven alias rejection applied to contrast-enhanced angiography.,” *Magnetic resonance in medicine*, vol. 56, pp. 811–23, 10 2006.

[157] M. Lustig, J. M. Santos, D. L. Donoho, and J. M. Pauly, “k-t SPARSE: High frame rate dynamic MRI exploiting spatio-temporal sparsity,” in *International Society for Magnetic Resonance in Medicine*, p. 2420, 2006.

[158] H. Jung, K. Sung, K. S. Nayak, E. Y. Kim, and J. C. Ye, “k-t FOCUSS: a general compressed sensing framework for high resolution dynamic MRI.,” *Magnetic Resonance in Medicine*, vol. 61, pp. 103–16, 1 2009.

[159] I. P. Ponce, M. Blaimer, F. A. Breuer, M. A. Griswold, P. M. Jakob, and P. Kellman, “Auto-calibration approach for k-t SENSE.,” *Magnetic resonance in medicine*, vol. 71, pp. 1123–9, 3 2014.

[160] J. Tsao, S. Kozerke, P. Boesiger, and K. P. Pruessmann, “Optimizing spatiotemporal sampling for k-t BLAST and k-t SENSE: application to high-resolution real-time cardiac steady-state free precession.,” *Magnetic resonance in medicine*, vol. 53, pp. 1372–82, 6 2005.

[161] M. Lustig, D. Donoho, and J. M. Pauly, “Sparse MRI: The application of compressed sensing for rapid MR imaging.,” *Magnetic Resonance in Medicine*, vol. 58, pp. 1182–95, 12 2007.

[162] S.-Z. Dong, M. Zhu, and F. Li, “Preliminary experience with cardiovascular magnetic resonance in evaluation of fetal cardiovascular anomalies.,” *Journal of Cardiovascular Magnetic Resonance*, vol. 15, p. 40, 1 2013.

[163] S. Fratz, T. Chung, G. F. Greil, M. M. Samyn, A. M. Taylor, E. R. Valsangiacomo Buechel, S.-J. Yoo, and A. J. Powell, "Guidelines and protocols for cardiovascular magnetic resonance in children and adults with congenital heart disease: SCMR expert consensus group on congenital heart disease.," *Journal of Cardiovascular Magnetic Resonance*, vol. 15, p. 51, 1 2013.

[164] J. F. van Amerom, A. N. Price, P. Aljabar, S. J. Malik, C. Malamateniou, K. Pushparajah, J. M. Allsop, M. J. Fox, M. A. Rutherford, R. Razavi, and J. V. Hajnal, "Fetal cardiac cine imaging using realtime MRI and image-based spatiotemporal motion-correction," in *European Society for Magnetic Resonance in Medicine and Biology*, pp. 85–86, 2015.

[165] J. F. P. van Amerom, M. Kuklisova Murgasova, A. N. Price, S. J. Malik, P. Aljabar, D. A. Lloyd, K. Pushparajah, M. Lohezic, M. J. Fox, J. M. Allsop, M. A. Rutherford, R. Razavi, and J. V. Hajnal, "Fetal cardiac cine imaging from motion-corrected super-resolution reconstruction of highly-accelerated real-time MRI," in *Proceedings of the International Society for Magnetic Resonance in Medicine*, p. 458, 2016.

[166] J. F. van Amerom, D. A. Lloyd, M. K. Murgasova, A. N. Price, S. J. Malik, P. Aljabar, J. M. Allsop, A. Gomes, M. A. Rutherford, K. Pushparajah, R. Razavi, and J. V. Hajnal, "Fetal cardiac volume reconstruction from motion-corrected multi-slice dynamic MRI," in *International Society for Magnetic Resonance in Medicine*, p. 3263, 2017.

[167] J. F. van Amerom, D. F. Lloyd, A. N. Price, M. Kuklisova Murgasova, P. Aljabar, S. J. Malik, M. Lohezic, M. A. Rutherford, K. Pushparajah, R. Razavi, and J. V. Hajnal, "Fetal cardiac cine imaging using highly accelerated dynamic MRI with retrospective motion correction and outlier rejection," *Magnetic Resonance in Medicine*, vol. 79, pp. 327–338, 1 2018.

[168] J. F. P. van Amerom, D. F. A. Lloyd, M. K. Murgasova, A. N. Price, S. J. Malik, M. V. Poppel, K. Pushparajah, M. A. Rutherford, R. Razavi, and J. V. Hajnal, "Fetal whole-heart 3D cine reconstruction using motion-corrected multi-slice dynamic imaging," in *International Society for Magnetic Resonance in Medicine*, p. 1052, 2018.

[169] K. Keraudren, B. Kainz, O. Oktay, V. Kyriakopoulou, M. Rutherford, J. V. Hajnal, and D. Rueckert, "Automated Localization of Fetal Organs in MRI Using Random Forests with Steerable Features," in *Medical Image Computing and Computer-Assisted Intervention – MICCAI*, vol. 9351, pp. 620–627, Springer, Cham, 10 2015.

[170] R. Demesmaeker, T. Kober, J. Yerly, J. Chaptinel, M. Prsa, Y. Mivelaz, L. Alamo, G. Berchier, C. Rohner, M. Stuber, and D. Piccini, "Automated Heartbeat Detection for Self-Gated Fetal Cardiac MRI," in *International Society for Magnetic Resonance in Medicine*, p. 0633, 2017.

[171] P. Charbonnier, L. Blanc-Feraud, G. Aubert, and M. Barlaud, "Deterministic edge-preserving regularization in computed imaging," *IEEE Transactions on Image Processing*, vol. 6, no. 2, pp. 298–311, 1997.

[172] B. Kainz, M. Steinberger, W. Wein, M. Murgasova, C. Malamateniou, K. Keraudren, P. Aljabar, M. Rutherford, J. V. Hajnal, D. Rueckert, M. Kuklisova-Murgasova, C. Malamateniou, K. Keraudren, T. Torsney-Weir, M. Rutherford, P. Aljabar, J. V. Hajnal, and D. Rueckert, "Fast Volume Reconstruction from Motion Corrupted Stacks of 2D Slices.," *IEEE transactions on medical imaging*, vol. 34, pp. 1901–1913, 3 2015.

[173] M. Alexa, Marc, Alexa, and Marc, "Linear combination of transformations," in *Computer Graphics and Interactive Techniques*, vol. 21, p. 380, ACM Press, 2002.

[174] P. Aljabar, K. K. Bhatia, M. Murgasova, J. V. Hajnal, J. P. Boardman, L. Srinivasan, M. A. Rutherford, L. E. Dyet, A. D. Edwards, and D. Rueckert, "Assessment of brain growth in early childhood using deformation-based morphometry.," *NeuroImage*, vol. 39, pp. 348–58, 1 2008.

[175] P. J. Rousseeuw and C. Croux, "Alternatives to the Median Absolute Deviation," *Journal of the American Statistical Association*, vol. 88, pp. 1273–1283, 12 1993.

[176] "iFIND: intelligent Fetal Imaging and Diagnosis." www.ifindproject.com/.

[177] L. Wissmann, C. Santelli, W. P. Segars, and S. Kozerke, "MRXCAT: Realistic Numerical Phantoms for Cardiac Magnetic Resonance Imaging," *Journal of Cardiovascular Magnetic Resonance*, vol. 16, p. 63, 8 2014.

[178] W. P. Segars, G. Sturgeon, S. Mendonca, J. Grimes, and B. M. W. Tsui, "4D XCAT phantom for multimodality imaging research," *Medical Physics*, vol. 37, no. 9, p. 4902, 2010.

[179] "The Visible Human Project." www.nlm.nih.gov/research/visible/visible_human.html.

[180] F. Kording, J. Yamamura, M. T. de Sousa, C. Ruprecht, E. Hedström, A. H. Aletras, P. Ellen Grant, A. J. Powell, K. Fehrs, G. Adam, H. Kooijman, and B. P.

Schoennagel, “Dynamic fetal cardiovascular magnetic resonance imaging using Doppler ultrasound gating,” *Journal of Cardiovascular Magnetic Resonance*, vol. 20, p. 17, 12 2018.

[181] R. S. Beroukhim, A. Prakash, E. R. V. Buechel, J. R. Cava, A. L. Dorfman, P. Festa, A. M. Hlavacek, T. R. Johnson, M. S. Keller, R. Krishnamurthy, N. Misra, S. Moniotte, W. J. Parks, A. J. Powell, B. D. Soriano, M. B. Srichai, S.-J. Yoo, J. Zhou, and T. Geva, “Characterization of cardiac tumors in children by cardiovascular magnetic resonance imaging: a multicenter experience.,” *Journal of the American College of Cardiology*, vol. 58, pp. 1044–54, 8 2011.

[182] L. Zhao, Y. Wu, S. Chen, Y. Ren, P. Chen, J. Niu, C. Li, and K. Sun, “Feasibility Study on Prenatal Cardiac Screening Using Four-Dimensional Ultrasound with Spatiotemporal Image Correlation: A Multicenter Study,” *PLOS ONE*, vol. 11, p. e0157477, 6 2016.

[183] D. F. A. Lloyd, B. Kainz, J. F. P. V. Amerom, K. Pushparajah, J. M. Simpson, V. Zidere, O. Miller, G. K. Sharland, T. Zhang, M. Lohezic, J. M. Allsop, M. J. Fox, C. Malamateniou, M. A. Rutherford, J. V. Hajnal, and R. Razavi, “Three-Dimensional Modelling of the Fetal Vasculature from Prenatal MRI using Motion-Corrected Slice-to-Volume Registration,” in *International Society for Magnetic Resonance in Medicine*, p. 1677, 2016.

[184] B. Madore, G. H. Glover, and N. J. Pelc, “Unaliasing by fourier-encoding the overlaps using the temporal dimension (UNFOLD), applied to cardiac imaging and fMRI.,” *Magnetic Resonance in Medicine*, vol. 42, pp. 813–28, 11 1999.

[185] M. Blaimer, I. P. Ponce, F. A. Breuer, P. M. Jakob, M. A. Griswold, and P. Kellman, “Temporal filtering effects in dynamic parallel MRI.,” *Magnetic resonance in medicine*, vol. 66, pp. 192–8, 7 2011.

[186] A. N. Price, L. Cordero-Grande, S. J. Malik, and J. V. Hajnal, “Accelerated Cine Imaging of the Heart using Blipped Multiband SSFP,” in *International Society for Magnetic Resonance in Medicine*, p. 0631, 2017.

[187] L. H. Jackson, A. N. Price, J. Hutter, L. Cordero-grande, A. Ho, P. J. Slator, A. D. Santo, J. F. van Amerom, M. Murgasova, L. Mccabe, M. A. Rutherford, and J. V. Hajnal, “Respiration resolved imaging using continuous steady state multiband excitation with linear frequency sweeps,” in *International Society for Magnetic Resonance in Medicine*, p. 4134, 2018.

[188] A. C. Larson, R. D. White, G. Laub, E. R. McVeigh, D. Li, and O. P. Simonetti, "Self-gated cardiac cine MRI.," *Magnetic resonance in medicine*, vol. 51, pp. 93–102, 1 2004.

[189] G. M. Nijm, A. V. Sahakian, S. Swiryn, J. C. Carr, J. J. Sheehan, and A. C. Larson, "Comparison of self-gated cine MRI retrospective cardiac synchronization algorithms," *Journal of Magnetic Resonance Imaging*, vol. 28, pp. 767–772, 9 2008.

[190] J.-F. Nielsen and K. S. Nayak, "Referenceless phase velocity mapping using balanced SSFP," *Magnetic Resonance in Medicine*, vol. 61, pp. 1096–1102, 5 2009.

[191] F. Kording, B. P. Schoennagel, M. Tavares De Sousa, K. Fehrs, G. Adam, J. Yamamura, and C. Ruprecht, "Evaluation of a Portable Doppler Ultrasound Gating Device for Fetal Cardiac MR Imaging: Initial Results at 1.5T and 3T," *Magnetic Resonance in Medical Sciences*, 2018.

[192] K. Haris, E. Hedström, F. Kording, S. Bidhult, F. Testud, K. Steding-ehrenborg, C. Ruprecht, E. Heiberg, H. Arheden, and A. Aletras, "Feasibility of Free-Breathing Fetal Cine Cardiac MRI based on Doppler Ultrasound , Compressed Sensing and Motion Compensation," in *International Society for Magnetic Resonance in Medicine*, p. 0760, 2018.

[193] E. Hedström, K. Steding-ehrenborg, S. Bidhult, F. Kording, and A. H. Aletras, "Quantitative phase-contrast CMR of blood ow in fetal vessels gated by Doppler ultrasound : comparison with metric optimized gating The aims of the current study were therefore to evaluate the DUS method for fetal quantitative blood ow in the fetal descend," in *International Society for Magnetic Resonance in Medicine*, p. 2944, 2018.

[194] C. W. Roy, M. Seed, and C. K. Macgowan, "Accelerated MRI of the fetal heart using compressed sensing and metric optimized gating," *Magnetic Resonance in Medicine*, vol. 77, pp. 2125–2135, 6 2017.

[195] C. W. Roy, M. Seed, J. C. Kingdom, and C. K. Macgowan, "Motion compensated cine CMR of the fetal heart using radial undersampling and compressed sensing," *Journal of Cardiovascular Magnetic Resonance*, vol. 19, no. 1, p. 29, 2017.

[196] K. Haris, E. Hedström, S. Bidhult, F. Testud, N. Maglaveras, E. Heiberg, S. R. Hansson, H. Arheden, and A. H. Aletras, "Self-gated fetal cardiac MRI with

tiny golden angle iGRASP: A feasibility study," *Journal of Magnetic Resonance Imaging*, 2 2017.

[197] J. Chaptinel, J. Yerly, Y. Mivelaz, M. Prsa, L. Alamo, Y. Vial, G. Berchier, C. Rohner, F. Gudinchet, and M. Stuber, "Fetal cardiac cine magnetic resonance imaging in utero," *Scientific Reports*, vol. 7, p. 15540, 12 2017.

[198] C. W. Roy, M. Seed, and C. K. Macgowan, "Preliminary Experience Using Motion-Robust Dynamic MRI to Visualize Fetal Congenital Heart Disease : Comparison to Static MRI," in *International Society for Magnetic Resonance in Medicine*, vol. 39, p. 4815, 2017.

[199] C. Roy, M. Seed, and C. Macgowan, "Accelerated phase contrast measurements of fetal blood flow using compressed sensing," in *Journal of Cardiovascular Magnetic Resonance*, vol. 18, p. P30, BioMed Central, 1 2016.

[200] D. S. Goolaub, C. Roy, D. Sussman, M. Seed, and C. Macgowan, "Rapid single slice multidimensional fetal flow imaging with MRI," in *International Society for Magnetic Resonance in Medicine*, p. 4565, 2018.

[201] F. Kording, B. P. Schoennagel, C. Ruprecht, D. Giese, E. Heiberg, and M. Tavares, "Feasibility of 4D phase-contrast MRI for the assessment of blood ow in the fetal aorta using Doppler ultrasound gating : preliminary results," in *International Society for Magnetic Resonance in Medicine*, p. 3438, 2018.

[202] M. Spatz, P. Garcia-Polo, B. Keil, C. Ha, and L. L. Wald, "A 64 channel 3T array coil for highly accelerated fetal imaging at 22 weeks of pregnancy," in *International Society for Magnetic Resonance in Medicine*, p. 1220, 2017.

[203] Q. Chen, G. Xie, C. Luo, X. Yang, J. Zhu, J. Lee, S. Su, D. Liang, X. Zhang, X. Liu, Y. Li, and H. Zheng, "A Dedicated 36-channel Receive Array for Fetal MRI at 3 T," *IEEE Transactions on Medical Imaging*, pp. 1–1, 2018.